Phase Transitions Between Asynchronous and Synchronous Neural Dynamics

Theoretical Insight Into the Mechanisms Behind Neural Oscillations in Parkinson's Disease

Von der Fakultät für Physik und Geowissenschaften
der Universität Leipzig
genehmigte
Dissertation
zur Erlangung des akademischen Grades
Doktor der Naturwissenschaften
Dr. rer. nat.

vorgelegt von M. Sc. Richard Gast
geb. am 09.07.1990 in Bautzen.

Gutachter:
Prof. Dr. Harald E. Möller
Prof. Dr. Gustavo Deco

Tag der Verleihung: 15.11.2021

Bibliographische Beschreibung:

Gast, Richard
Phase Transitions Between Asynchronous and Synchronous Neural Dynamics
Universität Leipzig, Dissertation
127 S., 280 Lit., 25 Abb., 1 Tab.

Referat:

In Parkinson's disease (PD) treten Zustände verstärkter neuronaler Synchronisierung in großen Teilen des Gehirns auf. Diese Zustände gehen sowohl mit motorischen Einschränkungen als auch mit dem Absterben dopaminerger Neurone einher. In dieser Dissertation befassen wir uns mit der Frage, wie die verringerte dopaminerge Innervation der Basalganglien (BG) parkinsonsche Synchronisierung beeinflusst. Dazu entwickeln wir Netzwerkmodelle der BG und untersuchen sie mittels Bifurkationsanalyse. Zuerst leiten wir Mean-Field Modelle her, welche verschiedene Formen von Kurzzeitplastizität berücksichtigen. Wir zeigen, dass Kurzzeitplastizität zu stark synchronisiertem, periodischem Bursting führen kann, und diskutieren die Relevanz dieses Burstings für parkinsonsche Oszillationen. Desweiteren zeigen wir, dass die typischen parkinsonschen Oszillationen nicht allein aus dem globus pallidus pars externa (GPe), einem zentralen Nukleus der BG, hervorgehen können. Dennoch scheint der GPe zum Auftreten von Kreuzfrequenzkopplungen beizutragen, welche in parkinsonschen Oszillationen beobachtet wurden. Abschließend beschreiben wir eine frei zugängliche Python Software, welche wir zur Implementierung und Analyse von Mean-Field Modellen neuronaler Dynamiken entwickelt haben. Somit wurden durch diese Dissertation sowohl Erkenntnisse über Synchronisierung der BG gewonnen, als auch mathematische Grundlagen und Software für zukünftige Studien neuronaler Synchronisierung geschaffen.

Abstract:

In Parkinson's disease (PD), large parts of the brain transition into states of enhanced neural synchronization. These phase transitions have been associated with the death of dopaminergic neurons as well as with impaired motor function. In this thesis, we address the much-debated question of how parkinsonian synchronization depends on dopamine depletion in the basal ganglia (BG). To this end, we develop spiking neural network (SNN) models of BG circuits and study them via bifurcation analysis. First, we derive mean-field models that allow to account for various forms of short-term plasticity (STP) in SNNs. We show that such STP mechanisms can lead to highly synchronous, periodic bursting dynamics and discuss the relevance of this bursting regime for PD. Second, we find that the globus pallidus pars externa (GPe), an important part of the BG, cannot cause parkinsonian oscillations autonomously. However, our results suggest that the GPe may contribute to the emergence of cross-frequency coupling that has been reported for parkinsonian oscillations. Finally, we describe an open-source Python toolbox that we developed to implement and analyze mean-field models of neural dynamics. Together, this thesis provides insight into BG synchronization processes as well as the mathematical basis and software for future studies of neural synchronization.

Titelblatt der Zusammenfassung

Zusammenfassung der Dissertation

Phase Transitions Between Asynchronous and Synchronous Neural Dynamics -
Theoretical Insight Into the Mechanisms Behind Neural Oscillations in Parkinson's Disease

Von der Fakultät für Physik und Geowissenschaften der Universität Leipzig
eingereicht von

M. Sc. / Richard / Gast

angefertigt an

Brain Networks Group / Max Planck Institute for Human Cognitive and Brain Sciences

Juli 2021

Summary:

Introduction: The brain is a complex dynamical system, composed of a large number of interconnected neurons ($\approx 10^{10}$). Different brain functions have been associated with different spatiotemporal patterns of neural activity and interactions. Such spatiotemporal patterns can be perceived as emergent, macroscopic phenomena, and qualitative changes between these patterns can be viewed as phase transitions of brain dynamics. The main phase transition that has been employed to explain brain function and dysfunction is the phase transition from asynchronous to synchronous neural dynamics. In Parkinson's disease (PD), large parts of the basal ganglia (BG), a set of interconnected sub-cortical nuclei in the brain, transition from mostly asynchronous dynamics (healthy state) to synchronized dynamics (pathological state). This synchronous, pathological state of PD is characterized by an increased power in the beta frequency band (12-30 Hz) and an increased modulation of amplitudes of high-frequency gamma oscillations (> 30 Hz) by the phase of beta oscillations. The neural mechanisms behind the parkinsonian changes of neural synchronization processes in the BG are a matter of on-going research.
Motivation: Various attempts have been made to gain insight into these mechanisms by analyzing the conditions under which mathematical models of the BG expressed beta oscillations. Unfortunately, the different mathematical models that have been applied in this regard delivered inconsistent results across models. An important factor that limits the comparability of these models is the scale at which they describe neural activity. Previous BG models either considered spiking neural network (SNN)s that were substantially smaller than their biological counterpart or neural mass models that cannot account for spike synchronization mechanisms. Both approaches may fail to capture neural synchronization processes in the BG that emerge due to the collective interactions of many spiking neurons. In this work, we aimed to address these problems by (1) developing mathematical models that allow to study neural synchronization

processes in SNNs at the scale of neural populations, and (2) by applying these models to the study of parkinsonian oscillations in the BG.

Results: To address goal (1), we applied the Ott-Antonsen (OA) ansatz that allows to derive exact mean-field equations for the dynamics of networks of coupled oscillators. Our results show that this ansatz can be applied to networks of quadratic integrate-and-fire (QIF) neurons subject to different short-term plasticity (STP) mechanisms, and indicate that these STP mechanisms play an important role in neural synchronization processes:

- For two types of STP, spike-frequency adaptation (SFA) and a neuron-wide form of synaptic depression (SD), we derive and validate exact, closed-form mean-field equations.
- In the case of pre-synaptic short-term plasticity, we provide different mean-field approximations that we compare with respect to their accuracy and we discuss the mathematical problems that would need to be solved to derive exact mean-field equations.
- Using bifurcation analysis, we find that all of these STP mechanisms can induce states of strong synchronization, reminiscent of population bursting.

We discuss the implications of these findings for the modeling of parkinsonian oscillations as well as neural synchronization processes in general.

With respect to goal (2), we studied the role of the globus pallidus pars externa (GPe), a main nucleus of the BG, in the generation of parkinsonian oscillations. To this end, we developed an exact mean-field model of the GPe that accounts for the existence of two major neuron types in the GPe (prototypical and arkypallidal neurons) as well as for the synaptic interactions between these neuron types. The results of our model analysis suggest that this model can account for various characteristics of neural activity in the GPe and that parkinsonian oscillation generation requires extended BG networks instead of the mere GPe:

- We find that the GPe cannot generate parkinsonian beta oscillations autonomously in PD, but may generate gamma oscillations with a frequency of approximately 50-60 Hz.
- The amplitude of these gamma oscillations can undergo strong modulations when the GPe is subject to periodic synaptic input from other BG structures.

We discuss the implications of the latter for the emergence of beta-gamma phase-amplitude coupling in PD.

As a final result, we describe PyRates, an open-source Python toolbox that we developed for implementing and analyzing custom mean-field models of neural activity. We introduce the mathematical formalism, the user interfaces, and pre-implemented models in this software. Additionally, we demonstrate how the mean-field models we used and developed throughout this work can be implemented and examined via PyRates. This allows to replicate and extend our work in future studies.

In conclusion, we provide new mathematical models and software solutions for the study of SNNs subject to STP mechanisms. We applied these tools to gain insight into the phase transitions of the GPe in PD. Together, this work provides a broad basis for future studies of neural synchronization processes in the BG and other brain systems via mean-field equations of SNNs.

List of publications:

1. Leon R. Sütfeld, Richard Gast, Peter König and Gordon Pipa. "Using Virtual Reality to Assess Ethical Decisions in Road Traffic Scenarios: Applicability of Value-of-Life-Based Models and Influences of Time Pressure". In: *Frontiers in behavioral neuroscience* 11 (July 2017), p. 122. ISSN: 1662-5153. DOI: 10.3389/fnbeh.2017.00122.
    - I performed the statistical analysis.
    - My co-authors and I contributed equally to the study design and hypothesis generation.
    - I contributed to the data collection and processing.
2. Holger Finger et al. “Probing neural networks for dynamic switches of communication pathways”. In: *PLOS Computational Biology* 15.12 (Dec. 2019), e1007551. ISSN: 1553-7358. DOI: 10.1371/journal.pcbi.1007551.
    - Holger Finger and I contributed equally to the model simulations and analyses.
    - Holger Finger and I contributed equally to the design and ideas of this study.
    - I drafted approximately two thirds of the manuscript.
3. Richard Gast et al. “PyRates—A Python framework for rate-based neural simulations”. In: *PLOS ONE* 14.12 (Dec. 2019), e0225900. ISSN: 1932-6203. DOI: 10.1371/journal.pone.0225900.
    - **I used this publication for chapter 5 of my thesis.**
    - I was and am the main developer of PyRates, the software described in the paper.
    - I drafted the following sections: Abstract, introduction, neural population models, results, discussion.
    - I performed all numerical model analyses and generated all the model simulation results.
4. Konstantin Weise et al. “Pygpc: A sensitivity and uncertainty analysis toolbox for Python”. In: *SoftwareX* 11 (Jan. 2020), p. 100450. ISSN: 2352-7110. DOI:10.1016/j.softx.2020.100450.
    - I contributed to the interface between Pygpc and PyRates.
    - I performed the numerical simulations of the employed neural mass models.
    - Konstantin Weise and I contributed equally to section 3.
5. Richard Gast, Helmut Schmidt, and Thomas R. Knösche. “A Mean-Field Description of Bursting Dynamics in Spiking Neural Networks with Short-Term Adaptation”. In: *Neural Computation* 32.9 (July 2020), pp. 1615–1634. ISSN: 0899-7667. DOI: 10.1162/neco_a_01300.
    - **I used this publication for chapter 3 of my thesis.**

- I drafted the following sections: Abstract, introduction, model definition, synaptic depression, effects of SFA, finite size effects, discussion.
- I performed all bifurcation analyses and model simulations reported in this paper.
- I created all the data and figures presented in this paper.
- I am the main contributor with respect to the design and ideas of this study.

6. Ruxue Gong et al. “Spatiotemporal features of β-γ phase-amplitude coupling in Parkinson’s disease derived from scalp EEG”. In: *Brain* 144.2 (Feb. 2021), pp. 487–503. ISSN: 0006-8950. DOI:10.1093/brain/awaa400.

    - I contributed to the draft of the manuscript.
    - I contributed to the discussion of the neurobiological correlates of EEG phase-amplitude coupling.

7. Richard Gast et al. “On the role of arkypallidal and prototypical neurons for phase transitions in the external pallidum”. In: *Journal of Neuroscience* (June 2021), ISSN: 0270-6474, 1529-2401. DOI:10.1523/JNEUROSCI.0094-21.2021.

    - **I used this publication for chapter 4 of my thesis.**
    - I drafted the entire manuscript.
    - I performed all bifurcation analyses and model simulations reported in this paper.
    - I created all figures and the corresponding data reported in this paper.
    - I am the main contributor with respect to the design and ideas of this study.

8. Richard Gast, Thomas R. Knösche, and Helmut Schmidt. “Mean-field approximations of networks of spiking neurons with short-term synaptic plasticity”. In: *arXiv preprint* (Jan. 2021), arXiv: 2101.06057.

    - **I used this preprint for chapter 3 of my thesis.**
    - I drafted the following sections: Abstract, section I, section II, section IV, final paragraph of section V (starting on page 10, left column), first paragraph of section VI (ending on page 12, left column), section VII.
    - I performed all bifurcation analyses reported in this manuscript.
    - I performed the model simulations and analyses for the following results figures: Fig. 3, 4 and 6.
    - Helmut Schmidt and I contributed equally to the design and ideas of this study.

Declaration of authorship:

In the following, I provide a list of all contributions and collaborations that are part of my thesis. Publication references refer to the list of publications preceding this section.

- Daniel Rose contributed substantially to the development of PyRates, the software described in chapter 5, by developing the frontend and user interfaces.
- Daniel Rose drafted the framework chapter of publication 3 (Gast et al., 2019, PLOS ONE), which I used in an adapted form for section 5.2 of my thesis.
- Daniel Rose created Fig. 2 and contributed to the design of Fig. 1 of publication 3 (Gast et al., 2019, PLOS ONE), which I used as Fig. 5.2 and Fig. 5.1 of my thesis, respectively.
- Christoph Salomon performed the simulations that were used for Fig. 4 of publication 3 (Gast et al., 2019, PLOS ONE), which I used in adapted form as Fig. 5.4 of my thesis.
- Helmut Schmidt drafted section 4.1 of publication 5 (Gast et al., 2020, Neural Computation), which I used in adapted form for section 3.3 of my thesis.
- Helmut Schmidt drafted the first paragraph of section V as well as the second paragraph of section VI of publication 8 (Gast et al., 2021, arXiv), which I used in adapted form for sections 3.4.4 and 3.4.5 of my thesis, respectively.
- Helmut Schmidt created Figures 2, 5 and 7 of publication 8 (Gast et al., 2021, arXiv), which I used as Figures 3.8, 3.13, and 3.11 of my thesis, respectively.

I, Richard Gast, declare that this thesis titled "Phase Transitions Between Asynchronous and Synchronous Neural Dynamics" and the work presented in it are my own. I confirm that:

- This work was done wholly or mainly while in candidature for a doctoral degree at this University.
- Where any part of this thesis has previously been submitted for a degree or any other qualification at this University or any other institution, this has been clearly stated.
- Where I have consulted the published work of others, this is always clearly attributed.
- Where I have quoted from the work of others, the source is always given. With the exception of such quotations, this thesis is entirely my own work.
- I have acknowledged all main sources of help.
- Where the thesis is based on work done by myself jointly with others, I have made clear exactly what was done by others and what I have contributed myself.

Signed: Richard G

Date: 02.07.2021

Supervision:

First supervisor: Thomas R. Knösche, head of the Brain Networks group[1]
Second supervisor: Harald E. Möller, head of the Nuclear Magnetic Resonance group[1]

[1] Max Planck Institute for Human Cognitive and Brain Sciences, Leipzig, Germany

I dedicate this thesis to anyone contributing to openly accessible science, knowledge and education.

Acknowledgements

I would like to thank Helmut Schmidt and Thomas R. Knösche for the support, scientific exchange, and mentorship they offered me throughout the process of this thesis. They were always open to reflect and discuss my ideas, thus providing a supportive environment for my work. Furthermore, Harald E. Möller provided me with scientific advice, supervision and financial support without which I could not have finished this project. I am grateful for that. Finally, I would like to thank the Studienstiftung des Deutschen Volkes for their continued intellectual and financial support that ensured a well-paced progression of my work.

Table of Contents

4 Phase Transitions and Neural Synchronization in the External Pallidum 55

5 Modeling of Neural Mean-Field Dynamics Via PyRates 75

List of Figures

List of Tables

Abbreviations

BG basal ganglia.

CO coupling operator.

CPU central processing unit.

DBS deep brain stimulation.

EEG electroencephalography.

EIN excitatory interneuron.

FFT fast Fourier transform.

FIR finite impulse response.

fMRI functional magnetic resonance imaging.

FRE firing rate equations.

GPe globus pallidus pars externa.

GPe-a arkypallidal GPe neurons.

GPe-p prototypical GPe neurons.

GPU graphical processing unit.

HWHM half-width at half-maximum.

IIN inhibitory interneuron.

IR intermediate representation.

JRC Jansen-Rit circuit.

KL-MI Kullback-Leibler-based modulation index.

LFP local field potential.

MEG magnetoencephalography.

MPA	multi-population approximation.
MRI	magnetic resonance imaging.
OA	Ott-Antonsen.
ODE	ordinary differential equation.
PAC	phase-amplitude coupling.
PC	pyramidal cell.
PD	Parkinson’s disease.
PPC	phase-phase coupling.
PRO	potential-to-rate operator.
PSD	power-spectral density.
QIF	quadratic integrate-and-fire.
RPO	rate-to-potential operator.
SD	synaptic depression.
SFA	spike-frequency adaptation.
SNN	spiking neural network.
STN	subthalamic nucleus.
STP	short-term plasticity.
STR	striatum.

Mathematical Notation

$*$ the convolution operator, i.e. $y(t) = a(t) * x(t) = \int_{-\infty}^{t} a(t - t')x(t')dt'$ defines y as the convolution of x with integral kernel a.

B bi-exponential function.

C can either refer to (i) the capacitance of the membrane of a neuron, or (ii) the global coupling parameter of the Jansen-Rit model.

G Green's function to a dynamical system.

H Heaviside step function.

I input current, can be stationary or time-dependent, i.e. $I(t)$.

J global coupling strength in a system of coupled neurons or neural populations.

L linearization matrix.

M number of neural populations in a multi-population network.

N number of network units.

R only used as a subscript, such as in X_R, where R denotes that X_R refers to a reset value of X.

S can either refer to (i) the spiking activity of a neuron, or (ii) a sigmoidal function.

T can either refer to (i) the period of an oscillation, or (ii), if used as a subscript such as in X_T, T denotes that X_T refers to a threshold value of X.

U short-term synaptic facilitation variable of a neuron.

$U0$ baseline efficacy of a synapse.

V membrane potential of a neuron.

X can either be (i) a short-term plasticity variable of a neuron, or (ii) a state variable of the Stuart-Landau oscillator.

Y can either be (i) a short-term plasticity variable of a neuron, or (ii) a state variable of the Stuart-Landau oscillator.

Δ can either be (i) the half-width-at-half-maximum of a Lorentzian distribution over a network parameter, or (ii), if used in combination with another variable such as in Δx, it refers to a small amount of x.

Γ density function of a gamma probability distribution.

α can either refer to (i) the rate of a short-term plasticity variable, or (ii) the maximum of a sigmoidal function.

$\bar{\eta}$ center of a Lorentzian distribution over the network parameter η.

β shape parameter of a gamma probability distribution.

δ Dirac delta function.

$\dot{x}$ shorthand notation for the first derivative of x with respect to time t, i.e. $\dot{x} = \frac{\mathrm{d}x}{\mathrm{d}t}$.

η background input or excitability of a neuron.

γ scale parameter of a gamma probability distribution.

κ steepness parameter of a sigmoidal function.

ω angular frequency of an oscillation.

ρ density function of a probability distribution over a state variable of a dynamical system.

σ can either refer to (i) the first Kuramoto order parameter, i.e. the phase coherence in an ensemble of phase oscillators, or (ii) the average variation in the duration of repeatedly performing a numerical simulation on a computer.

τ can either refer to (i) the time constant of the evolution of a dynamic variable, or (ii) a delay constant in a set of delayed differential equations.

θ phase of an oscillator.

ξ vector of parameters of a dynamical system.

d duration of performing a numerical simulation on a computer.

f can either denote (i) a not-further specified function, or (ii) the frequency of an oscillation.

g density function of a probability distribution over a network parameter.

h can either be (i) a function that generates the Fourier coefficients of the Ott-Antonsen ansatz, or (ii) the efficacy parameter of a synapse in the Jansen-Rit model.

k global coupling strength in a system of coupled oscillators.

p density of synaptic coupling in a neural network, i.e. the fraction of non-zero synaptic connections from all possible synaptic connections.

r average firing rate across neurons of a neural network.

s global synaptic input in a neural network.

t time.

u can either refer to (i) the mean-field variable expressing the average synaptic facilitation of a neural network, or (ii) the extrinsic, time dependent input to the Jansen-Rit model.

v average membrane potential across neurons of a neural network.

w can either refer to (i) a complex-valued state variable of a dynamical neural network system, or (ii) a real-valued state variable of a neural mass model.

x can either denote (i) a not-further specified state variable of a dynamical system, or (ii) a mean-field short-term plasticity variable of a neural network.

x^+ value of state variable x of a neuron, just after that neuron emitted a spike (right limit with respect to the spike).

x^- value of state variable x of a neuron, just before that neuron emitted a spike (left limit with respect to the spike event).

x^* complex conjugate of x. If $x = a + ib$ is a complex variable, then $x^* = a - ib$ is its complex conjugate.

$x_\star$ solution of a differential equation, i.e. $x_\star(t) = \int_{-\infty}^{t} \dot{x} dt$.

y can either be (i) the center of a Lorentzian probability distribution over the state variables of a dynamical system, or (ii) a mean-field short-term plasticity variable of a neural network.

z half-width-at-half-maximum of a Lorentzian probability distribution over a state variable of a dynamical system.

1

Introduction

1.1 A complex systems perspective of the brain

Complex systems are defined as collections of interacting particles or units that are capable of self-organized pattern formation, such that spatiotemporal dynamics or functions can emerge [1, 2, 3]. Emergent dynamics or functions of a complex system cannot be explained from the isolated microscopic units. Instead, emergence requires that the number of units of a system be large, that they express some form of non-linearity, and that there is interaction between them [4]. Thus, emergence can be perceived as a collective, macroscopic phenomenon of the system, the study of which has been at the center of statistical physics [1, 2, 5]. Typical examples of emergence in complex systems include chemical reactions, coherence of laser light, fluid dynamics, or ferromagnetism. In the latter, magnetization is a collective property of the iron magnet and depends on local interactions between large numbers of non-linear spins [2]. It is thus a prime example of how the function of a complex system is best understood via collective, macroscopic states of the system (i.e. the magnetization of the iron magnet), rather than via the individual microscopic states (i.e. the spin orientations).

Given the above definition, the brain can be considered a complex system as well. It is a biological system composed of a large number of hierarchically organized, interacting cells [6]. Measures of brain activity have revealed spatiotemporal patterns that vary across different brain states and express characteristics of collective phenomena [4, 7, 8, 9]. Furthermore, various functions have been shown to emerge from the interaction of brain cells, such as the human ability to understand and produce speech, precisely control the body, and integrate varying sensory information into stable percepts [10]. How these activation patterns and functions depend on each other and on the underlying brain structure is a matter of on-going research [8, 11, 12, 13, 14]. To gain further insight into these structure-function relationships, approaches that have been successfully applied to other complex systems may be applied to study the brain as well [1, 4, 15]. With respect to ferromagnetism, macroscopic spin patterns associated with the emergence of magnetization have been identified and their dependence on the temperature has been studied [2]. In analogy, macroscopic states associated with certain brain functions may be identified to study how they depend on the underlying brain cell interactions. To this end, it is required to define the microscopic units of the brain and how they interact.

The major cell type that allows for interactions between different parts of the brain is the neuron [10]. Neurons are non-linear, excitable elements that interact with each other via electrochemical connections called synapses. In the human brain, neuron numbers have been estimated to be in the order of 10^{10}, connected by approximately 10^{15} synapses [16, 17]. These neurons are hierarchically organized into different brain regions, layers and nuclei and are considered as the basic unit of brain function [10, 18, 19]. Here, we adopt a complex systems perspective on the brain that focuses on the interaction between neurons [15, 20, 21]. Specifically, we consider the neural subsystem of the brain as a complex system capable of expressing collective phenomena. By studying collective behavior in models of coupled neurons, we aim to learn about the emergence of brain function and how it depends on neural structure and interaction.

1.2 Brain function and the phase transition to synchronized neural activity

The field of synergetics suggests that complex systems best be studied around phase transitions, where small changes can push the system past a critical point and induce a qualitative change in the system behavior [1, 3, 22]. Near such phase transitions, the system is particularly sensitive to changes in its parameters, thus allowing to identify system properties that control the emergence of collective phenomena. Phase transitions from asynchronous to synchronized neural activity play arguably the most important role for the study of brain function [23, 24, 25]. For instance, synchronization of neural activity has been suggested as a crucial mechanism for the binding of distinct neural information into combined representations [26], and for neural gating and information routing [27, 28, 29]. In both of these examples, phase relationships between neural elements are proposed as determinants of successful information transmission. Additionally, changes in the level of neural synchronization at specific rhythms have been associated with brain functions such as working memory [30], motor control [31], or attention [32]. It is thought that different brain functions are encoded by phase synchronization at distinct frequencies, which could allow for parallel processing of different functions via nested oscillations [24, 33, 34, 35, 36]. Besides these relationships between normal brain function and neural synchronization, abnormal neural synchronization has also been reported in a variety of neurological disorders [37, 38]. For example, increased synchronization of neural activity has been found in various brain areas affected by Parkinson's disease (PD) and has been directly linked to parkinsonian motor symptoms [39, 40, 41]. In summary, the above reported evidence suggests that an intricate pattern of neural synchronization at different rhythms underlies healthy brain function and that deviations from it may result in disease. For the development of a complex systems perspective on the brain that describes brain function as a collective property of neural interactions, it is therefore pivotal to study (I) which phase transitions to synchronized neural activity can emerge in a given neural system, (II) how these phase

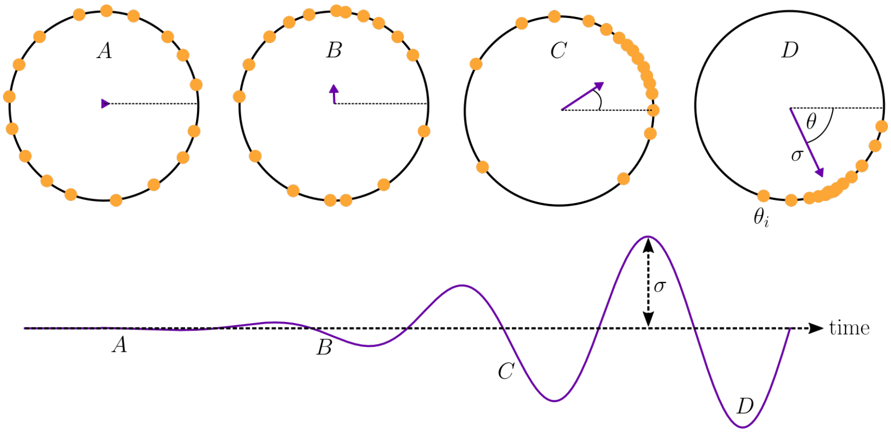

Figure 1.1: Phase synchronization in a system of coupled phase oscillators. In the upper row, the distribution of the phases of microscopic neural oscillators θ_i (orange) is depicted on the unit circle at four different time points. The associated first and second Kuramoto order parameters σ and θ are depicted as the magnitude and phase of the averaged phase vector (purple). In the bottom row, the dynamics of the Kuramoto order parameter σ are depicted over time.

transitions depend on the underlying neural structure, and (III) how these phase transitions relate to brain function.

In this thesis, we are concerned with the study of questions (I) and (II). Specifically, we consider macroscopic phase transitions to synchronized activity in networks of synaptically coupled neurons. To clarify this point, lets make the simplifying assumption that each neuron in a network of N neurons behaves like a linear phase oscillator

$$\dot{\theta}_i = \omega_i + \sum_{j=1}^{N} f(\theta_i, \theta_j), \tag{1.1}$$

where θ_i is the phase of neuron i, ω_i is a neuron-specific oscillation frequency, and f is a coupling function. If the latter is defined as $f(\theta_i, \theta_j) = \sin(\theta_j - \theta_i)$, eq. (1.1) is equivalent to the Kuramoto oscillator model [42]. The order parameters of such a system can be defined in complex form as

$$\sigma e^{i\theta} = \frac{1}{N} \sum_{j=1}^{N} e^{i\theta_j}, \tag{1.2}$$

where the order parameters σ and θ represent the phase coherence and the average phase of the system, respectively [42]. Fig. 1.1 provides a conceptual depiction of the relationship between order parameters and system dynamics. In a state of asynchronous neural activity $\sigma = 0$ and the microscopic phases θ_i are uniformly distributed between all possible phases (see Fig.1.1A). At the microscopic level, every neuron evolves according to its own intrinsic frequency ω_i. Macroscopically, however, no oscillations can be observed since the individual phases θ_i cancel each other out. When a phase transition to synchronous neural activity occurs, parts of the system start to evolve according to a global rhythm with phase θ instead of their own rhythms ω_i. As a consequence, the microscopic phases start to align, thus making their distribution non-uniform (see Fig.1.1B-D). For a system given by eq. (1.1), this behavior can only be observed for sufficiently strong, non-linear coupling between the neurons and is thus an emergent phenomenon. At the macroscopic level, a global rhythm with phase θ and amplitude σ can be observed, where the latter scales with the amount of phase synchrony between the microscopic units. It is this phase transition from asynchronous to synchronous neural activity that we refer to in (I) and (II), and that we consider as the basis for a complex systems perspective on brain function.

1.3 Low-dimensional manifolds of synchronized neural activity

Clearly, the evaluation of eq. (1.2) is of interest to the study of phase transitions from asynchronous to synchronous dynamics in neural systems. However, this requires the knowledge of the phases of each neural oscillator in time and thus the solution to a set of microscopic system equations such as given by eq. (1.1). Even though eq. (1.1) is an extremely simplified representation of a biological neural network, analytical solutions to this system can generally not be obtained. Instead, the study of such systems requires the use of numerical methods, the computational costs of which scale with the system dimensionality [43]. Since neural systems can be of extremely large dimensionality (up to 10^{10} neurons), severe practical limits are placed on the numerical study of neural systems. Fortunately, an immediate consequence of the phase transition to synchronized neural activity is that the effective dimensionality of the system is reduced. In an asynchronous system state, the neural phases θ_i evolve independently of each other and thus an N dimensional phase space is required to describe the evolution of a system with N neurons. As more microscopic units become aligned with the phase θ of a global rhythm, the necessary dimensions to describe the evolution of the system become less, since the dynamics of some neurons express strong similarities. If all neurons are perfectly phase aligned with θ, the system is reduced to a single phase oscillator with an effective dimensionality of $m = 1$. In such cases of reduced effective system dimensionality, the system is said to evolve on a low-dimensional manifold of its phase space [43]. Hence, the practical limits on the study of neural systems can be reduced substantially via the derivation of evolution equations that directly describe the system activity along the low-dimensional manifold. In the best case scenario, evolution equations can be found for macroscopic order parameters such as θ and σ. This would allow to study phase transitions directly at the macroscopic level, in a mathematical form that does not scale with the system size N.

Interestingly, stable low-dimensional neural manifolds do not only exist in idealized neural oscillator system but have also been repeatedly reported in recordings of neural activity [44, 45, 46, 47, 48]. The brain can generate a variety of highly complex and chaotic patterns of neural activity [49]. However, given the vast number of neurons in the brain, these patterns appear to be less complex than they could be theoretically, indicating a high level of neuronal redundancy [4, 7]. Electrophysiological recordings of macroscopic neural activity have revealed highly stereotyped responses to sensory stimulation as well as strongly synchronized regimes of neural activity [50, 51, 52, 53]. More recently, multi-unit recordings have demonstrated that strong redundancies are present at the level of spiking neurons as well [54, 55]. For instance, low-dimensional manifolds have been identified in recordings of neural population activity during a reaching task in sensorimotor brain areas of monkeys [48]. These low-dimensional manifolds remained stable over the time span of years, even though individual neurons changed their response pattern over this period. Based on these data we argue that synchronization-dependent, low-dimensional manifolds of neural activity represent important constituents of stable brain function. Therefore, it is not only of practical, computational interest to derive evolution equations for low-dimensional neural manifolds. For a theory of brain function centered around the collective behavior of neurons, it is a major goal to find mathematical expressions that relate these constituents of brain function to the underlying system parameters.

In conclusion, the study of (I) and (II) would clearly benefit from mathematical descriptions of low-dimensional manifolds of neural activity. While such descriptions have been derived for specific classes of neural network models already (see [56, 57] and references therein), much work remains to be done for low-dimensional neural network descriptions to be applicable to the study of synchronization processes in biological systems. Therefore, one main task addressed in this thesis is the derivation of such descriptions and the assessment of their applicability to biological neural networks.

1.4 Phase transitions to synchronized neural activity in Parkinson's disease

Another topic of this thesis is the study of neural synchronization processes in concrete neurobiological cases, using low-dimensional descriptions of neural activity. PD is a case that is particularly suited for the study of emerging neural synchronization. It is a common neurological disorder that leads to hypokinetic motor symptoms such as rigidity, slowness of movements, postural deficits and tremor, though it includes non-motor symptoms as well [58]. The most prominent feature of neural dynamics in PD is an increased synchrony in the so-called beta frequency band (12-30 Hz) [39, 40]. Furthermore, the strength of neural synchronization at high gamma frequencies (50-250 Hz) appears to depend stronger on the phase of beta synchronization in PD compared to healthy brain states [59, 60]. This is in stark contrast to the healthy state, where most of the brain regions affected by PD express asynchronous neural dynamics. Since both the increased beta synchronization and the increased modulation of gamma synchronization have been related to PD motor symptoms, the emergence of synchronized macroscopic states might be directly related to a loss of neural function in PD [39, 61].

On the structural level, PD is associated with the cell death of neurons that innervate brain areas affected by PD with the neuromodulator dopamine [58, 62, 63]. How the resulting dopamine depletion relates to PD motor symptoms and pathological brain dynamics is a matter of on-going research [64, 65]. Evidence has accumulated over the past years, however, that the globus pallidus pars externa (GPe) plays an important role in the generation of pathologically synchronized neural dynamics in PD [66, 67, 68, 69]. On the microscopic level, GPe neurons express periodic firing and may thus be studied in the framework of coupled neural oscillators described in section 1.2. On the macroscopic level, however, GPe activity has been described as particularly asynchronous under healthy conditions [70]. It has been suggested, that this asynchronous state is supported by the strongly heterogeneous activity of GPe neurons [70]. The latter can be accounted for by a high variance across the microscopic frequencies ω_i in neural oscillator systems as given by eq. (1.1). Under parkinsonian conditions, neural activity of the GPe becomes more synchronized with a particularly strong increase in macroscopic beta oscillations and beta-related modulations of gamma oscillations [60, 71, 72, 73]. Extrinsic suppression of GPe activity in PD attenuates pathological neural dynamics as well as motor symptoms in PD [69]. In conclusion, the GPe represents a particularly interesting neurobiological system for examining phase transitions between asynchronous and synchronized states. The study of the emergence of synchronized oscillations in the GPe under parkinsonian conditions is therefore the second central topic of this thesis.

1.5 Thesis overview

Above, we established the theoretical framework of this thesis. The general subject of our studies is the brain and we approach its study from a complex systems perspective. We developed the hypothesis that brain function emerges from the collective interactions of neurons and can be directly linked to macroscopic, spatiotemporal patterns of neural synchronization. As the overarching goal of our work, we identified the development of a complex systems theory of brain function centered around phase transitions between asynchronous and synchronous neural dynamics. In this regard, the specific contributions of this thesis are (a) the development of methodological tools for studying such phase transitions in neural network models, and (b) the study of pathological neural synchronization in PD via these tools.

In the subsequent chapter, we describe the basic mathematical model and the numerical methods that we used in for (a) and (b). The chapter includes a short overview over mathematical models of neural activity in general and a motivation for the concrete neural model we chose for our studies. Furthermore, we describe the basic concepts and methods from dynamical systems theory that are relevant for the understanding and replication of our results. This is followed by chapter 3 which regards the development of mathematical models of low-dimensional neural manifolds via mean-field theory. First, we provide a short overview over previous mean-field approaches to the modeling of low-dimensional neural manifolds. Then, we present our own contributions to this topic, with a focus on low-dimensional manifolds of neural activity in neural networks that incorporate short-term plasticity mechanisms. We show for which formulations of short-term plasticity the derivation of evolution equations for the manifolds is possible, for which formulations it is not, and under which conditions the derived equations accurately describe the neural network dynamics. Furthermore, we examine the effects of short-term plasticity on the neural network dynamics. In chapter 4, we apply mean-field methods to the study of neural synchronization in the GPe under parkinsonian conditions. As such, the chapter provides a road-map of how to apply the mathematical models developed in chapter 3 to a concrete biological system. In addition, chapter 4 provides a comprehensive complex systems perspective on the collective behavior of GPe neurons in health and disease. Chapter 5 is dedicated to the description of an open-source software that provides various tools for the modeling and analysis of neural network models. It introduces a graph-based framework for neurodynamic modeling that reflects the complex systems perspective on the brain that is the basis of this thesis. Additionally, it describes implementations and exemplary numerical analyses of neural mean-field models such as introduced in chapter 3. This way, we provide the means to replicate the findings of this thesis via a freely available, well documented Python software. In the final chapter, we summarize the findings of our work, integrate them into the current literature on pathological neural synchronization processes in PD, and provide an outlook of how our analysis of GPe dynamics (chapter 4), the mean-field models we derived (chapter 3), and the software we developed (chapter 5) can form the basis of future studies of neural synchronization processes in PD and healthy brain function.

2

Mathematical Model and Methods

2.1 A non-linear oscillator model of neural activity

In this section, we establish the basic mathematical model that we used for our studies of neural systems. As mentioned earlier, we regard neurons as the basic, microscopic units of which complex brain circuits are composed. Many models have been proposed for the activity of neurons that vary in their level of abstraction, biological detail and mathematical complexity [18, 74]. The most abstract models approximate neurons as mere functions that instantaneously translate their synaptic input into an output [15, 75, 76]. As such, these models consider all neuron-intrinsic dynamics as negligible in comparison to the time scale of interactions between neurons. Furthermore, they neglect the fact that neuronal inputs and outputs are based on very short events, so-called spikes that last ≈ 2 ms [75], and instead approximate neural activity by a rate of these events. Typical functions used in this regard are the Heaviside step function or any kind of sigmoidal function. The most biological detailed models split a single neuron into multiple compartments, each of which is modeled by the Hodgkin-Huxley model, a set of equations that describes the dynamics of conductance changes along the membrane of the neuron [77]. Such neuron models have been demonstrated to be able to accurately approximate the activity of various neuron types under a multitude of conditions [78, 79, 80, 81]. However, their mathematical complexity makes them difficult to study, analytically as well as numerically. For the purpose of this thesis, neither the most abstract nor the most detailed neuron models represent appropriate abstractions of neural behavior. On the one hand, it has been established that neuron-intrinsic dynamics and spike generation processes can play a crucial role for neural synchronization, thus rendering instantaneous input-output functions too simple for its study [18, 82, 83, 25]. On the other hand, it is a basic property of collective phenomena that they emerge from the interaction of many different units and should, to a certain degree, be independent of the exact description of the microscopic dynamics [1, 4]. Therefore, multi-compartment Hodgkin-Huxley models likely include many mathematical details that are not required for the study of macroscopic neural phase transitions, but make such studies much harder to carry out [20, 18]. As a compromise between those two extremes, our investigations of collective neural synchronization processes required a neuron model that is (a) simple enough for large neural network studies, (b) provides non-linear neural dynamics, (c) provides a spiking mechanism to account for neural spike synchronization.

Various simplifications of the Hodgkin-Huxley equations have been proposed that still allow to model central properties of neural activity, such as the Izhikevich model or the FitzHugh-Nagumo model [18, 74]. Considering a neuron as a point-like unit with no spatial extent, its membrane potential V_i is given by the balance of currents

$$C\dot{V}_i = -f(V_i, t) + I(t). \tag{2.1}$$

In this equation, C is the capacitance of the cell, $I(t)$ is a lumped representation of all synaptic and extrinsic current inputs to the cell, and $f(V_i, t)$ represents all cell-intrinsic, resistive membrane currents. In the Hodgkin-Huxley formalism, $f(V_i, t)$ is composed of sodium, potassium, and leakage currents, which in turn are described by voltage-dependent ion channels governed by separate dynamic equations [20, 77]. Simplifications of this formalism either approximate some of these currents and channel dynamics as instantaneous or lump them together in combined variables [18, 20]. A particularly drastic reduction in the dimensionality of the model is achieved by the quadratic integrate-and-fire (QIF) neuron, which uses the approximation $f(V_i, t) = -V_i^2$. Hence, it neglects ion channel dynamics altogether and approximates the intrinsic dynamics of a neuron by a one-dimensional, non-linear process. In its dimensionless form, the QIF neuron is defined as

$$\tau\dot{V}_i = V_i^2 + I(t), \tag{2.2}$$

with membrane time constant τ. If $V_i > V_T$, a spike is counted and the membrane potential is set to $V_i = V_R$, where V_T and V_R are a threshold and a reset value, respectively. As such, eq. (2.2) represents the most basic model of a neuron with non-linear intrinsic dynamics that involves a spike generation mechanism [18]. Since it meets the requirements (a-c) stated above, we chose the QIF neuron as the basic microscopic unit for all following neural network studies.

2.2 Dynamical systems methods for the study of neural network models

In this section, we briefly explain the concepts and methods from dynamical systems theory that are most relevant for the results reported in subsequent chapters. To address the questions of this thesis, we studied systems of the form

$$\dot{\mathbf{x}} = \mathbf{f}(\mathbf{x}, \xi, t),\ \mathbf{x} \in \mathbb{R}^n,\ \xi \in \mathbb{R}^m \tag{2.3}$$

where $\mathbf{x}$ is an n-dimensional state vector, ξ is a set of m constant parameters, $\mathbf{f}$ is a sufficiently smooth vector field $\mathbf{f} : \mathbb{R}^n \times \mathbb{R}^m \to \mathbb{R}^n$, and $\dot{x}$ denotes the derivative of x with respect to time t, i.e. $\frac{\mathrm{d}x}{\mathrm{d}t}$. This involved to obtain solutions to eq. (2.3) and examine their dependency on the system parameters ξ. However, for the non-linear neural network systems that we considered, the solutions are usually analytically intractable, i.e. the integral

$$\mathbf{x}(t) = \int_{t'=t_0}^{t'=t} \mathbf{f}(\mathbf{x}, \xi, t')dt' \tag{2.4}$$

with initial time t_0 cannot be solved in general. We thus employed two different numerical methods that can approximate eq. (2.4) to any degree of accuracy: Euler's method and a fifth-order Runge-Kutta method. Euler's method is a first-order method for approximating eq. (2.4) numerically [43]. Starting from an initial value $\mathbf{x}_0$ at $t = t_0$, the method uses an iterative procedure to integrate eq. (2.3) in fixed, discrete time steps Δt according to

$$\mathbf{x}(t_{n+1}) = \mathbf{x}(t_n) + \Delta t \mathbf{f}(\mathbf{x}(t_n), \xi, t_n), \tag{2.5}$$

where $n = 0, 1, 2, ..., T$, $t_{n+1} = tn + \Delta t$, and T is the number of discrete time steps Δt that the interval between t_0 and t is split into. The local approximation error of this method is in the order of $O(\Delta t^2)$, and very small integration step sizes are often required in practice to ensure the stability of the solution approximation. As a more accurate method that allows for larger integration step sizes, we used a fifth-order Runge-Kutta method with automatic step size adaptation based on a fourth-order approximation of the local error. While we employed custom implementations of Euler's method, we used the implementation provided by SciPy for application of the Runge-Kutta method [84]. Thus, a detailed mathematical treatment of this particular Runge-Kutta method is beyond the scope of this thesis, but can be found in [85]. In brief, the method uses an iterative procedure with an adaptive step size Δt. To perform a single integration step from $\mathbf{x}(t_n)$ to $\mathbf{x}(t_{n+1})$, the method evaluates the vector field $\mathbf{f}$ at five different points between t_n and t_{n+1}. Furthermore, it dynamically adapts the integration step size based on the local approximation error such that a desired approximation accuracy is reached. Often, the speed-accuracy trade-off of this method is superior to a fixed step-size Euler integration. Thus, we applied the fifth-order Runge-Kutta integration method in most cases. However, to integrate a spiking neural network (SNN), additional rules have to be defined to constrain the dynamics of eq. (2.3), such as the reset of the membrane potential of QIF neurons after a spike occurred (see section 2.1). For such systems, we employed custom implementations of the Euler integration method.

We examined parameter dependencies of solutions to eq. (2.3) via two different approaches. Either, we used the above described methods to calculate the solutions $\mathbf{x}(t)$ explicitly for multiple discrete values of ξ and observed how differences in ξ translated to differences in $\mathbf{x}(t)$. While suited for cases where the relationship between the solution and the parameters of interest is sufficiently smooth, the approach is ill-suited for cases where solutions can change abruptly due to very small changes in a parameter. To analyze the latter, we used methods from dynamical systems theory that allow for a continuous variation of the system parameters ξ [86]. The application of these methods require eq. (2.3) to be autonomous, i.e.

$$\dot{\mathbf{x}} = \mathbf{f}(\mathbf{x}, \xi). \tag{2.6}$$

In a first step, we searched for a steady-state solution (also called fixed point) of eq. (2.6), i.e. a solution $\mathbf{x}_\star(t)$ with $\mathbf{f}(\mathbf{x}_\star, \xi) = 0$. Starting from such a solution, we studied how it changed due to the continuation of a parameter $a \in \xi$ using Auto-07p [87, 88]. The latter is a software that provides various numerical methods for identifying and analyzing new solutions that arise from parameter perturbations around a known solution $\mathbf{x}_\star$. Thus, by using Auto-07p, we employed established implementations of numerical parameter continuation methods, rendering their detailed mathematical description beyond the scope of this thesis (but see [87, 86, 89] for such descriptions). Conceptually, the main idea of these methods is to linearize the system given by eq. (2.6) around a known solution $\mathbf{x}_\star$, perturb the system via a sufficiently small change in a system parameter Δa, and then apply Newton's method to find the new solution in the vicinity of the previous solution $\mathbf{x}_\star$ [90]. The existence of these new solutions is guaranteed by the Implicit Function Theorem as long as Δa is sufficiently small. An iterative procedure then allows to analyze the parameter dependency of eq. (2.6) over wider parameter ranges. Periodic solutions represent a class of solutions that require slightly different methods for their study. Starting from a known periodic solution $\mathbf{x}_\star$ with $\mathbf{x}_\star(t) = \mathbf{x}_\star(t+T)\ \forall t \in \mathbb{R}$ with a known period T, again a small change Δa is applied to a system parameter. For specifying a unique new solution, an additional boundary condition is imposed on the phase relationship between the old and the new solution. Then, Keller's pseudo-arclength continuation method can be used to find the new periodic solution [91, 87]. Again, iterative algorithms are implemented in Auto-07p that employ this procedure to follow families of periodic solutions [88].

Together, these methods allowed us to calculate continuous curves of steady-state and periodic solutions to eq. (2.6) in dependence of up to three different parameters of the system, i.e. elements of ξ. While the obtained solutions are called the equilibria of the system and define its qualitative, asymptotic behavior, the curves that define the relationship between equilibria and parameters are called solution branches. As a solution branch is calculated, the stability of a given equilibrium can in most cases be determined via linearization of the vector field $\mathbf{f}$ around the known solution $\mathbf{x}_\star$, i.e. by the local approximation

$$\dot{\mathbf{x}} = \mathbf{f}(\mathbf{x}, \xi) \approx \mathbf{L}(\xi, \mathbf{x}_\star)\mathbf{x}, \tag{2.7}$$

with linearization matrix $\mathbf{L} \in \mathbb{R}^{n \times n}$. A steady-state solution is said to be asymptotically stable if, after a sufficiently small perturbation $\mathbf{x}' = \mathbf{x}_\star + \epsilon$, it holds that $\mathbf{x}' \rightarrow \mathbf{x}_\star$ as $t \rightarrow \infty$. This condition is satisfied if all eigenvalues of $\mathbf{L}$ evaluated at the solution in question have negative real parts [86]. Similarly, a periodic solution is stable if it asymptotically relaxes back to its periodic orbit after a small perturbation, which can be tested via Floquet theory [86]. In general, the dynamics of eq. (2.6) can be governed by multiple stable and unstable equilibria for a given set of parameters ξ. The system is said to undergo a phase transition, when an external perturbation or a change of ξ forces the system from the stable equilibrium of one solution branch to the stable equilibrium of another solution branch. For this thesis, we were interested in studying neural systems of the form given by eq. (2.6) in regions of parameter space where both stable steady-state and stable periodic solutions exist nearby. In such regions, a phase transition from asynchronous to synchronous neural dynamics as depicted for the Kuramoto order parameter in Fig.1.1 can be induced by forcing the system from a steady-state solution into the basin of attraction of a periodic solution.

In general, phase transitions that are caused by changes in a system parameter $a \in \xi$ are called bifurcations and a is called the bifurcation parameter. The bifurcation point is the value of a that separates the different solution branches, i.e. two qualitatively different dynamic regimes of the system. In the remainder of this section, we provide an intuition for the most relevant bifurcations for the study of neural synchronization processes. For all bifurcations reported in this thesis, we used the automated bifurcation detection algorithms provided by Auto-07p [88]. Thus, a detailed mathematical definition of these bifurcations is beyond the scope of this thesis, but can be found together with a description of how bifurcations can be identified along a solution branch of a specific system in [86, 89]. We encountered codimension 1 and 2 bifurcations in the bifurcation analyses that we carried out, where the codimension of a bifurcation refers to the minimum number of free parameters that have to be varied to encounter a bifurcation. Two different codimension 1 bifurcations can occur on steady-state solution branches: Fold and Andronov-Hopf bifurcations. A fold bifurcation marks a point where a stable and an unstable steady-state solution collide. In 1D parameter space, a stable and an unstable solution branch approach each other as the bifurcation parameter is varied and collapse and disappear at the fold bifurcation. Thus, a system that is initiated in the basin of attraction of the stable fixed point will either diverge or converge to another equilibrium when forced over the fold bifurcation.

The Andronov-Hopf bifurcation (or Hopf bifurcation in short) marks a point where the stability of a fixed point changes and a periodic orbit, also called limit cycle, emerges. Depending on whether the emerging limit cycle is stable or unstable, the bifurcation is called a supercritical or subcritical Hopf bifurcation, respectively. When a stable fixed point is continued towards a supercritical Hopf bifurcation in 1D parameter space, its basin of attraction is characterized by a focus, meaning that the system expresses damped oscillations when converging to the fixed point. These focus dynamics become stronger when approaching the Hopf bifurcation, until the fixed point loses its stability and gives rise to a minimum-amplitude stable limit cycle at the Hopf bifurcation (see Fig. 2.1A). At a subcritical Hopf bifurcation, an unstable fixed point turns into a stable fixed point instead and gives rise to an unstable limit cycle (see Fig. 2.1B). A typical scenario that can occur when continuing the periodic solution branch of the unstable limit cycle in the bifurcation parameter, is that the unstable limit cycle collides with a stable limit cycle in a fold of limit cycle bifurcation. Similarly to the fold bifurcation, the stable and unstable limit cycle branches approach each other in 1D parameter space and collapse and disappear at the fold of limit cycle bifurcation. In this scenario, the parameter space between the subcritical Hopf bifurcation and the fold of limit cycle bifurcation poses a multi-stable regime in which a stable fixed point and a stable limit cycle branch exist, separated by an unstable limit cycle branch (see Fig. 2.1C).

For studying phase transitions from asynchronous to synchronous system dynamics, the super- and subcritical Hopf bifurcation and the fold of limit cycle bifurcation are the most essential codimension 1 bifurcations. By continuing these bifurcations in two free parameters, it is possible to compute curves of these bifurcations in the parameter plane. Along such curves, codimension 2 bifurcations may be encountered, which mark points in the parameter plane from which multiple codimension 1 bifurcation curves arise. Examples of codimension 2 bifurcations are the cusp bifurcation where two fold bifurcation curves emerge, the generalized Hopf bifurcation where a fold of limit cycle curve and two Hopf curves (one super- and one subcritical) emerge, or the zero Hopf bifurcation where a fold and a Hopf curve tangentially

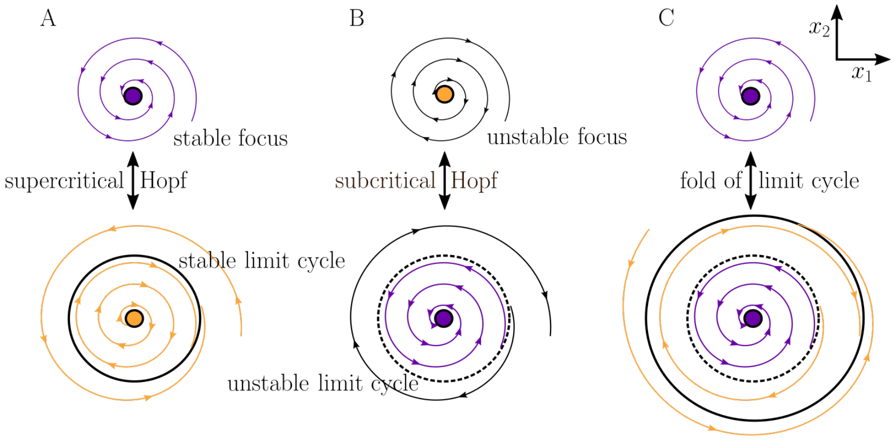

Figure 2.1: Codimension 1 bifurcations that lead to the birth of a limit cycle. The vector field f and the equilibria of a two dimensional dynamical system with (not further specified) state variables x_1 and x_2 are depicted around three different codimension 1 bifurcation points. The top and bottom row depict the two distinct dynamical regimes of the system that the respective bifurcation separates. Large dots filled with purple (orange) represent stable (unstable) fixed points. Circles with solid (dashed) lines represent stable (unstable) limit cycles. Spirals are a qualitative depiction of system solutions following the vector field f. Black, purple and orange spirals represent system solutions that diverge, converge to a fixed point, and converge to a limit cycle, respectively. **A:** Emergence of a stable limit cycle from a previously stable focus via a supercritical Hopf bifurcation. **B:** Emergence of an unstable limit cycle from a previously unstable focus via a subcritical Hopf bifurcation. **C:** Emergence of a stable and an unstable limit cycle via a fold of limit cycle bifurcation.

intersect. In the context of this thesis, we used bifurcation analysis to identify the relevant system parameters for inducing phase transitions to synchronized system states via Hopf bifurcations or fold of limit cycle bifurcations. To this end, we employed 1D parameter continuations to find Hopf bifurcations in the system and subsequently analyzed the Hopf curves in different parameter planes. This way, we performed detailed studies of how macroscopic states of synchronous neural activity could be induced via changes in the underlying control parameters of a neural system.

2.3 Dynamics of a single QIF neuron

In this section, we provide a conceptual intuition for single QIF neuron dynamics as well as a mathematical analysis thereof. This shall serve as a basis for the study of QIF networks in subsequent chapters.

Using the change of variables

$$\theta_i = 2 \arctan V_i, \tag{2.8}$$

and considering the limits $V_T \to \infty$ and $V_R \to -\infty$, the QIF neuron can be shown to be equivalent to the theta neuron [92]. The theta neuron is a neural oscillator model where the phase of the neuron θ_i is given by

$$\tau \dot{\theta}_i = 1 - \cos \theta_i + (1 + \cos \theta_i) I(t). \tag{2.9}$$

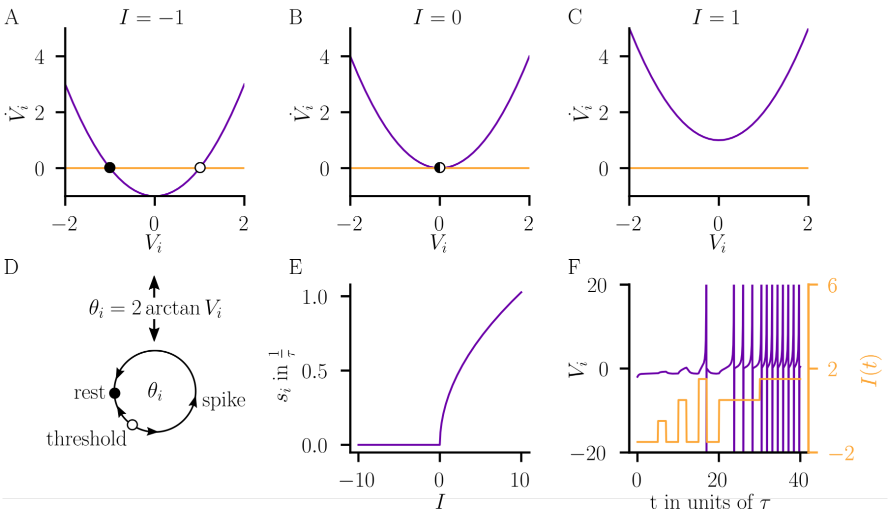

Figure 2.2: Dynamics of a single QIF neuron. **A-C:** Depiction of the relationship between $\dot{V}_i$ and V_i of the QIF neuron for three different values of I. **A:** QIF dynamics for $I < 0$ are governed by a stable fixed point (black, filled circle) and an unstable fixed point (empty circle). **B:** At the bifurcation point $I = 0$, the two fixed points collide and form a saddle. **C:** For $I > 0$ no fixed points exist. **D:** Depicts the relationship between the QIF neuron and the theta neuron. **E:** Depicts the relationship between input I and firing rate s_i of a QIF neuron. Periodic firing, with input-dependent frequency emerges for $I > 0$. **F:** QIF dynamics under transient changes of the input $I(t)$. Small inputs merely perturb the system around the stable resting potential, whereas sufficiently strong inputs elicit spiking activity.

Inserting eq. (2.8) into eq. (2.9) yields

$$\tau \frac{\mathrm{d}(2\arctan V_i)}{\mathrm{d}t} = 1 - \cos(2\arctan V_i) + (1 + \cos(2\arctan V_i))I(t), \tag{2.10}$$

which is equivalent to eq. (2.2) under the trigonometric relationships $\cos(2\arctan x) = \frac{1}{x^2+1} \frac{x^2}{x^2+1}$ and $\frac{\mathrm{d}\arctan x}{\mathrm{d}x} = \frac{1}{x^2+1}$. This equivalence means that the QIF neuron can be considered a non-linear neural phase oscillator model and thus naturally lends itself to the study of phase synchronization processes (see Fig.2.2A and D).

The qualitative dynamics of the QIF neuron depend on its input parameter $I(t)$, which we consider as constant for now, i.e. $I(t) = I \; \forall t$. From eq. (2.2), it is apparent that the QIF neuron has two equilibria for $I < 0$, one stable fixed point at $V_i = -\sqrt{I}$ and a saddle at $V_i = \sqrt{I}$. The two equilibria approach each other when I grows towards zero and collapse and annihilate each other at $I = 0$. For $I > 0$, no equilibria exist anymore. This phase transition is depicted in Fig. 2.2A-C. In the latter case, the solution to eq. (2.2) is given by

$$V_i(t) = \sqrt{I} \tan\left(\frac{It}{\tau} + \arctan \frac{V_i(t_0)}{\sqrt{I}}\right), \tag{2.11}$$

with initial condition $V_i(t_0)$. As expected, eq. (2.11) reveals that the QIF neuron expresses periodic spiking behavior over time for $I > 0$. The rate s_i of this spiking activity can be found by choosing $V_i(t_0) = V_R$ and solving eq. (2.11) for the time t_1 it takes until $V_i(t_1) = V_T$. It is given by

$$s_i = \frac{1}{t_1} = \frac{\sqrt{I}}{\tau(\arctan \frac{V_T}{\sqrt{I}} - \arctan \frac{V_R}{\sqrt{I}})}, \tag{2.12}$$

which reduces to $s_i = \frac{\sqrt{I}}{2\pi}$ in the limits $V_T \to \infty$ and $V_R \to -\infty$, i.e. when the QIF neuron becomes equivalent to the theta neuron. Regardless of these limits, eq. (2.12) shows that s_i scales with the square root of the input I (see Fig.2.2E).

The phase transition from steady-state resting behavior for $I < 0$ towards periodic spiking activity for $I > 0$ happens via a so-called saddle-node on invariant circle bifurcation [18, 43]. When a QIF neuron is in the steady-state, it will asymptotically approach the stable fixed point at $-\sqrt{I}$, which thus represents the resting membrane potential of the neuron. In this state, extrinsic perturbation via transient input may force the system away from the stable fixed point. If this perturbation is sufficiently strong such that $V_i(t) > \sqrt{I}$, the neuron is pushed out of the basin of attraction of the stable fixed point. Its membrane potential will grow until it reaches V_T, thus generating a spike and causing a membrane potential reset $V_i = V_R$. As long as no further perturbations occur, the neuron will then approach its stable fixed point again. Due to this behavior, the neuron is said to be in an excitable state where it rests at $-\sqrt{I}$ until input pushes the membrane potential beyond the spiking threshold at $\sqrt{I}$ and a single spike is elicited. When the neuron is in the periodic spiking state instead, transient inputs can merely increase or decrease the spike frequency by advancing or delaying the phase of the neuron, respectively. From eq. (2.12), it is apparent that the spike rate s_i positively scales with the input $I(t)$ in this spiking regime.

The above described behavior is called type-I excitability and the QIF neuron is the canonical form of type-I excitable neurons [92, 93]. Depending on their input, type-I excitable neurons can be in an excitable state, controlled by a resting membrane potential and a firing threshold, or in a state of periodic spiking activity with an input-dependent spiking rate. If no additional dynamic variables are added to the model definition, no other dynamics can arise from a single QIF neuron. Hence, any QIF network dynamics that cannot be explained via these single neuron properties must emerge from the network interactions.

3

Low-Dimensional Dynamics in Spiking Neural Networks

Based on:

(i) A Mean-field description of bursting dynamics in spiking neural networks with short-term adaptation

(ii) Mean-field approximations of networks of spiking neurons with short-term synaptic plasticity

Richard Gast[1,*], Helmut Schmidt[1], Thomas R. Knösche[1,2].

[1] Max Planck Institute for Human Cognitive and Brain Sciences, Leipzig, Germany
[2] Institute for Biomedical Engineering and Informatics, TU Ilmenau, Germany

* corresponding author (email: rgast@cbs.mpg.de)

(i) Published in Neural Computation 32(9): 1615-1634, September 01, 2020.
(ii) Pre-print published at arXiv on June 16, 2021 as arXiv:2101.06057v2.

3.1 Mean-field approaches in neuroscience

3.1.1 Mean-field models of neural networks

In chapter 1, we introduced a complex systems perspective on the brain, where brain states are defined by the collective dynamics of large neural populations rather than by the activities of each single cell. As argued in section 1.3, these collective states typically evolve on low-dimensional manifolds of the system due to neural synchronization processes. In this section, we introduce different mathematical approaches to the description of such low-dimensional manifolds. This serves as a foundation for the following two sections, where the results are presented that we published in Neural Computation [94] and at arXiv [95] on low-dimensional manifolds of SNN with short-term plasticity (STP). While the former is concerned with neuron-specific STP mechanisms, the latter considers synaptic STP. In both cases, we derive mathematical descriptions of the low-dimensional manifolds of neural dynamics and apply dynamical systems methods to examine their parameter dependencies. Thereby, special emphasis is placed on phase transitions between asynchronous and synchronized neural activity.

The identification and description of low-dimensional manifolds of neural dynamics has been a central topic of neuroscientific research for many years [96, 97, 98, 99, 100, 101]. Different approaches rooted in mean-field theory have been proposed for the mathematical modeling of low-dimensional neural dynamics [2, 19]. Among those are classic neural mass models that use direct, heuristic descriptions of macroscopic measures of neural dynamics [102, 103, 104, 105, 106]. In other words, they have not been derived from a corresponding SNN, but were designed to resemble experimentally observed macroscopic features of neural behavior, such as input-output relationships of a population or spectral features of population activity [102, 105, 106]. The Wilson-Cowan model is arguably the most influential neural mass model [102]. To derive the macroscopic evolution equations for the rate dynamics of two coupled populations of excitatory and inhibitory neurons, Wilson and Cowan approximated the average input-output relationship of the populations via a non-linear, instantaneous function (typically a sigmoidal function). While such neural mass models have been shown to provide good approximations of the steady-state equilibria of SNNs [107], they cannot account for spike synchronization mechanisms that arise due to the dynamic interactions between neurons [83]. As a consequence, transient responses of SNNs to fluctuating inputs and phase transitions to synchronous activity states are not well captured by classic neural mass models. Therefore, different mean-field models are required for the study of collective neural synchronization processes. By now, alternative mean-field approaches are available that account for the underlying dynamical processes of neural interactions. These approaches define so-called order parameters as a general starting point, i.e. macroscopic variables that govern the microscopic dynamics of the system [3, 22]. Typical order parameters that have been defined for SNNs are the average firing rate, the average membrane potential, or the level of phase synchronization (i.e. the Kuramoto order parameter). Next, an attempt is made to derive the values of these order parameters self-consistently from the microscopic system equations. Various methods from statistical physics such as the master equation or the Fokker-Planck equations have been applied to this end [2, 108]. For appropriately chosen order parameters, the derived equations represent the macroscopic, low-dimensional system dynamics.

On the one hand, this approach has been applied to SNNs with finite numbers of neurons, in which finite-size fluctuations exist [109, 110, 111, 112, 113]. Accurately capturing the mean-field dynamics of such systems is a non-trivial problem that has been approached either numerically [113], or by imposing strong additional restrictions on the system dynamics such as the absence of a critical regime [110] or that the SNN be in an asynchronous, irregular firing regime [108]. The work on coupled oscillator systems by Watanabe and Strogatz poses an important contribution to this line of work [114]. Considering a globally coupled population of N identical Kuramoto oscillators as given by eq. (1.1) with $f(\theta_i, \theta_j) = \cos(\theta_j - \theta_i)$ and $\omega_i = \omega \; \forall i \in \{1, 2, 3, ..., N\}$ they derived three dynamic equations together with $N - 3$ constants of motion that self-consistently capture the full microscopic system dynamics [114, 57]. The ansatz made by Watanabe and Strogatz provides valuable insight into the dynamics of coupled neural oscillator systems with a finite number of neurons [115, 57]. However, its restriction to systems of identical neural oscillators with identical synaptic input limits its applicability to biological neural networks that express considerable heterogeneity across neurons and their synaptic coupling.

On the other hand, mean-field theoretic concepts have been applied to the dynamics of SNNs in the thermodynamic limit ($N \to \infty$) [116, 117, 118, 119, 120]. While finite-size fluctuations disappear in such systems, complex macroscopic dynamics may arise due to neural heterogeneity. Thus, different SNN families have been considered that treat different system parameters such as the synaptic coupling strengths or the neural firing thresholds as distributed quantities. For most families of SNNs, the mean-field equations could not be derived analytically, though, and numerical approximations of the order parameter dynamics were employed instead [118, 119, 120]. However, for some special SNN families the mean-field equations have been derived analytically. As an early example, the mean-field dynamics of randomly coupled leaky integrate-and-fire neurons have been derived under the assumption that the input to any neuron can be described by a Gaussian stochastic process [116]. In this case, the system can be treated as a drift-diffusion system, thus allowing to apply the Fokker-Planck formalism. By imposing the additional constraint that the system be in an asynchronous, irregular firing regime, Brunel was able to derive the mean-field equations. Importantly, these mean-field equations cannot be applied to examine regimes of synchronous neural dynamics. A major breakthrough in the field has been achieved by the seminal work of Ott and Antonsen [121]. They showed that, in the thermodynamic limit, a low-dimensional, stable manifold exists in the state space of a globally coupled system of oscillators with distributed microscopic oscillator frequencies ω_i [122]. Most importantly, a closed-form, low-dimensional set of ordinary differential equations can be derived for particular choices of the frequency distribution. This ODE set exactly expresses the evolution of the macroscopic order parameters of the system. In other words, the Ott-Antonsen (OA) ansatz allows one to derive mean-field equations for coupled oscillator systems that are exact in the thermodynamic limit and allow to study phase transitions between asynchronous and synchronous macroscopic regimes. Clearly, the OA ansatz represents an invaluable method for this thesis and we thus provide a short outline of it below.

For a system of $N \to \infty$ oscillators as given by eq. (1.1) with $f(\theta_i, \theta_j) = \sin(\theta_j - \theta_i)$, the state of the system can be described via a probability distribution with $\rho(\omega, \theta, t)$ representing the probability density that oscillators with intrinsic frequency ω have a phase θ at time t. The Kuramoto order parameter of this system is given by

$$\sigma(t) = \int_{-\infty}^{\infty} \int_{0}^{2\pi} \rho(\omega, \theta, t) e^{-i\theta} d\theta d\omega, \tag{3.1}$$

and the OA ansatz has been devised to solve eq. (3.1). Under the conservation of oscillators, the system dynamics obey the continuity (or master) equation given by

$$\frac{\partial \rho}{\partial t} = -\frac{\partial}{\partial \theta}[\nu \rho], \quad \nu = \omega + \frac{k}{2i}(\sigma(t) e^{-i\theta} - \sigma^*(t) e^{i\theta}), \tag{3.2}$$

where k represents the global coupling strength of the oscillators and $\sigma^*(t)$ is the complex conjugate of $\sigma(t)$. Then, $\rho(\omega, \theta, t)$ can be expanded in a Fourier series in θ

$$\rho(\omega, \theta, t) = \frac{g(\omega)}{2\pi}(1 + F + F^*), \quad F = \sum_{n=1}^{\infty} \rho_n(\omega, t) e^{in\theta}, \tag{3.3}$$

where $g(\omega) = \int_0^{2\pi} \rho(\omega, \theta, t) d\theta$ represents the parameter distribution in the system. The OA ansatz now assumes that all Fourier coefficients of this expansion are powers of a single function, i.e. $\rho_n(\omega, t) = h(\omega, t)^n$ with $|h(\omega, t)| \leq 1$. By substituting this ansatz into eq. (3.2), a strong reduction in complexity is achieved:

$$\frac{\partial h}{\partial t} = \frac{k}{2}(\sigma^* - \sigma h^2) - i\omega h, \quad \sigma^* = \int_{-\infty}^{\infty} h(\omega, t) g(\omega) d\omega. \tag{3.4}$$

Finally, for appropriate choices of $g(\omega)$, the integral in eq. (3.4) can be solved analytically and a finite number of closed-form mean-field equations are received that describe the dynamics of the order parameters of the system exactly [121, 122, 57]. It is this ansatz that we will apply to networks of globally coupled QIF neurons in the following sections.

3.1.2 Low-dimensional dynamics in QIF networks

As described above, the OA ansatz allows one to derive exact mean-field equations that describe the low-dimensional dynamics of globally coupled oscillator systems in the thermodynamic limit [121]. While originally introduced for networks of Kuramoto oscillators, the OA ansatz applies to a broader family of oscillator systems. Most importantly, it has also been applied to systems of neural oscillators such as given by networks of theta neurons [123, 124, 57]. Thus, the OA ansatz does not only apply to systems of linear phase oscillators, but also generalizes to non-linear phase oscillators that can either express periodic or excitable behavior (see section 2.3). Recently, the OA ansatz has also been shown to allow for the derivation of exact mean-field equations for systems of all-to-all coupled QIF neurons [125]. We will provide an account of this in the following.

As described in section 2.3, the QIF neuron is the canonical form of type-I neurons. In this chapter, we consider networks of N all-to-all coupled, heterogeneous QIF neurons, where the evolution equation of the membrane potential V_i of a single QIF neuron i is defined as

$$\tau \dot{V}_i = V_i^2 + \eta_i + I(t) + \frac{J\tau}{N} \sum_{j=1}^{N} S_j, \tag{3.5a}$$

$$S_i = \sum_{k \backslash t_i^k < t} \int_{-\infty}^{t} G(t - t') \delta(t' - t_i^k) dt', \tag{3.5b}$$

with neuron-specific background current η_i, and global parameters given by the synaptic strength J, the evolution time constant τ, and the extrinsic input $I(t)$. A neuron i emits its k^{th} spike at time t_i^k when it reaches a threshold V_T upon which V_i is reset to $V_R = -V_i$. Consequently, eq. (3.5b) represents a convolution of the spikes of neuron i with a synaptic response kernel G, e.g. $G(t) = \mathrm{e}^{-t/\tau_s}/\tau_s$ in the case of exponential synapses with synaptic time scale τ_s. The term $s = \frac{1}{N}\sum_{i=1}^{N} S_i$ in the right-hand side of eq. (3.5a) thus represents the mean-field synaptic input that enters each QIF neuron in the network. Without loss of generality, we consider the limit $\tau_s \to 0$, such that $S_i \approx \sum_{k \backslash t_i^k < t} \delta(t' - t_i^k)$ represents the spiking activity of neuron i and $r = s = \frac{1}{N} \sum_{i=1}^{N} S_i$ is the average firing rate of the network.

As described in detail in section 2.3, the membrane potential V_i of a neuron can be directly related to its phase via the transform $V_i = \tan\left(\frac{\theta_i}{2}\right)$ if the limit $V_T \to \infty$ is considered. Under this transformation, eqs. (3.5a) and (3.5b) represent a network of theta neurons [92], which can be considered a network of globally coupled oscillators. Thus, the network satisfies the conditions for the existence of the OA manifold if $N \to \infty$ [121, 123]. This manifold can be described for the system given by eqs. (3.5a) and (3.5b) by following the Lorentzian ansatz described in [125], i.e. by making the assumption that the state variables V_i are distributed according to a Lorentzian at any given time:

$$\rho(V|\eta,t) = \frac{1}{\pi} \frac{z(\eta,t)}{[V - y(\eta,t)]^2 + z(\eta,t)^2}. \tag{3.6}$$

The center $y(\eta,t)$ and half-width at half-maximum (HWHM) $z(\eta,t)$ of eq. (3.6) are associated with the mean firing rate $r(\eta,t)$ and the membrane potential average over all neurons $v(\eta,t)$ via $z(\eta,t) = \pi r(\eta,t)$, and $y(\eta,t) = v(\eta,t)$, respectively. Thus, the mean firing rate and membrane potential are the two macroscopic quantities that are chosen as order parameters of the system by the Lorentzian ansatz and for which the dynamic equations are derived as follows.

Due to the conservation of the number of neurons, the network dynamics obey the continuity equation

$$\frac{\partial}{\partial t}\rho + \frac{\partial}{\partial V}\left[\left(\frac{V^2 + \eta + I}{\tau} + Js\right)\rho\right] = 0. \tag{3.7}$$

By inserting eq. (3.6) into eq. (3.7) it can be shown that the dynamics of $z(\eta,t)$ and $y(\eta,t)$ obey

$$\frac{\partial}{\partial t} w(\eta,t) = i\left[\frac{-w(\eta,t)^2 + \eta + I}{\tau} + Js\right], \tag{3.8}$$

for any η, with $w(\eta,t) = z(\eta,t) + iy(\eta,t) = \pi r(\eta,t) + iv(\eta,t)$. This equation describes the OA manifold of the system. However, since η is considered neuron-specific and thus a distributed quantity governed by a probability density $g(\eta)$, eq. (3.8) is still an infinite dimensional system. To find a closed set of equations for the order parameters of the system r and v, the following integral has to be solved:

$$\dot{w} = \int_{-\infty}^{\infty} \frac{\partial}{\partial t} w(\eta,t) g(\eta) d\eta. \tag{3.9}$$

While it is generally not possible to achieve this analytically, some particular choices of $g(\eta)$ allow for an analytic solution [121, 122, 125]. The most drastic reduction in the dimensionality of the system can be achieved by choosing the neural background excitabilities to be distributed according to a Lorentzian with density function

$$g(\eta) = \frac{1}{\pi} \frac{\Delta}{(\eta - \bar{\eta})^2 + \Delta^2} \tag{3.10}$$

as well, where $\bar{\eta}$ and Δ are the center and HWHM of the distribution, respectively. Using the residue theorem of complex analysis, eq. (3.9) can be solved merely by evaluating eq. (3.8) at the two poles of eq. (3.10) given by $\bar{\eta} \pm i\Delta$ [121, 125]. Subsequently, eq. (3.8) can be solved for

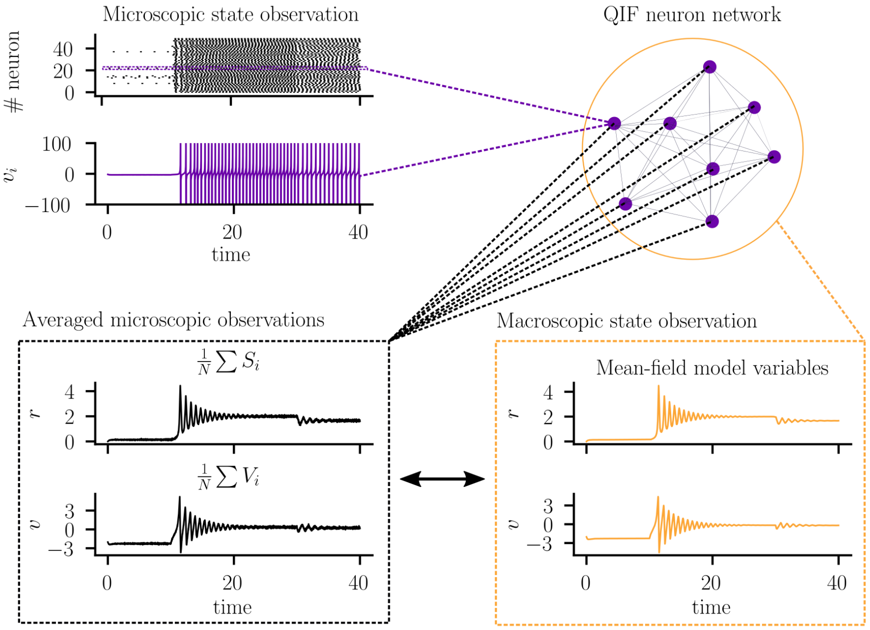

Figure 3.1: Relationship between the QIF network dynamics and the low-dimensional mean-field model dynamics. QIF network simulations were performed with $N = 10000$ neurons. Spikes are shown for 50 randomly selected neurons. Model parameters: $\Delta = 2$, $J = 15\sqrt{\Delta}$, $\bar{\eta} = -4\Delta$, $I(t) = 2.5$ if $10.0 \leq t < 30$ and $I(t) = 0$ otherwise.

r and v, yielding

$$\tau\dot{r} = \frac{\Delta}{\pi\tau} + 2rv, \tag{3.11a}$$

$$\tau\dot{v} = v^2 + \bar{\eta} + I(t) + Jr\tau - (\pi r\tau)^2, \tag{3.11b}$$

where we made use of $s = r$ again. These two coupled ordinary differential equations are a closed-form, exact representation of the macroscopic order parameter dynamics of the infinite dimensional system given by eqs. (3.5a) and (3.5b). A visual summary of this relationship between the microscopic system and the macroscopic variables governed by eqs. (3.11a) and (3.11b) is provided in Fig. 3.1. Due to the relationship between theta and QIF neurons, the average firing rate r and the average membrane potential v can be directly linked to the Kuramoto order parameter σ via $\sigma = \frac{1-W^*}{1+W^*}$ where $W = \pi r + iv$ [125]. This link also elucidates that the Lorentzian ansatz and the OA ansatz are essentially equivalent. This means that r and v are inherently linked to the macroscopic synchronization of the system and studying the system given by eqs. (3.11a) and (3.11b) is equivalent to studying macroscopic synchronization processes in the considered QIF network. In the following, we introduce STP mechanisms to the definition of the QIF network given by eqs. (3.5a) and (3.5b) and follow the Lorentzian ansatz outlined above to derive the mean-field equations.

3.1.3 Mean-field equations of QIF networks with short-term plasticity

For studying emergent phenomena in QIF networks, it is of interest to know how well the derivation of the mean-field equations generalizes to other descriptions of neural dynamics than the particular family of QIF networks given by eqs. (3.5a) and (3.5b). While these equations represent the case of instantaneous, linear synaptic interactions, it is reasonable to expect that dynamic, possibly nonlinear forms of synaptic transmission and other types of neural coupling may enrich the dynamic repertoire of the network with new collective states. Consequently, different extensions of the QIF model have been proposed that added biophysical details to the neural interactions and used those to explain collective neurodynamic phenomena such as the onset of synchronous neural activity. So far, these extensions either included descriptions of synaptic transmission delays [126, 127], or electrical coupling between QIF neurons [128, 129]. The latter coupling mechanism is also known as gap junctions and allows neighbouring neurons to interact through a direct exchange of ions via channels in their membrane, which happens on a much faster time scale than the relatively slow synaptic interactions. One important family of neurodynamic mechanisms that has not been considered in the context of collective QIF network dynamics yet, is given by short-term plasticity (STP) mechanisms [18, 130]. STP describes a family of self-organization mechanisms that cause activity-dependent, transient adaptations of the input-output relationship of single neurons or synapses. At the level of neurons, STP refers to spike-triggered balancing currents that lead to the adaptation of the neuron's spiking frequency in response to a given input [131, 132]. Thus, they are also known as spike-frequency adaptation (SFA) mechanisms. At the synaptic level, STP refers to all mechanisms that lead to the transient adaptation of the efficacy of a synapse after pre-synaptic stimulation of the synapse [130]. Short-term synaptic depression (SD), for example, can be caused by pre-synaptic processes such as resource depletion and post-synaptic processes such as receptor desensitization [133, 134]. Generally, STP mechanisms have been demonstrated to be an important determinant of neural synchronization processes [18, 130, 135, 136, 137, 138]. For instance, it has been demonstrated that SFA can lead to the emergence of highly synchronous bursting states in networks of coupled spiking neurons [131, 139, 140]. In healthy neural communication, emergent bursting activity may allow for a more reliable information transmission via chemical synapses [141]. This can be explained by the synchronized activity of the population during the burst, which stabilizes neural information transmission against different types of noise [28]. On the other hand, increased bursting activity has been found in various neurological diseases, such as epilepsy or Parkinson's disease and can act disruptively on neural communication, if exceeding certain levels of occurrence [142, 143]. If STP mechanisms are an important determinant of such emergent bursting, they may play a critical role for theories of brain function based on collective neural synchronization processes.

In the following sections, we derive and study mean-field equations for SNNs subject to different forms of STP. First efforts into this direction were made for the special case of SFA in a network of coupled linear integrate-and-fire neurons, where the Fokker-Planck formalism and an adiabatic approximation were employed for the mean-field reduction [140]. Analyzing the mean-field model, Gigante et al. were able to identify different types of collective synchronization. Here, we apply the OA ansatz to three different forms of STP in networks of globally coupled QIF neurons: SFA, post-synaptic STP, and pre-synaptic STP. Subsequently, we use bifurcation analysis to identify states of collective synchronization as well as the limiting conditions for such synchronous states to occur.

3.2 Dynamics of QIF networks with post-synaptic STP

The first STP mechanism we consider is post-synaptic depression (SD), which is a multiplicative down-scaling of the synaptic efficacy. Neurobiologically, this can represent various mechanisms such as post-synaptic receptor desensitization, alterations in the density of post-synaptic receptors, or resource depletion at the synapse [134, 130].

3.2.1 Mean-field equations for QIF networks with post-synaptic STP

To introduce short-term SD to our system, we change eq. (3.5a) as follows

$$\tau \dot{V}_i = V_i^2 + \eta_i + I(t) + (1 - X_i)\frac{J\tau}{N}\sum_{j=1}^{N} S_j, \tag{3.12}$$

This adds a dependency of the mean-field synaptic input on an adaptation variable X_i pertaining to the i^{th} post-synaptic neuron. The latter follows the microscopic evolution equations

$$\begin{aligned} X_i &= \int_{-\infty}^{t} \frac{\alpha}{N} \sum_{j=1}^{N} \sum_{k \backslash t_j^k < t} G_X(t - t')\delta(t' - t_j^k)\mathrm{d}t', && \text{(3.13a)} \\ &= \alpha G_X * r, && \text{(3.13b)} \\ G_X(t) &= \tau_x^{-2} t e^{-t/\tau_x}, && \text{(3.13c)} \end{aligned}$$

which express SD as a convolution with an alpha kernel with rate α and time scale τ_x. This choice accounts for (a) the delay between post-synaptic activation and peak adaptation, (b) the slow decay of SD to baseline, and (c) the exponential shape of the rise and decay of SD that have been reported in experimental studies [134, 144, 135, 130]. The alpha kernel results from the bi-exponential kernel when the rise and decay time constants of the bi-exponential dynamics are identical [106]. This relationship allows one to apply our model to scenarios where the adaptation dynamics can be described by up to two different timescales and it allows for an easy extension of our STP mechanism to differentiate between rise and decay times of STP. Importantly, this kind of STP mechanism has no effect on an isolated neuron, because it only affects the susceptibility to synaptic input which is effectively zero shortly after it spiked (due to refractoriness). Therefore, any changes to the network behavior caused by SD have to emerge from the interaction between the network units. Furthermore, SD is coupled to the mean-field firing rate of the population, i.e. each spike in the network triggers SD at all network units. This becomes clear from eq. (3.13a), where X_i is driven by the mean firing rate r of the network and thus behaves like a global variable x that can be written as eq. (3.13b), where $*$ denotes the convolution operation. Therefore, the synaptic input to each neuron behaves like a mean-field variable as well and we can simply follow the steps outlined in section 3.1.2 to derive the mean-field equations. To this end, we use $s = (1 - x)r$ instead of the original $s = r$ to solve eq. (3.8) with post-synaptic depression x given by eqs. (3.13b) and (3.13c). Finally, by solving the convolution integral in eq. (3.13a), we receive the following macroscopic evolution equations for a QIF system with SD:

$$\tau\dot{r} = \frac{\Delta}{\pi\tau} + 2rv, \tag{3.14a}$$

$$\tau\dot{v} = v^2 + \bar{\eta} + I(t) + Jr\tau(1-x) - (\pi r\tau)^2. \tag{3.14b}$$

$$\tau_x\dot{x} = y, \tag{3.14c}$$

$$\tau_x\dot{y} = \tau_x\alpha r - 2y - x. \tag{3.14d}$$

We demonstrate the accuracy of this mean-field description below.

3.2.2 Effects of post-synaptic STP on the QIF network dynamics

To analyze the effects of short-term SD on the QIF network dynamics, we performed numerical bifurcation analysis of the four dimensional system defined by eqs. (3.14a-3.14d). For different values of α, we initialized the model at a low activity state and continued the model in $\bar{\eta}$. To this end, we used the software package Auto-07p [88]. The SD time scale was chosen as $\tau_x = 10\tau$, corresponding to slow SD relative to the evolution of the average membrane potential and firing rate. In accordance with the analysis of [125], we found two fold bifurcations for $\alpha = 0$, defining the borders of a bi-stable regime in $\bar{\eta}$ in which a stable fixed point (representing low firing activity) and a stable focus (representing high firing activity) are separated by a saddle. For an increasing adaptation rate α, we identified a parameter regime in which two subcritical Hopf bifurcations occur (see Fig. 3.2A). The unstable limit cycle emerging from the branch of fixed points (lower branch) only exists in a very narrow parameter range and gets annihilated quickly via a homoclinic bifurcation with the saddle. As shown in Fig. 3.2B, the unstable limit cycles that emerges from the branch of foci (upper branch) via a subcritical Hopf bifurcation undergoes a fold of limit cycle bifurcation, marking the birth of a second stable limit cycle. Continuation of the stable limit cycle in $\bar{\eta}$ led to a second fold of limit cycle bifurcation. This fold bifurcation occurred at a value of $\bar{\eta}$ close to the one where the stationary states of the system undergo a saddle-node bifurcation. The period of this unstable limit cycle grew rapidly towards infinity, terminating at a homoclinic bifurcation close to the fold bifurcation. Since this model behavior can only be observed in a very small parameter range in our model, it is of limited relevance for macroscopic synchronization processes, which is why we omit a detailed analysis of this homoclinic bifurcation. However, this scenario has been reported in neural models with slow-fast dynamics before and was analyzed in detail in [145].

As shown in Fig. 3.2B, the stable regime of the limit cycle can co-exist with the high-activity focus and hence permits various transitions between synchronous and asynchronous dynamics. Fig. 3.2C and D demonstrate that the synchronous state can be transiently entered either from a low-activity state through excitation (Fig. 3.2C) or from a high-activity state through inhibition (Fig. 3.2D). Furthermore, the bi-stable regime allows for hysteresis, i.e. switching between limit cycle and focus equilibrium through transient excitatory and inhibitory inputs (Fig. 3.2E). In neural communication, this regime is particularly relevant, since it allows for quick transitions between highly different firing modes via transient inputs and introduces a form of network memory. However, it is also of interest for pathological neural dynamics such as observed in epilepsy, which have been proposed to reflect switching between a healthy

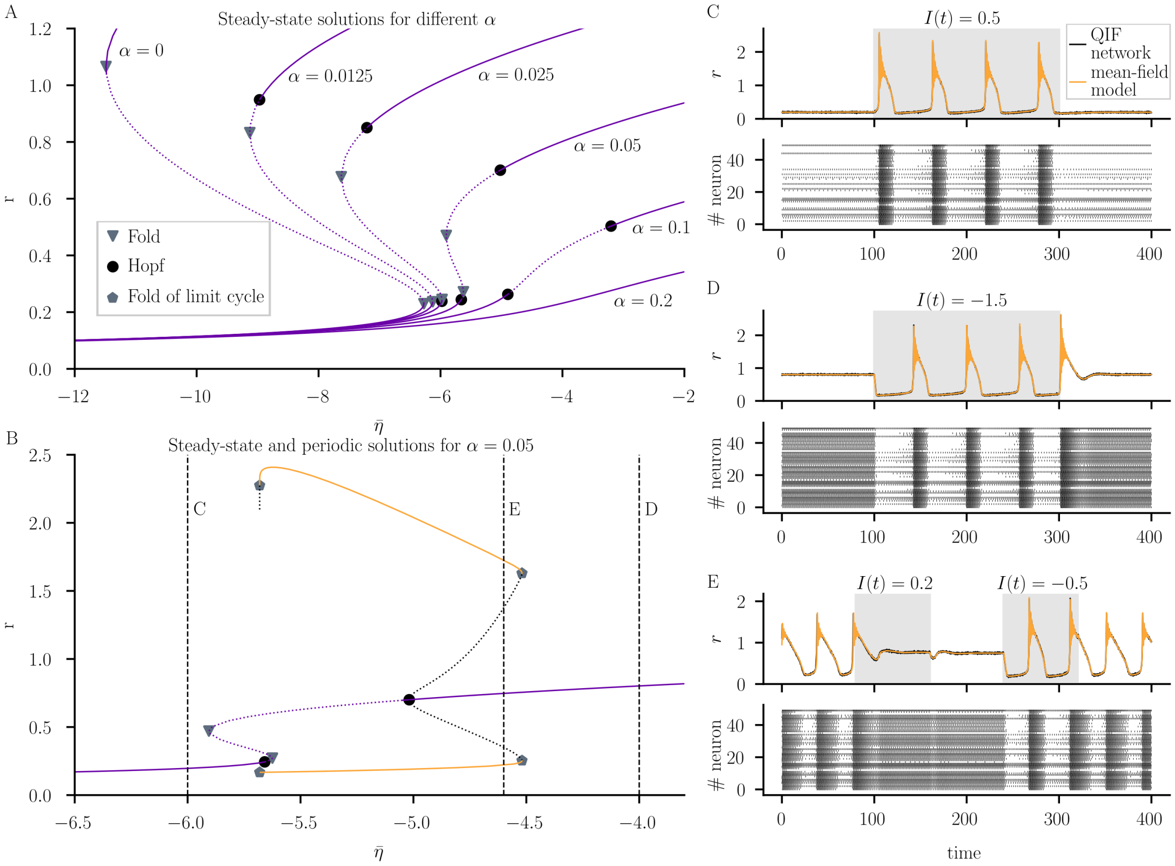

Figure 3.2: Phase transitions to synchronous neural activity in QIF networks with SD. **A:** 1D Bifurcation diagram of steady-state solutions in $\bar{\eta}$ for various values of α. Stable (unstable) equilibria are marked by solid (dotted) lines. **B:** Subcritical Hopf bifurcations and fold of limit cycle bifurcations give rise to a synchronous regime with large-amplitude macroscopic oscillations. Minimum and maximum of the limit cycle are depicted in orange. Vertical lines indicate values of $\bar{\eta}$ used for C-E. **C:** Transient oscillations induced by excitation. **D:** Transient oscillations induced by inhibition. **E:** In the bistable regime, excitatory and inhibitory stimuli switch the system between sustained oscillations and sustained steady-state firing. Microscopic network simulations were performed with $N = 10000$ neurons. Spikes are shown for 50 randomly selected neurons. Model parameters: $\Delta = 2$, $J = 15\sqrt{\Delta}$, $\tau = 1$, $\tau_x = 10$, $\alpha = 0.05$.

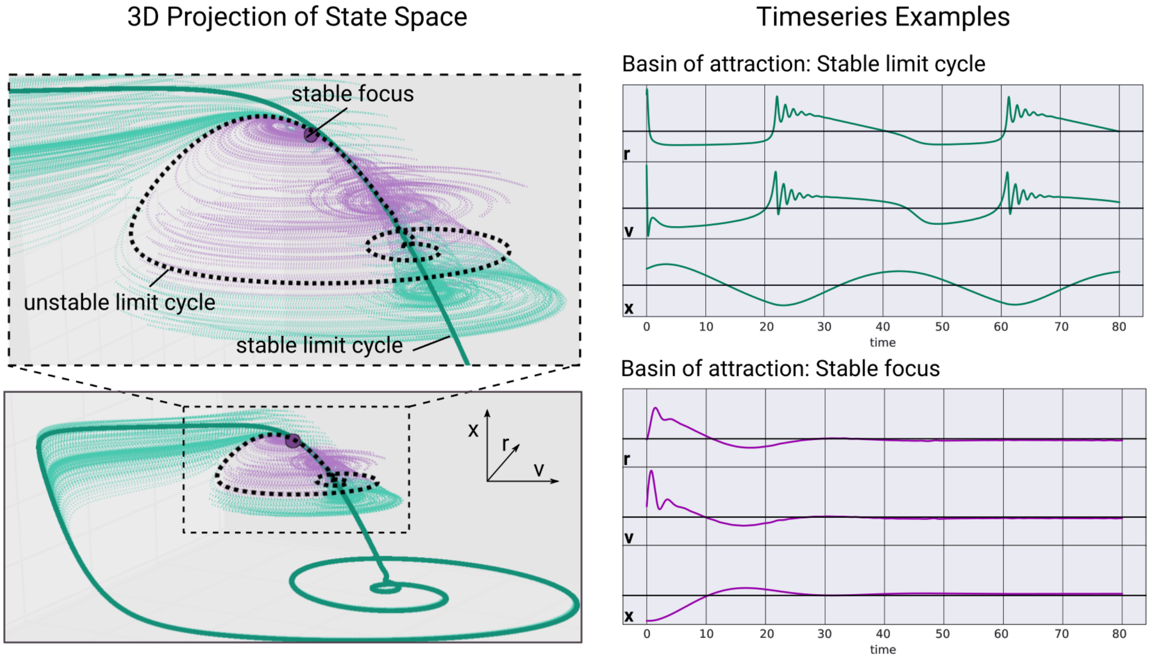

Figure 3.3: Co-existence of synchronous and steady-state behavior. **Left column:** 3-dimensional projection (onto r, v, and A) of the 4-dimensional state-space representation of the system dynamics. For the present parameters the stable limit cycle (bold green curve) coexists with a stable focus (purple dot) and an unstable limit cycle (black dashed curve). Thin curves mark trajectories with different initial conditions in the basin of attraction of the limit cycle (green) or the focus (purple). **Right column:** Two sample time series that have been initiated either in the basin of attraction of the stable limit cycle ($r_0 = 1.8$, $v_0 = 1.0$, $x_0 = 0.4$, $y_0 = 0.01$), or in the basin of attraction of the stable focus ($r_0 = 0.75$, $v_0 = -0.4$, $x_0 = 0.36$, $y_0 = 0.0$). Model parameters: $\Delta = 2$, $J = 15\sqrt{\Delta}$, $\tau = 1.0$, $\tau_x = 10$, $\alpha = 0.05$, $\bar{\eta} = -4.6$.

state of low neural synchrony and a co-existing pathological, synchronous state [146, 147]. Importantly, Fig. 3.2C-E show a close correspondence between numerical simulations of the mean-field model and the spiking neural network.

3.2.3 Characteristics of the synchronous QIF regime

For a better understanding of the bi-stable regime, we mapped out the basins of attraction with respect to the state variables x, r and v of the model given by eqs. (3.14c), (3.14a), and (3.14b), respectively. Fig. 3.3 visualizes different trajectories of this three-dimensional projection of the system when initialized at different points near the unstable limit cycle that separates the stable limit cycle (green) and the stable focus (purple). It is the unstable (saddle) limit cycle and its stable manifold (i.e. all points in state space from which the system converges onto the unstable limit cycle) that act as a separatrix between the stable focus and the stable limit cycle. This separating behavior is visible where the unstable manifold is orthogonal to the 3D-projection in Fig 3.3, especially along the left part of the unstable limit cycle.

In a next step, we performed a two-parameter continuation of the subcritical Hopf bifurcation in $\bar{\eta}$ and α, to examine the dependence of the macroscopic oscillations in the synchronous regime on the interplay between network excitation and SD rate. Fig. 3.4 shows that dynamic regimes of macroscopic QIF oscillations can be found for a range of the two parameters which is bounded by the fold of limit cycle bifurcations. For $\bar{\eta}$, the parameter

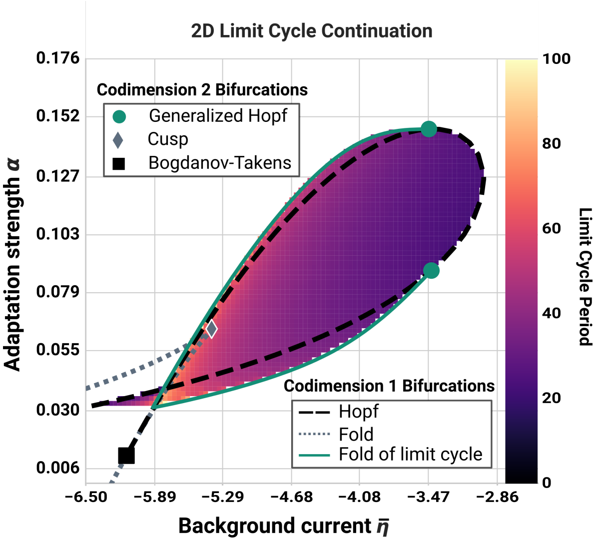

Figure 3.4: Existence and period of macroscopic oscillations. Lines indicate two-parameter continuations of codimension 1 bifurcations in the ($\bar{\eta}$,α) plane. The color-coded region shows the oscillation period of the stable limit cycle (depicted in units of τ). Other model parameters: $\Delta = 2$, $J = 15\sqrt{\Delta}$, $\tau = 1.0$, $\tau_x = 10$.

range in which the limit cycle exists corresponds to most of the cells in the population being in an excitable regime and has been reported for a number of models using QIF neurons (e.g. [125, 126, 148]). Within this range, the oscillation frequency scales with the input strength, which makes the latter an interesting parameter for tuning this model to reflect experimentally reported neural oscillations. In summary, we identified SD as a potential mechanism for synchronous neural dynamics to occur in networks of globally coupled spiking neurons. We demonstrated that this synchronization mechanism could be transiently switched on and off via transient input currents and found that the macroscopic oscillation frequency can be tuned via the input strength.

3.2.4 Finite Size Effects

So far, we examined phase transitions between synchronous and asynchronous regimes in a mean-field model of a QIF network with short-term SD. The mean-field model has been derived in the thermodynamic limit ($N \to \infty$) and under the constraint of all-to-all coupling. We demonstrated that the mean-field model is an accurate representation of the macroscopic behavior of an all-to-all coupled network with $N = 10^4$ QIF neurons. In this section, we investigate how well our findings generalize to more realistic network architectures. Specifically, we ask how sensitive our findings are with respect to the number of cells and the connection probabilities inside the QIF network. For this purpose, we constructed networks with varying numbers of QIF neurons N and varying coupling probabilities p and compared their dynamic behavior against the mean-field model given by eqs. (3.14a-3.14d). We initialized each model in a regime where a stable limit cycle is the mere existing equilibrium solution ($\bar{\eta} = -5.5$, $\Delta = 2$, $J = 15\sqrt{\Delta}$, $\tau_x = 10$, $\alpha = 0.05$) and performed numerical simulations over a time interval of $T = 1000\tau$. For comparison with the mean-field model, we calculated the average oscillation frequency as well as the peak amplitude of the oscillations. The results of this procedure are visualized in Fig. 3.5.

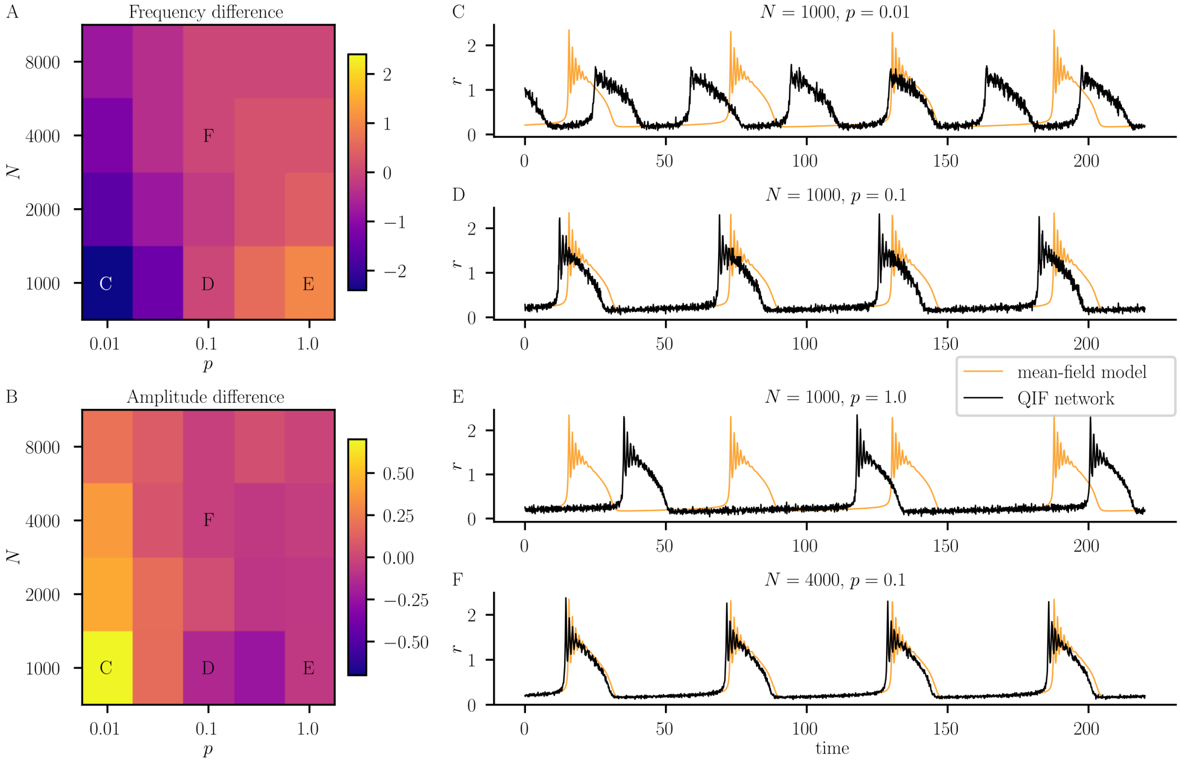

Figure 3.5: Finite size effects. **A, B:** Difference between mean-field model and spiking neural network in oscillation frequency (A) and maximum oscillation amplitude (B) for different network sizes (N) and coupling probabilities (p) of the spiking neural network. **C-F:** Sample time series of the mean-field model and spiking neural network for specific N and p. Model parameters: $\Delta = 2$, $\bar{\eta} = -5.5$, $J = 15\sqrt{\Delta}$, $\tau = 1$, $\tau_x = 10$, $\alpha = 0.05$.

Most importantly, we found stable oscillations in each of the microscopic networks we investigated, even in the smallest, most sparsely connected one (see Fig.3.5C). Furthermore, we observed that the oscillation frequency scales negatively with coupling probability whereas increases of the network size generally improved the correspondence with the mean-field model (see Fig. 3.5A). This led to the interesting behavior that the correspondence between small networks (e.g. with $N = 1000$ neurons) and the mean-field model had an optimum at intermediate coupling probabilities (e.g. $p = 0.1$). Regarding the oscillation amplitude, we observed that both a small network size and a small coupling probability led to a reduced amplitude, indicative of a decreased overall synchronization between QIF neurons (see Fig.3.5B). In summary, we found that our mean-field model generalizes well to networks with realistic cell counts and coupling probabilities, even though it was derived for the special case of an infinitely large network with all-to-all coupling. Most importantly, our finding that synchronous neurodynamic regimes can emerge from the interaction of recurrent, excitatory coupling and STP have been reproduced in each QIF network we examined. Discrepancies between the mean-field model and the microscopic network were found for small, sparsely coupled networks in the oscillation frequency and the average synchronization in the network. Interpreting those quantities in the mean-field model should thus be handled cautiously in cases where the underlying QIF network may be of small size or very sparsely coupled.

3.3 Dynamics of QIF networks with spike-frequency adaptation

In this section, we examine the effects of SFA on the QIF network dynamics given by eqs. (3.5a) and (3.5b). SFA differs from the above described synaptic depression mechanism in two aspects: (1) It affects the pre-synaptic activity instead of the post-synaptic efficacy, and (2) it acts additively instead of multiplicatively [139, 140].

3.3.1 Mathematical Definition of SFA

SFA is a homeostatic mechanism that acts at the single cell level via spike-triggered balancing currents [131, 132]. As such, SFA is an adaptive mechanism driven by the firing rate of a single cell rather than the firing rate of the whole network. To model the neuron-specific SFA dynamics, we again employ the convolution of the single cell firing rate with an alpha kernel, which can be expressed by two coupled first order differential equations

$$\tau_x \dot{X}_i = X_i, \tag{3.15a}$$

$$\tau_x \dot{Y}_i = \alpha \tau_x S_i - 2Y_i - X_i, \tag{3.15b}$$

where the neuron-specific spiking activity S_i is still given by $S_i \approx \sum_{k \backslash t_i^k < t} \delta(t' - t_i^k)$. Adding the adaptation variable X_i to eq. (3.5a), we receive the following evolution equation for the membrane potential of the single neuron

$$\tau \dot{V}_i = V_i^2 + \eta_i - X_i + I(t) + J\tau r. \tag{3.16}$$

Here, we additionally used $r = \frac{1}{N}\sum_{i=1}^{N} S_i$, since the synaptic input does not directly depend on the adaptation variable anymore. In terms of the OA ansatz, this represents a more substantial change to the system than the previously described SD mechanism. As can be seen from eq. (3.16), the adaptation variable X_i affects the QIF dynamics in the same way as η_i. Therefore, the SFA mechanism leads to a dynamic adaptation of the firing frequency of the single QIF neurons, should they be in the periodic firing regime (see section 2.3 for a description of the dynamic regimes of a single QIF neuron). This violates the assumption made by the OA ansatz, however, that the intrinsic frequencies of the microscopic oscillators cannot change over time. To apply the OA ansatz nonetheless, we make the additional assumption that the adaption variables X_i change very slowly in comparison to V_i, i.e. that $\tau_x \gg \tau$. Under this assumption, we can remove the slow time scale of the adaptation via adiabatic elimination and consider the Lorentzian ansatz given by eq. (3.6) with respect to the fast time scale. In this limit, the variable X_i can effectively be regarded as constant and thus absorbed into η_i (for a similar approach see [140]).

Since the neuron-specific spiking activity S_i is associated with $z(\eta, t)$ via $S_i = z(\eta_i, t)/\pi$, the OA manifold is given by

$$\partial_t w = i[\eta + Jr + I - w^2 - \alpha G_X * \mathrm{Re}[w]/\pi]. \tag{3.17}$$

If $g(\eta)$ follows the Lorentzian distribution, then the evaluation of eq. (3.17) at the poles $\bar{\eta} \pm i\Delta$ yields

$$\pi\dot{r} + i\dot{v} = i[\bar{\eta} - i\Delta + Jr - (\pi r + iv)^2 - \alpha G_X * r]. \tag{3.18}$$

By solving eq. (3.17) for r and v, we receive the macroscopic evolution equations

$$\tau\dot{r} = \frac{\Delta}{\pi\tau} + 2rv, \tag{3.19a}$$

$$\tau\dot{v} = v^2 + \bar{\eta} + I(t) - x + Jr\tau - (\pi r\tau)^2, \tag{3.19b}$$

$$\tau_x\dot{x} = x, \tag{3.19c}$$

$$\tau_x\dot{y} = \alpha\tau_x r - 2y - x. \tag{3.19d}$$

Here, we additionally solved the convolution integral given by $G_X * r$ to turn the integro-differential system given by eq. (3.18) into a set of coupled ODEs.

3.3.2 Effects of SFA on the QIF network dynamics

Using the mean-field system defined by eqs. (3.19a-3.19d), we performed parameter continuations in $\bar{\eta}$ for different values of α again. This was done to compare the results we obtained for QIF networks with SD to the dynamics of QIF networks with SFA. As can be seen in Fig. 3.6A, we found results strikingly similar to the ones we found for SD. For sufficiently strong levels of SFA ($\alpha = 1.0$), we found a subcritical Hopf bifurcation in $\bar{\eta}$, marking the birth of an unstable limit cycle. Furthermore, we again found a bi-stable region, in which the unstable limit cycle separates the focus from a stable limit cycle. This regime exists between the subcritical Hopf bifurcation and a fold of limit cycle bifurcation from which the stable and the unstable limit cycle are born. As depicted in Fig. 3.6B, these regimes could be well traversed

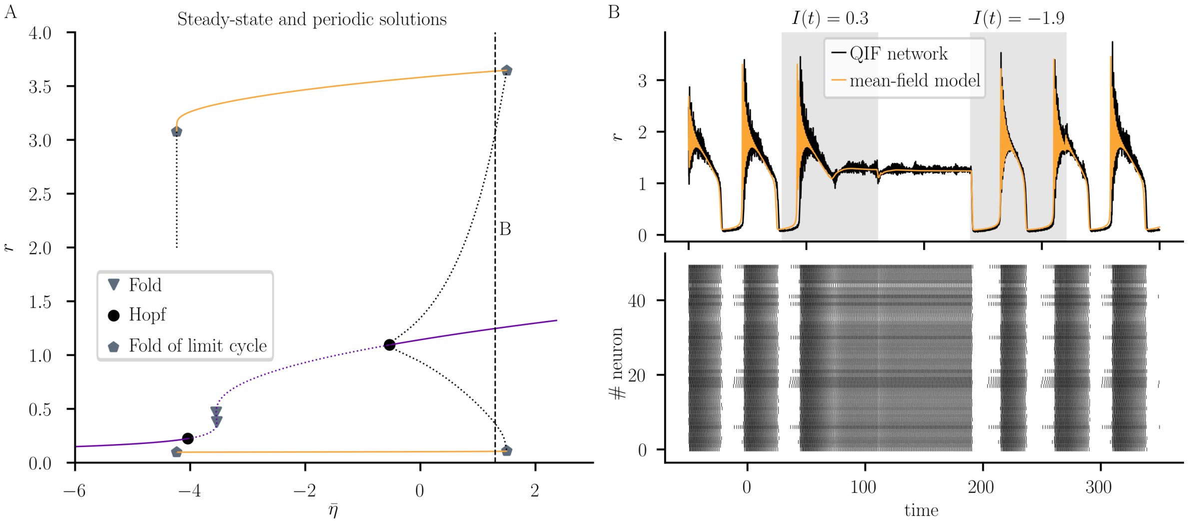

Figure 3.6: Phase transitions to synchronous neural activity in QIF networks with SFA. **A:** 1D bifurcation diagram of steady-state solutions (purple) in $\bar{\eta}$. Subcritical Hopf bifurcations and fold of limit cycle bifurcations lead to the emergence of macroscopic oscillations. The limit cycle minima and maxima are visualized in orange. Stable (unstable) equilibria are marked by solid (dotted) lines. The dashed vertical line marks the initialization point used for B. **B:** In the bistable regime, excitatory and inhibitory stimuli switch the system between sustained oscillations and steady-state firing. Microscopic simulations were performed with $N = 10000$ QIF neurons. Model parameters: $\Delta = 2$, $J = 15\sqrt{\Delta}$, $\tau = 1$, $\tau_x = 10$, $\alpha = 1.0$.

via transient inputs. Driving the microscopic model with the same transient inputs, we found that the spiking dynamics were still attracted to the low-dimensional manifold described by the macroscopic system. This shows, that even with $\tau_x = 10\tau$, the condition $\tau_x \gg \tau$ is sufficiently satisfied for the mean-field description of a QIF network with SFA to be valid.

3.4 Mean-field dynamics of QIF networks with pre-synaptic STP

As a next step, we discuss the descriptions of synaptic STP that are allowed for in the context of deriving Ott-Antonsen manifolds for heterogeneous QIF networks. In section 3.2, we demonstrated that mean-field equations can be derived for QIF networks with synaptic STP if two conditions are satisfied: First, each time a neuron spikes, it triggers synaptic STP at each of its outgoing synapses. Second, a single input spike triggers synaptic STP at all incoming synapses of a neuron. Under those conditions, synaptic STP is no longer neuron specific and can simply be treated as a macroscopic variable driven by the mean-field activity of the network. This form of STP affects only the total input to the post-synaptic neuron and could be used to model forms of receptor desensitization [134, 149], short-term changes in the number of available post-synaptic receptors [150, 151], or resource depletion at the post-synaptic complex [152, 153]. Importantly, it cannot be considered to represent pre-synaptic forms of plasticity, such as vesicle depletion [154, 133]. While the first assumption may still hold for pre-synaptic STP, the second assumption would not. Pre-synaptic resource depletion cannot be assumed to affect all incoming synapses of a neuron, but only the synapse via which a spike was transmitted (see Fig. 3.7). In this section, we address the question of

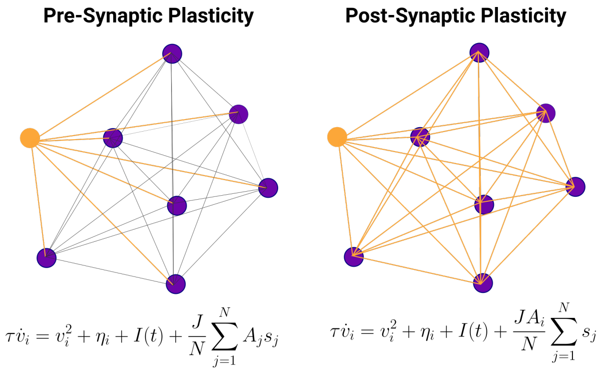

Figure 3.7: Pre- vs. Post-Synaptic Forms of Short-Term Plasticity. Nodes represent neurons in an all-to-all coupled network and edges between the nodes represent bidirectional synaptic couplings. Red nodes are active, i.e. did just spike, whereas blue nodes have not spiked for a sufficient period in time. Edges that are colored in red show adaptation in response to the activity of the red nodes, whereas grey edges do not. The two equations describe the membrane potential evolution of a QIF neuron for the cases of pre- and post-synaptic plasticity. Note that the adaptation variable A_i is specific for pre-synaptic source neurons for the former case, and specific to post-synaptic target neurons for the latter.

whether exact mean-field equations can be derived for QIF networks with pre-synaptic forms of short-term plasticity (STP).

A well established model of pre-synaptic STP is the phenomenological model introduced in [133], which describes the dynamics of pre-synaptic facilitation and depression. We will discuss the derivation of mean-field equations for QIF networks with pre-synaptic STP with respect to this model, though we will discuss the implications of our findings for general descriptions of pre-synaptic STP dynamics as well. In the following section, we define the microscopic model under consideration. This will be followed by sections in which we discuss different approaches to derive equations for the low-dimensional network dynamics. While we do not find the exact mean-field equations for QIF networks with pre-synaptic STP, we provide two different approximations that match well with the QIF network dynamics. We point to the problems that would have to be solved in future attempts at an exact mean-field derivation and evaluate the accuracy of our approximate solutions via numerical simulations and bifurcation analysis.

3.4.1 The OA manifold for QIF networks with pre-synaptic STP

We consider a network of N all-to-all coupled QIF neurons with pre-synaptic STP

$$\tau \dot{V}_i = V_i^2 + \eta_i + I(t) + \frac{J\tau}{N}\sum_{j=1}^{N} X_j^- U_j^+ S_j, \tag{3.20a}$$

$$\tau_x \dot{X}_i = 1 - X_i - \alpha X_i^- U_i^+ S_i \tau_x, \tag{3.20b}$$

$$\tau_u \dot{U}_i = U_0 - U_i + U_0(1 - U_i^-) S_i \tau_u, \tag{3.20c}$$

$$S_i = \sum_{k \backslash t_i^k < t} \int_{-\infty}^{t} G(t - t')\delta(t' - t_i^k)dt', \tag{3.20d}$$

where eq. (3.20d) represents a convolution of the spiking activity of neuron i with a synaptic response kernel G, e.g. in the case of exponential synapses $G(t) = \mathrm{e}^{-t/\tau_s}/\tau_s$ with synaptic time scale τ_s. A neuron i emits its k^{th} spike at time t_i^k when it reaches a threshold V_T upon which V_i is reset to $V_R = -V_i$. Without loss of generality, we consider the limit $\tau_s \rightarrow 0$, such that S_i represents the spiking activity of neuron i. Eqs. (3.20b) and (3.20c) resemble the pre-synaptic STP mechanism described in [133]. We note here that $\cdot^-$ denotes a quantity just before a spike occurs (left limit), and $\cdot^+$ denotes a quantity just after the neuron spiked (right limit). This discontinuity accounts for the biological fact that a pre-synaptic spike triggers synaptic facilitation before it can affect the post-synaptic neuron, by moving vesicles closer to the membrane. Synaptic depression, however, results from the consumption of vesicles for the synaptic transmission process and is thus affected slightly later than synaptic facilitation. We assume neural spiking activity to affect all outgoing synapses of a neuron equally, hence X_i and U_i can be considered as neuron- and not synapse-specific. The adaptation dynamics are controlled by the depression and facilitation time constants τ_x and τ_u, a depression strength α, and a baseline synaptic efficacy U_0. Eq. (3.20a) describes the evolution of the membrane potential V_i of neuron i, which depends on a background excitability parameter η_i, an extrinsic forcing term $I(t)$, the membrane time constant τ, and the coupling with the network activity. The latter is given by a sum over the output S_i of each neuron in the network, weighted by a global coupling strength J, and the neuron-specific synaptic depression X_i and facilitation U_i.

As discussed in section 3.1, the OA ansatz can be used to derive exact, closed-form mean-field equations for eqs. (3.20a-3.20d) in the limits $N \rightarrow \infty$ and $V_T \rightarrow \infty$, if X_i and U_i are constants, i.e. in QIF networks without STP [125]. Furthermore, we showed in section 3.2 that the mean-field derivation via the OA ansatz can also be achieved in cases where X_i and U_i are driven by the mean-field activity, i.e. when S_i is replaced by $\sum_{j=1}^N S_j$ in the right-hand sides of eqs. (3.20b) and (3.20c). However, for non-constant synaptic depression X_i and facilitation U_i driven by the pre-synaptic firing rates S_i, the mean-field equations are more difficult to derive. Following the Lorentzian ansatz described in [125], we make the assumption that the probability density associated with any value of V given a background excitability η is given by a Lorentzian density function at any time t:

$$\rho(V|\eta, t) = \frac{1}{\pi} \frac{z(\eta, t)}{[V - y(\eta, t)]^2 + z(\eta, t)^2}. \tag{3.21}$$

As described earlier, the center $y(\eta, t)$ and HWHM $z(\eta, t)$ of eq. (3.21) are related to the mean firing rate and the membrane potential average of the QIF network via $z(\eta, t) = \pi r(\eta, t)$, and $y(\eta, t) = v(\eta, t)$, respectively. The conservation of the number of neurons leads to the following continuity equation for the network dynamics:

$$\partial_t \rho + \partial_V \left[\left(\frac{V^2 + \eta + I}{\tau} + J r_{\text{eff}} \right) \rho \right] = 0, \tag{3.22}$$

where $r_{\text{eff}} = \frac{1}{N} \sum_{j=1}^N X_j^- U_j^+ S_j$ is the effective mean-field network activity that arrives at each neuron. By inserting eq. (3.21) into eq. (3.22) it can be shown that the dynamics of $w(\eta, t) = z(\eta, t) + iy(\eta, t)$ obey

$$\partial_t w(\eta, t) = i \left[-w(\eta, t)^2 + \frac{V^2 + \eta + I}{\tau} + J r_{\text{eff}} \right] \tag{3.23}$$

for any η. Since $r_{\text{eff}} = \frac{1}{N}\sum_{j=1}^{N} X_j^- U_j^+ S_j \neq r$ in general, r_{eff} must be calculated to arrive at closed-form equations for r and v. Two major problems have to be solved in this regard: (a) The effective network input r_{eff} has to be expressed via mean-field variables such as the average firing rate r and average depression and facilitation variables x and u. If this cannot be done, the mean-field equations would still contain neuron-specific variables, thus increasing their dimensionality dramatically. (b) The mean-field equations for the average depression $x = \frac{1}{N}\sum_{i=1}^{N} X_i$ and facilitation $u = \frac{1}{N}\sum_{i=1}^{N} U_i$ have to be solved. However, the evaluation of these sums requires one to solve the coupled, non-linear differential eqs. (3.20b) and (3.20c), which only has been achieved for stationary network input so far [133]. In the following section, we will address problem (b) and compare our results with recently proposed mean-field equations for a similar synaptic STP model [155]. The remainder of this section will address different attempts to solve problem (a).

3.4.2 Analytical solutions for microscopic STP

As argued in the previous section, finding closed-form mean-field equations for the system given by eq. (3.20) requires one to calculate the average depression $x = \frac{1}{N}\sum_{i=1}^{N} X_i$ and average facilitation $u = \frac{1}{N}\sum_{i=1}^{N} U_i$ across neurons. We start by considering a steady-state solution of eq. (3.20), where each neuron expresses periodic firing activity that produces a spike train $S_i(t) = \sum_{n=-\infty}^{\infty} \delta(t - nT_i)$. Thus, the neuron under consideration spikes periodically with a period T_i, which corresponds to a firing rate of $r_i = 1/T_i$. In this scenario, solutions for the microscopic STP variables can be obtained analytically [133]. The evolution equations for synaptic short-term depression X_i and short-term facilitation U_i are given by eqs. (3.20b) and (3.20c), respectively. For the remainder of this section, we will omit the neuron index i for brevity. The (relative) strength of a synapse is given by $0 < U^+X^- < 1$. We denote U by U_n^- just before the corresponding neuron emitted its n^{th} spike, and by U_n^+ just after the n^{th} spike. Solving the homogeneous part of the model equation, we obtain

$$U_{n+1}^- = U_0 + (U_n^+ - U_0)e^{-T/\tau_u}, \tag{3.24}$$

and the change of U due to a spike is found to be

$$U_{n+1}^+ = U_{n+1}^- + U_0(1 - U_{n+1}^-). \tag{3.25}$$

These expressions can be reformulated into the following iteration scheme:

$$U_{n+1}^+ = U_0 + (1 - U_0)(U_0 + (U_n^+ - U_0)\mathrm{e}^{-T/\tau_u}), \tag{3.26a}$$
$$U_{n+1}^- = U_0 + (1 - U_0)U_n^-\mathrm{e}^{-T/\tau_u}. \tag{3.26b}$$

For the depression variable X, we find the following set of equations:

$$X_{n+1}^+ = 1 + \Big((1 - \alpha U_n^+)X_n^- - 1\Big)\,\mathrm{e}^{-T/\tau_x}, \tag{3.27a}$$
$$X_{n+1}^- = (1 - \alpha U_{n+1}^+)(1 + (X_n^+ - 1)\mathrm{e}^{-T/\tau_x}). \tag{3.27b}$$

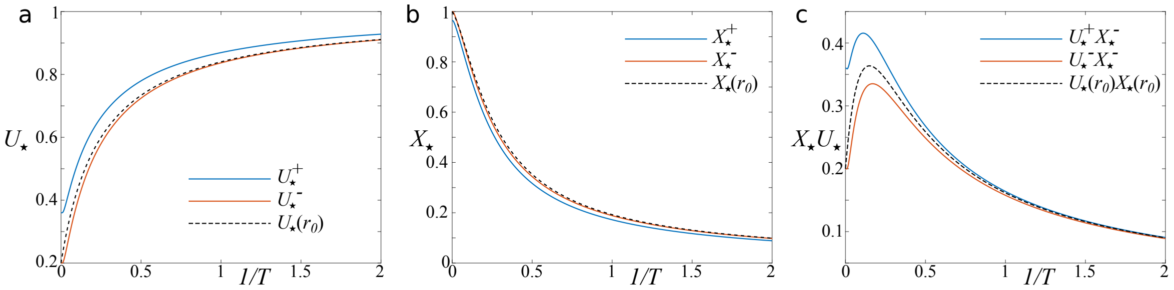

Figure 3.8: Comparison of the microscopic adaptation variables before and after spikes for discrete spikes, and for constant firing rates r_0. The inter-spike interval T is varied. The constant firing rate is expressed as $r_0 = 1/T$. Parameters: $\alpha = 0.1$, $U_0 = 0.2$, $\tau_x = 50.0$, $\tau_u = 20.0$.

In the stationary case, i.e. in the absence of transient dynamics, stationary solutions $U_\star^+ = U_n^+$, $U_\star^- = U_n^-$ and $X_\star^- = X_n^-$, $\forall n$ can be found:

$$U_\star^+ = \frac{U_0 + U_0(1-U_0)(1-\exp(-T/\tau_u))}{1-(1-U_0)\exp(-T/\tau_u)}, \tag{3.28a}$$

$$U_\star^- = \frac{U_0}{1-(1-U_0)\exp(-T/\tau_u)}, \tag{3.28b}$$

$$X_\star^+ = \frac{(1-\alpha U_\star^+)(1-\exp(-T/\tau_x))}{1-(1-\alpha U_\star^+)\exp(-T/\tau_x)}, \tag{3.28c}$$

$$X_\star^- = \frac{1-\exp(-T/\tau_x)}{1-(1-\alpha U_\star^+)\exp(-T/\tau_x)}. \tag{3.28d}$$

It is interesting to note that these results differ from the results when the firing rate is assumed to be a constant, i.e. when $S_i = r_0 \; \forall t$. In this case, we set $\dot{U} = \dot{X} = 0$, and obtain

$$U_\star = \frac{U_0 + U_0\tau_u/T}{1 + U_0\tau_u/T}, \tag{3.29a}$$

$$X_\star = \frac{1}{1 + \alpha\tau_x U_\star/T}, \tag{3.29b}$$

where we have made use of $U_\star^+ = U_\star^- = U_\star$, as well as $X_\star^+ = X_\star^- = X_\star$ since spike times are irrelevant. The spike and rate description can be compared by equating $r_0 = 1/T$.

In Fig. 3.8 we compare these solutions for varying values of T. As can be seen, the results for constant firing rates r_0 are more closely related to the adaptation variables before spikes than after spikes. This shows that it does matter for microscopic STP whether exact spike timings and the time of evaluation of U and X are considered or not, a finding which we expect to hold for non-stationary firing rates $S(t)$ as well.

The expressions derived above can be used to evaluate the mean-field quantities x and u, if the spike times or firing rates of all neurons are known. Alternatively, they can be used to evaluate r_{eff} directly. In the following sections, we will address the problem of evaluating r_{eff} to derive the mean-field equations for eq. (3.20). We will derive two different mean-field models, for which the results of this section will be used to refine the mean-field descriptions of the pre-synaptic STP dynamics. In this context, we will evaluate how eq. (3.28) vs. eq. (3.29) affect the mean-field dynamics of the QIF network.

3.4.3 Mean-Field derivation under a Poissonian assumption of neural dynamics

Recently, an approach for the derivation of a mean-field model for the system defined by eq. (3.20) has been presented in [156]. Taher et al. used a mean-field approximation of macroscopic quantities x and u, averaged over all neurons in the network, that has been proposed in [155]. In this section, a mean-field approximation of the effective network input

$$r_{\text{eff}}(t) = \frac{1}{N}\sum_{j=1}^{N} U_j^- X_j^- s_j, \tag{3.30}$$

is derived, where X_j^- and U_j^- are given by eqs. (3.20b) and (3.20c), respectively, with the modification that U_j^+ is replaced by U_j^-. Whereas the original STP model formulation described in [133] uses $U_j^+ X_j^-$ as the effective weight of a synapse at the time of an incoming spike, Schmutz et al. use $U_j^- X_j^-$ instead [155]. As shown in Fig. 3.8C, these two choices can lead to substantial differences of the synaptic weight for small input rates. Since an effective synaptic weight of $U_j^- X_j^-$ is also used in [156], we will discuss the validity of their mean-field description for both the spiking neural network given by eq. (3.20) and the spiking neural network considered in [156]. Henceforth, we will refer to the former as SNN_{pre} and to the latter as SNN_{pre} II. Under the assumption that all S_i follow independent Poisson processes, the effective network input in SNN_{pre} II is approximated by $r_{\text{eff}} \approx u(t)x(t)r(t)$, where $r(t)$ is the average firing rate across neurons at time t. This mean-field approximation rests on two assumptions: (I) Synapse indices can be randomized, i.e. the spike times matter, but not the synapses at which those spikes occur. (II) The average impact of a spike on X_i and U_i, $\forall i$ can be approximated by sampling from Gaussian distributions centered around the current values of x and u. A more detailed mathematical account of these assumptions is given in [155]. Making use of $r_{\text{eff}} \approx u(t)x(t)r(t)$, a first-order mean-field approximation is then given by

$$\tau_x \dot{x} = 1 - x - \alpha \tau_x x u r, \tag{3.31a}$$

$$\tau_u \dot{u} = U_0 - u + U_0 \tau_u (1-u) r. \tag{3.31b}$$

As can be seen from these equations, both x and u are driven by the average firing rate $r = \frac{1}{N}\sum_{j=1}^{N} S_j$ of the QIF network. This allows one to apply the Lorentzian ansatz in the same way as demonstrated for post-synaptic depression in [94]. The dynamics of the complex variable $w(\eta, t)$ can be expressed as

$$\partial_t w(\eta, t) = i[\frac{-w(\eta,t)^2 + \eta + I(t)}{\tau} + Jxur], \tag{3.32}$$

and by evaluating eq. (3.32) at $\pi r(t) + iv(t) = w(\bar{\eta} - i\Delta, t)$ one finds that the dynamics of r and v follow:

$$\tau \dot{r} = \frac{\Delta}{\pi\tau} + 2rv, \tag{3.33a}$$

$$\tau \dot{v} = v^2 + \bar{\eta} + I(t) + Jxur\tau - (\pi r \tau)^2. \tag{3.33b}$$

We will refer to the set of mean-field equations given by eqs. (3.31) and (3.33) as $\text{FRE}_{\text{Poisson}}$ where FRE stands for firing rate equations.

It is important to notice, however, that $\text{FRE}_{\text{Poisson}}$ cannot be considered exact. While assumption (I) holds for a network of independent, homogeneous Poisson neurons (hence called Poissonian assumption), it does not hold in general [155]. Therefore, the mean-field derivation essentially approximates a heterogeneous network of deterministic QIF neurons by a homogeneous network of stochastic Poisson neurons. Furthermore, the first-order approximation given by eqs. (3.31a) and (3.31b) ignores the non-linear interaction between X_i and U_i in eq. (3.20b). As shown in [155], considering second order dynamics can improve the accuracy of the mean-field approximation, especially in the vicinity of transient inputs to the network. Adding second-order dynamics would involve sampling from a multivariate Gaussian distribution over (x, u), however. This means that the mean-field derivation could not be considered deterministic and, hence, also not exact anymore.

Still, it has been shown in [156] that $\text{FRE}_{\text{Poisson}}$ can accurately describe the mean-field dynamics of SNN_{pre} II under certain conditions. To test whether this holds in general, we compared the dynamics of the two models for three different STP parametrizations, leading to synapses that are either depressing, facilitating, or depressing and facilitating. We solved the initial value problem of both sets of equations via an explicit Euler formalism with an integration step-size of $\text{dt} = 0.0001$. This step-size was sufficiently small to capture the dynamics of the network and was used for all subsequent numerical integration problems as well. We then applied rectangular input pulses to the models and observed their dynamic responses around these inputs. The resulting time series can be observed in Fig. 3.9. For purely depressing synapses, we find that there is a substantial mismatch between the mean-field dynamics of SNN_{pre} II and $\text{FRE}_{\text{Poisson}}$. As can be seen in Fig. 3.9A for the average depression x, there is a considerable offset between the mean-field model (orange) and the average of X_i evaluated across neurons in the QIF network (black). With respect to purely facilitating synapses, we find that the mean-field model provides a reasonable approximation of the QIF network. Even though offsets can be observed between the mean-field model and the QIF network (see dynamics of v in Fig. 3.9B), the qualitative behavior of the QIF network is captured well by the mean-field model. This holds both in the steady-state regimes and during transient behavior around the on- and offsets of the input $I(t)$. In the case of synapses with short-term depression and facilitation, the mean-field model expresses a substantial mismatch to the QIF network dynamics again. For example, Fig. 3.9C shows that the dynamics of the average firing rate r express focus dynamics for $\text{FRE}_{\text{Poisson}}$ after the onset of the first stimulus, whereas the average firing inside SNN_{pre} II does not show such behavior. In the upper row of Fig. 3.9, we show the evolution of the distribution over the combined synaptic state $X_i U_i$ in the microscopic model. We find that this distribution tends to express multi-modalities in regions with a strong mismatch between mean-field and microscopic model. These results suggest that the mean-field model can approximate the low-dimensional dynamics of the QIF network only if X_i and U_i express uni-modal, narrow distributions. This finding makes intuitive sense, since the mean-field approximation of the dynamics of U_i and X_i given by eq. (3.31) represents a first order approximation. Our results confirm that this approximation only performs well if the mean over X_i and U_i contains much information about the actual underlying distributions.

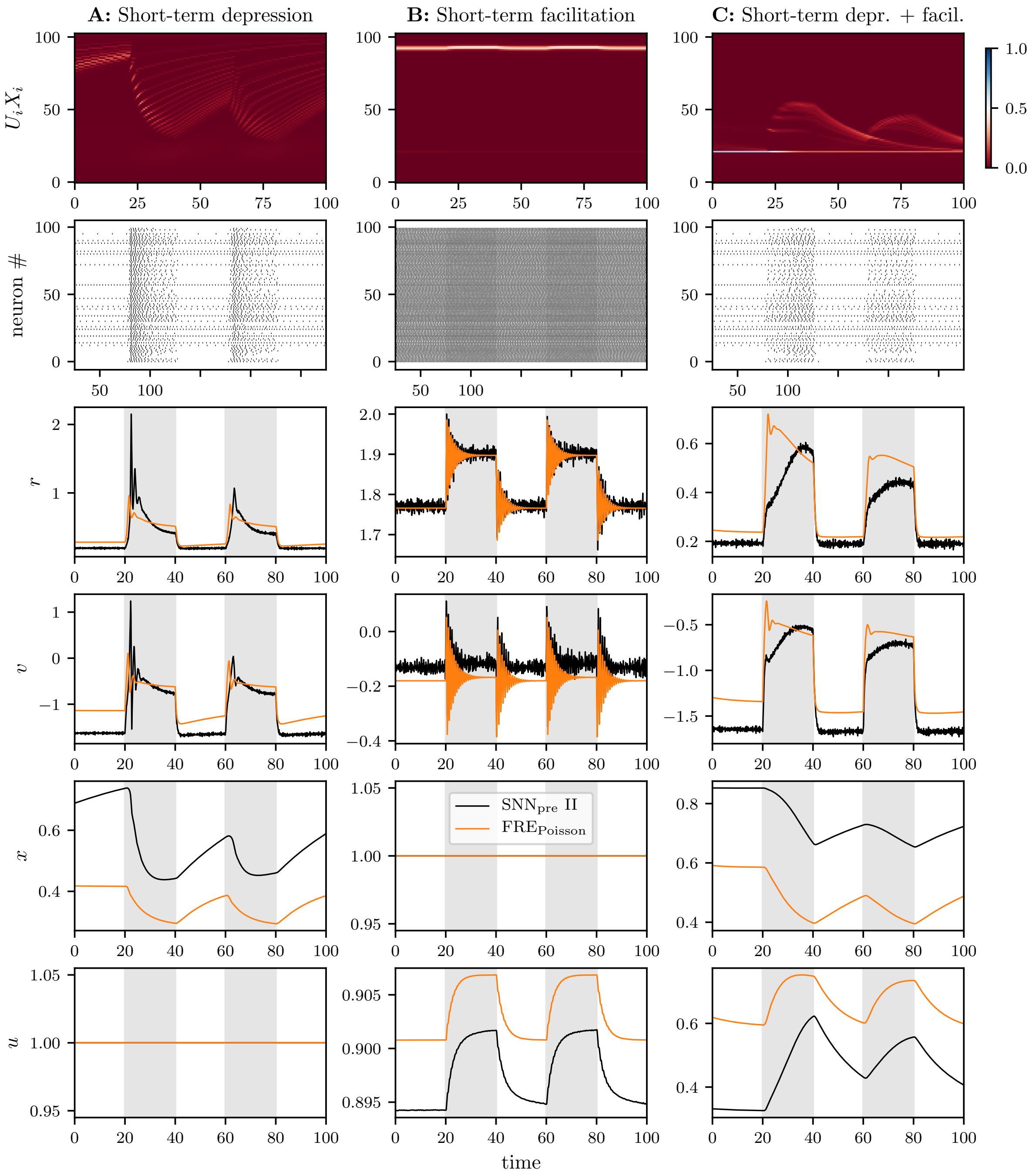

Figure 3.9: Evolution of the state variables of a QIF network and a mean-field approximation thereof for three different types of synaptic short-term plasticity (**A:** depression, **B:** facilitation, combined **C:** depression and facilitation). The first two rows show the distribution over the synaptic state $X_j U_j$ and the spiking activity of 100 randomly selected neurons, respectively. The last 4 rows show a comparison between the spiking neural network (black) and the mean-field approximation (orange) for the average firing rate r, the average membrane potential v, the average depression x, and the average facilitation u. In the SNN, averages were calculated across neurons i. Grey-shaded areas depict time intervals in which a rectangular input of $I(t) = 2.0$ was applied to the model. Color bars depict the probability density inside a given bin of the distribution over $X_i U_i$. Parameters for **A**: $U_0 = 1.0$, $\alpha = 0.1$. Parameters for **B**: $U_0 = 0.2$, $\alpha = 0.0$. Parameters for **C**: $U_0 = 0.2$, $\alpha = 0.1$. Other model parameters: $\tau = 1.0$, $\Delta = 2.0$, $\bar{\eta} = -3.0$, $J = 15.0\sqrt{\Delta}$, $\tau_x = 50.0$, $\tau_u = 20.0$, $N = 10000$.

Thus, by providing these counter examples, we have shown that the mean-field model resulting from the Poisson assumption does not provide an exact mean-field description of the QIF network.

Since we are actually interested in the mean-field equations for $\mathrm{SNN}_{\mathrm{pre}}$ given by eq. (3.20), we now examine whether $\mathrm{FRE}_{\mathrm{Poisson}}$ can nonetheless provide an approximation of $\mathrm{SNN}_{\mathrm{pre}}$ under some conditions. To gain further insight into the relationship between the mean-field equations and the QIF network, we asked whether there exists a QIF network description for which the mean-field model given by eqs. (3.31a, 3.31b, 3.33a, 3.33b) can be considered exact. Indeed, such a network exists and is easy to find. Since x and u are only driven by the mean-field firing rate r, we can just introduce microscopic variables U_i and X_i that enter the microscopic evolution equation for v_i in the same way as the macroscopic evolution equation for v (eq. 3.33b) and are also driven by the mean-field activity of the QIF network:

$$\tau \dot{V}_i = V_i^2 + \eta_i + I(t) + \frac{J\tau}{N} U_i X_i s, \tag{3.34a}$$

$$\tau_x \dot{X}_i = 1 - X_i - \alpha X_i U_i s \tau_x, \tag{3.34b}$$

$$\tau_u \dot{U}_i = U_0 - U_i + U_0 (1 - U_i) s \tau_u, \tag{3.34c}$$

$$s = \sum_{j=1}^{N} \sum_{k \backslash t_j^k < t} \int_{-\infty}^{t} \delta(t' - t_j^k) dt', \tag{3.34d}$$

where $s = r$ is the mean firing rate across all neurons in the network. Apart from the description of the STP dynamics, this network description is equivalent to the one used in [94] for a QIF network with post-synaptic depression. Indeed, under a first-order approximation of the dynamics of x and u via the Poissonian assumption, the system given by eq. (3.20), a QIF network with pre-synaptic STP, is essentially approximated by eq. (3.34), a QIF network with post-synaptic STP (see Fig. 3.7 for a visualization of the differences between the two). Hence, we will refer to the network given by eq. (3.34) as $\mathrm{SNN}_{\mathrm{post}}$.

Next, we compared the behavior of the two different QIF network descriptions ($\mathrm{SNN}_{\mathrm{pre}}$ and $\mathrm{SNN}_{\mathrm{post}}$) to the mean-field model dynamics. This was done to verify that $\mathrm{FRE}_{\mathrm{Poisson}}$ is indeed an exact mean-field model of $\mathrm{SNN}_{\mathrm{post}}$ and to see under which conditions pre- and post-synaptic STP have similar or different effects on the QIF network dynamics. To this end, we used bifurcation analysis to identify phase transitions in the mean-field model around which we compared the behavior of the three models. This way, we were able to set up stimulation paradigms that induce strong changes in the dynamic behavior of the mean-field model and evaluate whether the QIF networks express qualitatively similar phase transitions or not. Bifurcation analysis was performed numerically, using the Python software PyRates [157], which provides an interface to the parameter continuation software Auto-07p [88]. We initialized the mean-field model with either purely depressing synapses ($U_0 = 1.0$, $\alpha = 0.04$) or purely facilitating synapses ($U_0 = 0.2$, $\alpha = 0.0$). In each case, we performed a parameter continuation in the background excitability $\bar{\eta}$ for two different values of $\Delta \in \{0.01, 0.4\}$. The latter introduces two different levels of firing rate heterogeneity to the QIF network. We expected this firing rate heterogeneity to directly affect the broadness of the distributions over

X_i and U_i. If that is indeed the case, the mean-field model should provide a better description of the $\mathrm{SNN}_{\mathrm{pre}}$ dynamics for $\Delta = 0.01$ than for $\Delta = 0.4$.

As can be seen in Fig. 3.10A and B, we identified fold bifurcations for facilitating synapses for $\Delta = 0.4$ as well as $\Delta = 0.01$. These fold bifurcations mark the outer limits of a bi-stable regime in which a stable high-activity focus and a stable low-activity node can co-exist, separated by a saddle-focus. Indeed, we find that the steady-state behavior of the mean-field model and $\mathrm{SNN}_{\mathrm{post}}$ can be forced towards either of the two stable equilibria via extrinsic stimulation. As shown for $\Delta = 0.4$ and $\Delta = 0.01$ in Fig. 3.10A and B, respectively, there is always a very good agreement between those two models. Regarding $\mathrm{SNN}_{\mathrm{pre}}$, we failed to identify the bi-stable regime for $\Delta = 0.4$. In Fig. 3.10A, it can be seen that the system behavior is only governed by a high-activity focus, even though the mean-field model predicts the co-existence of a low-activity stable node for $\bar{\eta} = -0.6$. Thus, the mean-field model fails to predict the behavior of the QIF network with pre-synaptic STP in this case. However, in the case of very low heterogeneity, we identified both stable states exists in $\mathrm{SNN}_{\mathrm{pre}}$ and found a good agreement with the mean-field model (see Fig. 3.10B).

For depressing synapses, we found regimes of synchronized oscillations that emerge via Andronov-Hopf bifurcations for small as well as for high firing rate heterogeneity (see Fig. 3.10C and D). Again, these oscillations could be induced in $\mathrm{FRE}_{\mathrm{Poisson}}$ as well as in $\mathrm{SNN}_{\mathrm{post}}$ with a very good match between the two. Consistent with our findings for facilitating synapses, $\mathrm{SNN}_{\mathrm{pre}}$ expressed oscillations only for $\Delta = 0.01$ (see Fig. 3.10D). For higher firing rate heterogeneity ($\Delta = 0.4$), the network did not show any tendency to oscillate at all, even though the mean-field model predicted oscillations to be present at $\bar{\eta} = -0.85$ (see Fig. 3.10C).

Thus, our results confirm that $\mathrm{FRE}_{\mathrm{Poisson}}$ is indeed an exact mean-field equation of $\mathrm{SNN}_{\mathrm{post}}$. Furthermore, they demonstrate that $\mathrm{SNN}_{\mathrm{pre}}$ and $\mathrm{SNN}_{\mathrm{post}}$ can express either different or similar dynamics, depending on the firing rate heterogeneity inside the network. In our simulations, we were able to control this heterogeneity successfully via the parameter Δ. In regimes of low firing rate heterogeneity, $\mathrm{SNN}_{\mathrm{pre}}$ and $\mathrm{SNN}_{\mathrm{post}}$ expressed similar behavior, thus allowing for a good approximation of the mean-field dynamics of $\mathrm{SNN}_{\mathrm{pre}}$ via $\mathrm{FRE}_{\mathrm{Poisson}}$. In regimes of high firing rates heterogeneity, the opposite was the case. In the next sections, we investigate whether more accurate mean-field models of QIF networks with pre-synaptic STP can be derived and, if so, how they perform near the parameter regimes described in this section.

3.4.4 Multi-population approximation of distributed parameters in the QIF network

In the previous section, we have found that $\mathrm{FRE}_{\mathrm{Poisson}}$ is in good agreement with the dynamics of $\mathrm{SNN}_{\mathrm{pre}}$, when the distribution of η_i is particularly narrow, i.e. when $\Delta \ll 1$. Here, we exploit this fact and approximate the mean field dynamics by dividing the microscopic network into sub-networks with narrow distributions in η_i. In other words, the Lorentzian distribution with $\{\bar{\eta}, \Delta\}$ is divided into a set of M Lorentzian distributions with $\{\bar{\eta}_m, \Delta_m\}$, $m = 1, \ldots, M$, such that

$$\frac{\Delta/\pi}{(\eta - \bar{\eta})^2 + \Delta^2} \approx \frac{1}{M} \sum_{m=1}^{M} \frac{\Delta_m/\pi}{(\eta - \bar{\eta}_m)^2 + \Delta_m^2}. \tag{3.35}$$

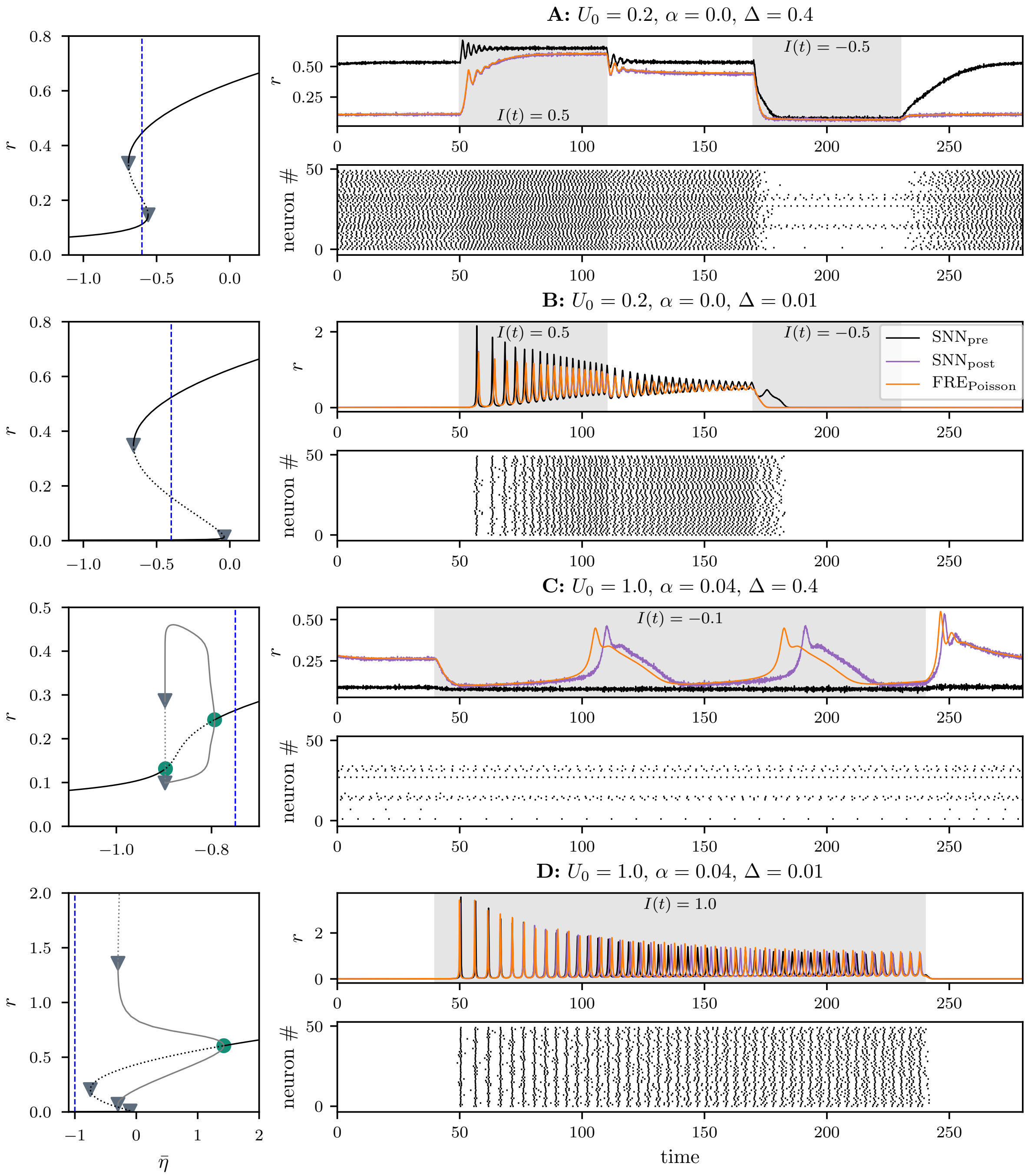

Figure 3.10: Comparison between $\mathrm{FRE}_{\mathrm{Poisson}}$ (orange), $\mathrm{SNN}_{\mathrm{pre}}$ (black), and $\mathrm{SNN}_{\mathrm{post}}$ (purple) for 4 different parameter sets (**A-D**). The first column shows 1D bifurcation diagrams in $\bar{\eta}$. Grey triangles represent fold bifurcations and green circles represent Andronov-Hopf bifurcations. Blue dashed lines mark the value of $\bar{\eta}$ that was used for the firing rate and spike raster plots in the second column. Spike raster plots show the spiking activity of 50 randomly selected neurons of $\mathrm{SNN}_{\mathrm{pre}}$. Grey shaded areas represent time intervals during which an extrinsic input $I(t)$ was applied to the models. Remaining model parameters: $J = 8.0$, $\tau_u = 20.0$, $\tau_x = 50.0$, $\tau = 1.0$, $N = 10000$

The resulting set of equations for the evolution of the mean field variables is then given by

$$\tau\dot{r}_m = \frac{\Delta_m}{\pi\tau} + 2r_m v_m, \tag{3.36a}$$

$$\tau\dot{v}_m = v_m^2 + \bar{\eta}_m + I(t) + \frac{J}{M}\sum_{n=1}^{M} x_n u_n r_n \tau - (\pi r_m \tau)^2, \tag{3.36b}$$

$$\dot{x}_m = \frac{1-x_m}{\tau_x} - \alpha u_m x_m r_m, \tag{3.36c}$$

$$\dot{u}_m = \frac{U_0 - u}{\tau_u} + U_0(1-u_m)r_m. \tag{3.36d}$$

We will refer to this set of mean-field equations as $\mathrm{FRE}_{\mathrm{MPA}}$, for multi-population approximation. One assumption we make here is that each sub-network contains the same number of neurons, which means that the weights for each sub-network are the same, and the mean field variables can be obtained by computing the mean $y = (1/M)\sum_{m=1}^{M} y_m$, where y represents the mean field variable under consideration. The parameters $\bar{\eta}_m$ and Δ_m are chosen as follows:

$$\bar{\eta}_m = \bar{\eta} + \Delta \tan\frac{\pi(2m-M-1)}{2(M+1)}, \tag{3.37a}$$

$$\Delta_m = \Delta(\tan\frac{\pi(2m-M-1/2)}{2(M+1)} - \tan\frac{\pi(2m-M-3/2)}{2(M+1)}). \tag{3.37b}$$

The density of the parameters η_m follows the Lorentzian distribution, and the Δ_m are chosen such that the half-widths approximately match the distances between the centers of the distributions of the sub-networks, i.e. $\bar{\eta}_{m+1} - \bar{\eta}_m \approx \Delta_{m+1} + \Delta_m$. As can be seen in Fig. 3.11(a-c), even at large M the adaptation variables still show a small discrepancy with the result obtained from the spiking neural network $\mathrm{SNN}_{\mathrm{pre}}$. We hypothesise that this difference is due to different results for the adaptation variables when the firing rate is assumed constant, and when it is assumed to be a spike train with constant ISI, as shown in Fig. 3.8. In other words, we expect that accounting for the fact that $\mathrm{FRE}_{\mathrm{Poisson}}$ was derived for $\mathrm{SNN}_{\mathrm{pre}}$ II instead of $\mathrm{SNN}_{\mathrm{pre}}$ will reduce the difference. As the adaptation variables are in essence time-averaged quantities, the adaptation variables could be posed as $x = (X^- + X^+)/2$ and $u = (U^- + U^+)/2$. However, with the update rules $U^+ = U^- + U_0(1-U^-)$ and $X^+ = X^- - \alpha U^+ X^-$, this would yield out-of-bound values for X^- at $x = 1$, and U^- at $u = 0$. The results shown in Fig. 3.8 suggest that the mean field variables are closest to X^- and U^-, which is why we set $X^- \approx x$, and $U^- \approx u$. The update rule for U^+ gives the following correction term:

$$U^+(u) \approx u + U_0(1-u). \tag{3.38}$$

Inserting this term into the mean field equations for $\mathrm{FRE}_{\mathrm{MPA}}$ produces a closer match of the mean field variables with the results of the microscopic model $\mathrm{SNN}_{\mathrm{pre}}$ (see Fig. 3.11A vs. B).

As a final test of the predictive accuracy of $\mathrm{FRE}_{\mathrm{MPA}}$, we examined how well the model can predict the onset of oscillations in the QIF network. Using bifurcation analysis, we identified the Hopf bifurcation leading to the oscillations in Fig. 3.10E and investigated the locus of that Hopf bifurcation in the 2D parameter space spanned by $\bar{\eta}$ and Δ. This, we did for both $\mathrm{FRE}_{\mathrm{Poisson}}$ and $\mathrm{FRE}_{\mathrm{MPA}}$ with $M = 100$ mean-field populations. As can be seen in Fig.3.12A, we found that the Hopf curves emerged from a Bogdanov-Takens bifurcation in both FRE models. This

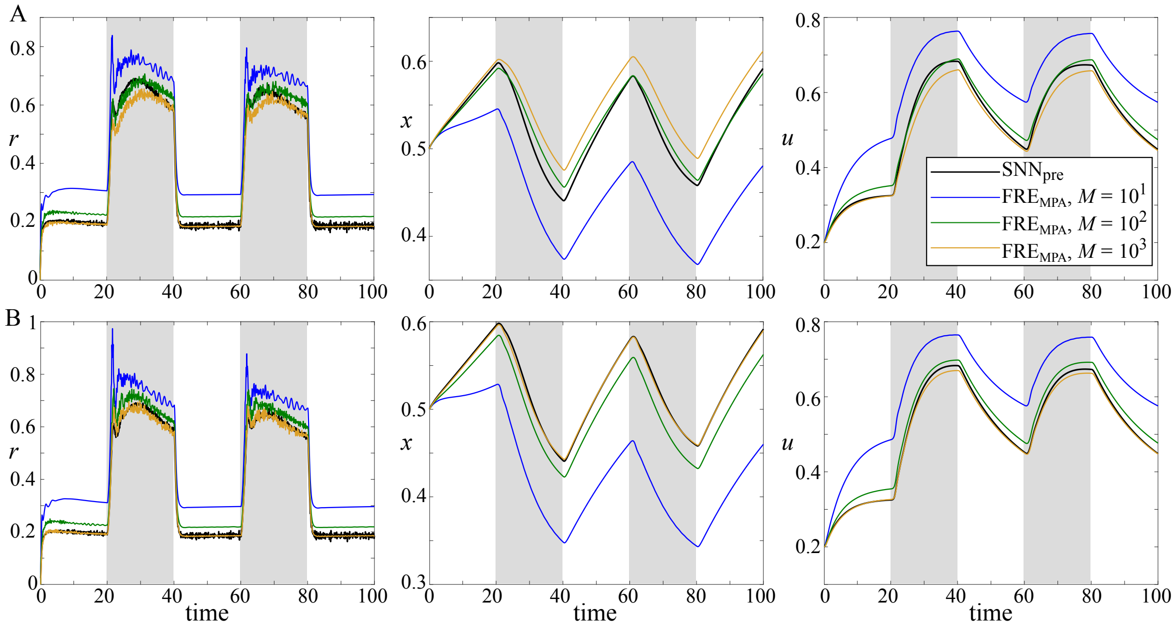

Figure 3.11: Comparison of the mean field variables of the microscopic spiking neural network, and the mean field model of the spiking neural network divided into M sub-networks with narrow distribution (multi-population approximation, MPA). Grey shaded areas indicate time intervals with $I(t) = 3.0$. **A**: MPA with standard mean field description, **B**: MPA with correction term for U^+. Parameters: $\alpha = 0.1$, $\tau = 1.0$, $\Delta = 2.0$, $\bar{\eta} = -3.0$, $J = 15.0\sqrt{\Delta}$, $\tau_x = 50.0$, $\tau_u = 20.0$, $N = 10000$.

represents the same bifurcation structure as we already identified for QIF networks with SD in section 3.2 (see Fig. 3.4 for the corresponding 2D bifurcation diagram). Furthermore, we have shown the corresponding 1D bifurcation diagrams for the $\mathrm{FRE}_{\mathrm{Poisson}}$ model for $\Delta = 0.4$ and $\Delta = 0.01$ in Fig. 3.10C and D, respectively. Thus, we expect stable oscillations to exist in the regions enclosed by the Hopf curves. As shown in Fig.3.12A, the difference between the Hopf curves predicted by $\mathrm{FRE}_{\mathrm{Poisson}}$ and $\mathrm{FRE}_{\mathrm{MPA}}$ becomes larger when Δ increases. For $\Delta = 0.4$, $\mathrm{FRE}_{\mathrm{Poisson}}$ predicts stable oscillations to exist at $\bar{\eta} = -0.85$, which we already failed to find in the QIF network in Fig.3.10D. $\mathrm{FRE}_{\mathrm{MPA}}$ predicts the existence of a stable node at $\bar{\eta} = -0.85$, however, and the existence of stable oscillations for $-0.66 < \bar{\eta} < -0.6$. To see whether the oscillations predicted by $\mathrm{FRE}_{\mathrm{MPA}}$ indeed exist in $\mathrm{SNN}_{\mathrm{pre}}$, we performed numerical simulations where we initialized the QIF network at $\bar{\eta} = -0.85$ and then forced it towards $\bar{\eta} = -0.62$ via extrinsic stimulation. As can be seen in Fig.3.12B, the QIF network expressed steady-state behavior for $\bar{\eta} = -0.85$ and started to oscillate when pushed to $\bar{\eta} = -0.62$. Hence, $\mathrm{FRE}_{\mathrm{MPA}}$ correctly predicted the existence of oscillatory bursts in the QIF network for $M = 100$, but not for $M = 1$, for which $\mathrm{FRE}_{\mathrm{MPA}}$ reduces to $\mathrm{FRE}_{\mathrm{Poisson}}$. The bursts have similar properties as the ones found in QIF networks with post-synaptic plasticity [94] and can be expected to result from the interaction between synaptic short-term depression and recurrent excitation via the network. Comparing the firing rate dynamics of $\mathrm{FRE}_{\mathrm{MPA}}$ and $\mathrm{SNN}_{\mathrm{pre}}$ in Fig.3.12 reveals a slight difference between the oscillation period of the mean-field model and the QIF network. This difference shows that $\mathrm{FRE}_{\mathrm{MPA}}$ can not be considered an exact mean-field model, even for $M = 100$. Still, we find that it captures the phase transitions inside $\mathrm{SNN}_{\mathrm{pre}}$ well and thus provides a reasonable trade-off between accuracy and computational complexity.

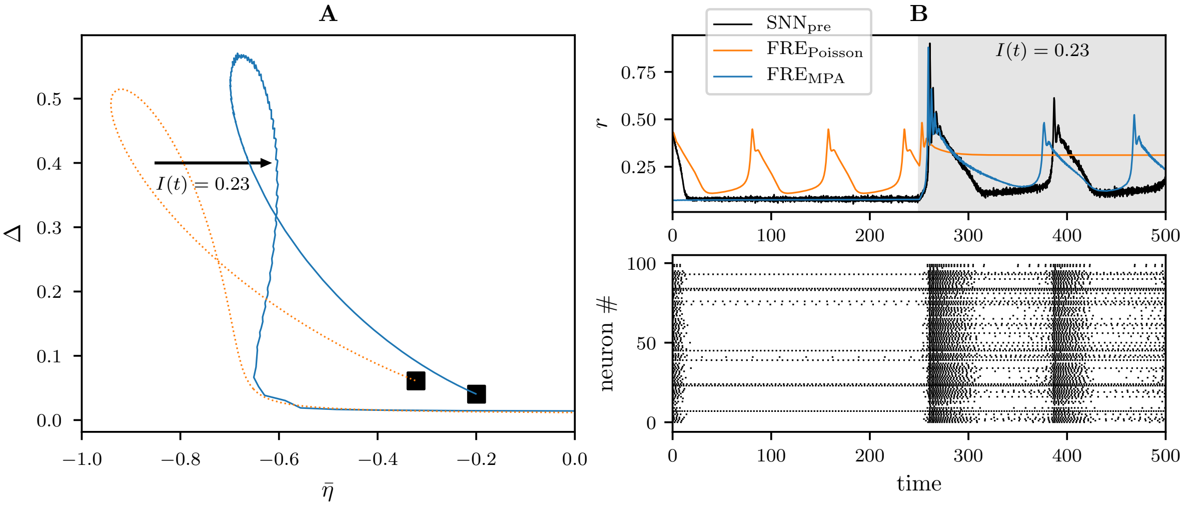

Figure 3.12: Phase transitions between steady-state and oscillatory regimes in $\mathrm{FRE}_{\mathrm{Poisson}}$ and $\mathrm{FRE}_{\mathrm{MPA}}$. **A:** 2D bifurcation diagram of the Hopf curve in $\mathrm{FRE}_{\mathrm{Poisson}}$ (orange) and $\mathrm{FRE}_{\mathrm{MPA}}$ (blue). The arrow represents the phase transition introduced by I(t) in either model. The black square represents the Bogdanov-Takens bifurcation from which the Hopf bifurcations emerge. **B:** The first row shows the simulated firing dynamics of the spiking neural network and both mean-field models. The second row shows the corresponding spiking activity of 100 randomly selected neurons of $\mathrm{SNN}_{\mathrm{pre}}$. Parameters: $\alpha = 0.04$, $U_0 = 1.0$, $\tau = 1.0$, $\Delta = 0.4$, $\bar{\eta} = -0.85$, $J = 8.0$, $\tau_x = 50.0$, $\tau_u = 20.0$, $N = 10000$, $M = 100$, $I(t) = 0.23$ for $t > 250$ and $I(t) = 0.0$ otherwise.

3.4.5 Adiabatic approximation of STP dynamics

For simplification, we will consider synapses with mere short-term depression in this section, since we showed in section 3.4.3 that the mismatch between the mean-field model $\mathrm{FRE}_{\mathrm{Poisson}}$ and the QIF networks $\mathrm{SNN}_{\mathrm{pre}}$ and $\mathrm{SNN}_{\mathrm{pre}}$ II could be reproduced in this simpler case as well. We thus consider the microscopic system given by

$$\tau \dot{V}_i = V_i^2 + \eta_i + I(t) + \frac{J\tau}{N} \sum_{j=1}^{N} X_j^- S_j, \tag{3.39a}$$

$$\tau_x \dot{X}_i = 1 - X_i - \alpha X_i^- S_i \tau_x, \tag{3.39b}$$

$$S_i = \sum_{k \backslash t_j^k < t} \int_{-\infty}^{t} G(t-t')\delta(t'-t_j^k)dt'. \tag{3.39c}$$

In this system, we approximate the STP dynamics via a linear differential operator L, i.e. $LX_i(t) = S_i(t)$. In such a case, a Green's function $G_X(t)$ exists that allows one to express the dynamics of X_i via a convolution of $G_X(t)$ with the spiking activity of neuron i:

$$X_i(t) = \int_{-\infty}^{t} G_X(t-t')S_i(t')dt' = G_X * S_i. \tag{3.40}$$

Then, since S_i is related to $z(\eta_i, t)$ via $S_i\pi = z(\eta_i, t)$, eq. (3.23) can be written as

$$\partial_t w(\eta, t) = i[\frac{-w(\eta,t)^2 + \eta + I(t)}{\tau} + J(G_X * \frac{\mathrm{Re}[w]}{\pi})\,\mathrm{Re}[w]]. \tag{3.41}$$

To solve eq. (3.41) for r and v, the effective firing rate $r_{\mathrm{eff}} = \int_{-\infty}^{\infty} (G * r(\eta)) r(\eta) g(\eta) \mathrm{d}\eta$ must be determined, which requires one to evaluate the product between the single cell firing rate and a convolution of itself. This makes it difficult to find a closed-form solution for r and v, since the synaptic depression kernel G_X cannot simply be pulled out from the convolution integral. The simplest approximation of this problem is to replace the convolution integral by a mean synaptic depression, as is done for the Poissonian assumption. Alternatively, we assume that the dynamics of X_i are slow in comparison to the dynamics of v_i. For the relaxation dynamics of X_i, this assumption is met if $\tau_x \gg \tau$. We note here, however, that the spiking activity of the neuron also introduces a relatively fast time scale to eq. (3.39b), which may violate our assumption. Still, under this assumption, we can apply an adiabatic approximation to the system and consider the dynamics of the fast sub-system for effectively constant adaptation (see [140, 94] for a similar approach):

$$\tau \dot{V}_i = V_i^2 + \eta_i + I(t) + \frac{J\tau}{N} \sum_{j=1}^{N} X_j^- S_j, \tag{3.42a}$$

$$S_i = \sum_{k \backslash t_j^k < t} \int_{-\infty}^{t} \delta(t' - t_j^k) \mathrm{d}t', \tag{3.42b}$$

where X_j is approximated as neuron-specific constant. Due to the Lorentzian distribution of the background excitabilities η_i and the resulting heterogeneity of single cell firing rates in the network, X_i cannot be assumed as homogeneous across neurons. Instead, it must be considered a distributed quantity, governed by a probability distribution $h(X_i)$. Then, the main difficulty in developing the mean field description lies in the fact that $h(X_i)$ is generally unknown if a mean field variable is considered. More precisely, if we consider the mean field variable x that describes the average synaptic depression across the network, little is known about the distribution of the microscopic variables X_i, which is required to determine the effective firing rate r_{eff}. By using the adiabatic approximation, we argue that an approximation of r_{eff} can be obtained by estimating the distributions $X(\eta)$ and $r(\eta)$ from the mean field variables in the stationary case, and solving

$$r_{\mathrm{eff}} = \int_{0}^{1} \int_{-\infty}^{\infty} X r(\eta) h(X|\eta) g(\eta) \mathrm{d}\eta \mathrm{d}X. \tag{3.43}$$

Assuming independent Lorentzian density functions for h and g, i.e. $h(X|\eta)g(\eta) = h(X)g(\eta)$, eq. (3.41) would only need to be evaluated at the poles in the lower half-planes $\pi r(t) + iv(t) = w(\bar{\eta} - i\Delta, \bar{X} - i\Delta_X, t)$, where $\bar{X}$ and Δ_X would represent the center and HWHM of the Lorentzian distribution over X, respectively. Then, the effect of pre-synaptic STP on the network dynamics would effectively reduce to a distribution over the coupling parameter J. For the mean-field equations of a QIF network with distributed coupling parameters see [125]. However, h and g cannot be assumed to be independent, since η_i controls the firing rate of neuron i, which in turn controls its synaptic depression X_i. Furthermore, X is bound between $[0, 1]$ and hence a Lorentzian distribution cannot be assumed. In the upper row of Fig. 3.9, we show the evolution of the distribution over $X_i U_i$ for three different parametrizations, corresponding to a purely depressing synapse, a purely facilitating synapse, and a synapse with facilitation and depression acting on different time scales. Importantly, the evolution of the distribution reveals that it is not always uni-modal. For purely depressing synapses, it clearly expresses an at least bi-modal distribution over the whole time course. Thus, finding an appropriate form of h that holds in general is a highly non-trivial problem that we did not find a solution for.

To further simplify the problem, we assume that the depression of a neuron's efferent synapses X_i is merely a function of the firing rate r_i of the same neuron. The stationary firing rate of a QIF neuron in response to an external Input I_{in} is $\sqrt{I_{in}}/\pi$ if $I_{in} > 0$, and zero otherwise. Hence, the distribution of firing rates for a given input is (in the stationary case) given by

$$r(\eta; I_{in}) = H(\eta + I_{in})\sqrt{\eta + I_{in}}/\pi, \tag{3.44}$$

where H is the Heaviside step function. Therefore, for any given mean field firing rate r one can find a unique constant I_r for which

$$r = \int_{-\infty}^{\infty} r(\eta; I_r) g(\eta) \mathrm{d}\eta, \tag{3.45}$$

which allows us to translate the mean field variable r into the distribution $r(\eta; I_r)$.

Similarly, we can use the assumption that X_i is a function of r_i to translate the mean field variable for synaptic depression, x, into the distribution $X(\eta; I_x)$. First, we use the rate relationship given by eq. (3.29) to approximate

$$x(\eta; I_x) = 1/(1 + \alpha\tau_x r(\eta; I_x)), \tag{3.46}$$

for any given input I_x, and then define

$$x_1 = \int_{-\infty}^{\infty} g(\eta)/(1 + \alpha\tau_x r(\eta; I_x)) \mathrm{d}\eta. \tag{3.47}$$

Alternatively, we can use eq. (3.28) to approximate the distribution $x(\eta)$ in the spiking scenario:

$$x(\eta; I_x) = \frac{1 - x_r}{1 - (1 - \alpha)x_r}, \tag{3.48}$$

with $x_r = \exp\left(\frac{-1}{\tau_x} r(\eta; I_x)\right)$, which yields

$$x_2 = \int_{-\infty}^{\infty} \frac{(1 - x_r) g(\eta)}{1 - (1 - \alpha)x_r} \mathrm{d}\eta. \tag{3.49}$$

Having obtained I_r and I_x, we can ultimately compute

$$r_{\text{eff}} = \int_{-\infty}^{\infty} r(\eta; I_r) x(\eta; I_x)) g(\eta) \mathrm{d}\eta, \tag{3.50}$$

where $x(\eta; I_x)$ is either chosen for the rate scenario (i.e. eq. 3.46), or in the spike scenario (i.e. eq. 3.48). This requires us to solve

$$r_{\text{eff}} = \frac{\Delta}{\pi^2} \int\limits_{\min(-I_x, -I_r)}^{\infty} \frac{1}{1+\alpha\tau_x\sqrt{\eta+I_x}} \frac{\sqrt{\eta + I_r}}{(\eta - \bar{\eta})^2 + \Delta^2} \mathrm{d}\eta, \tag{3.51}$$

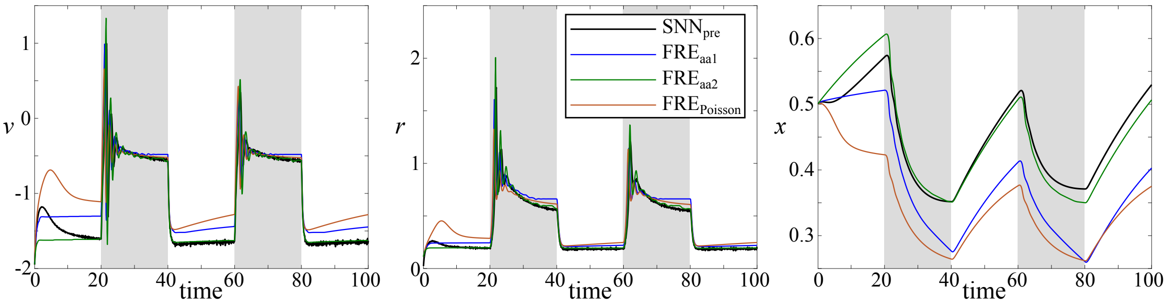

Figure 3.13: Comparison of the mean field variables of the microscopic spiking neural network, the mean field model using the Poissonian assumption, and the mean field model with approximation of the effective firing rate. Grey shaded areas indicate time intervals with $I(t) = 3.0$. Parameters: $\alpha = 0.1$, $\tau = 1.0$, $\Delta = 1.0$, $\bar{\eta} = -2.0$, $J = 15.0$, $\tau_x = 50.0$, $\tau_u = 20.0$, $N = 10000$.

in the rate scenario, and

$$r_{\text{eff}} = \frac{\Delta}{\pi^2} \int\limits_{\min(-I_x, -I_r)}^{\infty} \frac{x_\star - 1}{x_\star - (1-\alpha)} \frac{\sqrt{\eta + I_r}}{(\eta - \bar{\eta})^2 + \Delta^2} \mathrm{d}\eta, \tag{3.52}$$

in the spiking scenario, where we used $x_\star = \exp\left(\frac{\pi}{\tau_x \sqrt{\eta + I_x}}\right)$. We refer to this mean-field model as FRE$_{\text{aa}}$ for adiabatic approximation, with FRE$_{\text{aa1}}$ and FRE$_{\text{aa2}}$ denoting the mean-field model considering the rate and spike scenario, respectively.

The integrals involved in this approximation are hard to evaluate analytically, therefore we solve these integrals numerically for a range of values of I_r and I_x and create look-up tables for I_r, I_x and r_{eff} in order to be able to integrate the resulting model equations numerically. In Fig. 3.13 we compare the results of the mean-field model FRE$_{\text{aa}}$ with the dynamics of the spiking neural network SNN$_{\text{pre}}$, and the mean field model FRE$_{\text{Poisson}}$. We find that FRE$_{\text{aa}}$ is closer to the microscopic dynamics of SNN$_{\text{pre}}$ than FRE$_{\text{Poisson}}$.

3.5 Discussion

3.5.1 Deriving mathematical descriptions for low-dimensional manifolds of neural activity

The Ott-Antonsen ansatz describes a master equation approach to derive the evolution equations for the Kuramoto order parameters for systems of globally coupled oscillators in the thermodynamic limit [121, 122]. This ansatz can be applied to neural networks as well, as long as the single neuron dynamics can be reduced to a phase oscillator [123, 125, 57]. Here, we applied the OA ansatz to networks of globally coupled QIF neurons, which can be conceived as phase oscillators that are either in an excitable or in a periodic firing regime (see section 2.3). We extended the QIF network definition by various short-term plasticity mechanisms that have been shown to serve important regulatory functions in the brain and attempted to derive the evolution equations for the order parameters of the system via the OA ansatz.

One family of STP mechanisms that we considered are neuron-specific mechanisms that directly affect the membrane potential of a neuron via additional currents. A characteristic example of such an STP mechanism is spike-frequency adaptation. In QIF networks with SFA, the spiking of each QIF neuron in the network triggers an adaptation current that leads to a hyper-polarization of the respective neuron [131, 132]. Thus, the SFA mechanism is not simply driven by the mean-field activity of the network, but by the spiking activity of the single QIF neurons. Such SFA-based hyper-polarization causes a transient reduction of the firing frequency of the QIF neurons after they produced a spike, thus violating the assumption of static microscopic oscillation frequencies made by the OA ansatz [121]. In fact, all STP mechanisms that directly act on the membrane potential of a neuron can transiently alter the firing frequency of that neuron and thus violate this core assumption of the OA ansatz. As shown in section 3.3, the OA ansatz can be used for SFA nonetheless, if an adiabatic approximation can be applied to the SFA time scale [140]. Therefore, the OA ansatz can be applied to SNNs with adaptive neurons, as long as the adaptation time scale is sufficiently slow in comparison to the membrane potential evolution. For the results of section 3.3, an adaptation time scale that was ten times slower than the membrane potential time scale sufficed. To generalize these results, we propose to perform a systematic analysis of the relationship between those two time scales and how it affects the accuracy of the OA ansatz. As a further restriction, the SFA mechanism considered in section 3.3 is spike-triggered. Other neuron-specific STP mechanisms exist, however, which are directly coupled to the membrane potential of a neuron instead of its spiking activity. This is the case in popular model neurons such as the Izhikevich neuron or the adaptive exponential integrate-and-fire neuron [18, 158]. In contrast to spike-triggered STP mechanisms such as SFA, the dynamics of these adaptation variables can generally not be expressed as a convolution of the input variable, i.e. the membrane potential, with an integral kernel. This makes it harder to find a closed set of mean-field equations, since it requires that the mean-field expression of the adaptation variable has to be derived as well.

The derivation of the mean-field equations for more complex neuron models such as the Izhikevich neuron and the adaptive exponential integrate-and-fire neuron would be extremely valuable for theoretical neuroscience, despite the idea of complex systems theory that emergent phenomena are somewhat independent of the specific microscopic details. Using a two-dimensional description of the single neuron dynamics, these models have been shown to be capable of generating nearly all characteristic dynamics reported in neurons [18, 158]. As such, they represent a reasonable trade-off between mathematical complexity and neurophysiological plausibility. A first step into this direction would be the derivation of the mean-field equations for the Izhikevich neuron, which can be conceived as a QIF neuron with neuron-specific STP driven by its own membrane-potential [18]. The OA ansatz in combination with the adiabatic approximation presented in section 3.3 may be a good starting point to approach this problem.

Synapse-specific STP mechanisms are another family of STP mechanisms that we studied. They act on the efficacy of a synapse based on its previous activity [130]. Thus, synaptic STP mechanisms modulate the effective mean-field input that a single neuron receives from the rest of the network, rendering this input a weighted sum of the incoming spikes, where the weights are given by synaptic depression and facilitation terms. Finding a closed-form set of mean-field equations for SNNs subject to synaptic STP via the OA ansatz requires the derivation of an expression of this effective mean-field input. We show in sections 3.2 and 3.4.3 that this can be done under the assumption that synaptic STP is homogeneous across all incoming synapses of a neuron, meaning that synaptic STP can be conceived as a post-synaptic process that equally affects all post-synaptic efficacies. Under this assumption, all post-synaptic STP variables are driven by the same input in a globally coupled SNN, i.e. by the mean-field firing rate, thus allowing for the closed-form mean-field derivation via the OA ansatz. While this assumption may be sufficient to study post-synaptic STP such as receptor desensitization [134, 149], short-term changes in the number of available post-synaptic receptors [150, 151], or resource depletion at the post-synaptic complex [152, 153], we showed in section 3.4.3 that it does not hold for pre-synaptic forms of synaptic STP such as vesicle depletion [154, 133, 130]. In the latter case, the efficacies of all outgoing synapses of a neuron are modulated. We attempted to derive the mean-field equations for heterogeneous, all-to-all coupled QIF networks subject to the pre-synaptic STP model described in [133] in section 3.4. We identified the evaluation of the effective network input r_{eff} as the central problem for finding closed-form mean-field equations for QIF networks with pre-synaptic STP via the OA ansatz. Though all network units are still driven by the same mean-field input r_{eff}, finding an analytic expression of r_{eff} is hard since it directly depends on the microscopic, pre-synaptic STP dynamics. In the following paragraphs, we discuss the three approaches that we used to solve that problem.

We extracted the first approach from a recent study that suggested to approximate the effective network input r_{eff} by a modulation of the mean-field firing rate with an average depression and an average facilitation [156]. Our analysis revealed that this approach essentially approximates pre-synaptic STP with post-synaptic STP. We compared the behavior of QIF networks with pre- vs. post-synaptic STP ($\mathrm{SNN}_{\mathrm{pre}}$ and $\mathrm{SNN}_{\mathrm{post}}$) and found that they can express substantial qualitative differences in their dynamics, especially when $\mathrm{SNN}_{\mathrm{pre}}$ expresses a high firing rate heterogeneity across neurons. Near such regimes, $\mathrm{FRE}_{\mathrm{Poisson}}$ follows the dynamics of $\mathrm{SNN}_{\mathrm{post}}$, and thus fails to capture the behavior of $\mathrm{SNN}_{\mathrm{pre}}$. It is worth noticing that the mean-field derivation via the Poissonian assumption works well for networks of homogeneous Poisson neurons with independent noise [155]. In such networks, single cell firing rates can differ momentarily due to noise, but approach the same rate when averaged over increasing time intervals. This is a very different scenario compared to the QIF network considered in this work, where the Lorentzian distribution over η_i causes substantial heterogeneity in the single cell firing rates. Hence, the Poissonian approximation becomes worse the stronger the heterogeneity of single cell firing rates inside the QIF network is. In [156], where the Poissonian approximation was first applied to a QIF network with pre-synaptic STP, the authors chose QIF networks with relatively low firing rate heterogeneity, leading to a good correspondence with the mean-field model. Here, we clarified that this correspondence does not generalize to regimes where the QIF network expresses more heterogeneous firing rates. Populations of neurons that naturally express heterogeneous firing rates exist in sub-cortical structures, for example. Single cell firing rates in the globus pallidus have been shown to differ substantially across neurons [159, 160]. This firing rate heterogeneity has been suggested as an important de-synchronization mechanism of pallidal activity [70]. As elaborated above, our results suggest that studying the mean-field dynamics in such a population via $\mathrm{FRE}_{\mathrm{Poisson}}$ comes at the risk of substantial errors.

We thus developed a mean-field model that addresses the issue of high firing rate heterogeneities. Since the distribution over η_i is the source of heterogeneity in the QIF network, we attempted to improve the mean-field model by considering a set of coupled sub-networks with distinct, but narrow distributions over η_i. This way, the neurons inside each sub-population are parameterized such that they express a considerably lower firing rate heterogeneity than the overall network. We found that, by increasing the number of sub-populations, the mean-field model converges to the QIF network behavior. This approach leads to mean-field models of relatively high dimensionality. Still, we found that a mean-field model with 100 sub-populations (i.e. a 400-dimensional model), accurately predicted phase transitions of the QIF network from steady-state to oscillatory behavior in a regime where $\mathrm{FRE}_{\mathrm{Poisson}}$ failed to do so. Thus, we argue that this multi-population approximation provides a flexible mean-field description, the dimensionality of which can be chosen based on the expected firing rate heterogeneity in the neural population under investigation. In other words, it allows for a flexible trade-off between the accuracy and the computational complexity of the mean-field approximation. The microscopic parameter distribution which we approximated via the multi-population approach is usually assumed to be a Lorentzian since its mathematically most easy to handle [121, 125, 57]. Recently, it has been shown, however, that the accuracy of this multi-population mean-field approximation can be further improved if the microscopic parameter distributions follow a Gaussian instead [161]. Meanwhile, improved mean-field approximations may be derived under the assumption that the network units are subject to noise. Under this assumption, it could be attempted to apply the Gaussian ansatz described in [162] instead of the OA ansatz to describe the low-dimensional manifold of the SNN dynamics. This ansatz might render the Poissonian approximation more accurate, since it would allow to derive the mean-field equations for networks of globally coupled, noisy oscillators and thus provides the stochastic framework required for the Poissonian approximation [155].

As another alternative to the Poissonian approximation, we applied an adiabatic approximation to the QIF network, assuming slow STP dynamics in comparison to the QIF dynamics. This assumption is supported by experimental results that suggest depression and facilitation recovery time scales that are at least 10 times slower than typical membrane potential time scales [154, 133, 156]. Previously, this approach has been used successfully for the derivation of mean-field equations for neural networks with spike-frequency adaptation [140, 94]. By approximating the pre-synaptic STP dynamics as slow, they can be considered as constant, distributed quantities in the fast sub-system. This way, the STP dynamics do not have to be considered for the evaluation of r_{eff} in the fast sub-system. Instead, appropriate distributions over the STP constants have to be chosen. In our work, we derived analytical solutions of the microscopic STP dynamics in the stationary case and used these solutions to approximate the STP distributions. This approach can be considered exact for the description of steady-state solutions, but not for transient dynamics. That is, the network must have converged to an equilibrium for our approximation to be accurate. Still, we find that our adiabatic approximation provides a more accurate approximation of the mean-field dynamics of the QIF network dynamics than the Poissonian approximation, even for transient dynamics. A disadvantage of this method is, however, that we had to approximate the integrals over the STP distribution numerically and calculate r_{eff} via look-up tables. This makes it more difficult to implement the model equations and perform parameter continuations. We thus raise the integration problem that has to be solved for finding an analytic, closed-form mean-field expression of r_{eff} as an open mathematical problem.

3.5.2 The role of STP for neural synchronization and brain function

Interestingly, the different STP types studied in chapter 3 all led to very similar collective phenomena in recurrently coupled SNNs, even though both their mathematical form and the network parameters they acted on differed substantially. For example, the short-term SD mechanism considered in section 3.2 acts multiplicatively on the overall strength of synaptic input to a neuron, whereas the SFA mechanism considered in section 3.3 acts additively on the membrane potential of a neuron. Still, both mechanisms led to the emergence of synchronized, oscillatory regimes. As another example, the synaptic STP model considered in section 3.4 uses the non-linear model described in [154, 133] and acts multiplicatively on the efficacies of all outgoing synapses of a neuron. Nonetheless, the mechanism can induce macroscopic regimes of synchronized oscillations that emerge from the same bifurcations and are of very similar form as the ones described for SD and SFA (see section 3.4.4). It is a typical property of complex systems that their collective dynamic regimes are to a certain degree independent of the concrete formulation of the microscopic dynamics [4, 2]. Hence, these findings emphasize the emergent nature of the synchronized oscillations found in QIF networks subject to STP.

All three STP mechanisms provide the QIF network with a slow, inhibitory process that counteracts the fast, recurrent excitation from the synaptic input and thus acts as a synchronization mechanism. The resulting oscillations share many properties with neural population bursting, a particularly strong mode of collective synchronization that plays a major role in both healthy and pathological neural dynamics. At the single neuron level, bursting is characterized by the neuron firing a train of spikes, followed by a period of quiescence [18]. Importantly, bursting has also been reported in populations of cells without intrinsic bursting mechanisms [18, 163, 164]. In such cases, bursting can be conceived as a property of the collective dynamic interactions within the population. The mechanisms behind emergent bursting are not well understood, since most of the computational literature on bursting focuses on single cells [131, 18]. Typical approaches to model bursting at the population level either use coupled circuits of excitatory and inhibitory populations [165, 164], or include an explicit bursting mechanism such as the action of a neuromodulator [163], feed-forward inhibition [166], or SFA [139]. In our studies, most neurons in the QIF networks expressed bursting behavior in the synchronous regimes, even though these neurons do not have an intrinsic bursting mechanism. Furthermore, the macroscopic dynamics of the QIF networks were reminiscent of bursting as well. The fast focus dynamics of the spike synchronization determined the intra-burst frequency and the slow STP dynamics determined the inter-burst frequency. Therefore, our results suggest that synaptic STP as well as SFA allow for states of population bursting to emerge in SNNs.

Strongly synchronous neural dynamics, such as we observed in the bursting regime described above, are thought to result in macroscopically observable brain rhythms [24]. To date, most of the modeling work on observable spatiotemporal activation patterns of the brain considers synaptic dynamics as origin [19, 167]. Specifically, synaptic currents are thought to trigger the potential changes visible in macroscopic electrophysiological recordings of brain activity, and different synapse types come with different dynamic characteristics that are pivotal for our understanding of brain dynamics [158]. Classic neural mass models, for example, make use of different synaptic time scales to model rhythm generation in the brain [103, 105, 106]. The QIF mean-field reduction we considered generalizes to any convolution of the synaptic input with a synaptic response kernel [125, 126] and, hence, allows one to derive mean-field descriptions of QIF networks with standard descriptions of synaptic dynamics such as employed in neural mass models [105, 106]. Our results suggest that STP mechanisms can add additional time scales to such synaptic current dynamics. Indeed, neural mass models have also employed STP mechanisms to capture the different time scales of neural synchronization [168, 169, 170]. The STP mechanisms we considered can express tremendously different time scales, ranging from a few hundred milliseconds (e.g. spike-frequency adaptation [137]) to several hours (e.g. post-synaptic receptor density reduction [151]). Different STP mechanisms governed by distinct time constants can act on the dynamics of an SNN. For example, cortical pyramidal cells have been demonstrated to express SFA as well as different forms of synaptic STP at glutamatergic and GABAergic synaptic inputs [154, 171, 172, 173]. It is currently unknown how the dynamic interactions between those different STP mechanisms may affect neural synchronization processes. However, it is likely that they provide separate time scales at which a neural population may resonate at, if subject to periodic stimulation [137]. Additionally, the time scales and properties of STP can vary substantially across brain regions [174, 175, 176, 177]. Therefore, they provide interesting candidate mechanisms for a mechanistic examination of how the complex spatiotemporal neural synchronization patterns of the brain may emerge.

In conclusion, the STP mechanisms we considered represent important determinants of neural synchronization processes and their role in the generation of characteristic brain rhythms and synchronization patterns should be further investigated. The mean-field models derived in this chapter can provide the mathematical basis for such studies. Specifically the mean-field models for SFA and SD have been derived based on rather general descriptions of the adaptation dynamics that can easily be adjusted to resemble concrete STP mechanisms in a biological system. Based on these models, the role of synaptic STP for brain functions such as working memory [156] or the maintenance of a critical regime [178] can be investigated.

4

Phase Transitions and Neural Synchronization in the External Pallidum

Based on:

On the role of arkypallidal and prototypical neurons for phase transitions in the external pallidum

Richard Gast[1,*], Ruxue Gong[1], Helmut Schmidt[1], Hil G.E. Meijer[2], Thomas R. Knösche[1,3].

[1] Max Planck Institute for Human Cognitive and Brain Sciences, Leipzig, Germany
[2] Department of Applied Mathematics, Technical Medical Centre, University of Twente, Netherlands
[3] Institute for Biomedical Engineering and Informatics, TU Ilmenau, Germany

* corresponding author (email: rgast@cbs.mpg.de)

Published in The Journal of Neuroscience: JN-RM-0094-21, June 30 2021.

The previous chapters served to establish a conceptual and mathematical framework for studying macroscopic phase transitions of neural activity. Thereby, the phase transition from asynchronous to synchronous neural activity was emphasized as particularly important for brain function. In this chapter, we apply this framework to the concrete case of pathological neural synchronization in Parkinson's disease. To this end, we present our results on the role of the globus pallidus pars externa (GPe) for the emergence of pathological neural synchronization in PD that we published in The Journal of Neuroscience [179].

4.1 A new perspective on GPe structure and function

The basal ganglia (BG) are a set of interconnected sub-cortical nuclei that form different feedback loops with cortex and thalamus [180, 181]. In Parkinson's disease (PD), a neurodegenerative disease that leads to dopamine depletion in the BG, synchronized oscillations have been reported throughout all major BG nuclei [39, 71, 40, 72, 65]. These oscillations are characterized by transient power increases in the beta frequency band (12-30 Hz) and an increased phase-amplitude coupling (PAC) between the phase of a beta signal and the amplitude of a high-frequency gamma signal (50-250 Hz) [182, 183, 61]. Since these parkinsonian neural synchronization patterns have been linked to motor dysfunctions, it is of neuroscientific and clinical interest to understand the mechanisms behind those synchronization patterns [61]. Both computational and experimental studies have suggested that the recurrent coupling between GPe and subthalamic nucleus (STN) is responsible for the beta oscillations [72, 73, 66, 184, 185]. However, a recent study in mice found that optogenetic inhibition of the GPe, but not of the STN led to a strong attenuation of parkinsonian beta power [69]. Thus, the question arises whether PD beta activity might emerge either via other feedback loops of the GPe with BG structures such as the striatum (STR) or autonomously at the GPe. Both of these theories have become more likely in the light of recent data on the GPe structure [186, 187, 188].

In classic theories of BG function, the GPe is regarded as a homogeneous, inhibitory relay station that processes striatal inputs and projects them downstream to BG output structures [180, 181]. Consequently, most computational studies on parkinsonian oscillation generation regarded the GPe as a homogeneous population of GABAergic projection neurons that receive input from STR and STN and project to STN and BG output structures [189, 190, 191, 192]. However, two major cell types have been identified within the GPe, which differ in their electrophysiological properties, firing rates, and firing patterns: prototypical GPe neurons (GPe-p) and arkypallidal GPe neurons (GPe-a) [193, 186, 68]. Regarding their efferent synapses, it has been shown that GPe-p cells preferentially project to STN and BG output nuclei, whereas GPe-a cells provide feedback to STR [194, 187, 195]. Furthermore, it has been shown that GPe-p and GPe-a receive differential synaptic input from STN and STR [196, 197], and also express synaptic contacts with each other [194]. Regarding cell-type specific differences in the latter, there is evidence from experiments in mice that prototypical cells express more numerous axon collaterals than arkypallidal cells [194, 196, 198]. Still, a substantial number of arkypallidal axon collaterals was identified that targeted prototypical GPe cells [194]. Under dopamine depletion, the synaptic currents at GABAergic connections between GPe cells have been shown to increase in strength [199]. We hypothesize that increased synaptic coupling between GPe-p and GPe-a cells may cause the onset of parkinsonian oscillations.

Whereas the GPe operates in a particularly asynchronous regime under normal conditions, it also expresses synchronized oscillations in the beta frequency band in PD [183]. Furthermore, parkinsonian GPe dynamics reveal increased PAC between the phase of a beta rhythm and the amplitude of a gamma rhythm [182, 65]. In this chapter, we examine the effects of GPe coupling patterns on neural synchronization in the GPe. For this purpose, we derive and analyze a mean-field description of two fully coupled inhibitory populations (GPe-p and GPe-a), following the approach described in section 3.1. Importantly, this mean-field description captures the exact macroscopic dynamics of the underlying, heterogeneous spiking neural network and can thus capture population-intrinsic spike resonance phenomena that classic mean-field approaches would miss. This in itself makes our modeling approach interesting for the understanding of synchronization processes inside the GPe. Using bifurcation analysis, we examine the influence of dopamine-dependent changes of intra-pallidal connectivity on the GPe dynamics. We find that increased self-inhibition of prototypical cells can induce oscillations, whereas increased inhibition of prototypical cells by arkypallidal cells leads to the emergence of a bi-stable regime. Furthermore, we show that oscillatory input to the GPe, arriving from striatum, leads to characteristic patterns of cross-frequency coupling observed at the GPe. Based on these findings, we propose two different hypotheses of how dopamine depletion at the GPe may lead to phase-amplitude coupling between the parkinsonian beta rhythm and a GPe-intrinsic gamma rhythm. Finally, we show that these findings generalize to realistic spiking neural networks of sparsely coupled GPe neurons.

4.2 GPe model definition and analysis

4.2.1 Model definition

Mathematical formulation of population dynamics

We consider the GPe as a nucleus of two distinct populations of GABAergic projection neurons [200, 68]. While prototypical neurons express high average spontaneous firing rates of 50-70 Hz [201, 71, 202], arkypallidal neurons fire with considerably reduced average firing rates of 5-15 Hz [186, 187, 188, 203]. To model synaptic influences on the spike timings of GPe neurons, it is important to know their type of excitability. This can be inferred from their phase-response curve [204]. Experimental investigations only revealed type-I excitable GPe neuron dynamics so far [70], even though computational studies demonstrated that both type-I and type-II excitability can be identified in single cell models of GPe neurons [205, 206]. Furthermore, it has been shown that coupled networks of type-I excitable neurons can express type-II excitability on the network level [207]. Thus, we use the quadratic integrate-and-fire (QIF) neuron as a base neuron model, which is the canonical form of type-I excitable neurons and expresses a quadratic and thus non-linear input-output relationship [18]. This choice also accounts for the non-linear input-output relationship reported in prototypical and arkypallidal cells [200, 186]. The evolution equation of the i^{th} QIF neuron embedded within either the GPe-p or GPe-a is given by

$$\tau\dot{V}_i = V_i^2 + \eta_i + I(t) + JS_i\tau, \tag{4.1a}$$

$$S_i = \frac{1}{N}\sum_{j=1}^{N}\sum_{k\backslash t_j^k<t}\int_{-\infty}^{t} G(t-t')\delta(t'-t_j^k)\mathrm{d}t', \tag{4.1b}$$

with neural excitability η_i, synaptic strength J, evolution time constant τ, extrinsic input $I(t)$ and synaptic input S_i. A neuron i generates its k^{th} spike at time t_i^k. At this time, it reaches the spiking threshold V_T and the membrane potential V_i is reset to a reset potential V_R. The integral kernel $G(t)$ represents synaptic dynamics, e.g. in the case of mono-exponential synapses

$G(t) = \mathrm{e}^{-t/\tau_s}/\tau_s$ with synaptic time scale τ_s. We introduce the exact shape and timescales of G in the following sub-section. Eqs. (4.1a) and (4.1b) represent an all-to-all coupled network of N QIF neurons with homogeneous connection strengths J. Assuming all-to-all connectivity as well as infinitely large neural populations, we can use the mean-field model proposed in [125]. As described in section 3.1, the system dynamics given by eqs. (4.1a) and (4.1b) can be reduced to a set of two coupled differential equations describing the evolution of the macroscopic firing rate r and membrane potential v of the QIF population:

$$\tau \dot{r} = \frac{\Delta}{\pi \tau} + 2rv, \tag{4.2a}$$

$$\tau \dot{v} = v^2 + \bar{\eta} + I(t) + Js\tau - (\pi r \tau)^2, \tag{4.2b}$$

$$s = \int_{-\infty}^{t} G(t-t')r(t')\mathrm{d}t' = G * r. \tag{4.2c}$$

Here, the synaptic activation s takes the form of a simple convolution of the average firing rate r with the synaptic response kernel G, abbreviated by the convolution operator $*$. The parameters $\bar{\eta}$ and Δ are the center and half width at half maximum of a Lorentzian distribution over the single neuron parameters η_j. Thus, $\bar{\eta}$ and Δ allow to control the average and heterogeneity of the firing rates inside the QIF population, respectively. Spontaneous firing rates of GPe cells cannot be explained by glutamatergic input alone, since brain slice recordings still showed autonomous activity of up to 26 Hz after synaptic transmission was blocked pharmacologically [208]. In other words, GPe cells are strong pacemaker cells that show regular firing at a cell-specific frequency under synaptic isolation [160, 209]. Across GPe cells, a substantial amount of heterogeneity of the intrinsic firing frequencies has been reported [70]. By considering the background excitabilities η_i as distributed quantities, we account for these findings.

We are aware that the all-to-all coupling and infinite population sizes are in contrast to the actual GPe structure [70, 68]. However, we have shown that the mean-field model predictions can generalize to a fairly wide range of network sizes and coupling probabilities [94]. Even for QIF networks with recurrent coupling probabilities of 1%, we found that population sizes of $N = 8000$ neurons were sufficient to reproduce the macroscopic dynamics predicted by the mean-field model accurately (see section 3.2.4). Given that population sizes of primate GPe are on the order of 10^5 and recurrent coupling probabilities are around 5% [70], we expect that this mean-field model is sufficient to capture the macroscopic dynamics of QIF populations with realistic cell counts and coupling probabilities.

Mathematical formulation of axonal propagation and synaptic dynamics

In a next step, we define the coupling function G which, in our model, acts as a lumped representation of axonal propagation and synaptodendritic integration. In other words, G serves to link single spikes emitted by neuron i to changes in the membrane potential of any other neuron. GPe to GPe connections have been suggested to express axonal transmission delays of around 1.0 ms [202] and make use of GABAergic synapses [200]. Since axon collaterals can express a substantial variability in individual axon diameters and myelination properties [210], we modeled the axonal transmission delays via gamma distributions [211]. The probability density function of the gamma distribution can be written as

$$\Gamma(\gamma, \beta, t) = \frac{\gamma^{\beta} t^{\beta-1} e^{-\gamma t}}{(\beta-1)!}, \tag{4.3}$$

with shape parameter β and scale parameter γ. These parameters can be used to control the mean μ and width σ of the delay distribution via the functional relationships $\mu = \frac{\beta}{\gamma}$ and $\sigma^2 = \frac{\beta}{\gamma^2}$ [211]. Choosing eq. (4.3) as functional form of the function G in eq. (4.2c), the synaptic convolution operation can be expressed as the following set of coupled ordinary differential equation (ODE)s:

$$\dot{s}_i = \gamma(s_{i-1} - s_i), \tag{4.4}$$

where $i = 0, 1, 2, ..., \beta$ and $s_0 = r$ [211]. Using this formulation, the number of coupled ODEs depends on the shape parameter of the gamma function, which means that the overall dimensionality of the system depends on the order parameters β at each synaptic connection in the model.

In addition to the axonal delays, we also included a dynamic model of the electrochemical processes that lead to a change in the post-synaptic potential after a pre-synaptic action potential traveled down the axon. A popular choice to express these dynamics is via a convolution with a bi-exponential synaptic response kernel, for which the rise and decay time constants are specific to the type of pre- and post-synapse [19]. Such a bi-exponential synaptic response function is given by

$$B(\tau_r, \tau_d, t) = \frac{\tau_r \tau_d}{\tau_r + \tau_d}(e^{-\frac{t}{\tau_r}} - e^{-\frac{t}{\tau_d}}), \tag{4.5}$$

with τ_r and τ_d, denoting the synaptic rise and decay time constants, respectively. A convolution of the delayed axonal response s_β with eq. (4.5) can be approximated by two coupled ODEs of the form:

$$\dot{s} = y, \tag{4.6a}$$

$$\dot{y} = \frac{1}{\tau_r \tau_d}(s_\beta - y(\tau_r + \tau_d) - s), \tag{4.6b}$$

with s being the final synaptic input entering into eq. (4.2b). By defining $G = \Gamma * B$, we specify the convolution integral expressed by eq. (4.2c) in our model as subsequent convolutions of r with the gamma function given by eq. (4.3) and the bi-exponential function given by eq. (4.5). This allows us to capture the characteristics of both axonal delay distribution and post-synaptic currents.

Specification of the two-population GPe model

Based on these dynamic equations for neural populations and synaptic transmission, we can now introduce the full set of equations of our GPe model. Since the number of equations of the ODE expression (eq. 4.4) of the gamma kernel convolution given by eq. (4.2c) depends on the parameter β of eq. (4.3), we chose to provide a set of integro-differential equations for generality and brevity. However, for our results, each gamma kernel convolution was formulated as a set of coupled ODEs as given by eq. (4.4) and each convolution with a synaptic response kernel (see eq. 4.5) was formulated as the ODE system given by eqs. (4.6a) and (4.6b). The following set of coupled integro-differential equations describes the average firing rate and average membrane potential dynamics at GPe-p and GPe-a:

$$\tau_p \dot{r}_p = \frac{\Delta_p}{\pi \tau_p} + 2 r_p v_p, \tag{4.7a}$$

$$\tau_p \dot{v}_p = v_p^2 + \bar{\eta}_p + I_p(t) - (J_{pa} s_{pa} + J_{pp} s_{pp} + J_{pe} r_e - J_{ps} r_s)\tau_p - (\pi r_p \tau_p)^2, \tag{4.7b}$$

$$\tau_a \dot{r}_a = \frac{\Delta_a}{\pi \tau_a} + 2 r_a v_a, \tag{4.7c}$$

$$\tau_a \dot{v}_a = v_a^2 + \bar{\eta}_a + I_a(t) - (J_{ap} s_{ap} + J_{aa} s_{aa} + J_{ae} r_e - J_{as} r_s)\tau_a - (\pi r_a \tau_a)^2, \tag{4.7d}$$

where p and a are the subscripts for prototypical and arkypallidal GPe, respectively, and subscripts of the form A_{xy} represent the variable A that is specific to the synaptic transmission from population y to population x. Hence, each synaptic input s_{xy} is specific to a given synaptic connection and takes the form

$$s_{xy} = B(\tau_r^{xy}, \tau_d^{xy}, t) * \Gamma(\gamma_{xy}, \beta_{xy}, t) * r_y(t) \tag{4.8}$$

with specific synaptic rise and decay times τ_r^{xy} and τ_d^{xy} and axonal delay distribution shape and scaling γ_{xy} and β_{xy}. Finally, we added inputs from STN and STR to the model. These can affect GPe dynamics via their constant steady-state firing rates r_e and r_s, which are again scaled by population specific connectivity constants J_{xy}.

Mathematical formulation of extrinsic model inputs

Extrinsic input can generally be applied via the extrinsic forcing parameters $I_p(t)$ and $I_a(t)$ to GPe-p and GPe-a , respectively. In our simulations, we applied step function inputs to each of the populations. These are defined as

$$I_x(t) = \begin{cases} \alpha, & \text{if } t_{\text{start}} < t < t_{\text{end}} \\ 0, & \text{otherwise.} \end{cases} \tag{4.9}$$

Here, α defines the input strength, whereas t_{start} and t_{end} define the beginning and end of the time interval in which the input is applied. Furthermore, we also applied periodic input to the GPe-p , since the GPe-p seems to be most strongly affected by subthalamopallidal and striatopallidal inputs [203]. We used the Stuart-Landau oscillator as the generating model of a sinusoidal signal with period T [212]:

$$\dot{X} = -\frac{2\pi Y}{T} + X(1 - X^2 - Y^2), \tag{4.10a}$$

$$\dot{Y} = \frac{2\pi X}{T} + Y(1 - X^2 - Y^2). \tag{4.10b}$$

Additionally, to account for the bursting characteristics of typical striatal inputs arriving at the GPe [213], we applied a sigmoidal transformation to the Stuart-Landau oscillator, giving us the final input

$$I_p(t) = S(X(t), \alpha, \kappa, T, t_{on}) * B(\tau_r, \tau_d, t), \tag{4.11a}$$

$$S(X, \alpha, \kappa, T, t_{on}) = \frac{\alpha}{1.0 + e^{-\kappa\left(X - \cos\frac{t_{on}\pi}{T}\right)}}, \tag{4.11b}$$

where S represents a sigmoidal transform with steepness κ and maximum α. Thus, α denotes the strength of extrinsic input, no matter whether the input is defined as eq. (4.9) or eq. (4.11a). The cosine term in eq. (4.11b) ensures that the input $I_p(t)$ only expresses bursts around the maxima of X. We set the steepness of the bursts to $\kappa = 100.0$ and the width of the bursts to $t_{on} = 5.0$ms. For a more detailed description of this sigmoidal transformation of a sinusoidal signal to a periodic square wave, see [214]. Finally, the result of the sigmoidal transform is convoluted with a bi-exponential synaptic kernel, where the rise and decay times are chosen as $\tau_r = 0.5$ and $\tau_d = 5.0$, thus accounting for the time constants of GABAergic synapses reported in the GPe [215]. This way, the final input $I_p(t)$ reflects burst-like striatal input that enters at GPe-p neurons via GABAergic synapses.

4.2.2 Model analysis

To analyze the behavior of the model given by (4.7a-4.7d), we employed the open-source Python toolbox PyRates [157]. We chose PyRates' interface to the SciPy Runge-Kutta solver with adaptive integration step-size [84] for numerical integration of the model dynamics for a given initial condition. For bifurcation analysis, we used PyRates' interface to Auto-07p [88] to perform numerical parameter continuation and automatic bifurcation detection. For an in-depth explanation of these techniques, see [86, 89]. To analyze the behavior of the spiking neural networks corresponding to our mean-field models, we employed custom Matlab code. Numerical integration of the spiking neural network dynamics was performed via an explicit Euler algorithm with an integration step-size of 0.001 ms, which we found to be sufficiently small to capture all model dynamics. The scripts and configuration files for all simulations and parameter continuations are available at the following public Github repository: `https://github.com/Richert/GPe_Dynamics`.

4.2.3 Spectral analysis

We also analyzed the GPe model behavior in the frequency domain. To this end, we used time series of 320 seconds of simulated GPe-p firing rate dynamics sampled at 1 ms and cut off the first 20 s to remove initial transients from the time series. Then, we calculated the power-spectral density (PSD) from the raw simulation data using Welch's method. We used fast Fourier transform (FFT) segments of length 2048 and an overlap between segments of 1024 time steps. For quantification of phase-amplitude coupling (PAC) and phase-phase coupling (PPC) between different frequency components of the GPe-p firing rate dynamics, we followed the procedure described in [61]. PAC measures the amount of modulation of the amplitude of a high-frequency signal by the phase of a low-frequency signal and was evaluated by means of the Kullback-Leibler-based modulation index (KL-MI) [216]. Both the low- and high-frequency signals were acquired by band-pass filtering the GPe-p firing rate time series. Following the procedure described in [61], we evaluated the KL-MI for multiple pairs of phases at frequencies

$f_p \in 2, 4, 6, ..., 30$ Hz and amplitudes at frequencies $f_a \in 50, 60, 70, ..., 250$ Hz. For each pair of f_p and f_a, we filtered the GPe-p firing rate using an finite impulse response (FIR) band-pass filter centered at f_p with a band-width of 2 Hz and using another FIR band-pass centered at f_a with a band-width of f_p Hz. We then applied the Hilbert transform to the two band-pass filtered signals and extracted the phase from the signal filtered around f_p and the amplitude of the signal filtered around f_a. Phases were then sorted into 16 bins and the amplitudes corresponding to each bin were averaged. Then, the KL-MI of the distribution of the average amplitude across phase bins was calculated as described in [216], which measures the difference to a uniform distribution. Furthermore, we evaluated PPC for the GPe-p firing rates filtered around f_p and f_a using the waveform analysis described in [61]. In short, this method calculates the average waveform of the high-frequency signal, time-locked to the zero-crossing of the low-frequency signal. The resulting metric is bounded between 0 and 1, with ppc = 1 indicating that the phase of the high-frequency signal (filtered at f_a) is always the same at zero-crossings of the phase of the low-frequency signal (filtered at f_p). Hence, for a given GPe-p firing rate time series, we acquired a 15×21 PAC (PPC) matrix C_{pa} (C_{pp}) with entries for each pair of f_a and f_p. To evaluate the overall amount of PAC in a time series, we calculated the average across the PAC matrix (*mean PAC* in Fig. 4.4). Finally, we evaluated the similarity between PAC and PPC across low- and high-frequency components of a time series by calculating the Pearson correlation coefficient between the PAC and the PPC matrix (*PAC-PPC correlation* in Fig. 4.4).

4.2.4 Model parameters

The dynamics at GPe-p and GPe-a are each governed by membrane time constants τ and two parameters $\bar{\eta}$ and Δ that determine the center and half width at half maximum of the distribution of single cell firing rates inside the populations. Additionally, the four synaptic connections between GPe-p and GPe-a are each parameterized via a lumped synaptic strength J, two axonal delay parameters μ and σ and the synaptic rise and decay time constants τ_r and τ_d. To find a parameterization of the model that resembles realistic macroscopic neural dynamics inside the GPe, we imposed the following conditions for the model behavior: (I) The input-output relationship of isolated GPe-p and GPe-a QIF neurons should qualitatively replicate the f-I curves reported in [186] for in-vitro prototypical and arkypallidal neurons. (II) The distribution of single cell firing rates in the GPe-p and GPe-a populations should qualitatively resemble the firing rate distributions reported in [159, 199, 196, 203], which reveal more heterogeneous firing rates across prototypical neurons as compared to arkypallidal neurons. (III) The average firing rates of GPe-p and GPe-a neurons should behave as reported in [159, 71, 203] under control conditions as well as conditions of striatal stimulation (strongly increased (decreased) GPe-a (GPe-p) firing rates [203]), subthalamic inhibition (moderately increased (decreased) GPe-a (GPe-p) firing rates [203]), blockade of GABA_A transmission (increased GPe-p firing rates [159]), or blockade of GABA_A and AMPA transmission (similar GPe-p firing rates as in control condition [159]). By hand-tuning our model, we found the parameter set reported in Table 4.1 to meet these conditions well. We provided references for parameters that were additionally constrained by the literature. If not reported otherwise, model parameters were set to these default values. As can be seen in Fig. 4.1A, our model

Parameter	Value	Reference	Parameter	Value
τ_p	18.0 ms	[217]	Δ_p	9.0
τ_a	32.0 ms	[193]	Δ_a	3.0
μ_{pp}, μ_{aa}, μ_{pa}, μ_{ap}	1.0 ms	[202]	$\bar{\eta}_p$	12.0
σ_{pp}, σ_{aa}, σ_{pa}, σ_{ap}	0.6 ms	[202]	$\bar{\eta}_a$	26.0
τ_r^{pp}, τ_r^{aa}, τ_r^{pa}, τ_r^{ap}	0.5 ms	[215]	J_{pp}	15.0
τ_d^{pp}, τ_d^{aa}, τ_d^{pa}, τ_d^{ap}	5.0 ms	[215]	J_{ap}	20.0
r_e	20.0 Hz	[71]	J_{pa}	5.0
r_s	2.0 Hz	[71]	J_{aa}	1.0
J_{pe}	50.0	[197]	J_{ps}	100.0
J_{ae}	15.0	[197]	J_{as}	10.0

Table 4.1: Default model parameter values.

replicates the findings that GPe-p neurons express more heterogeneous firing rates than GPe-a neurons, whereas GPe-a includes a larger number of silent neurons than GPe-p [188, 203]. Furthermore, the f-I curves shown for GPe-p and GPe-a populations and single cells in Fig. 4.1B agree with the data in [186]. Finally, Fig. 4.1C shows that the model responses to extrinsic manipulation of inputs and synaptic strengths of the GPe populations match the experimental results reported in [159, 71, 203].

4.3 Phase transitions in the GPe under static and periodic input

In this section, we report the results of our analysis of the relationship between model parameters and neural dynamics for the GPe model given by (4.7a-4.7d). We focus on parameters that contribute to a difference between GPe-p and GPe-a , which include the coupling strengths within the GPe as well as additional inputs to the two populations.

4.3.1 Effects of GPe-intrinsic coupling

As the first part of our analysis, we performed a bifurcation analysis of the GPe mean-field model given by (4.7a-4.7d) to investigate whether different coupling patterns between GPe-p and GPe-a promote different macroscopic states and phase transitions. We started out from the GPe coupling strengths listed in Table 4.1, which represent a coupling pattern where GPe-p inhibition of GPe-a is strongest and GPe-a axon collaterals are weaker than GPe-p axon collaterals, but still exist (see [194, 196] for a comparison to experimental findings). In this default state, input to the GPe populations led to changes in their firing rates, but did not induce any phase transitions (see Fig. 4.2A). Still, inhibition of GPe-p caused a fast increase in GPe-a firing rates. This interaction pattern between GPe-p and GPe-a changes when the intrinsic connections of the GPe are altered. As shown in Fig.4.2C and D, increases in J_{pp} lead to the emergence of a stable limit cycle via a supercritical Andronov-Hopf bifurcation. The emerging oscillations express a frequency in the gamma range ($\approx 50 - 60$ Hz) and can be induced by changes in J_{pp} as well as changes in $\bar{\eta}_p$ (Fig.4.2D and E). The Hopf curve in the $\bar{\eta}_p$-J_{pp} plane shows that this emergence of synchronized oscillations critically depends on $J_{pp} > 0$ as well as a sufficient excitatory drive as given by $\bar{\eta}_p > 0$. We encountered a

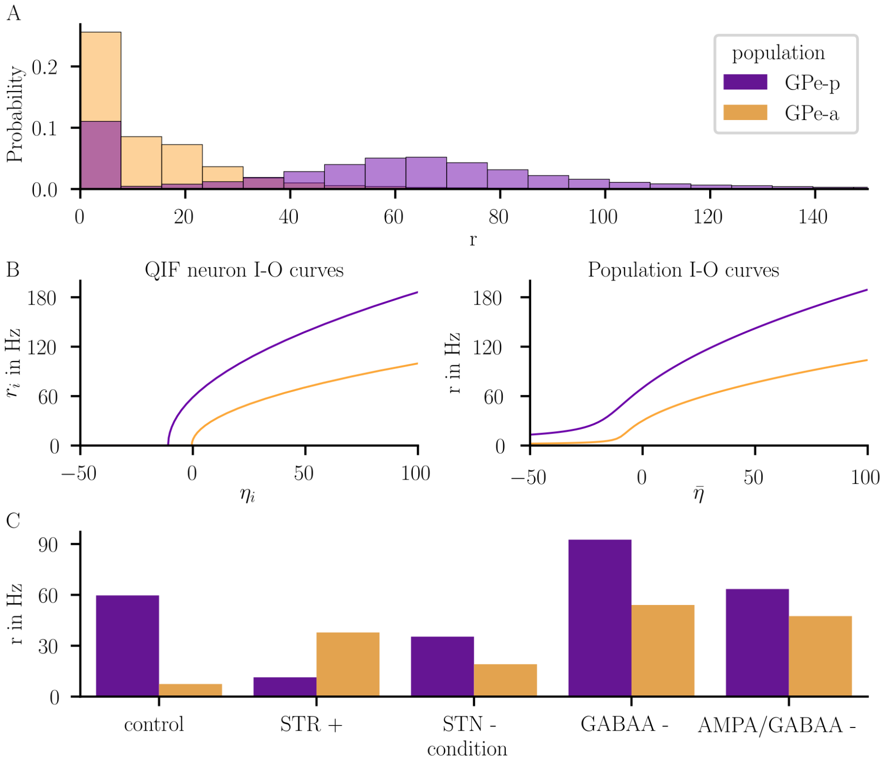

Figure 4.1: Configuration of the GPe model. **A:** Distributions of steady-state QIF firing rates under synaptic isolation, i.e. with $J_{xy} = 0 \forall x, y \in \{p, a, e, s\}$, for $\bar{\eta}_p = 11$ and $\bar{\eta}_a = 0.5$. **B:** f-I curves for single GPe-p and GPe-a neurons (left) and the GPe-p and GPe-a populations (right) under synaptic isolation, i.e. with $J_{xy} = 0 \ \forall x, y \in \{p, a, e, s\}$. **C:** Steady-state average firing rates of GPe-p and GPe-a calculated from 1s of model behavior under different conditions. (*control*) default parameters as reported in Table 4.1. (*STR +*) STR excitation, i.e. $r_s = 40$Hz. (*STN -*) STN inhibition, i.e. $r_e = 2$Hz. (*GABAA -*) blockade of GABAergic synaptic transmission, i.e. $J_{pp} = 1.5$, $J_{ap} = 2.0$, $J_{pa} = 0.5$, $J_{aa} = 0.1$, $J_{ps} = 10.0$ and $J_{as} = 1.0$. (*AMPA/GABAA -*) blockade of all glutamatergic and GABAergic synaptic transmission, i.e. $J^*_{xy} = \frac{J_{xy}}{10} \forall x, y \in \{p, a, e, s\}$ where J^*_{xy} represent the synaptic strengths used to calculate the firing rates.

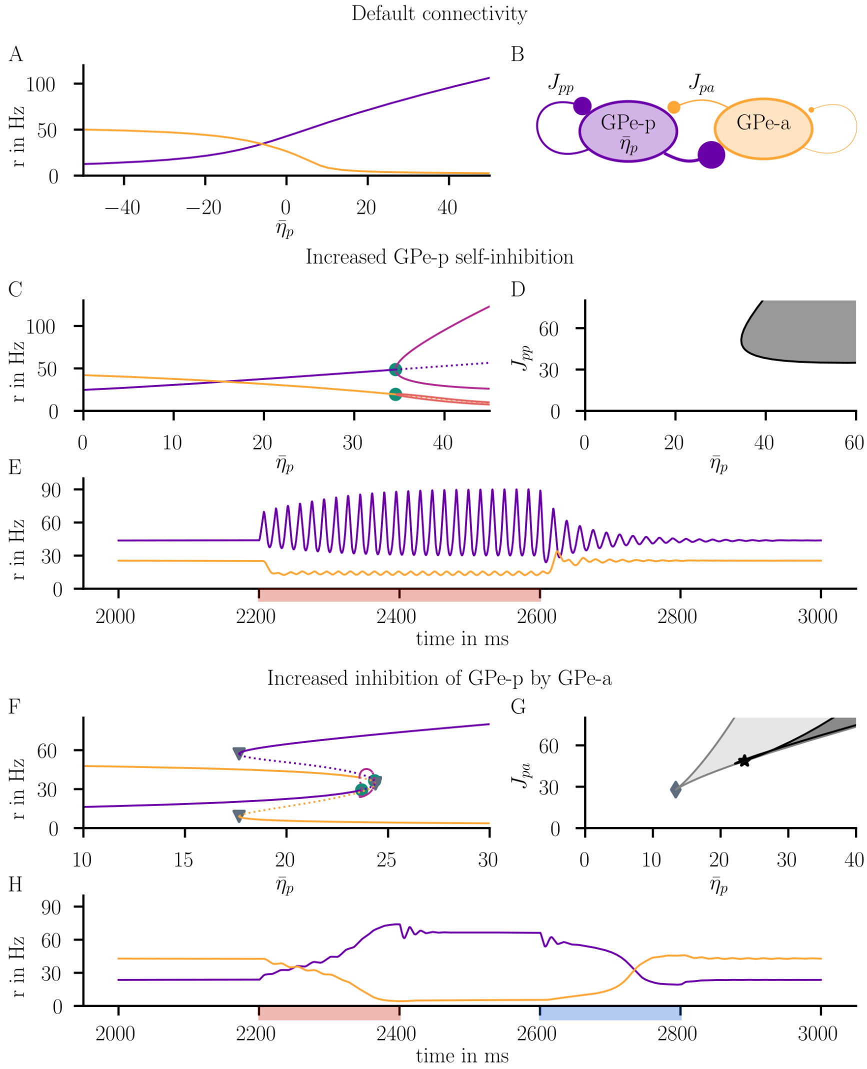

Figure 4.2: Phase transitions in the GPe. **A:** One-parameter bifurcation diagram varying the background input of GPe-p $\bar{\eta}_p$ for the default connectivity. **B:** Depiction of the GPe circuit and the bifurcation parameters. **C:** 1D parameter continuation in $\bar{\eta}_p$ for $J_{pp} = 50$. Green circles represent Andronov-Hopf bifurcations. Lines starting at the Hopf bifurcation represent the minima and maxima of the emerging limit cycle. Solid (dotted) lines represent stable (unstable) equilibria. **D:** 2D bifurcation diagram in $\bar{\eta}_p$ and J_{pp}. The black curve represents the continuation of the 1D Hopf bifurcation from C in the 2D parameter space. Shaded regions represent the parameter space where stable oscillations exist. **E:** GPe-p and GPe-a firing rates for $J_{pp} = 50$ and $\bar{\eta}_p = 30$ show that additional input $I_p(t) = 10.0$, applied between $2200 \leq t < 2600$, forced the system over the Hopf bifurcation. **F:** 1D parameter continuation in $\bar{\eta}_p$ for $J_{pa} = 50$. Grey triangles represent fold bifurcations. **G:** 2D bifurcation diagram in $\bar{\eta}_p$ and J_{pa}. The grey rhombus represents a cusp bifurcation and the black star represents a zero-Hopf bifurcation. **H:** GPe-p and GPe-a firing rates for $J_{pa} = 50$ and $eta_p = 21.0$ show switching between the two stable branches via $I_p(t) = 5$ applied between $2200 \leq t < 2400$ and $I_p(t) = -5$ applied between $2600 \leq t < 2800$.

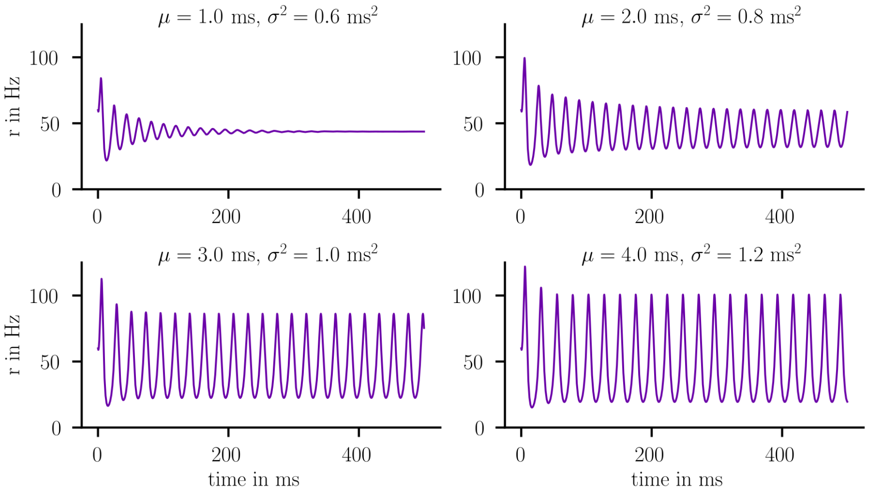

Figure 4.3: Effect of increasing axonal delays on GPe oscillations. Time series represent average firing rates of GPe-p , abbreviated as r. Reported values of μ and σ refer to changes the parameter μ_{xy} and $\sigma_{xy}, \forall x, y \in \{p, a\}$

different phenomenon when increasing J_{pa}, the connection strength from GPe-a to GPe-p . For sufficient increases in J_{pa}, the system expresses two fold bifurcations that mark the outer boundaries of a bi-stable regime, in which transient inputs to GPe-p (or GPe-a) allow to switch between two stable states (see Figure 4.2F and H). One of those two stable states is a focus for which the GPe-p is in a high-activity regime and forces the GPe-a to a low-activity regime. The other stable state is also a focus where the GPe-a is in a high-activity regime and forces the GPe-p to a low-activity regime. These two stable equilibria are separated by a saddle-focus. Thus, we found that strong bi-directional coupling between prototypical and arkypallidal GPe populations allows for the existence of a bi-stable activity regime, where the two populations compete over a high-activity state. In Figure 4.2G, we show the curve of the fold bifurcations in the $\bar{\eta}_p$-J_{pa} plane, which collapse in a cusp bifurcation when J_{pa} becomes small. Furthermore, we find another Hopf curve that touches the fold curve at a zero-Hopf bifurcation. This Hopf curve covers a relatively small parameter range, however, and only appears on the lower branch within the bi-stable regime. The oscillations emerging from this Hopf bifurcation are small-amplitude gamma oscillations.

As a next step, we investigated whether the frequency of the oscillations identified for increased self-inhibition of GPe-p critically depend on the axonal delays in our model, since estimates of these delays differ substantially in the literature [202, 196]. To this end, we simulated the behavior of our model for increasing values of $\mu_{xy}, \forall x, y \in \{p, a\}$. As can be seen in Fig. 4.3, increasing μ_{xy} appears to drive the system over a Hopf bifurcation, but does not affect the oscillation frequency in biologically plausible ranges.

4.3.2 GPe response to periodic forcing

By now, we have established an understanding of the intrinsic, coupling-dependent GPe response to static, afferent inputs. We found that a dichotomous organization of the GPe with two distinct populations GPe-a and GPe-p results in coupling-dependent dynamic behavior that situates the GPe either near a bi-stable regime or near an oscillatory regime. These two different scenarios may have substantially different consequences for the transmission and amplification of periodic input arriving at the GPe. Hence, as a next step, we analyzed the response of the GPe to periodic inputs when initialized either in the bi-stable regime, in the oscillatory regime or in the healthy steady-state regime. To this end, we applied periodic striatal input with period T and amplitude α to the prototypical population. The bursting properties of striatal input were generated by applying a sigmoidal transformation to a Stuart-Landau oscillator (see eqs. (4.10a)-(4.11b) in the methods section). In each regime, we performed numerical simulations of the model behavior for different values of T and α. We then evaluated the average PAC between the phase of low-frequency signal components (2-30 Hz) and the amplitude of high-frequency signal components (50-250 Hz) of the GPe-p firing rate dynamics. Furthermore, we evaluated the PPC, i.e. the phase dependency of the high-frequency components on the phase of the dominating low-frequency component. A detailed description of these measures is provided in the methods section. As can be seen in Figure 4.4, we find that the GPe responds differently to periodic input depending on its dynamic regime.

In Figure 4.4A, the GPe response to periodic input is depicted for the default coupling pattern. In this case, a stable focus is the only equilibrium, and the input perturbs the system around that equilibrium at the input frequency. After a perturbation, the system relaxes back to the focus via damped oscillations. The amplitude of these oscillations scales with α, as can be seen by comparing time series Figure 4.4A.1 vs. A.2. Thus, stronger inputs generate stronger modulation of high-frequency amplitudes by low-frequency phases, resulting in increased PAC. Since the high-frequency focus dynamics are directly elicited by the low-frequency perturbations, increases in PAC always co-occur with increased PPC.

Figure 4.4B depicts the response of a bi-stable GPe to periodic input. In this regime, periodic inhibition forces the GPe-p towards the low-activity regime, if sufficiently strong (see Figure 4.4B.1 vs. Figure 4.4B.2 for inputs that are too weak and sufficiently strong, respectively). If forced towards the low-activity regime, the GPe-p attempts to relax back to its natural high-activity regime (Figure 4.4B.2 and Figure 4.4B.4). In this relaxation process, the system is affected by the strong focus dynamics of the saddle that separates the two stable states. For most combinations of α and T, this behavior creates oscillations with interleaved large- and small-amplitude oscillations, where the large-amplitude oscillations act as an amplification of the low-frequency input and cause cross-frequency coupling with the high-frequency, small-amplitude focus dynamics. Stronger inputs generate stronger modulation of high-frequency amplitudes by low-frequency phases, as evaluated by PAC. Such increases in PAC occur together with increased phase locking between low- and high-frequency components. This can be observed by the generally high PAC-PPC correlations in Figure 4.4B. Interestingly, there also exists a relatively narrow window in T, where the periodic inhibition of the GPe-p forces the system to stay within the domain of influence of the unstable saddle-focus, thus causing periodic oscillations with strongly reduced PAC (see Figure 4.4B.3).

More complex, resonant behavior can arise for periodic forcing of the GPe, if the GPe already expresses oscillations autonomously (see Figure 4.4C and D). When increasing α, the system undergoes a torus bifurcation that emerges from the interaction between the intrinsic limit cycle and the extrinsic, periodic input. As can be seen from the firing rate dynamics in Figure 4.4C, strong amplitude modulations of the intrinsic limit cycle exist in the vicinity of this torus bifurcation. A continuation of the torus bifurcation in the T-α plane reveals that

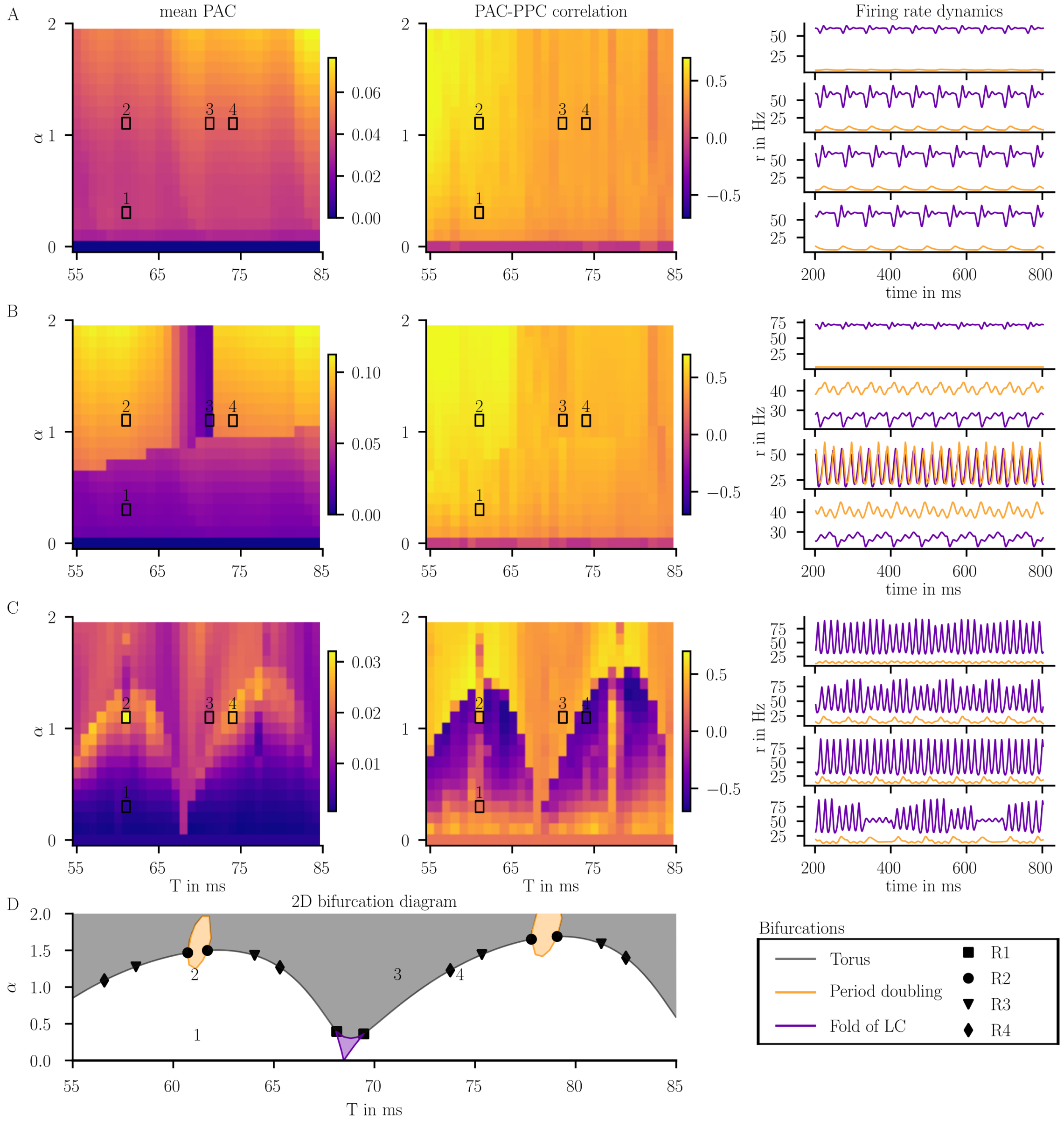

Figure 4.4: PAC and PPC in the periodically inhibited GPe. The input $I_p(t)$ was applied with different frequencies $\frac{1}{T}$ and amplitudes α. For each input, the mean PAC between phases of low-frequency components (2-30 Hz) and amplitudes of high-frequency components (50-250 Hz) of the GPe-p firing rate was calculated. Furthermore, the correlation between PAC and PPC values was evaluated across all pairs of low- and high-frequency components. Exemplary time-series are provided for GPe-p (purple) and GPe-a (orange) firing rates of four different inputs: (1) $T = 61$ ms, $\alpha = 0.3$, (2) $T = 61$ ms, $\alpha = 1.1$, (3) $T = 71$ ms, $\alpha = 1.1$, (4) $T = 74$ ms, $\alpha = 1.1$. **A:** Results for default parameters. **B:** Results for $J_{pa} = 50$ and $\bar{\eta}_p = 24$. **C:** Results for $J_{pp} = 50$ and $\bar{\eta}_p = 40$. **D:** 2D Bifurcation diagram in the $\alpha - T$ plane which shows emergence of resonant behavior and period doubling of GPe oscillations along a torus bifurcation curve.

the system expresses various resonances of the intrinsic limit cycle with the extrinsic input. Close to regimes of 1:2 resonances, we were able to identify small loci of period doubling bifurcations, suggesting the existence of chaotic regimes. These bifurcations are also reflected in the PAC and PPC profiles of the system. PAC values are low before the system undergoes the torus bifurcation and increase near and after the torus bifurcation. In the vicinity of the torus bifurcation, we find regimes where strong PAC can co-exist with low PPC values. These regions express negative correlations between PAC and PPC and are clearly separated from regions where increased PAC and PPC co-exist (see Figure 4.4C).

4.3.3 Model generalization to GPe spiking neural networks

In this section, we report how the above described findings generalize to SNNs of coupled GPe-p and GPe-a cells with realistic cell counts and coupling probabilities. To this end, we attempted to replicate the mean-field model dynamics shown in Fig. 4.4B.3 and Fig. 4.4C.4 in SNNs with (a) different network sizes and (b) different coupling probabilities. We created a total of four SNNs with (a) either all-to-all coupling or only 5 % of all possible connections, and (b) either $N_p = 4000$ ($N_a = 2000$) GPe-p (GPe-a) cells or $N_p = 40000$ ($N_a = 20000$) GPe-p (GPe-a) cells. We then repeated our simulations of the GPe response to periodic stimulation for spiking neural networks initialized near the bi-stable and in the oscillatory regime (same parameterizations as reported in Fig. 4.4 for the mean-field model). The dynamics of all four SNNs can be seen in comparison to the mean-field predictions in Fig. 4.5. As expected, we find that an all-to-all coupled SNN of large size behaves nearly identically to the mean-field prediction, where the remaining difference in the oscillation amplitude is an effect of the network size and would vanish if we increased the network size even further (see difference between SNNs with N_1 and N_2). Interestingly, we find that reducing the number of synaptic connections to $p = 5\%$ of all possible connections attenuates synchronized oscillations in the network for small network sizes. However, for a sufficiently large network, the SNN follows the macroscopic dynamics predicted by the mean-field model, even when $p = 5\%$. This holds for both the bi-stable as well as the oscillatory regime.

4.4 Discussion

4.4.1 Neural synchronization in the GPe under dopamine depletion

In vivo recordings of GPe dynamics have revealed a phase transition from asynchronous to synchronous dynamics in PD, a disease associated with BG dopamine depletion [71, 72, 73]. Under dopamine depletion, GABAergic post-synaptic currents of GPe-to-GPe synapses have been reported to increase in strength [199]. We tested the hypothesis that parkinsonian synchronization patterns arise due to increased synaptic coupling strengths in networks of interconnected prototypical and arkypallidal cells. As argued in section 3.1, exact mean-field models such as the ones described in chapter 3 are well suited to analyze mechanisms of neural synchronization processes via parameter studies. Consequently, we derived an exact mean-field model of a SNN and studied the dependence of its macroscopic dynamics on the underlying synaptic connection strengths. To this end, we focused on the synapses inhibiting the GPe-p,

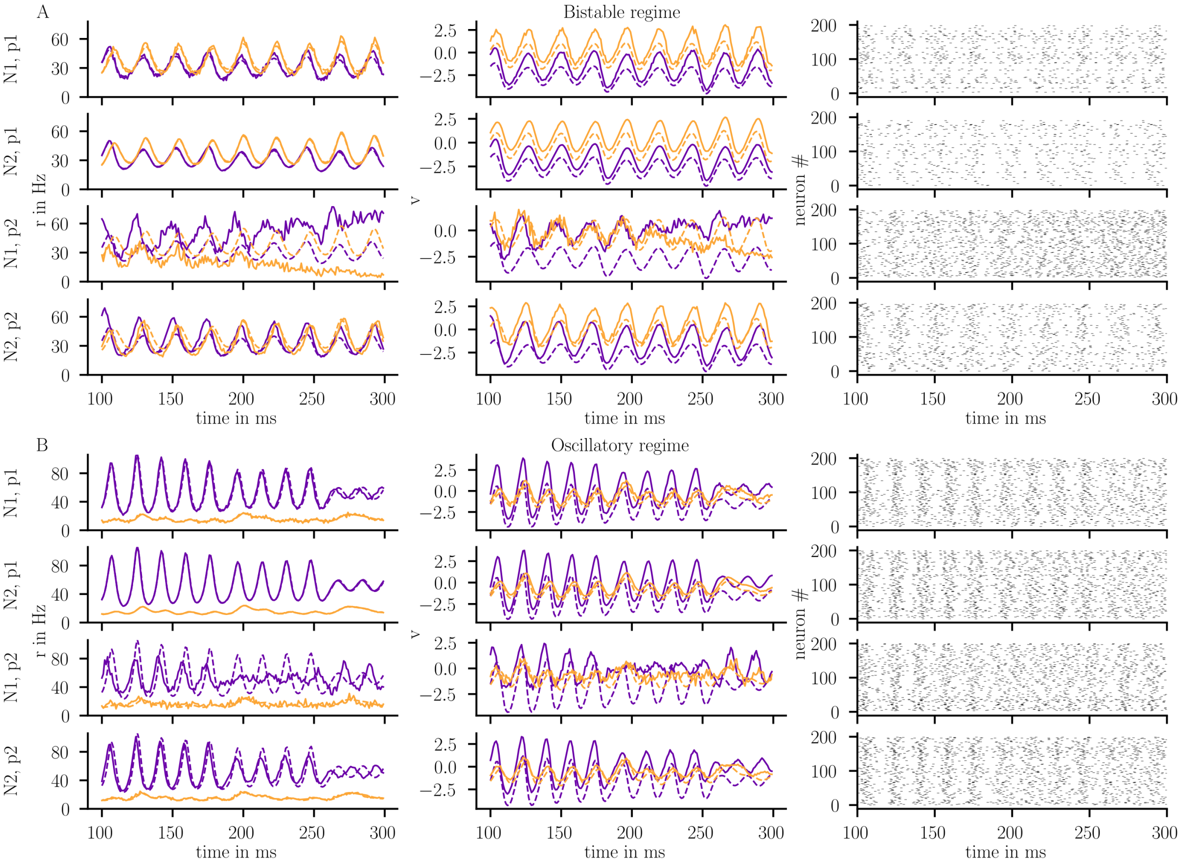

Figure 4.5: Comparison between mean-field model (dashed lines) and spiking neural networks (solid lines) under periodic stimulation. The first and second column show the average firing rate and average membrane potential across the population, whereas the last column depicts spike timings from 200 randomly chosen neurons of the population. SNNs are composed of $N_p = 4N_{1/2}$ GPe-p and $N_a = 2N_{1/2}$ GPe-a neurons, where $N_1 = 1000$ and $N_2 = 10000$. From all possible synaptic connections in the SNN, either $p_1 = 100\%$ or $p_2 = 5\%$ are established. **A:** Results for $J_{pa} = 50$, $\bar{\eta}_p = 24$, $\alpha = 1.1$ and $T = 71$. **B:** Results for $J_{pp} = 50$, $\bar{\eta}_p = 40$, $\alpha = 1.1$ and $T = 74$.

since increased inhibition of GPe-a would merely reduce its already low steady-state firing rates and, hence, not induce any phase transitions of the GPe dynamics [186, 203].

When the strength of GPe-p inhibition by GPe-a was increased, we found that a bi-stable regime emerged in which GPe-p and GPe-a competed over a high-activity state. This regime could provide a form of network memory and a reliable way to switch GPe output between the different projection targets of GPe-p (STN) and GPe-a (STR). Furthermore, if the GPe was situated in the bi-stable regime, periodic inputs from STR were amplified due to the existence of two different attracting states. Indeed, when we applied periodic input from STR to GPe-p in the beta frequency range characteristic for PD [39, 40], the GPe-p was periodically forced from a high-activity state down to a low-activity state, thus resonating at the input frequency. Importantly, this led to strong phase-amplitude as well as phase-phase coupling between beta and gamma components of the GPe-p firing rate dynamics. Interestingly, the synchronized neural activity that has been detected in recordings of STN and GPe activity from PD patients expressed not only increased power in the beta frequency band, but also increased PAC between the phase of beta components and the amplitude of gamma components [218]. Our model can explain these findings as follows: Dopamine depletion at the GPe leads to an increased strength of GPe-a to GPe-p synapses in PD [199]. This structural change moves the system closer to a bi-stable regime. By moving closer to the boundaries of the bi-stable regime, oscillatory inputs from STN or STR become more likely to elicit switching between the two stable states of the GPe. At both of these input sites, increased beta oscillations have been reported in PD [39, 219]. Periodic forcing of the bi-stable GPe would then perturb the system in a phase space controlled by multiple stable and unstable foci with focus frequencies in the gamma range, thus causing damped gamma oscillations with input-triggered amplitude modulations. Hence, in this scenario, PD-related intrinsic changes can cause increased susceptibility of the GPe to periodic inputs, but not autonomous GPe oscillations.

When we instead increased the GPe-p to GPe-p self-inhibition, we found that stable oscillations in a gamma frequency range ($\approx 50 - 60 Hz$) could emerge. These oscillations were driven by the dynamic interactions between the pace-making properties of the GPe-p and its delayed self-inhibition. Most likely, these oscillations reflect the same synchronization mechanism as reported for a single population with delayed self-inhibition in [220]. According to their results, oscillations are counteracted by neural heterogeneity. This way, our results can be linked to the considerations in [70], which suggest that strong firing rate heterogeneity together with recurrent inhibition inside GPe may serve to desynchronize GPe activity under healthy conditions. In accordance with experimental data, we modeled the GPe-p with highly heterogeneous single cell firing rates [199, 187, 196, 203]. This way, inhibitory feedback from the GPe-p provides the means to suppress synchronized oscillations inside the GPe, which supports these considerations. Experimental evidence from animal models of PD suggest that GPe activity shows increased synchronization in PD [71, 194]. Our model can explain these findings as follows: Dopamine depletion causes the strength of GPe-p self-inhibition to increase in PD [199]. This moves the GPe system closer to or even across the boundaries of an oscillatory regime. The emerging limit cycle leads to narrow-band gamma oscillations and thus cannot explain the emergence of beta oscillations in the parkinsonian BG [39, 40]. However, assuming that burst-like afferent inputs drive the GPe at a beta frequency, our findings predict that

GPe-intrinsic gamma oscillations can resonate with the input, leading to a waxing-and-waning of the gamma oscillations. Such waxing-and-waning behavior also implicates increased PAC, which may occur together with decreased PPC, according to our simulations. The latter finding was unique for the oscillatory regime of the GPe. Similarly, complex patterns of cross-frequency coupling have been reported previously in an instantaneously coupled two-population QIF model with sinusoidal forcing in the alpha frequency range (10 Hz) [221]. Thus, our results show under which conditions the GPe system can express the characteristic dynamics that have been identified in more abstract models of two populations with mutual inhibition.

In summary, our results predict that (I) the GPe cannot generate parkinsonian beta oscillations, but (II) that it can contribute to the emergence of pathological beta-gamma PAC under dopamine depletion. Thereby, the latter is predicted to result from an increased feedback inhibition of prototypical cells. Due to its synaptic projections to virtually every major BG nucleus, the GPe is well positioned to transmit its output throughout the BG and entrain the BG to its intrinsic synchronization rhythm [200].

4.4.2 GPe model validity

The validity of our results of course depends on the generalizability of the employed GPe model. Specifically, it depends on the impact of the following simplifying assumptions that we made for modeling the macroscopic GPe dynamics:

1. At the macroscopic scale, GPe dynamics only depend on the interactions between prototypical and arkypallidal neurons.
2. The dynamic interactions of prototypical and arkypallidal neurons can be well approximated by synaptically coupled QIF neurons.
3. At the macroscopic scale, neural interactions of the GPe can be approximated by all-to-all coupling.
4. Synaptic and axonal transmission delays can be well approximated by bi-exponential and gamma distributions, respectively.
5. The heterogeneity of GPe cells can be well approximated by a Lorentzian distribution of the QIF background input parameters.
6. The effects of dopamine depletion on the GPe can be approximated by increases in the GPe synaptic strengths.
7. The number of prototypical and arkypallidal cells is sufficiently large for the emergence of collective phenomena.

We consider some of those assumptions to put rather negligible constraints on the generalizability of the model. With respect to assumption 1, prototypical and arkypallidal cells make up around 90-95 % of the total GPe neurons [68]. Other neuron types would thus have to express a very dense innervation of the GPe to affect its macroscopic dynamics. Such a densely connected GPe neuron type has not been identified yet [68]. Regarding assumption 4, i.e. the synaptic and axonal transmission delays, bi-exponential and gamma kernels are well established macroscopic approximations [106, 19] and have previously been applied to model parkinsonian BG dynamics [190, 192]. We consider macroscopic deviations from these descriptions to be negligible for the emergent phenomena described in this chapter. Finally, the number of neurons in the GPe ranges from the order of 10^4 in rodents to 10^5 in primates, which is well within the range in which the thermodynamic limit has been shown to be a good approximation for the dynamics of globally coupled QIF networks [125, 94, 95]. We thus expect the GPe to express emergent dynamics and phase transitions of these dynamics that can be captured with SNNs (assumption 7). One important constraint regards assumption 2, i.e. the approximation of GPe neural activity via QIF neuron models. Prototypical neurons express very high, regular period firing activity, whereas arkypallidal neurons have been demonstrated to express less regular firing [186, 68]. While the former can be well approximated by QIF neurons in the periodic firing regime, the latter would require additional dynamic processes such as a balancing current [18]. Another crucial constraint is given by assumption 5, i.e. the Lorentzian distribution of background inputs of both prototypical and arkypallidal cells. This assumption is of mere phenomenological nature, since it serves to approximate the firing rate distributions reported for these neuron types [188, 186, 196], but does not correspond to a concrete biological parameter such as the overall number of pre-synaptic contacts or post-synaptic receptors of these neuron types. Nonetheless, despite these simplifying assumptions, the QIF model was well able to reproduce a considerable number of experimental results on GPe activity, such as the steady-state firing rates [71, 186], and the dynamic changes of these firing rates under altered synaptic input from STR, STN or the GPe itself [159, 203]. Furthermore, the model reproduced these results based on realistic f-I curves [186], membrane time constants [193], firing rate distributions [188], and synaptic coupling strengths [196, 197] of prototypical and arkypallidal cells. Finally, we show in section 4.3.3 that the GPe mean-field model dynamics are a good approximation of GPe SNNs with realistic neuron numbers on the order of $N = 10^4$ and realistic coupling probabilities of $p \approx 5\%$ [70, 68]. Thus, we consider the GPe model presented in chapter 4 a good approximation of macroscopic steady-state dynamics of the GPe. Whether it also provides a good approximation of the neural synchronization properties of the GPe is a matter of future experimental validation.

Several experimental paradigms are viable for the validation of our model predictions (I) and (II). Combinations of optogenetic or current stimulation with pharmacological interventions could be used in rodent models. To test the assumption that dopamine depletion increases the efficacy of specific GABAergic GPe-to-GPe synapses, the effects of dopamine antagonists could be compared to the effects of GABAergic agonists on synaptic transmission at GPe-p to GPe-p and GPe-a to GPe-p synapses [199]. Additionally, optogenetic stimulation of STN or STR could be used to control the static but also the periodic input to the GPe-p [203]. Thus, it could be tested whether an increased excitation of GPe-p via the STN in combination with an increased GPe-p self-inhibition can indeed elicit gamma oscillations in the GPe. Furthermore, it could be examined whether additional periodic input from STR could generate beta-gamma PAC and whether the PAC strength scales as predicted with the period and amplitude of the periodic striatal stimulation (see section 4.3). In human subjects with PD, the GPe model could be used to predict the effect of deep brain stimulation (DBS) at the GPe [222, 223, 224]. Specifically, the parameters of the Stuart-Landau oscillator model that we used for extrinsic stimulation of the GPe (see section 4.2) could be optimized such that they restore the healthy, asynchronous GPe regime and could then be used to inform DBS stimulation parameters. Of course, the latter would be more promising in an extended model that is capable of generating parkinsonian beta oscillations itself.

4.4.3 Neurodynamic mechanisms of oscillation generation in PD

Based on the findings that the GPe plays a causal role in the generation of parkinsonian beta oscillations [69] but cannot generate beta oscillations autonomously (see section 4.3), the most likely generators of parkinsonian beta oscillations are the feedback loops between GPe and STN or GPe and STR. Computational as well as experimental evidence exists that both the STN-GPe loop [72, 73, 66] and the GPe-STR loop [67] could be involved in the emergence of these oscillations. To find the cause of parkinsonian beta oscillations via a computational model that can be linked to experimental data such as presented in [203], we propose to use the GPe model described in section 4.2 and extend it by additional QIF populations that represent STN and STR. In this model, it would be possible to disentangle the influences of both feedback loops on the generation of beta oscillations and identify most likely model parameters that could both be affected by dopamine depletion and cause the onset of beta oscillations. It would further be interesting to examine whether the mechanisms for PAC generation described in section 4.3 still hold in such a model.

The QIF -based GPe model has several advantages over other computational models that have been used in this regard [225, 66, 184, 185]. First, it is based on large SNNs and can thus account for collective spike synchronization phenomena [83]. Second, it has an exact corresponding mean-field description that allows for efficient parameter studies via methods such as bifurcation analysis [94]. Third, it allows to account for neural heterogeneity in the BG via continuous parameter distributions across cells (see section 4.2). Finally, it can account for both synapse-specific dynamics and axonal transmission delays (see section 4.2). In conclusion, the modeling approach described in section 4.2 accounts for several of the problems of BG modeling that have been identified in [185]. The combination of next-generation mean-field models of neural dynamics with neurophysiological details of BG composition provides a novel, promising approach to examine the mechanisms behind phase transitions from asynchronous to synchronous BG dynamics, such as observed in PD. With new mean-field models becoming available for SNNs with gap junctions [128, 129], spike-frequency adaptation [94], and synaptic plasticity [94, 95], this approach becomes feasible for extended BG systems.

5

Modeling of Neural Mean-Field Dynamics Via PyRates

Based on:

PyRates - A Python Framework for rate-based neural Simulations

Richard Gast[1,*¶], Daniel Rose[1,¶], Christoph Salomon[1], Harald E. Möller[1], Nikolaus Weiskopf[1], Thomas R. Knösche[1,2].

[1] Max Planck Institute for Human Cognitive and Brain Sciences, Leipzig, Germany
[2] Institute for Biomedical Engineering and Informatics, TU Ilmenau, Germany

¶These authors contributed equally to this work.

* corresponding author (e-mail: rgast@cbs.mpg.de)

Published in PLoS ONE 14(12): e0225900, December 16, 2019.

In the previous chapters, we presented different mathematical models of neural interactions and analyzed their dynamics via numerical methods. Such numerical analysis requires software for the implementation of the respective models and the application of numerical analysis methods to these model implementations. In this chapter, we describe PyRates, a Python software framework that we developed to implement and study the models described in chapters 3 and 4. PyRates provides intuitive access to and modification of all mathematical operators in a graph, thus allowing for a highly generic model definition. For computational efficiency and parallelization, the model is translated into a compute graph. Using the example of two different neural models belonging to the family of rate-based population models, we explain the mathematical formalism, software structure and user interfaces of PyRates.

5.1 Computational modeling in neuroscience

5.1.1 Computational modeling software

Numerical simulations and parameter continuations are the primary methods used to investigate neural models beyond pure analytical techniques and to link model variables with experimental data (see section 2.2). These numerical methods are computationally expensive and scale with the model size, simulation time, and temporal resolution of the simulation. Different software tools have been developed for neural modeling that offer various solutions to render numerical model analysis methods more efficient (e.g. TVB [226], DCM [227], Nengo [228], NEST [229], ANNarchy [230], Brian [231], and NEURON [232]). Each of these tools has been built for neural models of certain families. For example, the setup and simulation of complex multi-compartment models of single spiking neurons is supported by NEURON, Nest, and Brian. Tools dedicated to networks of point neurons, on the other hand, include ANNarchy, Nengo, and PCSIM (though NEURON, Nest, and Brian support point neuron models as well). Finally, neural population models that describe the evolution of macroscopic quantities of neural activity are the focus of TVB and DCM. The state variables of such models represent averages of activity across multiple neurons and do not require information about spikes of single neurons anymore.

In this thesis, we considered models of low-dimensional manifolds of neural activity that can best be described by the family of neural population models and are thus compatible with tools such as TVB and DCM. For these tools, a pool of pre-implemented population models are available that the user can choose from. With the development of a new generation of neural population models via exact mean-field appraoches such as the OA ansatz [124, 57] there is a need for new models to be added to these pools. However, adding new models or modeling mechanisms to this pool is not naturally supported by these tools. This holds true especially if one wants to benefit from the optimization features of the respective software. For single neuron networks, tools like ANNarchy and Brian exist that include code-generation mechanisms [230, 231]. These allow the user to define the mathematical equations that certain parts of the model are governed by and that are automatically translated into the same representations that the pre-implemented models follow. To address the aims of this thesis, a neural population modeling software that provides such a code-generation mechanism would be optimal. Specifically, we required a tool that would allow us to readily implement novel mean-field models of neural dynamics such as the ones we developed in chapter 3 and embed them in extended networks such as the basal ganglia network we studied in chapter 4. Thus, we developed PyRates, an open-source Python framework for rate-based neural modeling (freely available at `https://www.cbs.mpg.de/departments/neurophysics/software/pyrates` and `https://github.com/pyrates-neuroscience/PyRates`). Thereby, rate-based refers to the family of neural models that PyRates was designed for, i.e. models such as neural population models that express neural activity via mean rates instead of single spikes.

PyRates follows two basic principles for model implementation: (1) The full set of model-defining equations can be provided and adjusted by the user and will be translated into an efficient implementation via a code-generation approach. (2) The definition of these model equations is done as a compute graph, where the mathematical equations merely need to be provided for the basic constituents of a neural network, for example for a single neural population, and can then be put into a hierarchical network structure. In principle this will allow the implementation of any kind of dynamic neural system that can be expressed as a graph of nodes and edges, with the former representing the model units (i.e. neural populations) and the latter the information transfer between them. The underlying model equations are translated into a compute graph, specifying which parts of the equations have to be evaluated serially and which parts can be processed in parallel. Parallel hardware that PyRates can employ for this purpose includes CPUs, GPUs, and compute clusters with multiple machines. In the following sections, we will introduce the features and capacities of the framework, explain how to define a model in PyRates, and demonstrate how to use the software to perform numerical studies of neural dynamics. First, we introduce the mathematical syntax of PyRates, followed by an explanation how single mathematical equations can be put into a structure that represents a neural network model. To this end, we provide a step-by-step example of how to configure and simulate a particular neural population model. Second, we replicate characteristic dynamics of two exemplary, well-described neural population models. This is done for validation purposes, i.e. to demonstrate that PyRates provides an accurate implementation of these models as well as of the employed numerical analysis methods. Finally, we provide a short introduction into the neural population models that come pre-implemented in PyRates and the numerical methods that the software provides for their analysis. Importantly, all the mean-field models presented in chapter 3 as well as the mathematical constituents of the GPe model presented in chapter 4 are available in PyRates and can be used in the context of extended neural networks and neurodynamic studies. We argue that PyRates is a well-documented, thoroughly tested, and computationally powerful framework for neural modeling and numerical analyses.

5.1.2 Examples of neural population models

Investigating the human brain via EEG/MEG or fMRI means working with signals that are assumed to represent changes in the average activity of large cell populations [233, 234]. While these signals can be explained by detailed models of single cell processes, such models come with a state space of much higher dimensionality than the measured signals. Indeed, several approaches exist that employ this strategy to model the neural processes underlying macroscopic brain signals [235, 236] via tools such as the *Human Neocortical Neurosolver* or *LFPy* [237, 238]. As an alternative approach, neural mass models have widely been used to model the dynamics of the macroscopic brain signals of interest [239]. That is, they describe the average activity of large cell populations in the brain via a mean-field approach, rendering their investigation computationally much less expensive than single cell approaches [103, 104, 19]. As a downside, all information about the underlying single cell activity is lost, except for the fluctuations of macroscopic state variables, averaged across the entire population. Thus, their application is limited to neurodynamic questions addressing changes in those macroscopic variables. Often, neural mass models express the state of each neural population by an average membrane potential and an average firing rate. Classic neural mass models typically formulate the dynamics and transformations of these state variables via three few mathematical operators. The first two describe the input-output structure of a single population: While the rate-to-potential operator (RPO) transforms synaptic inputs into average membrane potential changes, the potential-to-rate operator (PRO) transforms the average membrane potential into an average firing rate output. Widely used forms for these operators are a convolution operation with an exponential kernel for the RPO (e.g. [105, 240, 241]) and a sigmoidal, instantaneous transformation for the PRO (e.g. [103, 168, 170]). The third operator is the coupling operator (CO) that transforms outgoing into incoming firing rates and is thus used to establish connections across populations. By describing the dynamics of large neural population networks via three basic transforms (RPO, PRO & CO), neural mass models combine computational feasibility with biophysical interpretability. Due to these desirable qualities, neural mass models have become an attractive method for studying neural dynamics on a meso- and macroscopic scale [19, 239, 242]. They have been established as one of the most popular methods for modeling macroscopic measurements of brain activity and have been able to account for various dynamic properties of experimentally observed neural activity [243, 244, 245, 246, 241, 100, 247, 248].

A particular neural mass model that we will use repeatedly in later sections is the three-population circuit introduced by Jansen and Rit [105]. The Jansen-Rit circuit (JRC) was originally proposed as a mechanistic model of the macroscopic potential fluctuations at the visual cortex [249, 105]. Historically, however, it has been used as a canonical model of cell population interactions in a cortical column [243, 245, 248]. Its basic structure can be seen in Fig.5.1B, which can be thought of as a single cortical column. The signal generated by this column is the result of dynamic interactions between a pyramidal cell (PC) population, an excitatory interneuron (EIN) population and an inhibitory interneuron (IIN) population. For certain parametrizations, the JRC has been shown to be able to produce key features of visual cortex potential fluctuations, such as the waxing-and-waning alpha oscillations [105, 240, 250]. A detailed account of the model's mathematical description is given in the next section, where we demonstrate how to implement models in PyRates, using the example of the JRC equations. We chose to employ the JRC as an exemplary population model in this article since it is an established model used in numerous publications that the reader can compare with our report.

Another neural population model that we will employ in this chapter is the one described by Montbrió and colleagues [125] that we made extensive use of in chapter 3. It has been mentioned as one of the next generation neural mass models that provide a more precise mean-field description of neural synchronization processes than classic neural population models like the JRC [83, 124]. As shown in section 3.1, the model proposed by Montbrió and colleagues represents a mathematically exact mean-field derivation of a network of globally coupled quadratic integrate-and-fire neurons [125]. It can thus represent every macroscopic state the single cell network may fall into. This distinguishes it from the JRC, which has no such correspondence between a single-cell network and the population descriptions. Furthermore, the macroscopic states (average membrane potential and average firing rate) of the QIF mean-field model can be linked directly to the synchronicity of the underlying single-cell network, a property that benefits the investigation of EEG phenomena such as event-related (de-)synchronization [125]. By demonstrating how to implement and handle this mean-field model in PyRates, we provide the reader with all necessary information to replicate the mean-field model studies lined out in chapters 3 and 4.

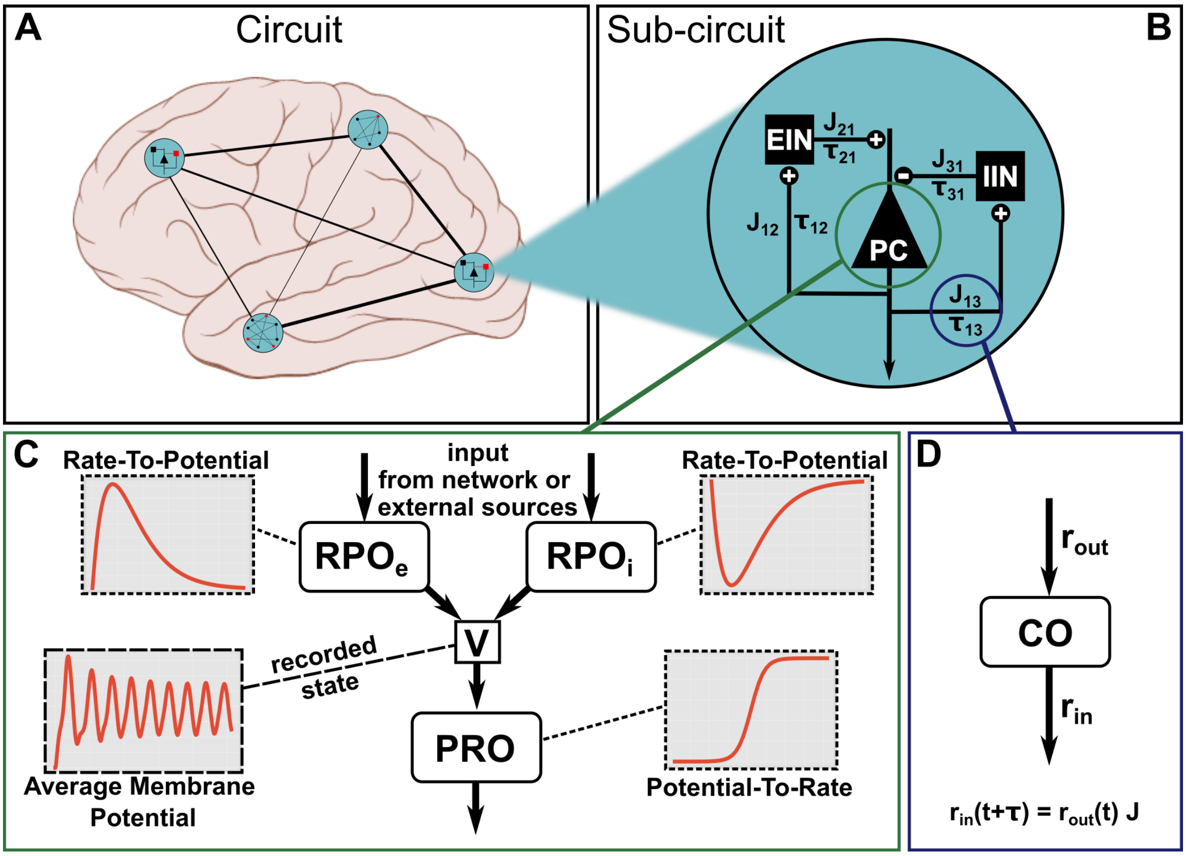

Figure 5.1: Model structure in PyRates. The largest organizational unit of a network model is the *Circuit*. Any circuit may also consist of multiple hierarchical layers of subcircuits. **A:** depiction of an imaginary circuit of four subcircuits that represent one brain region each. **B:** One of these local subcircuits is a Jansen-Rit circuit, consisting of three neural populations (PC, EIN, IIN) and the connections between them. **C:** One node may consist of multiple operators containing the mathematical equations. Here, two rate-to-potential operators (RPO) convolute incoming firing rates with an alpha kernel to produce post-synaptic potentials. These are summed into a combined membrane potential v. The potential-to-rate operator (PRO) transforms v into an outgoing firing rate r_{out} via a sigmoidal function. Inset graphs give a qualitative representation of the operators and evolution of the membrane potential. Edges (lines in A and B) represent information transfer between nodes. **D:** Edges may also contain operators. By default, edges apply a multiplicative weighting constant J and can optionally delay the information passage with respect to time via delay constants τ. The equation shown in panel D depicts this default behavior.

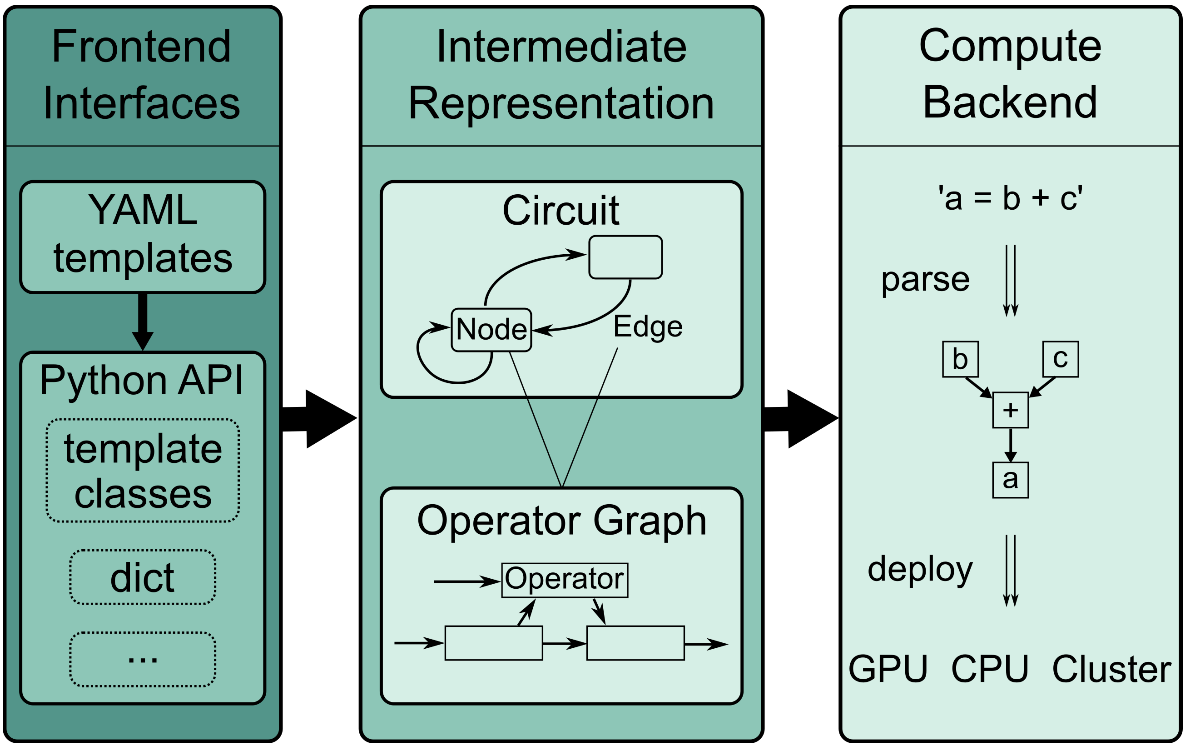

Figure 5.2: Schematic of software layers. PyRates is separated into frontend, intermediate representation (IR) and backend. The frontend features a set of interfaces to define network models. These are then translated into a standardized structure, called the IR. Simulations are realized via the backend, which transforms the high-level IR into lower-level representations for efficient computations. The frontend can easily be extended with new interfaces, while the backend can be swapped out to target a different computation framework.

5.2 The Framework

PyRates requires an installation of Python 3.6 or newer and can be installed via the package manager *pip*, simply by calling `pip install pyrates` from the command line. The core goal of PyRates is to let scientists focus on the model definition, *i.e.* working out the equation structure, while the software takes care of transforming them into computationally efficient network structures and numerical simulations thereof.

This goal is reflected in the modular software design and user interface. Model configuration and simulation are realized as separate software layers as depicted in Fig.5.2. The *frontend* features multiple user interfaces for different levels of programming expertise and allows scientists to flexibly implement custom models. The models are then transformed into a graph-based *intermediate representation* that the *backend* interprets to perform efficient computations. We employ a custom mathematical syntax and domain specific model definition language. Both focus on readability and are much reduced in comparison to general-purpose languages. The following paragraphs explain the user interfaces and how to define models and run simulations. More details on implementation and installation can be found in the online documentation (see pyrates.readthedocs.io).

5.2.1 Mathematical syntax

Neural network models are usually defined by a set of (differential) equations and corresponding parameters. In PyRates, users can define computational models in terms of algebraic equations and relations between different equations. The mathematical syntax strongly follows the conventions used in Python, though in some cases common alternatives are allowed as well. For example, the equation $a = \frac{5\cdot(b+c)}{d^2}$ can be written as `a = 5 * (b + c) / d**2`. Here, the power operator is a double asterisk `**` as used in Python. However, the commonly used caret `^` symbol is implemented as a synonym. Parentheses, such as in `(b + c)`, indicate grouping. Arguments to a function are also grouped using parenthesis, e.g. `exp(2)` or `sin(4 + 3)`.

Currently, PyRates does not include a full computer algebra system. By convention, the variable of interest is positioned on the left-hand-side of the equality sign and all other variables and operations on the right-hand-side. First-order differential equations are allowed as an exception: The expression `d/dt * a` is treated as a new variable and can thus be positioned as the variable of interest on the left-hand-side as in

$$\texttt{d/dt * a = a + d} \tag{5.1}$$

As a short-hand synonym, the expression `a'` may be used as well (e.g. $a' = a + d$). Higher order differential equations must be given as a set of coupled first-order differential equations. For example the equation

$$\frac{d^2a}{dt^2} + \frac{da}{dt} + a = b + c \tag{5.2}$$

can be reformulated as the following set of two coupled first-order differential equations:

$$\frac{da}{dt} = x \qquad \Leftrightarrow \texttt{d/dt * a = x} \tag{5.3}$$

$$\frac{dx}{dt} = b + c - x - a \qquad \Leftrightarrow \texttt{d/dt * x = b + c - x - a} \tag{5.4}$$

In simulations, this type of equation will be integrated for each time step of size dt. The following is an example for equations of a single neural mass in the classic Jansen-Rit model [249], which will be reused in later examples:

```
RPO:  d/dt * w = h/tau * r_in - 1/tau**2 * v - 2 * 1/tau * w      (5.5)
      d/dt * v = w                                                 (5.6)
PRO:  r_out = r_max / (1 + exp(kappa*(v_T - v)))                   (5.7)
```

The PRO in line (5.7) represents the transformation of the population-average membrane potential v to an outgoing firing rate r_{out} via a sigmoidal function with slope κ, maximum firing rate r_{max} and firing threshold v_T. This formulation contains a function call to the exponential function via `exp(...)`. Using the pre-implemented `sigmoid` function, line (5.7) can be simplified as

`r_out = r_max * sigmoid(kappa*(v-v_T))` (5.8)

Multiple arguments to a function call are comma separated, e.g. the sum along the rows of matrix A can be expressed as: `sum(A, 0)`. Using comparison operators as function arguments, it is also possible to encode events, e.g. a spike, when the membrane potential v exceeds the threshold v_T:

`spike = float(v>v_T)` (5.9)

The variable `spike` takes the decimal value `1.0` in case of a spike event and `0.0` otherwise.

The above examples assumed scalar variables, but vectors and higher-dimensional variables may also be used in PyRates. In particular, indexing is possible via square brackets `[...]` and mostly follows the conventions of *numpy* [251], the *de facto* standard for numerics in Python. Supported indexing methods include single element indexing `a[3]`, slicing `[1:5]`, slicing along multiple axes separated by commas [0:5,3:7], multi-element indexing `a[[3], [4]]`, and slicing via Boolean masks `a[a>5]` for variable `a` of suitable dimensions. A full list of supported mathematical symbols and pre-implemented functions can be found in [157].

5.2.2 Components of a network model

In contrast to most other neural simulation frameworks, PyRates treats network models as network graphs rather than matrices. This works well for densely connected graphs, but gives the most computational benefit for sparse networks. Fig.5.1 gives an overview of the different components that make up a model. A network graph is called a *circuit* and is spanned by *nodes* and *edges*. For a neural population model, one node may correspond to one neural population with the edges encoding coupling between populations. In addition, circuits may be nested arbitrarily within other circuits. Small, self-contained network models can thus easily be reused in larger networks with a clear and intuitive hierarchy. Fig.5.1 A illustrates this feature with a fictional large-scale circuit which comprises four brain areas and connections between them. Each area may consist of a single node or a more complex *sub-circuit*. Edges between areas are depicted as lines. Fig.5.1 B zooms in on one brain area containing a three-node sub-circuit. This local model corresponds to the previously defined Jansen-Rit model [249, 105].

An individual network node consists of *operators*. One operator defines a scope, in which a set of equations and related variables are uniquely defined. It also acts as an isolated computational unit that transforms any number of input variables into one output. Whether an equation belongs to one operator or another decides the order in which equations are evaluated. Equations belonging to the same operator will be evaluated simultaneously, whereas equations in different operators can be evaluated in sequence. As an example, Fig.5.1 C shows the operator structure of a pyramidal cell population in the Jansen-Rit model. There are two rate-to-potential operators (eqs. 5.5 and 5.6), one for inhibitory synapses ($\mathrm{RPO_i}$) and one for excitatory synapses ($\mathrm{RPO_e}$). The two RPOs contain identical equations but different values assigned to the parameters. The subsequent potential-to-rate operator (PRO, eq. (5.7)) sums both synaptic contributions into one membrane potential that is transformed into an outgoing firing rate. In this configuration, the two synaptic contributions are evaluated independently, but possibly in parallel. The equation in the PRO on the other hand will only be evaluated after the synaptic RPOs. The exact order of operators is determined based on the respective input and output variables.

Apart from nodes, edges may also contain coupling operators. An example is shown in Fig.5.1 D. Each edge propagates information from a *source* node to a *target* node. In between, one or more operators can transform the relevant variable, representing coupling dynamics between source and target nodes. This could represent an axon or bundle of axons that propagates firing rates between neural masses. Depending on distance, location or myelination, these axons may behave differently, which is encoded in operators. Note that edges can read any one variable from a source population and can thus be used to represent dramatically different coupling dynamics than those described above.

The described distinction between circuits, nodes, edges and operators is meant to provide an intuitive understanding of a model while giving the user many degrees of freedom in defining custom models.

5.2.3 Model definition language

PyRates provides multiple interfaces to define a network model (see Fig.5.2). *Templates* are building blocks that can be reused at multiple scales. Complex heterogeneous networks will consist of many different templates whereas large homogeneous networks may reuse a few templates many times. For brevity, we will focus on the *YAML*-based template interface which is most suitable for users with little programming expertise. *YAML* is a data serialization standard using a syntax that is reduced to the absolute necessities and focuses on readability (version 1.2, [252]).

All examples in this section are based on the popular Jansen-Rit model [105]. Additionally, we will briefly discuss the implementation of the QIF mean-field model [125] for completeness. The Jansen-Rit model is a three-population neural mass model whose basic structure is illustrated in Fig.5.1. The model is formulated in two state-variables: Average membrane potential v and average firing rate r. Incoming presynaptic firing rates r_{in} are converted to post-synaptic potentials via the RPO. In the Jansen-Rit model, this is a second-order, linear, ordinary differential equation:

$$\text{RPO}: \quad \left(\frac{d}{dt} + \frac{1}{\tau}\right)^2 v(t) = \frac{h}{\tau} r_{in}(t) \tag{5.10}$$

with synaptic gain h and lumped time constant τ. The population-average membrane potential is then transformed into a mean outgoing firing rate r_{out} via the PRO

$$\text{PRO}: \qquad r_{out} = \frac{r_{max}}{1 + e^{-\kappa(v - v_T)}} \tag{5.11}$$

which is an instantaneous logistic function with maximum firing rate r_{max}, maximum steepness κ, and average firing threshold v_T. The equations above define a neural mass with a single synapse type. Multiple sets of these equations are coupled to form a model with three coupled neural populations. For the two interneuron populations, eq. (5.10) represents synaptic excitation. The pyramidal cell population uses this equation twice with two different parametrizations, representing synaptic excitation and inhibition, respectively. This model can be extended to include more populations or to model multiple cortical columns or areas that interact with each other. For such use-cases PyRates allows for the definition of templates that can be reused and adapted on-the-fly. The following defines a *YAML*-template for a rate-to-potential operator that contains eq. (5.10):

```
JansenRitSynapse:  # name of the template
  description: ... # optional descriptive text
  base: OperatorTemplate  #  parent template or Python class to use
  equations:  # unordered list of equations
    - 'd/dt * v = w'
    - 'd/dt * w =  h/tau * r_in - (1./tau)^2 * v - 2./tau*w'
  variables:
    # additional information to define variables in equations
    r_in:
      default: input  # defines variable type
    v:
      default: output
    w:
      description: integration variable  # optional
      default: variable
    tau:
      description: Synaptic time constant
      default: constant
    h:
      default: constant
```

Similar to Python, *YAML* structures information using indentation to improve readability. The *base* attribute may either refer to the Python class that is used to load the template or a parent template. Using the *equations* attribute, an unsorted list of string-based equations should be provided. These equations will be evaluated simultaneously during simulations and need to follow the above defined mathematical syntax. The *variables* attribute gives additional information regarding the variables used within *equations*. The only mandatory attribute of variables is *default* which defines the variable type, data type and initial value. Additional attributes can be defined, e.g. a *description* may help users to understand the template itself or variables in the equations.

For the Jansen-Rit model, it is useful to define sub-templates for excitatory and inhibitory synapses. These share the same equations, but have different values for the constants τ and h which can be set in sub-templates, e.g. (values based on [249]):

```
ExcitatorySynapse:
  base: JansenRitSynapse  # parent template
  variables:
    h:
```

```
    default: 3.25e-3
  tau:
    default: 10e-3
```

Above, the *JansenRitSynapse* template is reused as the *base* template and only the relevant variables are adapted. A single neural mass in the Jansen-Rit model may be implemented as a network node with one or more synapse operators and one operator that transforms the average membrane potential to an average firing rate, i.e. and operator using the eq. (5.7):

```
PyramidalCellPopulation:
  base: NodeTemplate  # Python class for node templates
  operators:
    - ExcitatorySynapse  # output: v
    - InhibitorySynapse  # output: v
    - PotentialToRateOperator  # input: v
```

This node template represents the neural population of pyramidal projection cells as depicted in Fig.5.1C. PyRates internally orders operators based on their input and output variables. This way, complex operator hierarchies can be built without any additional syntax as long as input and output variable names are consistent across all operators. In this example, two synapse operators receive input from other neural masses (or external sources), transforming firing rates r into membrane potentials v (RPO). The synapse operators are independent and on the same hierarchical level. Equations in these two operators can thus be evaluated in parallel. Both synapse operators define the membrane potential V as output. The PRO on the other hand, receives v as input. This is recognised as a dependency and the PRO will be evaluated after the synapse operators have been processed. Note that cyclic operator dependencies are not allowed. If necessary, self-edges can be used to connect variables to each other within one node, to implement cyclic dependencies.

As described earlier, circuits are used in PyRates to represent one or more nodes and their connecting edges. The following circuit template represents the Jansen-Rit model as depicted in Fig.5.1B:

```
JansenRitCircuit:
  base: CircuitTemplate
  nodes:  # list nodes and label them
    EIN: ExcitatoryInterneurons
    IIN: InhibitoryInterneurons
    PC: PyramidalCellPopulation
  edges:  # assign edges between nodes
    # - [<source>, <target>, <template_or_operators>, <values>]
    - [PC/PRO/r_out, IIN/RPO_e/r_in, null, {weight: 33.75}]
    - [PC/PRO/r_out, EIN/RPO_e/r_in, null, {weight: 135.}]
    - [EIN/PRO/r_out, PC/RPO_e/r_in, null, {weight: 108.}]
    - [IIN/PRO/r_out, PC/RPO_i/r_in, null, {weight: 33.75}]
```

The *nodes* attribute specifies which node templates to use and assigns labels to them. These labels are used in *edges* to define source and target, respectively. Each edge is defined by a list (square brackets) of up to four elements: (1) source specifier, (2) target specifier, (3) template (containing operators), and (4) additional named values or attributes. The format for source and target is `<node_label>/<operator>/<variable>`, i.e. an edge establishes a link to a specific variable in a specific operator within a node. Multiple edges can thus interact with different variables on the same node. Note that for brevity the operators were abbreviated here in contrast to the definitions above.

In addition to source and target, it is also possible to include operators inside an edge that allow additional transformations specific to the coupling between the source and target variables. These operators can be defined in a separate edge template that is referred to in the third list entry. In this particular example, the entry is left empty ("null"). The fourth list entry contains named attributes, which are saved on the edge. Two default attributes exist: `weight` scales the output variable of the edge before it is projected to the target and defaults to `1.0`; `delay` determines whether the information passing through the edge is applied instantaneously (i.e. in the next simulation time step) or after a delay (defined in seconds). If a delay is defined, an additional attribute called `spread` can be defined. In this case, PyRates automatically translates the `delay` and `spread` into a set of differential equations representing a gamma-kernel convolution, using the procedure described in [211]. Such a gamma-kernel convolution can be used to model edge delays as continuous distributions, whereas a mere discrete delay provides a constant offset in the signal transmission. While the former allows to model delays in the framework of ordinary differential equations, the latter requires to treat a model as a set of delayed differential equations. By default, no delays are set. Additional attributes may be defined, e.g. to adapt values of operators inside the edge.

In the above example, all edges project the outgoing firing rate r_{out} from one node to the incoming firing rate r_{in} of a different node, re-scaled by an edge-specific weight. Values of the latter are taken from the original paper by Jansen and Rit [105] and lead to a JRC regime of waxing-and-waning alpha oscillations. Jansen and Rit also investigated how more complex components of visual evoked potentials arise from the interaction of two circuits, one representing visual cortex and one prefrontal cortex [105]. In PyRates, circuits can be inserted into other circuits alongside nodes. A template for the two-circuit example from [105] could look like this:

```
DoubleJRCircuit:
  base: CircuitTemplate
  circuits:  # define sub—circuits and their labels
    \acrshort{jrc}1: JansenRitCircuit
    \acrshort{jrc}2: JansenRitCircuit
  edges:  # assign edges between nodes in sub—circuits
    - [JRC1/PC/PRO/r_out, \acrshort{jrc}2/PC/RPO_e/r_in, null, {weight: 10.,
                                                              delay: 0.0}]
    - [JRC2/PC/PRO/r_out, \acrshort{jrc}1/PC/RPO_e/r_in, null, {weight: 10.,
                                                              delay: 0.0}]
```

Circuits are added to the template in the same way as nodes, the only difference being the attribute name *circuits*. Edges are also defined similarly. Source and target keys start with the assigned sub-circuit label, followed by the label of the population within that circuit and so on. For heterogeneous or small networks it makes sense to build the entire circuit hierarchy with templates. For large-scale networks, PyRates also allows the loading of a connectivity matrix from which to build the network. This is realized via the Python interface. Assuming that a JRC template has been set up containing the three nodes (PC, EIN, IIN), the syntax for adding edges from a matrix is:

```
jrc = circuit_template.apply()
jrc.add_edges_from_matrix(source_var='RPO/r_out',
                          target_var='RPO_e_pc/r_in',
                          nodes=['PC', 'EIN', 'IIN'],
                          weight=J)
```

Here, J refers to a 3 x 3 matrix containing the connection strengths. It is also possible to define entire models (or even templates) using mere Python. Similar to YAML templates, templates defined in Python can also be adapted when they are referenced, to perform minor tweaks instead of defining multiple templates for small variations. For more information on alternative ways to set up a network and further examples, we refer the interested reader to the online documentation at pyrates.readthedocs.io.

5.2.4 Implementing the QIF mean-field model

The QIF mean-field model is a single-population model derived from all-to-all coupled QIF neurons [125]. It establishes a mathematically exact correspondence between macroscopic (population level) and microscopic (single cell level) states and equations. The model consists of two coupled differential equations that describe the dynamics of mean membrane potential v and mean firing rate r:

$$\frac{dr}{dt} = \frac{\Delta}{\pi\tau^2} + \frac{2rv}{\tau} \tag{5.12}$$

$$\frac{dv}{dt} = \frac{1}{\tau}\left(v^2 + \overline{\eta} + I(t)\right) + Jr - \tau\pi^2 r^2 \tag{5.13}$$

with intrinsic coupling J and input current $I(t)$. Δ and $\overline{\eta}$ are the width and center of a Lorentzian distribution over the excitability levels within the population (see section 3.1 for a detailed derivation of the mean-field equations). The following operator template implements these equations in PyRates:

```
MontbrioOperator:
  base: OperatorTemplate
  equations:
    - "d/dt * r = Delta/(PI * tau**2) + 2.*r*v/tau"
    - "d/dt * v = (v**2 + eta + inp) / tau + J*r - tau*(PI*r)**2"
  variables:
```

```
    ...
```

Variable definitions are omitted in the above template for brevity. Based on this operator, a PyRates model with a single QIF population can be set up as follows:

```
MontbrioPopulation:
  base: NodeTemplate
  operators:
    - MontbrioOperator

MontbrioNetwork:
  base: CircuitTemplate
  nodes:
    Pop1: MontbrioPopulation
  edges:
```

This template can be used to replicate the simulation results obtained from the QIF mean-field model that are presented in the following sections.

5.3 Pre-implemented methods for neural modeling workflows

5.3.1 Numerical simulations

All frontend interfaces translate a user-defined model into a set of Python objects that we call the *intermediate representation* (IR, middle layer in Fig.5.2). This paragraph will give more details on the IR and explain how a simulation can be started and evaluated based on a previously defined model. A model circuit is represented by the `CircuitIR` class, which builds a network graph representation of the model using the software package *networkx* [253]. The package is commonly used for graph-based data representation in Python and provides many interfaces to manipulate, analyze and visualize graphs. The `CircuitIR` contains additional convenience methods to plot a network graph or access and manipulate its content. The following lines of code load the `JansenRitCircuit` template that was defined in section 5.2.3 and transforms the template into a `CircuitIR` instance:

```
from pyrates.frontend import CircuitTemplate
# read YAML template and convert to Python object
template = CircuitTemplate.from_yaml("path/to/file/JansenRitCircuit")
# transform template object to intermediate representation
circuit_ir = template.apply()
```

The `apply` method also accepts additional arguments to change parameter values while applying the template.

Actual simulations take place in the compute backend (see Fig.5.2). Currently, the user can choose between two backend implementations. The default backend is based on *NumPy* and provides particularly fast simulations on a single CPU and, in combination with the Python distribution provided by Intel, on multiple CPUs. The alternative backend is based on *tensorflow*

2.0 [254], which makes use of dataflow graphs to run parallel computations on CPUs and GPUs. For optimal parallelization of network representations, PyRates can summarize identical sets of (scalar) mathematical operations into more efficient vector operations. Automatic vectorization can be enabled via the `vectorization` keyword argument of the `compile` method:

```
net = circuit_ir.compile(vectorization=True, step_size=0.0001, solver='euler')
```

where `vectorization=False` indicates that the model should be processed as is, while `vectorization=True` reduces identical nodes to one vectorized node. The additional two arguments specify how PyRates should perform the numerical integration of the evolution equations of the model. PyRates provides two choices for the `solver` argument. One choice is shown in the above example, where the model equations are integrated using an explicit Euler algorithm with a time discretization step-size of `step_size = 0.0001` seconds. In general, the unit of `step_size` and the choice of a suitable value depends on time constants defined in the model. As an alternative choice, the numerical integration library of SciPy can be used via `solver='scipy'` [84]. This library provides access to a number of common numerical integration methods, such as Runge-Kutta algorithms with automatic step-size adaptation (see section 2.2).

A simulation can be executed by calling the `run` method, e.g.:

```
results, time = net.run(simulation_time = 10.0,  # in seconds
                        outputs={'v': 'PC/PRO/v'},
                        sampling_step_size = 0.01)  # in seconds
```

This example defines a total *simulation time* of 10 seconds and specifies that only the membrane voltage from *PC* nodes should be returned. Note that variable histories will only be stored for variables defined as output. All other data is overwritten during numerical integration to save memory. Along this line, a sampling step-size can be defined that determines the distance in time between observation points of the output variable histories. Collected data is formatted as a `DataFrame` from the *pandas* package [255], a powerful data structure for serial data that comes with many convenience methods, e.g. for plotting or statistics. To study the dynamics of this JRC model in response to external input, it is possible to manually apply pre-defined inputs via *input* variables. For example, a pre-synaptic input to the excitatory synapse of the pyramidal cells may be applied by modifying the `JansenRitSynapse` as follows:

```
JansenRitSynapse_with_input:
  base: JansenRitSynapse
  equations:
    replace:  # insert u by replacing r_in by a sum
      r_in: (r_in + u)
  variables:
    u:  # adding the new additional variable u
      default: input
```

We reused the previously defined `JansenRitSynapse` template and added the variable `u` as an input variable by replacing occurrences of `r_in` by `(r_in + u)` using string replacement. The previously defined equation

```
d/dt * w = h/tau * r_in - (1./tau)^2 * v - 2./tau*w
```

thus turns into

```
d/dt * w = h/tau * (r_in + u) - (1./tau)^2 * v - 2./tau*w
```

This modification enables the user to apply arbitrary input to the excitatory synapse of the pyramidal cells, using the `inputs` parameter of the `run` method:

```
results, time = net.run(simulation_time = 10.0,
                        outputs={'V': 'PC/PRO/v'},
                        inputs={'PC/RPO_e/u': ext_input})
```

In this example, `ext_input` would be an array defining the input value for each simulation step. This subsumes a working implementation of a single Jansen-Rit model that can be used as a base unit to construct models of cortico-cortical networks. By using the *YAML* template defined in sections 5.2.3 and 5.2.4, all simulations described in the following sections can be replicated.

5.3.2 Available model templates

PyRates provides a number of pre-implemented neural population models which can be directly analyzed via methods such as numerical simulations and parameter studies, without having to go through the model implementation as described in section 5.2.3. All pre-implemented models come in the form of *YAML* templates, meaning that all parts of the defined models, from `OperatorTemplate` to `CircuitTemplate`, are accessible and can be re-used for custom model definitions. For instance, one could use the `CircuitTemplate` of the QIF mean-field model to construct a new `CircuitTemplate` that consists of multiple interconnected QIF populations. Currently, we provide templates for the following neural population models:

- The neural mass model by Jansen and Rit [105],
- The neural mass model by Wilson and Cowan [256],
- The Kuramoto oscillator model [257],
- The QIF mean-field model [125],
- The QIF mean-field models with SD and SFA as described in sections 3.2 and 3.3, respectively.

All of these models can be found at `pyrates.model_templates`. For example, a `CircuitTemplate` instance of a QIF population with SFA (see section 3.3) can be obtained in Python via the following few lines of code:

```
from pyrates.frontend import CircuitTemplate
qif_template = CircuitTemplate.from_yaml(
    "pyrates.model_templates.montbrio.simple_montbrio.QIF_sfa")
```

This template could then be used for numerical simulations as described in the previous section, or for parameter studies as described in the following section.

5.3.3 Exploring model parameter spaces

Exploring the relationship between model dynamics and model parameterization is a key step in any neural network analysis. PyRates offers different solutions in this regard. On the one hand, parameter sweeps can be performed on parallel computation hardware. On the other hand, parameter continuation and bifurcation methods can be used via PyAuto, the PyRates interface to the numerical parameter continuation software Auto-07p [88]. Concrete examples for how to perform both types of parameter studies are available at pyrates.readthedocs.io. For performing parameter sweeps, the function `pyrates.utility.grid_search` takes a single model template along with a specification of the parameter grid to sample sets of parameters from. It then constructs multiple model instances with differing parameters and adds them to the same circuit, but without edges between individual instances. All model instances can thus be computed efficiently in parallel on the same parallel hardware instead of executing them consecutively. How many instances can be simulated on a single piece of hardware depends on the memory capacities and number of parallel compute units. Additionally, PyRates provides an interface for deploying large parameter grid searches across multiple work stations. This allows the splitting of large parameter grids into smaller grids that can be run in parallel on multiple machines. For a tutorial on how to use those functionalities, we refer the interested reader to the use examples that can be found at pyrates.readthedocs.io.

5.3.4 Visualization and data analysis

PyRates features built-in functions for quick data analysis and visualization as well as native support for external libraries due to its commonly used data structures. On the one hand, network graphs are based on *networkx* Graph objects [253]. Hence, the entire toolset of networkx is natively supported, including an interface to the *graphviz* [258] library. Additionally, we provide functions for quick visualization of a network model within PyRates. On the other hand, simulation results are returned as a *pandas.DataFrame* which is a widely adopted structure for tabular data with powerful built-in analysis methods [255]. While this data structure already allows for an intuitive interface to the *seaborn* plotting library by itself, we also provide a number of visualization functions such as time-series plots, heat maps, and polar plots in PyRates. Most of those provide direct interfaces to plotting functions from *seaborn* and *MNE-Python*, the latter being an analysis toolbox for EEG and MEG data [259, 260].

5.4 Results

The aim of this section is to (1) demonstrate that numerical simulations of models implemented in PyRates show the expected results and (2) analyze the computational capabilities and scalability of PyRates on a number of benchmarks. As explained previously, we chose the models proposed by Jansen and Rit and Montbrió and colleagues as exemplary models for these demonstrations. We will replicate the basic model dynamics under extrinsic input as reported in the original publications. To this end, we will compare the relationship between changes in the model parametrization and the model dynamics with the relationship reported in the literature. For this purpose, we will use the grid search functionality of PyRates, allowing evaluation of the model behavior for multiple parametrizations in parallel. Having validated the model implementations in PyRates, we will use the JRC as base model for a number of benchmark simulations. All simulations performed throughout this section use an explicit Euler integration scheme with a simulation step size of 0.1 ms. They have been run on a custom Linux machine with an NVidia Geforce Titan XP GPU with 12GB G-DDR5 graphic memory, a 3.5 GHz Intel Core i7 (4th generation) and 16 GB DDR3 working memory. Note that we provide Python scripts that can be used to replicate all of the simulation results reported below. They are available at `https://github.com/pyrates-neuroscience/PyRates/tree/master/documentation`.

5.4.1 Validation of model implementations

Jansen-Rit circuit

The Jansen-Rit circuit has been shown to be able to produce a variety of steady-state responses [105, 240, 250]. In other words, the JRC has a number of bifurcation parameters that can lead to qualitative changes in the model's state dynamics. In their original publication, Jansen and Rit delivered random synaptic input between 120 and 320 Hz to the projection cells while changing the scaling C of the four internal connectivities, depicted by the parameters J_{xy} in Fig.5.1B [105]. As visualized in Fig. 3 of [105], the model produced (noisy) sinusoidal oscillations in the alpha band for connectivity scalings $C = 128$ and $C = 135$, thus reflecting a major component of the EEG signal in primary visual cortex. For other scalings, it produced either random noise ($C = 68$ and $C = 1350$) or large-amplitude spiking behavior ($C = 270$ and $C = 675$). We chose to replicate this figure with our implementation of the JRC in PyRates. We simulated 2 s of JRC behavior for each internal connectivity scaling $C \in \{68, 128, 135, 270, 675, 1350\}$. All other model parameters were set according to the parameters chosen in [105]. The average membrane potential of the projection cell population (labeled as PC in Fig.5.1B) is depicted in the left panel of Fig. 5.3A for each condition. Results are in line with our expectations, showing random noise for both the highest and the lowest value of C, alpha oscillations for $C = 128$ and $C = 135$, and large-amplitude spiking behavior for the remaining conditions. Furthermore, the membrane potential amplitudes were in the same range as reported in [105] in each condition.

Next to the connectivity scaling, the synaptic time scales τ of the JRC are further bifurcation parameters that have been shown to be useful to tune the model to represent different frequency bands of the brains' EEG signal [240]. As demonstrated by David and Friston [240], varying these time scales between 1 and 60 ms leads to JRC dynamics that are representative of the delta, theta, alpha, beta and gamma frequency bands in the EEG. Due to its practical importance, we chose to replicate this parameter study as well. We systematically varied the excitatory and inhibitory synaptic timescales (τ_e and τ_i) between 1 and 60 ms. For each condition, we adjusted the excitatory and inhibitory synaptic efficacies, such that the product $h\tau$ was held constant. All other parameters were chosen as reported in [240] for the respective simulation. We then simulated the JRC behavior for 1 min and evaluated the maximum frequency of the power spectral density of the pyramidal cells membrane potential fluctuations.

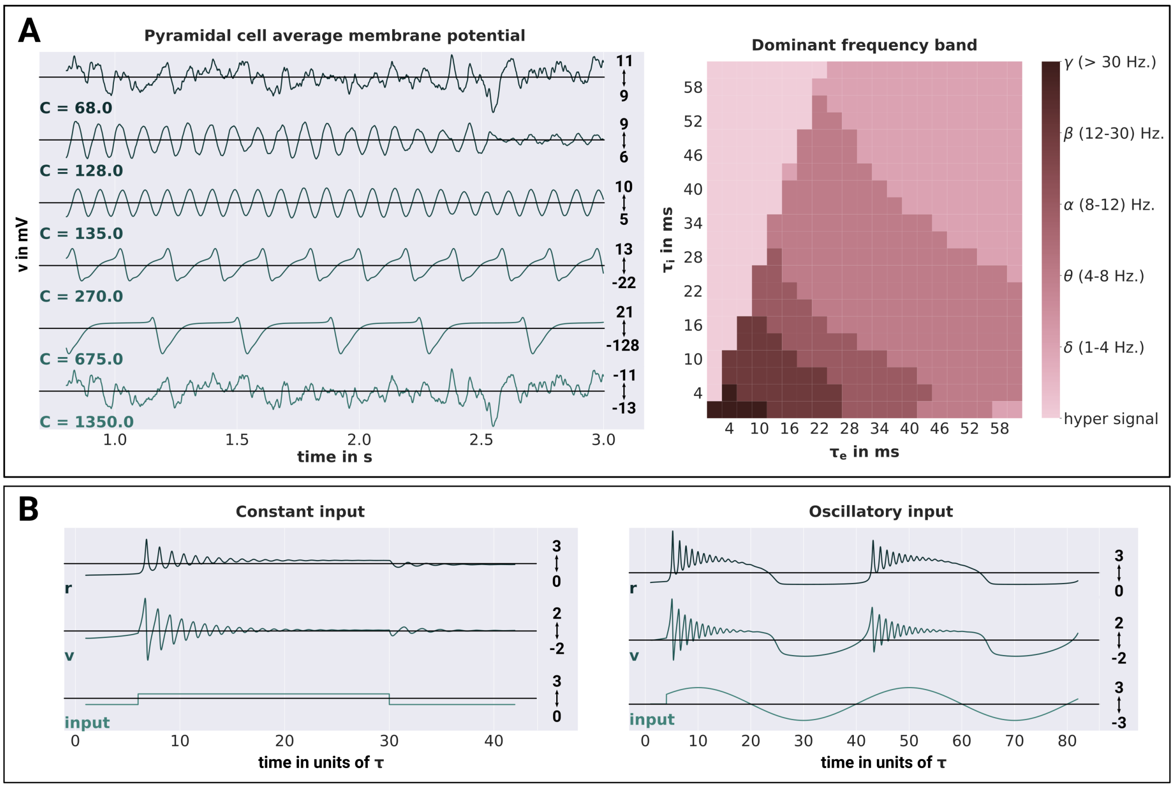

Figure 5.3: Jansen-Rit and QIF mean-field model validations. **A:** Simulation results obtained from a single Jansen-Rit model. On the left hand side, the average membrane potentials of the pyramidal cell population are depicted for different connectivity scalings C. On the right hand side, the dominant oscillation frequency of the pyramidal cell membrane potentials (evaluated over a simulation period of 60 seconds) is depicted for different synaptic time-scales τ_e and τ_i. The frequencies are categorized into the following bands: δ (1-4 Hz), θ (4-8 Hz), α (8-12 Hz), β (12 - 30 Hz), γ ($>$ 30 Hz) and h.s. (hyper signal) for signals not representative of any EEG component. **B:** Simulation results obtained from a single QIF mean-field model. The average membrane potentials v, average firing rates r and input currents are depicted for constant and oscillatory input on the left and right hand side, respectively. Time-dependent variables are reported in units of τ, which was set to $\tau = 1.0$ in accordance with the simulations performed by Montbrió and colleagues. Following the definitions of Montbrió and colleagues, membrane potential and input are reported as unit-less variables.

The results of this procedure are visualized in the right panel of Fig. 5.3A. They are in accordance with the results reported in [240], showing response frequencies that range from the delta (1-4 Hz) to the gamma ($>$ 30 Hz) range, as well as the hyper signal not representative of any EEG signal for too high ratios of $\frac{\tau_i}{\tau_e}$. Together, we are confident that our implementation of the JRC in PyRates accurately resembles the originally proposed model within the investigated dynamical regimes. Note, however, that faster synaptic time-constants or extrinsic input fluctuations should be handled carefully. For such cases, we recommend either reducing the above reported integration step size or choosing a more elaborate numerical solver such as the Runge-Kutta algorithm described in section 2.2 in order to avoid numerical instabilities.

QIF mean-field model

Even though the QIF mean-field model is only a single-population model, it has been shown to have a rich dynamic profile with bi-stable and even chaotic regimes if subject to periodic input [125]. To investigate the response of the model to non-stationary inputs, Montbrió and colleagues initialized the model in a bi-stable dynamic regime and applied (1) constant and (2) sinusoidal extrinsic forcing within a short time-window. In the constant forcing condition they were able to show that the two different stable dynamic regimes of the model (stable focus and stable fixed point) could be switched between via a simple, transient step-function input. In the oscillatory forcing condition, on the other hand, they demonstrated that smooth changes in the extrinsic input were also able to elicit the same phase transitions in the model. This behavior can be observed in Fig. 2 in [125] and we chose to replicate it with our implementation of the QIF mean-field model in PyRates. With all model parameters set to the values reported in [125] for this experiment, we simulated the model's behavior for the constant and periodic forcing conditions. For both conditions, the external forcing strength was chosen as $I = 30$, while the angular frequency of the oscillatory forcing was chosen as $\omega = \frac{\pi}{20}$. Note that in accordance with the model definition of Montbrió and colleagues, time-dependent variables are reported in units of τ (which was set to $\tau = 1$), while all other variables such as v and I are unit-less [125]. As shown in Fig. 5.3B, we were able to replicate the above described model behavior. Constant forcing led to damped oscillatory responses of different frequency and amplitude at both onset and offset of the stimulus, whereas oscillatory forcing led to damped oscillatory responses around the peaks of the sinusoidal stimulus. Again, we take this as strong evidence for the correct representation of the QIF mean-field model by PyRates.

5.4.2 Benchmarks

Neural simulation studies can differ substantially in the size and structure of the networks they investigate, leading to different computational loads. In PyRates, a number of backends and parallelization strategies are available for numerical simulations and their optimal choice may depend on the network architecture. In this section, we describe how simulation durations in PyRates scale as a function of network size and connectivity and how this scaling behavior differs between different backends and parallelization types. For this purpose, we considered parallelization on a single machine vs. parallelized computations on multiple machines and simulations using the NumPy backend (CPU-based, version 1.17.2) vs. simulations using the tensorflow backend (supporting GPU parallelization, version 2.0.0-rc0).

In a first benchmark, we simulated the behavior of different JRC networks using either the NumPy or the tensorflow backend. Each network consisted of $N \in \{2^0, 2^1, 2^2, ..., 2^{11}\}$ randomly coupled JRCs with a coupling density of $p \in \{0.0, 0.25, 0.5, 0.75, 1.00\}$. Here, the latter refers to the relative number of pairwise connections between all pairs of JRCs that were established. Each JRC was parametrized such that it expressed waxing-and-waning alpha oscillations ($C = 135.0$; for all other parameters see [105]). The behavior of these networks was evaluated for a total of 1 s, leading to an overall number of 10^4 simulation steps to be performed in each condition (given a step-size of 0.1 ms). To make the benchmark comparable to realistic simulation scenarios, we applied extrinsic input to each JRC and tracked the average membrane potential of every JRC's projection cell population with a time resolution of 1 ms as output. Thus, the number of input and output operations also scaled with the network size. We assessed the time in seconds needed by PyRates to execute the run method of its backend in each condition, thus excluding the model initiation time. This was done via the Python internal package *time*. To account for random fluctuations due to background processes, we chose to report average simulation durations over $N_R = 10$ repetitions of each condition. To provide an estimate of these fluctuations, we calculated the average variation in the simulation duration d over conditions as $\sigma(d) = \frac{1}{N_c} \sum_{c=1}^{N_c} \frac{\max(d_c) - \min(d_c)}{\langle d_c \rangle}$, with N_c being the number of conditions and $\langle d \rangle$ representing the expectation of d. We found average variations of $\sigma(d) = 0.42s$ and $\sigma(d) = 1.55s$ for the NumPy and tensorflow backend, respectively, which reflects the slightly stronger noise in the simulation duration we found for the tensorflow backend. The average simulation durations over conditions are visualized in Fig.5.4A and B for the NumPy and tensorflow backend, respectively. The average run times of the NumPy and tensorflow backend ranged between 2.5 and 18.1 seconds, and 13.2 and 20.3 seconds, respectively. Thus, the NumPy backend (running merely on CPUs) outperformed the tensorflow backend (running on CPUs and GPUs) on all considered network configurations. However, on large and densely connected networks, the tensorflow and NumPy backend expressed nearly the same simulation duration. This reflects the stronger parallelization capacities of the tensorflow backend, which is visible in its weaker scaling of the simulation duration with network size and coupling density. We expect this trend to lead to an advantage of the tensorflow backend for even larger networks. However, simulations of larger network sizes exceeded the working memory capacities of the machine we ran our benchmarks on. Together, these results demonstrate the effectiveness of PyRates' backends in parallelizing network computations on CPUs and GPUs. While the NumPy backend showed the shortest run times for this benchmark, the tensorflow backend expressed less scaling behavior with the problem size. Thus, the latter might be superior in large-scale neural model simulations performed on a machine with better hardware configurations.

In a second benchmark, we examined the simulation time scaling in parameter sweeps performed via the grid search functionalities of PyRates on a single machine and on a cluster of 3 machines. The hardware specifications of each of those 3 machines were comparable to the ones reported in the beginning of this section. As an exemplary parameter sweep, we explored a parameter set which is prototypically investigated within the fields of connectomics and coupled oscillators, i.e. the connectivity scaling and propagation delay. To this end, we set up a network of 2 JRCs, with bidirectional coupling between their pyramidal cell populations. The bidirectional coupling was parametrized via a homogeneous coupling strength J and a homogeneous propagation delay τ (in seconds). In each benchmark condition a parameter sweep was performed across all combinations of J and τ. Thereby, the parameters were always varied within the ranges of $J \in [0.0, 200.0]$ and $\tau \in [0.0, 0.01]$, and only the number of steps between the limits of those ranges was varied across benchmark conditions. For example, a benchmark condition with 10 steps, would translate into a parameter sweep across all combinations of 10 different values of J and τ and would hence result in $N = 100$ differently parametrized versions of the 2 coupled JRCs. All other parameters of the JRCs were the same as in the first benchmark. In each benchmark condition, 10 numerical simulation were performed for every network parametrization with a simulation time of 1 second. Their average duration in dependence of N is visualized in Fig.5.4C for simulations performed on a single machine and on a 3-machine cluster, either using the NumPy or the tensorflow backend. Note that we also plotted the standard deviations across the 10 repetitions in each condition as error bars. However, those deviations were too small to be visible in Fig.5.4C. Also, these durations were in general larger than the ones reported in the first benchmark, because they include both the time to build the network and the time to perform the actual simulation. Since the network building process is not yet parallelized in PyRates, its duration shows stronger scaling behavior with the network size than the mere simulation times. As can be seen, the single machine outperformed the cluster for $N < 900$. Again, this can be explained by the overhead generated by the distribution of parameter chunks across the different machines and the collection of results from those machines after they finished their simulations. However, with increasing N, the benefit of parallelized simulations on multiple machines started to outweigh those costs, until reaching a maximum speed-up at $N = 10000$, where the 3-machine cluster was approximately three times faster than the single machine. This demonstrates that the maximal speed-up of parameter sweeps performed on compute clusters directly scales with the size of the cluster, which is a beneficial property for investigations of high-dimensional parameter spaces. In addition, Fig.5.4C shows that the speed-ups that resulted from different choices of backends were relatively small in comparison to the speed-ups achieved by running a parameter sweep on a single machine or on a cluster. This reflects the strong influence of the time it takes PyRates to build the network on the overall simulation duration d. Since these network building times do not differ between backends, we found a relatively small difference between NumPy and tensorflow backends in those parameter sweeps. Nonetheless, the tensorflow backend eventually outperformed the NumPy backend on large parameter sweeps ($N \geq 2500$).

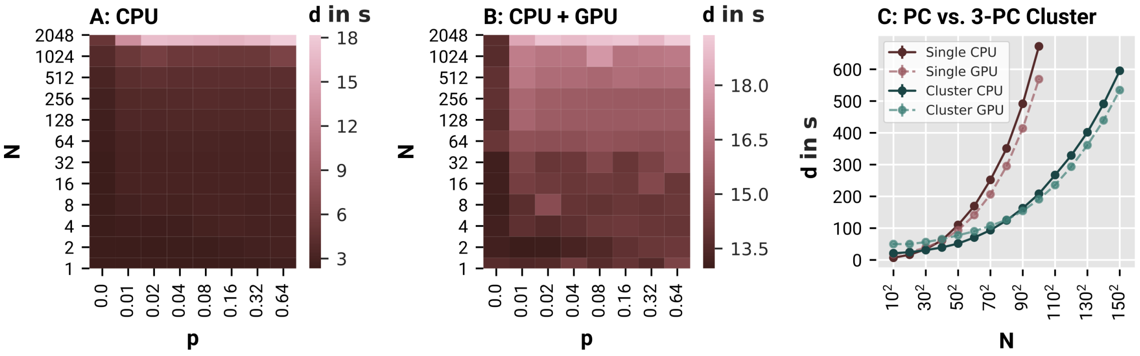

Figure 5.4: PyRates benchmarks. Benchmark results for 1 s simulations run in PyRates with a simulation step-size of 0.1 ms. **A, B:** Average simulation duration d over 10 independent simulations for networks with different numbers of Jansen-Rit circuits (N) and differently dense coupling between the JRCs (p), performed on the NumPy (A: CPU) and tensorflow (B: CPU+GPU) backend, respectively. **C:** Average simulation duration d for parameter sweeps over N different parametrizations of a network of 2 bidirectionally, delay-coupled Jansen-Rit circuits. Averages were again calculated over 10 independent runs of each parameter sweep.

5.5 Discussion

5.5.1 PyRates in the context of existing neural simulation frameworks

Within the domain of neural simulation frameworks, PyRates belongs to the family of graph-based neural simulators. In both its frontend and backend, it represents a neural model as a network of nodes connected by edges. PyRates makes no inherent assumptions concerning the spatial scale of nodes and edges in its networks, thus rendering it feasible for neural networks of any type. Additionally, PyRates allows for merging and hierarchical organization of neural networks by building graphs from sub-graphs. Hence, our tool can also be used to build multi-scale models, *e.g.* a macroscopic network of connected micro-circuits, with each micro-circuit being modeled as a sub-network of specific interacting neural populations.

This being said, PyRates has only been systematically tested on rate-based population models. These differ qualitatively from spiking neuron models in terms of output variable, which is continuous for rate-based models but discrete for spiking neuron models. While it is in principle possible to implement such discrete spiking mechanisms, the compute engine is not optimized for it, since it projects output variables at each time-step to their targets in the network. This means that the projection operation will be performed regardless of whether a spike is produced or not, leading to considerable increases in computation time for large, densely connected, single cell networks. Hence, when dealing with neuroscientific questions that implicate the use of spiking neuron models, we currently recommend to use simulation tools such as Nengo [228], NEST [229], ANNarchy [230], Brian [231], NEURON [232], BioNet [261] or NetPyNE [262]. Such questions may involve problems where specific spike-timings have a non-negligible influence, where dendritic tree architectures are important or, more generally, where the variable of interest loses its meaning when averaged over time or over many neurons.

Of course, all of the above listed tools can be applied in other scenarios as well, even for macroscopic neural network simulations. However, if the variable of interest in a given model can be expressed as an average over many cells and single cell dynamics can be neglected, mean-field approaches such as the neural population models used throughout this article will be considerably faster and thus allow for the investigation of larger networks and parameter spaces. In general, most frameworks that feature generic code generation should allow the implementation of such models. From the above mentioned tools, Brian and ANNarchy belong to that category. Brian is strictly aimed at spike-based simulations and thus not optimized for continuous output variables like firing rates, whereas ANNarchy provides features for spike- and rate-based neural simulations. Nonetheless, it is designed for single-cell network simulations, so most of the templates it provides for neurons or populations are not necessarily applicable to mean-field models. Other simulation frameworks that provide explicit mean-field modeling mechanisms include TVB [263], DCM [227], DiPDE [264] and MIIND [265]. Among these, the latter two focus strongly on so-called population density techniques, which can describe the full voltage probability distribution of a population of neurons, instead of merely the mean. Both DiPDE and MIIND focus on the leaky integrate-and-fire neuron as the underlying model to derive the voltage probability distribution from. The advantage of this technique is the more direct and precise relationship between the single cell activity and the population level as compared to mean-field approaches. However, this advantage is payed for by higher computational demands, since a discretized probability distribution is computed at each simulation step instead of a mere point-estimate (i.e. the mean). TVB and DCM, on the other hand, focus on the same mathematical group of neurodynamic models as currently implemented in PyRates, i.e. neural population models. The focus of TVB lies in the simulation of large-scale brain networks via established, preferably homogeneous, local population models. DCM is explicitly designed to infer parameters of a fixed set of pre-implemented models based on a given measure of brain activity. While being the optimal choice for their respective use-cases, both tools lack functionalities that help when implementing custom models.

We consider the core strengths of PyRates to be its highly generic model definition (comparable to a pure code generation approach) and its two graph-based backends. The former distinguishes PyRates from other simulation frameworks, since it allows the customization of every part of a neural network, as long as a network structure with nodes and edges defined by mathematical operators is maintained. Every single computation that is performed in a PyRates simulation, and every variable that it uses, is defined in the frontend and can be accessed and edited by the user. This allows, for example, the addition of custom synapse types, plasticity mechanisms, complex somatic integration mechanisms, or even axonal cable properties. In addition, edges can access and connect all variables existing pre- or post-node, thus enabling the implementation of projections or plasticity mechanisms that depend on population variables other than firing rates. This generic approach makes PyRates particularly valuable for neuroscientists interested in developing novel neural models or extending existing ones.

A note of caution should be added here. The degrees of freedom we provide for setting up models and simulations in PyRates imply that we do not provide safeguards for questionable model definitions. Except for their syntactical correctness, model equations and their hierarchical relationships will not be questioned further by PyRates. Also, inputs and outputs to the model will be added exactly as defined by the user. In other words, while PyRates does provide a considerable number of convenience functions to quickly set up and simulate large neural networks, it still requires users to be aware of potential numerical issues they could run into, if the model or simulation would not be set up correctly. Typical pitfalls include numerical overflows if variables become to large or small for the chosen data type, simulation step sizes that were chosen too large for the internal timescales of a given model, and random variables that are sampled at each simulation step without taking into account the dependency between sampling frequency and simulation step size. Finally, the choice of the numerical solver must be appropriate for a given model. For example, the SciPy solvers with automatic adaptations of the integration step-size are not designed to handle stochastic or delayed differential equations. PyRates does not prevent the use of those solvers for such models, however. Instead, it will use local interpolation techniques when neural models with constant synaptic delays or random inputs are integrated via adaptive step-size solver algorithms. While this might still provide good results, the order of approximation of the numerical integration procedure is not ensured anymore. We thus recommend to use the Euler algorithm for such cases. Stochastic inputs can then simply be scaled with the square root of the integration step-size to allow for a correct integration of stochastic differential equations.

Regarding PyRates' second core strength, its backends, we have demonstrated its computational power in various scenarios. It provides optimized representations of large neural networks for simulations on CPUs and GPUs. Parallel execution of network simulations are particularly efficient when its nodes and edges are similar in their mathematical operators, since those similarities are exploited by the automatic vectorization mechanisms of PyRates. In turn, this means that the effectiveness of the parallelization scales negatively with the relative amount of heterogeneity or sequentiality of the network. Networks that consist of highly diverse neural units governed by many, hierarchically dependent operators will take considerably longer to simulate than networks with very similar elements and a flat operator hierarchy. Thus, PyRates is particularly suited for simulating large, homogeneous networks or conducting parameter studies on small- to medium sized networks. For the latter, PyRates scales particularly well, since the size of the parameter sweep that can be computed in parallel grows with the size of the compute cluster among which our cluster distribution mechanism can distribute the different parametrizations.

5.5.2 Integrating PyRates into neuroscientific work-flows

Neural population models such as the Jansen-Rit model [105] were originally conceived to understand or predict physical measures of brain activity such as LFPs, EEG/MEG or fMRI. Modern neuroscientific workflows, however, go beyond forward simulations of brain activity. For example, The Virtual Brain [263] allows the use of structural (including diffusion-weighted) MRI scans to specify 3-dimensional structure and connectivity of a network design. Dynamic Causal Modeling [227] on the other hand can make use of measured brain activity to infer model parameters (e.g. connectivity constants) that best fit the given data. Both approaches have in common, that brain network models are adapted to individual subjects based on measured data.

PyRates integrates well with this concept for two reasons. (1) It is designed to provide an easy-to-use interface to construct and adapt network models with more flexibility than comparable tools. (2) Due to its modular software structure, PyRates can easily be extended to interface with existing tools. While the intermediate representation serves as a standard interface, the front- and backends can be exchanged to integrate with other software. For example, PyRates could be extended with a frontend that makes use of structural MRI data via tools provided by TVB. At the same time, the current backend could be extended to generate region-specific models compatible with TVB's node model interface. In that case, PyRates could be used to integrate next-generation neural mass models such as the mean-field models based on Kuramoto oscillators [121], theta neurons [123, 124], or QIF neurons [125, 128, 94, 129] into TVB.

Currently, PyRates already provides a number of useful interfaces to tools that can be used for setting up models, subsequent analyses of simulated timeseries or model optimization. Two of those interfaces come with the graph representations PyRates uses for networks. As mentioned before, every PyRates network can either be translated into a NumPy- or tensorflow-based compute graph. This enables the usage of every NumPy or tensorflow function that could come in handy for setting up a model in PyRates, be it mathematical functions like *sine* or *max*, variable manipulation methods like *reshape* or *squeeze* or higher-level functions like error measurements or learning-rate decays. For the future, we also plan to provide interfaces to *tensorflow's* model training features, which would allow to optimize parameters of neural models via gradient-descent based algorithms [254]. As an experimental feature, model parameter optimization is already possible via genetic algorithms, for which an interface is provided in the utility module of PyRates. They allow the definition of an arbitrary objective function for a given model and optimization of that function via subsequent model parameter updates employing mechanisms such as parameter re-combinations and mutations [266]. As with parameter sweeps, these algorithms can be executed either on a single or on multiple machines.

Since the intermediate representation fully builds on *networkx* graphs, the networkx API can be used to create, modify, analyze or visualize models. This includes inter-operability with explicit graph visualization tools like Graphviz [255] or Cytoscape [267] that contain more elaborate features for visualizing complex biological networks. For the processing, analysis and visualization of simulation results, we provide a number of tools that mostly wrap *MNE-Python* [259, 260] and *seaborn* [268] functions. For extended use of *MNE-Python*, we also provide a wrapper that allows the translation of every output of a PyRates simulation into an *MNE-Python* object. This is particularly useful for forward simulations of EEG/MEG data, since *MNE-Python* comes with an extensive range of methods for the processing, analysis and visualization of such data. Finally, PyRates can also be used in combination with *pygpc*, a generalized polynomial chaos (GPC) toolbox for uncertainty quantification and sensitivity analysis publicly available under `https://github.com/konstantinweise/pygpc` [269]. Via this interface it is possible to define a model plus a set of model parameters, including their respective uncertainties, and estimate how sensitive the model behavior is to changes in these parameters. It is important to note however, that the GPC cannot replace a proper bifurcation analysis and should currently only be used for parameter ranges where no bifurcations or multi-stabilities occur.

In summary, PyRates is readily integrated into complex neuroscientific workflows as a tool for bottom-up neural simulations. It provides interfaces to other Python tools that have been specifically designed to manage other parts of such workflows (e.g. data processing or visualization). More interfaces can easily be implemented due to the modular structure of the framework. This is further aided by the widely used data structures PyRates is built upon, like YAML-based configuration files, networkx graphs or pandas DataFrames. PyRates can thus be included as one independent component of larger neuroscientific workflows that can handle the definition, setup, numerical study and optimization of neural models.

6

Conclusion and Outlook

Complex systems are ubiquitous in nature [3]. Any system consisting of many elements, the interaction of which gives rise to a system function or dynamics that cannot be explained from the isolated elements, is by definition a complex system [2]. Hence, the brain is a complex system as well and its functions and dynamics can be considered phenomena that emerge from the interactions of its many neurons (see section 1.1). In fact, first ideas into this direction have already been formulated in the early 20^{th} century, when Gestalt psychologists argued that human psychological phenomena such as perception and cognition cannot simply be understood as a sum of more basic constituents of human psychology [270]. This implies that certain aspects of human psychological phenomena should be conceived as collective properties of the human mind. Here, we adopted this view of brain function and used methods from complex systems theory for its study. In sections 1.2 and 1.3, we identified the phase transition from asynchronous to synchronous neural activity as a major process in brain function and argued for its study via mathematical models of low-dimensional neural activity manifolds, respectively. Such phase transitions have not only been reported in healthy, task-related brain activity [33, 24, 36], but also in many neurological disorders [37, 38]. The latter case is particularly interesting for studying brain function, how it depends on neural synchronization processes, and how those are supported by the underlying neural structure. Often, neurological disorders are well characterized regarding the behavioral symptoms they cause, the changes in neural dynamics that accompany those symptoms, and the pathology of the underlying neural structure. However, the mechanistic relationship between these different characteristics is usually not known, i.e. how exactly certain structural brain damage causes changes in the neural dynamics and how the latter affects neural function and thus also behavior. Theoretical, neurodynamic modeling studies can provide insight into these mechanistic questions.

Parkinson's disease is a well-studied neurological disorder for which this mechanistic insight is still missing [65]. Structurally, PD is associated with the death of dopaminergic projection neurons that innervate large parts of the BG [271, 272]. The strength of dopaminergic innervation of the BG seems to affect their neural synchronization processes. Oscillations in the beta frequency band as well as beta-gamma PAC increase in strength under parkinsonian conditions [39, 40, 65, 61]. Furthermore, the tendency of BG neurons to fire in synchronous bursts increases [71, 183]. These dynamics are drastically different from the healthy state, where BG activity remains largely asynchronous [70], and they appear to be related to parkinsonian motor symptoms [39, 41, 273, 61]. However, how exactly dopamine depletion affects neural synchronization processes and how these may cause some of the motor symptoms in PD, is a matter of ongoing research [185, 65]. In this thesis, we contributed to the study of neural synchronization processes in general and in the specific case of PD.

Identifying the cause of parkinsonian beta oscillations in the BG has been a major subject of computational and experimental research in neuroscience [66, 184, 185, 65]. It is generally agreed upon that BG dopamine depletion affects the dynamic interactions within the BG and between cortex and BG in a way that synchronization in the beta frequency band is facilitated. Some studies proposed that beta oscillations in PD are generated by the BG and propagated to the cortex [72, 73, 184], whereas others have suggested that they are of cortical origin and the BG merely become more susceptible to these oscillations under dopamine depletion [219, 274]. Regarding potential generators of beta oscillations within the BG , the loop between STN and GPe has most frequently been proposed to play an important role [72, 73, 66, 184]. For example, Terman et al. demonstrated that oscillatory activity can be elicited in a SNN model of the rat STN-GPe network by increasing the input from STR to GPe and weakening the recurrent inhibition within the GPe [189]. A different approach has been chosen by Holgado et al., who searched for conditions for oscillatory behavior in a delay-coupled neural mass model of the STN-GPe system [191]. In this model, each population was expressed by Wilson-Cowan equations of the population dynamics [102]. They found that strong connection strengths between STN and GPe, long synaptic delays relative to the membrane time constants, and strong cortical input relative to the striatal input were necessary for their model to express beta oscillations [191]. Alternative mechanisms of beta oscillation generation in the STN-GPe system that have been proposed by computational models include an increased striatopallidal innervation [190], an increased corticosubthalamic innervation together with a decreased subthalamopallidal innervation [192], or a general decrease in striatal synaptic conductances combined with increased intra-GPe coupling [275]. In summary, these studies contributed to an improved understanding of the relationship between oscillatory activity and synaptic coupling strengths within the STN-GPe system. However, as of today they were not able to identify a mechanism that could explain the emergence of beta oscillations due to parkinsonian changes across different STN-GPe models and experimental data sets [185]. Thus, it is not clear whether the STN-GPe system does indeed generate parkinsonian beta oscillations autonomously, or via the interaction with other BG nuclei, or just resonates with beta oscillatory input from its afferents (such as STR, cortex or thalamus).

One factor contributing to these inconsistent results is the different level of biological detail across computational models. Different results have been reported regarding the mechanisms of beta oscillations in STN-GPe models that use SNNs vs. mean-field models, for example. Both of these approaches suffer from limitations regarding the analysis of neural synchronization processes. If a beta rhythm emerges via spike synchronization mechanisms inside the STN or GPe population (such as in [127]), classic neural mass models might fail to detect it, since they cannot describe the amount of synchronization among the neurons inside a population (see

[83] or our argumentation in section 3.1). Similarly, these neural mass models cannot account for the de-phasing between spiking neurons due to mutual inhibition. On the other hand, it is difficult to study collective synchronization phenomena in SNNs due to the basic property of these phenomena, that they require large numbers of interacting units [2, 4]. Computational studies of SNNs might thus fail to capture the true patterns of neural synchronization in a network, due to insufficient network sizes. As outlined in sections 1.3 and 3.1, exact mean-field models that capture the macroscopic dynamics of corresponding SNNs do not suffer from these problems. The mean-field model presented in [125] is such an exact macroscopic description. It has been derived from networks of globally coupled QIF neurons in the thermodynamic limit and can be directly related to the average phase synchronization in the network (see section 3.1 for the mathematical derivation). Therefore, it can account for both spike synchronization mechanisms and collective synchronization phenomena.

In chapter 4, we applied the QIF mean-field model to the study of parkinsonian oscillation generation in the BG. We hypothesized that an increased recurrent coupling in GPe microcircuits contributes to the generation of parkinsonian oscillations. This hypothesis was based on two studies: One recent study in mice that showed that optogenetic inhibition of the GPe, but not of STN or cortex, attenuated parkinsonian beta oscillations [69]. And another study that found the recurrent inhibitory coupling between GPe neurons to be enhanced under dopamine depletion [199]. To test our hypothesis, we constructed a QIF network of the two main cell types that have been identified in the GPe: prototypical and arkypallidal cells [68]. Applying bifurcation analysis to an exact mean-field model of this QIF network, we found that a strengthening of GPe-to-GPe synapses could indeed induce a phase transition from an asynchronous to a synchronous regime. Since the resulting oscillations were in a gamma frequency range, they could not explain the emergence of parkinsonian beta oscillations though. However, the GPe model expressed characteristic patterns of beta-gamma PAC and PPC when subject to periodic input in the beta frequency range. The strength of both PAC and PPC could also increase due to dopamine depletion, i.e. due to stronger recurrent coupling in the GPe. Thus, we found that the GPe might become more susceptible to periodic input under dopamine depletion and generate gamma oscillations, coupled to the phase of a beta input. Due to its strong interconnectedness with other BG structures, the GPe is well positioned to propagate such oscillations throughout the entire BG, as well as to thalamus and cortex [200].

As argued in section 4.4, our GPe model provides a mathematical basis for the study of parkinsonian beta oscillations in extended BG networks such as the STN-GPe-STR system. Due to the mathematical nature of the QIF mean-field model, it is particularly suited to study neural synchronization processes and might thus overcome issues of previous BG modeling studies [185]. The STN-GPe-STR system includes various neuron types with characteristic dynamic properties that could affect neural synchronization processes and might be affected by dopamine depletion. Those include the strong gap junction coupling reported at striatal interneurons [276, 277], the different spike-frequency adaptation patterns of projection neurons in STR and STN [278, 279], and the synaptic depression at synapses between STN and GPe [135, 136]. To account for these properties, the QIF mean-field theory has to be extended for the respective neurodynamic mechanisms. We contributed to these issues by extending the QIF mean-field theory to QIF networks that include SFA (see section 3.3) and synaptic

STP mechanisms (see section 3.2 and 3.4). Importantly, we found that both SFA and synaptic STP can induce states of collective, synchronized bursting in QIF networks. Moreover, we identified bi-stable regimes in such networks where bursting and steady-state equilibria co-existed. Interestingly, increased bursting dynamics have also been reported in the BG under dopamine depletion [71, 219, 143, 280]. Moreover, bi-stable bursting regimes could be of interest for parkinsonian oscillations, since the latter typically appear in transient bursts and might thus reflect switching between an asynchronous, healthy state and a co-existing synchronous, pathological state with increased bursting behavior [143, 273]. Therefore, we propose that the incorporation of the extended QIF mean-field models introduced in chapter 3 into BG network models could account for the bursting characteristics of both neural firing activity [143] and macroscopic beta oscillations [273] in PD. Additionally, the exact mean-field description that has recently been derived for QIF networks with gap junctions may be incorporated to account for their influence on neural synchronization processes in STR [128, 129]. By following the model analysis pipeline outlined in chapter 4, we expect that such exact mean-field models of the STN-GPe-STR system will provide novel, improved insight into the neural synchronization mechanisms that govern BG dynamics and how they are altered in PD .

In summary, we have gained mechanistic insight into the phase transitions that govern the dynamic interactions between prototypical and arkypallidal neurons and how they relate to parkinsonian oscillation generation. This was achieved via a GPe model that can provide a basis for a new generation of BG models based on exact mean-field models of SNNs. We have contributed to the development of these models by extending the required mean-field theory to QIF networks subject to short-term plasticity mechanisms. Finally, we have developed an open-source software that provides the means of constructing and analyzing such novel BG models. Of course, both the mathematical models and the software developed in this thesis may be applied to brain systems other than the BG as well. Thus, they serve towards developing a complex systems theory of brain function centered around phase transitions between asynchronous and synchronous neural dynamics. To this end, we have focused on the question of how such phase transitions depend on the underlying neural network characteristics, be they the synaptic coupling strengths in GPe networks or the rate of STP in a single QIF population. It remains an open question, how exactly brain function, i.e. neural information processing capacities, depend on such phase transitions. This is a central question to answer on the road towards a complex systems theory of brain function.

References

[1] Mark C. Cross and Pierre C. Hohenberg. “Pattern formation outside of equilibrium”. In: *Reviews of Modern Physics* 65.3 (July 1993), pp. 851–1112. DOI: `10.1103/RevModPhys.65.851`.

[2] Kim Christensen and Nicholas R. Moloney. *Complexity and Criticality*. World Scientific Publishing Company, Oct. 2005. ISBN: 978-1-911298-33-5.

[3] Axel Hutt. “Synergetics: An Introduction”. In: *Synergetics*. Ed. by Axel Hutt and Hermann Haken. Encyclopedia of Complexity and Systems Science Series. New York, NY: Springer US, 2020, pp. 1–3. ISBN: 978-1-07-160421-2. DOI: `10.1007/978-1-0716-0421-2_534`.

[4] Dante R. Chialvo. “Emergent complex neural dynamics”. In: *Nature Physics* 6.10 (Oct. 2010), pp. 744–750. ISSN: 1745-2481. DOI: `10.1038/nphys1803`.

[5] Henrik Jeldtoft Jensen and Professor Henrik Jeldtoft Jensen. *Self-Organized Criticality: Emergent Complex Behavior in Physical and Biological Systems*. Cambridge University Press, Jan. 1998. ISBN: 978-0-521-48371-1.

[6] Dana H. Ballard. *Brain Computation as Hierarchical Abstraction*. MIT Press, Feb. 2015. ISBN: 978-0-262-02861-5.

[7] Gustavo Deco, Viktor K. Jirsa, and Anthony R. McIntosh. “Emerging concepts for the dynamical organization of resting-state activity in the brain”. In: *Nature Reviews Neuroscience* 12.1 (Jan. 2011), pp. 43–56. ISSN: 1471-0048. DOI: `10.1038/nrn2961`.

[8] Gustavo Deco and Morten L. Kringelbach. “Turbulent-like Dynamics in the Human Brain”. In: *Cell Reports* 33.10 (Dec. 2020), p. 108471. ISSN: 2211-1247. DOI: `10.1016/j.celrep.2020.108471`.

[9] Krishna Pusuluri, Huiwen Ju, and Andrey Shilnikov. “Chaotic Dynamics in Neural Systems”. In: *Synergetics*. Ed. by Axel Hutt and Hermann Haken. Encyclopedia of Complexity and Systems Science Series. New York, NY: Springer US, 2020, pp. 197–209. ISBN: 978-1-07-160421-2. DOI: `10.1007/978-1-0716-0421-2_738`.

[10] Eric Kandel, James Schwartz, and Thomas Jessell. *Principles of Neural Science*. McGraw-Hill Medical, Jan. 5, 2000. ISBN: 0-8385-7701-6.

[11] Leland H. Hartwell et al. “From molecular to modular cell biology”. In: *Nature* 402.6761 (Dec. 1999), pp. C47–C52. ISSN: 1476-4687. DOI: `10.1038/35011540`.

[12] David Sussillo. “Neural circuits as computational dynamical systems”. In: *Current Opinion in Neurobiology.* Theoretical and computational neuroscience 25 (Apr. 2014), pp. 156–163. ISSN: 0959-4388. DOI: `10.1016/j.conb.2014.01.008`.

[13] Laura E. Suárez et al. “Linking Structure and Function in Macroscale Brain Networks”. In: *Trends in Cognitive Sciences* 24.4 (Apr. 2020), pp. 302–315. ISSN: 1364-6613. DOI: `10.1016/j.tics.2020.01.008`.

[14] Morten L. Kringelbach and Gustavo Deco. “Brain States and Transitions: Insights from Computational Neuroscience”. In: *Cell Reports* 32.10 (Sept. 2020), p. 108128. ISSN: 2211-1247. DOI: `10.1016/j.celrep.2020.108128`.

[15] John J. Hopfield. “Neural networks and physical systems with emergent collective computational abilities”. In: *Proceedings of the National Academy of Sciences* 79.8 (Apr. 1982), pp. 2554–2558. ISSN: 0027-8424, 1091-6490. DOI: `10.1073/pnas.79.8.2554`.

[16] Yong Tang et al. “Total regional and global number of synapses in the human brain neocortex”. In: *Synapse* 41.3 (2001), pp. 258–273. ISSN: 1098-2396. DOI: `https://doi.org/10.1002/syn.1083`.

[17] Frederico A. C. Azevedo et al. “Equal numbers of neuronal and nonneuronal cells make the human brain an isometrically scaled-up primate brain”. In: *Journal of Comparative Neurology* 513.5 (2009), pp. 532–541. ISSN: 1096-9861. DOI: `https://doi.org/10.1002/cne.21974`.

[18] Eugene M. Izhikevich. “Neural excitability, spiking and bursting”. In: *International Journal of Bifurcation and Chaos* 10.06 (June 2000), pp. 1171–1266. ISSN: 0218-1274. DOI: `10.1142/S0218127400000840`.

[19] Gustavo Deco et al. “The dynamic brain: From spiking neurons to neural masses and cortical fields”. In: *PLOS Computational Biology* 4.8 (Aug. 2008), e1000092. DOI: `10.1371/journal.pcbi.1000092`.

[20] Larry F. Abbott and Thomas B. Kepler. “Model neurons: From Hodgkin-Huxley to hopfield”. In: *Statistical Mechanics of Neural Networks.* Ed. by Luis Garrido. Lecture Notes in Physics. Berlin, Heidelberg: Springer, 1990, pp. 5–18. ISBN: 978-3-540-46808-0. DOI: `10.1007/3540532676_37`.

[21] Luis Garrido and Miguel Rubi. “Introduction On the statistical-mechanical formulation of neural networks”. In: *Statistical Mechanics of Neural Networks.* Ed. by Luis Garrido. Lecture Notes in Physics. Berlin, Heidelberg: Springer, 1990, pp. 1–3. ISBN: 978-3-540-46808-0. DOI: `10.1007/3540532676_36`.

[22] Hermann Haken. “Synergetics: Basic Concepts”. In: *Synergetics.* Ed. by Axel Hutt and Hermann Haken. Encyclopedia of Complexity and Systems Science Series. New York, NY: Springer US, 2020, pp. 5–30. ISBN: 978-1-07-160421-2. DOI: `10.1007/978-1-0716-0421-2_533`.

[23] Emilio Salinas and Terrence J. Sejnowski. “Correlated neuronal activity and the flow of neural information”. In: *Nature Reviews Neuroscience* 2.8 (Aug. 2001), pp. 539–550. ISSN: 1471-0048. DOI: `10.1038/35086012`.

[24] Gyorgy Buzsaki. *Rhythms of the Brain*. Oxford University Press, Aug. 2006. ISBN: 978-0-19-804125-2.

[25] Andreas Daffertshofer and Bastian Pietras. “Phase Synchronization in Neural Systems”. In: *Synergetics*. Ed. by Axel Hutt and Hermann Haken. Encyclopedia of Complexity and Systems Science Series. New York, NY: Springer US, 2020, pp. 221–233. ISBN: 978-1-07-160421-2. DOI: `10.1007/978-1-0716-0421-2_693`.

[26] Andreas K. Engel and Wolf Singer. “Temporal binding and the neural correlates of sensory awareness”. In: *Trends in Cognitive Sciences* 5.1 (Jan. 2001), pp. 16–25. ISSN: 1364-6613. DOI: `10.1016/S1364-6613(00)01568-0`.

[27] Pascal Fries. “Rhythms for Cognition: Communication through Coherence”. In: *Neuron* 88.1 (Oct. 2015), pp. 220–235. ISSN: 0896-6273. DOI: `10.1016/j.neuron.2015.09.034`.

[28] Gerald Hahn et al. “Portraits of communication in neuronal networks”. In: *Nature Reviews Neuroscience* 20.2 (Feb. 2019), p. 117. ISSN: 1471-0048. DOI: `10.1038/s41583-018-0094-0`.

[29] Holger Finger et al. “Probing neural networks for dynamic switches of communication pathways”. In: *PLOS Computational Biology* 15.12 (Dec. 2019), e1007551. ISSN: 1553-7358. DOI: `10.1371/journal.pcbi.1007551`.

[30] Frédéric Roux and Peter J. Uhlhaas. “Working memory and neural oscillations: alpha–gamma versus theta–gamma codes for distinct WM information?” In: *Trends in Cognitive Sciences* 18.1 (Jan. 2014), pp. 16–25. ISSN: 1364-6613. DOI: `10.1016/j.tics.2013.10.010`.

[31] Andreas K Engel and Pascal Fries. “Beta-band oscillations—signalling the status quo?” In: *Current Opinion in Neurobiology*. Cognitive neuroscience 20.2 (Apr. 2010), pp. 156–165. ISSN: 0959-4388. DOI: `10.1016/j.conb.2010.02.015`.

[32] Simon Hanslmayr et al. “The role of alpha oscillations in temporal attention”. In: *Brain Research Reviews* 67.1 (June 2011), pp. 331–343. ISSN: 0165-0173. DOI: `10.1016/j.brainresrev.2011.04.002`.

[33] György Buzsáki and Andreas Draguhn. “Neuronal Oscillations in Cortical Networks”. In: *Science* 304.5679 (June 2004), pp. 1926–1929. ISSN: 0036-8075, 1095-9203. DOI: `10.1126/science.1099745`.

[34] Satu Palva and J. Matias Palva. “Discovering oscillatory interaction networks with M/EEG: challenges and breakthroughs”. In: *Trends in Cognitive Sciences* 16.4 (Apr. 2012), pp. 219–230. ISSN: 1364-6613. DOI: `10.1016/j.tics.2012.02.004`.

[35] Anne-Lise Giraud and David Poeppel. “Cortical oscillations and speech processing: emerging computational principles and operations”. In: *Nature Neuroscience* 15.4 (Apr. 2012), pp. 511–517. ISSN: 1097-6256, 1546-1726.

[36] Harris S. Kaplan et al. “Nested Neuronal Dynamics Orchestrate a Behavioral Hierarchy across Timescales”. In: *Neuron* 105.3 (Feb. 2020), 562–576.e9. ISSN: 0896-6273. DOI: `10.1016/j.neuron.2019.10.037`.

[37] Alfons Schnitzler and Joachim Gross. “Normal and pathological oscillatory communication in the brain”. In: *Nature Reviews Neuroscience* 6.4 (Apr. 2005), pp. 285–296. ISSN: 1471-0048. DOI: `10.1038/nrn1650`.

[38] Erol Başar. “Brain oscillations in neuropsychiatric disease”. In: *Dialogues in Clinical Neuroscience* 15.3 (Sept. 2013), pp. 291–300. ISSN: 1294-8322.

[39] Peter Brown. “Oscillatory nature of human basal ganglia activity: Relationship to the pathophysiology of Parkinson’s disease”. In: *Movement Disorders* 18.4 (Apr. 2003), pp. 357–363. ISSN: 1531-8257. DOI: `10.1002/mds.10358`.

[40] Constance Hammond, Hagai Bergman, and Peter Brown. “Pathological synchronization in Parkinson’s disease: networks, models and treatments”. In: *Trends in neurosciences* 30.7 (July 2007), pp. 357–364. ISSN: 0166-2236. DOI: `10.1016/j.tins.2007.05.004`.

[41] Ashwini Oswal, Peter Brown, and Vladimir Litvak. “Synchronized neural oscillations and the pathophysiology of Parkinson’s disease”. In: *Current Opinion in Neurology* 26.6 (Dec. 2013), pp. 662–670. ISSN: 1350-7540. DOI: `10.1097/WCO.0000000000000034`.

[42] Yoshiki Kuramoto. *Chemical Oscillations, Waves, and Turbulence.* Courier Corporation, Jan. 2003. ISBN: 978-0-486-42881-9.

[43] Steven H. Strogatz. *Nonlinear Dynamics and Chaos with Student Solutions Manual: With Applications to Physics, Biology, Chemistry, and Engineering, Second Edition.* CRC Press, Sept. 2018. ISBN: 978-0-429-68015-1.

[44] Mark M. Churchland et al. “Neural population dynamics during reaching”. In: *Nature* 487.7405 (July 2012), pp. 51–56. ISSN: 1476-4687. DOI: `10.1038/nature11129`.

[45] Juan A. Gallego et al. “Neural Manifolds for the Control of Movement”. In: *Neuron* 94.5 (June 2017), pp. 978–984. ISSN: 0896-6273. DOI: `10.1016/j.neuron.2017.05.025`.

[46] Juan A. Gallego et al. “Cortical population activity within a preserved neural manifold underlies multiple motor behaviors”. In: *Nature Communications* 9.1 (Oct. 2018), p. 4233. ISSN: 2041-1723. DOI: `10.1038/s41467-018-06560-z`.

[47] João D. Semedo et al. “Cortical Areas Interact through a Communication Subspace”. In: *Neuron* 102.1 (Apr. 2019), 249–259.e4. ISSN: 0896-6273. DOI: `10.1016/j.neuron.2019.01.026`.

[48] Juan A. Gallego et al. “Long-term stability of cortical population dynamics underlying consistent behavior”. In: *Nature Neuroscience* 23.2 (Feb. 2020), pp. 260–270. ISSN: 1546-1726. DOI: `10.1038/s41593-019-0555-4`.

[49] Erol Başar. *Chaos in Brain Function: Containing Original Chapters by E. Basar and T. H. Bullock and Topical Articles Reprinted from the Springer Series in Brain Dynamics.* Springer Science & Business Media, Dec. 2012. ISBN: 978-3-642-75545-3.

[50] Andreas K. Engel, Pascal Fries, and Wolf Singer. “Dynamic predictions: Oscillations and synchrony in top–down processing”. In: *Nature Reviews Neuroscience* 2.10 (Oct. 2001), pp. 704–716. ISSN: 1471-0048. DOI: `10.1038/35094565`.

[51] Thomas R. Knösche et al. “Perception of phrase structure in music”. In: *Human Brain Mapping* 24.4 (2005), pp. 259–273. ISSN: 1097-0193. DOI: `10.1002/hbm.20088`.

[52] Teija Kujala, Mari Tervaniemi, and Erich Schröger. "The mismatch negativity in cognitive and clinical neuroscience: Theoretical and methodological considerations". In: *Biological Psychology* 74.1 (Jan. 2007), pp. 1–19. ISSN: 0301-0511. DOI: `10.1016/j.biopsycho.2006.06.001`.

[53] Viktor K. Jirsa et al. "On the nature of seizure dynamics". In: *Brain* 137.8 (Aug. 2014), pp. 2210–2230. ISSN: 0006-8950. DOI: `10.1093/brain/awu133`.

[54] Patrick T. Sadtler et al. "Neural constraints on learning". In: *Nature* 512.7515 (Aug. 2014), pp. 423–426. ISSN: 1476-4687. DOI: `10.1038/nature13665`.

[55] John D. Murray et al. "Stable population coding for working memory coexists with heterogeneous neural dynamics in prefrontal cortex". In: *Proceedings of the National Academy of Sciences* 114.2 (Jan. 2017), pp. 394–399. ISSN: 0027-8424, 1091-6490. DOI: `10.1073/pnas.1619449114`.

[56] Alain Destexhe and Terrence J. Sejnowski. "The Wilson–Cowan model, 36 years later". In: *Biological Cybernetics* 101.1 (July 2009), pp. 1–2. ISSN: 1432-0770. DOI: `10.1007/s00422-009-0328-3`.

[57] Christian Bick et al. "Understanding the dynamics of biological and neural oscillator networks through exact mean-field reductions: a review". In: *The Journal of Mathematical Neuroscience* 10.1 (May 2020), p. 9. ISSN: 2190-8567. DOI: `10.1186/s13408-020-00086-9`.

[58] Hagai Bergman and Günther Deuschl. "Pathophysiology of Parkinson's disease: From clinical neurology to basic neuroscience and back". In: *Movement Disorders* 17.S3 (Mar. 2002), S28–S40. ISSN: 1531-8257. DOI: `10.1002/mds.10140`.

[59] Andrew I. Yang et al. "Beta-Coupled High-Frequency Activity and Beta-Locked Neuronal Spiking in the Subthalamic Nucleus of Parkinson's Disease". In: *Journal of Neuroscience* 34.38 (Sept. 2014), pp. 12816–12827. ISSN: 0270-6474, 1529-2401. DOI: `10.1523/JNEUROSCI.1895-14.2014`.

[60] Allison T. Connolly et al. "Modulations in Oscillatory Frequency and Coupling in Globus Pallidus with Increasing Parkinsonian Severity". In: *Journal of Neuroscience* 35.15 (Apr. 2015), pp. 6231–6240. ISSN: 0270-6474, 1529-2401. DOI: `10.1523/JNEUROSCI.4137-14.2015`.

[61] Ruxue Gong et al. "Spatiotemporal features of β-γ phase-amplitude coupling in Parkinson's disease derived from scalp EEG". In: *Brain* 144.2 (Feb. 2021), pp. 487–503. ISSN: 0006-8950. DOI: `10.1093/brain/awaa400`.

[62] Yoland Smith and Rosa Villalba. "Striatal and extrastriatal dopamine in the basal ganglia: An overview of its anatomical organization in normal and Parkinsonian brains". In: *Movement Disorders* 23.S3 (Jan. 2008), S534–S547. ISSN: 1531-8257. DOI: `10.1002/mds.22027`.

[63] Jose A. Obeso et al. "The basal ganglia in Parkinson's disease: Current concepts and unexplained observations". In: *Annals of Neurology* 64.S2 (Dec. 2008), S30–S46. ISSN: 1531-8249. DOI: `10.1002/ana.21481`.

[64] Arun Singh. “Oscillatory activity in the cortico-basal ganglia-thalamic neural circuits in Parkinson’s disease”. In: *European Journal of Neuroscience* 48.8 (2018), pp. 2869–2878. ISSN: 1460-9568. DOI: `10.1111/ejn.13853`.

[65] Thomas Wichmann. “Changing views of the pathophysiology of Parkinsonism”. In: *Movement Disorders* 34.8 (2019), pp. 1130–1143. ISSN: 1531-8257. DOI: `10.1002/mds.27741`.

[66] Alex Pavlides, S. John Hogan, and Rafal Bogacz. “Computational models describing possible mechanisms for generation of excessive beta oscillations in Parkinson’s disease”. In: *PLoS Computational Biology* 11.12 (Dec. 2015). ISSN: 1553-734X. DOI: `10.1371/journal.pcbi.1004609`. URL: `https://www.ncbi.nlm.nih.gov/pmc/articles/PMC4684204/`.

[67] Victoria L. Corbit et al. “Pallidostriatal Projections Promote β Oscillations in a Dopamine-Depleted Biophysical Network Model”. In: *Journal of Neuroscience* 36.20 (May 2016), pp. 5556–5571. ISSN: 0270-6474, 1529-2401. DOI: `10.1523/JNEUROSCI.0339-16.2016`.

[68] Daniel J. Hegeman et al. “The external globus pallidus: progress and perspectives”. In: *European Journal of Neuroscience* 43.10 (May 2016), pp. 1239–1265. ISSN: 0953-816X. DOI: `10.1111/ejn.13196`.

[69] Brice de la Crompe et al. “The globus pallidus orchestrates abnormal network dynamics in a model of Parkinsonism”. In: *Nature Communications* 11.1 (Mar. 2020), p. 1570. ISSN: 2041-1723. DOI: `10.1038/s41467-020-15352-3`.

[70] Charles J. Wilson. “Active decorrelation in the basal ganglia”. In: *Neuroscience* 250 (Oct. 2013), pp. 467–482. ISSN: 0306-4522. DOI: `10.1016/j.neuroscience.2013.07.032`.

[71] Thomas Wichmann and Jesus Soares. “Neuronal firing before and after burst discharges in the monkey basal ganglia is predictably patterned in the normal state and altered in Parkinsonism”. In: *Journal of Neurophysiology* 95.4 (Apr. 2006), pp. 2120–2133. ISSN: 0022-3077. DOI: `10.1152/jn.01013.2005`.

[72] Nicolas Mallet et al. “Parkinsonian beta oscillations in the external globus pallidus and their relationship with subthalamic nucleus activity”. In: *Journal of Neuroscience* 28.52 (Dec. 2008), pp. 14245–14258. ISSN: 0270-6474, 1529-2401. DOI: `10.1523/JNEUROSCI.4199-08.2008`.

[73] Yoshihisa Tachibana et al. “Subthalamo-pallidal interactions underlying parkinsonian neuronal oscillations in the primate basal ganglia”. In: *European Journal of Neuroscience* 34.9 (2011), pp. 1470–1484. ISSN: 1460-9568. DOI: `10.1111/j.1460-9568.2011.07865.x`.

[74] Peter Dayan and Larry F. Abbott. *Theoretical Neuroscience: Computational and Mathematical Modeling of Neural Systems*. MIT Press, 2001. ISBN: 978-0-262-54185-5.

[75] Warren S. McCulloch and Walter Pitts. “A logical calculus of the ideas immanent in nervous activity”. In: *The bulletin of mathematical biophysics* 5.4 (Dec. 1943). ISSN: 1522-9602. DOI: `10.1007/BF02478259`.

[76] Mantas Lukoševičius and Herbert Jaeger. “Reservoir computing approaches to recurrent neural network training”. In: *Computer Science Review* 3.3 (Aug. 2009), pp. 127–149. ISSN: 1574-0137. DOI: `10.1016/j.cosrev.2009.03.005`.

[77] Alan L. Hodgkin and Andrew F. Huxley. “A quantitative description of membrane current and its application to conduction and excitation in nerve”. In: *The Journal of Physiology* 117.4 (1952), pp. 500–544. ISSN: 1469-7793. DOI: `https://doi.org/10.1113/jphysiol.1952.sp004764`.

[78] Alan L. Hodgkin and Richard D. Keynes. “Active transport of cations in giant axons from Sepia and Loligo”. In: *The Journal of Physiology* 128.1 (1955), pp. 28–60. ISSN: 1469-7793. DOI: `https://doi.org/10.1113/jphysiol.1955.sp005290`.

[79] Alan L. Hodgkin and Richard D. Keynes. “The potassium permeability of a giant nerve fibre”. In: *The Journal of Physiology* 128.1 (1955), pp. 61–88. ISSN: 1469-7793. DOI: `https://doi.org/10.1113/jphysiol.1955.sp005291`.

[80] Jo S. Coombs, John C. Eccles, and Paul Fatt. “Excitatory synaptic action in motoneurones”. In: *The Journal of Physiology* 130.2 (1955), pp. 374–395. ISSN: 1469-7793. DOI: `https://doi.org/10.1113/jphysiol.1955.sp005413`.

[81] Jo S. Coombs, John C. Eccles, and Paul Fatt. “The specific ionic conductances and the ionic movements across the motoneuronal membrane that produce the inhibitory post-synaptic potential”. In: *The Journal of Physiology* 130.2 (1955), pp. 326–373. ISSN: 1469-7793.

[82] Smeal Roy M., Ermentrout G. Bard, and White John A. “Phase-response curves and synchronized neural networks”. In: *Philosophical Transactions of the Royal Society B: Biological Sciences* 365.1551 (Aug. 2010), pp. 2407–2422. DOI: `10.1098/rstb.2009.0292`.

[83] Federico Devalle, Alex Roxin, and Ernest Montbrió. “Firing rate equations require a spike synchrony mechanism to correctly describe fast oscillations in inhibitory networks”. In: *PLOS Computational Biology* 13.12 (Dec. 2017), e1005881. ISSN: 1553-7358. DOI: `10.1371/journal.pcbi.1005881`.

[84] Pauli Virtanen et al. “SciPy 1.0: fundamental algorithms for scientific computing in Python”. In: *Nature Methods* 17.3 (Mar. 2020), pp. 261–272. ISSN: 1548-7105. DOI: `10.1038/s41592-019-0686-2`.

[85] John R. Dormand and Peter J. Prince. “A family of embedded Runge-Kutta formulae”. In: *Journal of Computational and Applied Mathematics* 6.1 (Mar. 1980), pp. 19–26. ISSN: 0377-0427. DOI: `10.1016/0771-050X(80)90013-3`.

[86] Hil G. E. Meijer, Fabio Dercole, and Bart Oldeman. “Numerical bifurcation analysis”. In: *Encyclopedia of Complexity and Systems Science*. Springer, July 2009, pp. 6329–6352. DOI: `10.1007/978-0-387-30440-3_373`.

[87] Eusebius J. Doedel. “Lecture Notes on Numerical Analysis of Nonlinear Equations”. In: *Numerical Continuation Methods for Dynamical Systems: Path following and boundary value problems*. Ed. by Bernd Krauskopf, Hinke M. Osinga, and Jorge Galán-Vioque. Understanding Complex Systems. Dordrecht: Springer Netherlands, 2007, pp. 1–49. ISBN: 978-1-4020-6356-5. DOI: `10.1007/978-1-4020-6356-5_1`.

[88] Eusebius J. Doedel et al. *AUTO-07P: Continuation and bifurcation software for ordinary differential equations*. Tech. rep. 2007.

[89] Yuri A. Kuznetsov. *Elements of Applied Bifurcation Theory. 3rd edition*. Springer Science & Business Media, Mar. 2004. ISBN: 978-1-4757-2421-9.

[90] John H. Hubbard and Beverly H. West. *Differential Equations: A Dynamical Systems Approach: Ordinary Differential Equations*. Springer, Nov. 2013. ISBN: 978-1-4612-0937-9.

[91] Herbert B. Keller. “Numerical solution of bifurcation and nonlinear eigenvalue problems.” In: *Applications of bifurcation theory*. Ed. by Paul H. Rabinowitz. Proc Advanced Sem. Univ Wisconsin, Madison: Academic Press, New York, 1977, pp. 359–384.

[92] G. Bard Ermentrout and Nancy J. Kopell. “Parabolic Bursting in an Excitable System Coupled with a Slow Oscillation”. In: *SIAM Journal on Applied Mathematics* 46.2 (Apr. 1986), pp. 233–253. ISSN: 0036-1399. DOI: `10.1137/0146017`.

[93] G. Bard Ermentrout. “Type I Membranes, Phase Resetting Curves, and Synchrony”. In: *Neural Computation* 8.5 (July 1996), pp. 979–1001. ISSN: 0899-7667. DOI: `10.1162/neco.1996.8.5.979`.

[94] Richard Gast, Helmut Schmidt, and Thomas R. Knösche. “A mean-field description of bursting dynamics in spiking neural networks with short-term adaptation”. In: *Neural Computation* 32.9 (July 2020), pp. 1615–1634. ISSN: 0899-7667. DOI: `10.1162/neco_a_01300`.

[95] Richard Gast, Thomas R. Knösche, and Helmut Schmidt. “Mean-field approximations of networks of spiking neurons with short-term synaptic plasticity”. In: *arXiv:2101.06057 [cond-mat, q-bio]* (June 2021). arXiv: 2101.06057 version: 2.

[96] Agnessa Babloyantz and Alain Destexhe. “Low-dimensional chaos in an instance of epilepsy”. In: *Proceedings of the National Academy of Sciences* 83.10 (May 1986), pp. 3513–3517. ISSN: 0027-8424, 1091-6490. DOI: `10.1073/pnas.83.10.3513`.

[97] J. A. Scott Kelso. *Dynamic Patterns: The Self-organization of Brain and Behavior*. MIT Press, 1995. ISBN: 978-0-262-61131-2.

[98] Alessandra Celletti and Alessandro E. P. Villa. “Low-dimensional chaotic attractors in the rat brain”. In: *Biological Cybernetics* 74.5 (May 1996), pp. 387–393. ISSN: 1432-0770. DOI: `10.1007/BF00206705`.

[99] Anil Bollimunta et al. “Neuronal Mechanisms of Cortical Alpha Oscillations in Awake-Behaving Macaques”. In: *Journal of Neuroscience* 28.40 (Oct. 2008), pp. 9976–9988. ISSN: 0270-6474, 1529-2401. DOI: `10.1523/JNEUROSCI.2699-08.2008`.

[100] Andreas Spiegler et al. "Modeling Brain Resonance Phenomena Using a Neural Mass Model". In: *PLOS Computational Biology* 7.12 (Dec. 2011), e1002298. ISSN: 1553-7358. DOI: `10.1371/journal.pcbi.1002298`.

[101] Gustavo Deco and Viktor K. Jirsa. "Ongoing Cortical Activity at Rest: Criticality, Multistability, and Ghost Attractors". In: *Journal of Neuroscience* 32.10 (Mar. 2012), pp. 3366–3375. ISSN: 0270-6474, 1529-2401. DOI: `10.1523/JNEUROSCI.2523-11.2012`.

[102] Hugh R. Wilson and Jack D. Cowan. "Excitatory and Inhibitory Interactions in Localized Populations of Model Neurons". In: *Biophysical Journal* 12.1 (Jan. 1972), pp. 1–24. ISSN: 0006-3495. DOI: `10.1016/S0006-3495(72)86068-5`.

[103] Fernando H. Lopes da Silva et al. "Model of brain rhythmic activity". In: *Biological cybernetics* 15.1 (Mar. 1974), pp. 27–37. ISSN: 1432-0770. DOI: `10.1007/BF00270757`.

[104] Walter J. Freeman. "Models of the dynamics of neural populations". In: *Electroencephalography and clinical neurophysiology. Supplement* 34 (1978), pp. 9–18. ISSN: 0424-8155.

[105] Ben H. Jansen and Vincent G. Rit. "Electroencephalogram and visual evoked potential generation in a mathematical model of coupled cortical columns". In: *Biological Cybernetics* 73.4 (Sept. 1995), pp. 357–366. ISSN: 1432-0770. DOI: `10.1007/BF00199471`.

[106] Peter A. Robinson, Christopher J. Rennie, and James J. Wright. "Propagation and stability of waves of electrical activity in the cerebral cortex". In: *Physical Review E* 56.1 (July 1997), pp. 826–840. DOI: `10.1103/PhysRevE.56.826`.

[107] Peter E. Latham et al. "Intrinsic Dynamics in Neuronal Networks. I. Theory". In: *Journal of Neurophysiology* 83.2 (Feb. 2000), pp. 808–827. ISSN: 0022-3077. DOI: `10.1152/jn.2000.83.2.808`.

[108] Sami El Boustani and Alain Destexhe. "A Master Equation Formalism for Macroscopic Modeling of Asynchronous Irregular Activity States". In: *Neural Computation* 21.1 (Jan. 2009), pp. 46–100. ISSN: 0899-7667. DOI: `10.1162/neco.2009.02-08-710`.

[109] Paul C. Bressloff. "Stochastic Neural Field Theory and the System-Size Expansion". In: *SIAM Journal on Applied Mathematics* 70.5 (Dec. 2009), pp. 1488–1521. ISSN: 0036-1399. DOI: `10.1137/090756971`.

[110] Michael A. Buice, Jack D. Cowan, and Carson C. Chow. "Systematic Fluctuation Expansion for Neural Network Activity Equations". In: *Neural Computation* 22.2 (Feb. 2010), pp. 377–426. ISSN: 0899-7667. DOI: `10.1162/neco.2009.02-09-960`.

[111] Michael A. Buice and Carson C. Chow. "Dynamic Finite Size Effects in Spiking Neural Networks". In: *PLOS Computational Biology* 9.1 (Jan. 2013), e1002872. ISSN: 1553-7358. DOI: `10.1371/journal.pcbi.1002872`.

[112] Moritz Deger et al. "Fluctuations and information filtering in coupled populations of spiking neurons with adaptation". In: *Physical Review E* 90.6 (Dec. 2014), p. 062704. DOI: `10.1103/PhysRevE.90.062704`.

[113] Tilo Schwalger, Moritz Deger, and Wulfram Gerstner. "Towards a theory of cortical columns: From spiking neurons to interacting neural populations of finite size". In: *PLOS Computational Biology* 13.4 (Apr. 2017), e1005507. ISSN: 1553-7358. DOI: `10.1371/journal.pcbi.1005507`.

[114] Shinya Watanabe and Steven H. Strogatz. "Integrability of a globally coupled oscillator array". In: *Physical Review Letters* 70.16 (Apr. 1993), pp. 2391–2394. DOI: `10.1103/PhysRevLett.70.2391`.

[115] Carlo R. Laing. "The Dynamics of Networks of Identical Theta Neurons". In: *The Journal of Mathematical Neuroscience* 8.1 (Feb. 2018), p. 4. ISSN: 2190-8567. DOI: `10.1186/s13408-018-0059-7`.

[116] Nicolas Brunel. "Dynamics of Sparsely Connected Networks of Excitatory and Inhibitory Spiking Neurons". In: *Journal of Computational Neuroscience* 8.3 (May 2000), pp. 183–208. ISSN: 1573-6873. DOI: `10.1023/A:1008925309027`.

[117] Duane Q. Nykamp and Daniel Tranchina. "A Population Density Approach That Facilitates Large-Scale Modeling of Neural Networks: Analysis and an Application to Orientation Tuning". In: *Journal of Computational Neuroscience* 8.1 (Jan. 2000), pp. 19–50. ISSN: 1573-6873. DOI: `10.1023/A:1008912914816`.

[118] John Hertz, Alexander Lerchner, and Mandana Ahmadi. "Mean Field Methods for Cortical Network Dynamics". In: *Computational Neuroscience: Cortical Dynamics*. Ed. by Péter Érdi et al. Lecture Notes in Computer Science. Berlin, Heidelberg: Springer, 2004, pp. 71–89. ISBN: 978-3-540-27862-7. DOI: `10.1007/978-3-540-27862-7_4`.

[119] Eilif Muller et al. "Spike-Frequency Adapting Neural Ensembles: Beyond Mean Adaptation and Renewal Theories". In: *Neural Computation* 19.11 (Nov. 2007), pp. 2958–3010. ISSN: 0899-7667. DOI: `10.1162/neco.2007.19.11.2958`. URL: `https://doi.org/10.1162/neco.2007.19.11.2958`.

[120] Javier Baladron et al. "Mean-field description and propagation of chaos in networks of Hodgkin-Huxley and FitzHugh-Nagumo neurons". In: *The Journal of Mathematical Neuroscience* 2.1 (May 2012), p. 10. ISSN: 2190-8567. DOI: `10.1186/2190-8567-2-10`.

[121] Edward Ott and Thomas M. Antonsen. "Low dimensional behavior of large systems of globally coupled oscillators". In: *Chaos: An Interdisciplinary Journal of Nonlinear Science* 18.3 (Sept. 2008), p. 037113. ISSN: 1054-1500. DOI: `10.1063/1.2930766`.

[122] Edward Ott and Thomas M. Antonsen. "Long time evolution of phase oscillator systems". In: *Chaos: An Interdisciplinary Journal of Nonlinear Science* 19.2 (May 2009), p. 023117. ISSN: 1054-1500. DOI: `10.1063/1.3136851`.

[123] Tanushree B. Luke, Ernest Barreto, and Paul So. "Complete classification of the macroscopic behavior of a heterogeneous network of theta neurons". In: *Neural Computation* 25.12 (Sept. 2013), pp. 3207–3234. ISSN: 0899-7667.

[124] Stephen Coombes and Aine Byrne. "Next Generation Neural Mass Models". In: *Nonlinear Dynamics in Computational Neuroscience*. Ed. by Fernando Corinto and Alessandro Torcini. PoliTO Springer Series. Cham: Springer International Publishing, 2019, pp. 1–16. ISBN: 978-3-319-71048-8. DOI: `10.1007/978-3-319-71048-8_1`.

[125] Ernest Montbrió, Diego Pazó, and Alex Roxin. "Macroscopic description for networks of spiking neurons". In: *Physical Review X* 5.2 (June 2015), p. 021028.

[126] Irmantas Ratas and Kestutis Pyragas. "Macroscopic self-oscillations and aging transition in a network of synaptically coupled quadratic integrate-and-fire neurons". In: *Physical Review E* 94.3 (Sept. 2016), p. 032215. DOI: `10.1103/PhysRevE.94.032215`.

[127] Aine Byrne, Matthew J. Brookes, and Stephen Coombes. "A mean field model for movement induced changes in the beta rhythm". In: *Journal of Computational Neuroscience* 43.2 (Oct. 2017), pp. 143–158. ISSN: 1573-6873. DOI: `10.1007/s10827-017-0655-7`.

[128] Bastian Pietras et al. "Exact firing rate model reveals the differential effects of chemical versus electrical synapses in spiking networks". In: *Physical Review E* 100.4 (Oct. 2019), p. 042412. DOI: `10.1103/PhysRevE.100.042412`.

[129] Ernest Montbrió and Diego Pazó. "Exact Mean-Field Theory Explains the Dual Role of Electrical Synapses in Collective Synchronization". In: *Physical Review Letters* 125.24 (Dec. 2020), p. 248101. DOI: `10.1103/PhysRevLett.125.248101`.

[130] Robert S. Zucker and Wade G. Regehr. "Short-Term Synaptic Plasticity". In: *Annual Review of Physiology* 64.1 (2002), pp. 355–405. DOI: `10.1146/annurev.physiol.64.092501.114547`.

[131] John Guckenheimer et al. "Bifurcation, Bursting, and Spike Frequency Adaptation". In: *Journal of Computational Neuroscience* 4.3 (July 1997), pp. 257–277. ISSN: 1573-6873. DOI: `10.1023/A:1008871803040`.

[132] Jan Benda and Andreas V. M. Herz. "A Universal Model for Spike-Frequency Adaptation". In: *Neural Computation* 15.11 (Nov. 2003), pp. 2523–2564. ISSN: 0899-7667. DOI: `10.1162/089976603322385063`.

[133] Misha Tsodyks, Klaus Pawelzik, and Henry Markram. "Neural Networks with Dynamic Synapses". In: *Neural Computation* 10.4 (May 1998), pp. 821–835. ISSN: 0899-7667. DOI: `10.1162/089976698300017502`.

[134] Mathew V. Jones and Gary L. Westbrook. "The impact of receptor desensitization on fast synaptic transmission". In: *Trends in Neurosciences* 19.3 (Mar. 1996), pp. 96–101. ISSN: 0166-2236. DOI: `10.1016/S0166-2236(96)80037-3`.

[135] Jesse E. Hanson and Dieter Jaeger. "Short-Term Plasticity Shapes the Response to Simulated Normal and Parkinsonian Input Patterns in the Globus Pallidus". In: *Journal of Neuroscience* 22.12 (June 2002), pp. 5164–5172. ISSN: 0270-6474, 1529-2401. DOI: `10.1523/JNEUROSCI.22-12-05164.2002`.

[136] Jérôme Baufreton and Mark D. Bevan. "D2-like dopamine receptor-mediated modulation of activity-dependent plasticity at GABAergic synapses in the subthalamic nucleus". In: *The Journal of Physiology* 586.8 (2008), pp. 2121–2142. ISSN: 1469-7793. DOI: `10.1113/jphysiol.2008.151118`.

[137] Galit Fuhrmann, Henry Markram, and Misha Tsodyks. "Spike Frequency Adaptation and Neocortical Rhythms". In: *Journal of Neurophysiology* 88.2 (Aug. 2002), pp. 761–770. ISSN: 0022-3077. DOI: `10.1152/jn.2002.88.2.761`.

[138] Johannes Zierenberg, Jens Wilting, and Viola Priesemann. “Homeostatic Plasticity and External Input Shape Neural Network Dynamics”. In: *Physical Review X* 8.3 (July 2018), p. 031018. DOI: `10.1103/PhysRevX.8.031018`.

[139] Carl van Vreeswijk and David Hansel. “Patterns of Synchrony in Neural Networks with Spike Adaptation”. In: *Neural Computation* 13.5 (May 2001), pp. 959–992. ISSN: 0899-7667. DOI: `10.1162/08997660151134280`.

[140] Guido Gigante, Maurizio Mattia, and Paolo Del Giudice. “Diverse Population-Bursting Modes of Adapting Spiking Neurons”. In: *Physical Review Letters* 98.14 (Apr. 2007), p. 148101. DOI: `10.1103/PhysRevLett.98.148101`.

[141] John E. Lisman. “Bursts as a unit of neural information: making unreliable synapses reliable”. In: *Trends in Neurosciences* 20.1 (Jan. 1997), pp. 38–43. ISSN: 0166-2236. DOI: `10.1016/S0166-2236(96)10070-9`.

[142] Barry W. Connors. “Initiation of synchronized neuronal bursting in neocortex”. In: *Nature* 310.5979 (Aug. 1984), p. 685. ISSN: 1476-4687. DOI: `10.1038/310685a0`.

[143] Collin J. Lobb. “Abnormal bursting as a pathophysiological mechanism in Parkinson’s disease”. In: *Basal Ganglia.* New views on entrainment, oscillations, bursting and perineuronal nets in basal ganglia function and dysfunction 3.4 (Apr. 2014), pp. 187–195. ISSN: 2210-5336. DOI: `10.1016/j.baga.2013.11.002`.

[144] Sooyoung Chung, Xiangrui Li, and Sacha B. Nelson. “Short-Term Depression at Thalamocortical Synapses Contributes to Rapid Adaptation of Cortical Sensory Responses In Vivo”. In: *Neuron* 34.3 (Apr. 2002), pp. 437–446. ISSN: 0896-6273. DOI: `10.1016/S0896-6273(02)00659-1`.

[145] Peter De Maesschalck and Martin Wechselberger. “Neural Excitability and Singular Bifurcations”. In: *Journal of Mathematical Neuroscience* 5.1 (Aug. 2015), p. 16. ISSN: 13408-015. DOI: `10.1186/s13408-015-0029-2`.

[146] Piotr Suffczynski, Stiliyan Kalitzin, and Fernando H. Lopes Da Silva. “Dynamics of non-convulsive epileptic phenomena modeled by a bistable neuronal network”. In: *Neuroscience* 126.2 (Jan. 2004), pp. 467–484. ISSN: 0306-4522. DOI: `10.1016/j.neuroscience.2004.03.014`.

[147] Daisuke Takeshita, Yasuomi D. Sato, and Sonya Bahar. “Transitions between multistable states as a model of epileptic seizure dynamics”. In: *Physical Review E* 75.5 (May 2007), p. 051925. DOI: `10.1103/PhysRevE.75.051925`.

[148] Helmut Schmidt et al. “Network mechanisms underlying the role of oscillations in cognitive tasks”. In: *PLOS Computational Biology* 14.9 (June 2018), e1006430. ISSN: 1553-7358. DOI: `10.1371/journal.pcbi.1006430`.

[149] Adrian Y. C. Wong et al. “Distinguishing between Presynaptic and Postsynaptic Mechanisms of Short-Term Depression during Action Potential Trains”. In: *Journal of Neuroscience* 23.12 (June 2003), pp. 4868–4877. ISSN: 0270-6474, 1529-2401. DOI: `10.1523/JNEUROSCI.23-12-04868.2003`.

[150] Gina G. Turrigiano. "The Self-Tuning Neuron: Synaptic Scaling of Excitatory Synapses". In: *Cell* 135.3 (Oct. 2008), pp. 422–435. ISSN: 0092-8674. DOI: `10.1016/j.cell.2008.10.008`.

[151] Karine Pozo and Yukiko Goda. "Unraveling Mechanisms of Homeostatic Synaptic Plasticity". In: *Neuron* 66.3 (May 2010), pp. 337–351. ISSN: 0896-6273. DOI: `10.1016/j.neuron.2010.04.028`.

[152] Yogesh S. Virkar et al. "Feedback control stabilization of critical dynamics via resource transport on multilayer networks: How glia enable learning dynamics in the brain". In: *Physical Review E* 94.4 (Oct. 2016), p. 042310. DOI: `10.1103/PhysRevE.94.042310`.

[153] Yu-Ting Huang et al. "Positive feedback and synchronized bursts in neuronal cultures". In: *PLOS ONE* 12.11 (Jan. 2017), e0187276. ISSN: 1932-6203. DOI: `10.1371/journal.pone.0187276`.

[154] Misha V. Tsodyks and Henry Markram. "The neural code between neocortical pyramidal neurons depends on neurotransmitter release probability". In: *Proceedings of the National Academy of Sciences* 94.2 (Jan. 1997), pp. 719–723. ISSN: 0027-8424, 1091-6490. DOI: `10.1073/pnas.94.2.719`.

[155] Valentin Schmutz, Wulfram Gerstner, and Tilo Schwalger. "Mesoscopic population equations for spiking neural networks with synaptic short-term plasticity". In: *The Journal of Mathematical Neuroscience* 10.1 (Apr. 2020), p. 5. ISSN: 2190-8567. DOI: `10.1186/s13408-020-00082-z`.

[156] Halgurd Taher, Alessandro Torcini, and Simona Olmi. "Exact neural mass model for synaptic-based working memory". In: *PLOS Computational Biology* 16.12 (Dec. 2020), e1008533. ISSN: 1553-7358. DOI: `10.1371/journal.pcbi.1008533`. (Visited on 01/04/2021).

[157] Richard Gast et al. "PyRates—A Python framework for rate-based neural simulations". In: *PLOS ONE* 14.12 (Dec. 2019), e0225900. ISSN: 1932-6203. DOI: `10.1371/journal.pone.0225900`.

[158] Wulfram Gerstner et al. *Neuronal Dynamics: From Single Neurons to Networks and Models of Cognition*. Cambridge University Press, July 2014. ISBN: 978-1-107-06083-8.

[159] Hitoshi Kita et al. "Role of ionotropic glutamatergic and GABAergic inputs on the firing activity of neurons in the external pallidum in awake monkeys". In: *Journal of Neurophysiology* 92.5 (Nov. 2004), pp. 3069–3084. ISSN: 0022-3077. DOI: `10.1152/jn.00346.2004`.

[160] Jeff N. Mercer et al. "Nav1.6 sodium channels are critical to pacemaking and fast spiking in globus pallidus neurons". In: *Journal of Neuroscience* 27.49 (Dec. 2007), pp. 13552–13566. ISSN: 0270-6474, 1529-2401. DOI: `10.1523/JNEUROSCI.3430-07.2007`.

[161] Vladimir Klinshov, Sergey Kirillov, and Vladimir Nekorkin. "Reduction of the collective dynamics of neural populations with realistic forms of heterogeneity". In: *Physical Review E* 103.4 (Apr. 2021), p. L040302. DOI: `10.1103/PhysRevE.103.L040302`.

[162] Kevin M. Hannay, Daniel B. Forger, and Victoria Booth. "Macroscopic models for networks of coupled biological oscillators". In: *Science Advances* 4.8 (Aug. 2018), e1701047. ISSN: 2375-2548. DOI: `10.1126/sciadv.1701047`.

[163] Eve Marder and Vatsala Thirumalai. "Cellular, synaptic and network effects of neuromodulation". In: *Neural Networks* 15.4 (June 2002), pp. 479–493. ISSN: 0893-6080. DOI: `10.1016/S0893-6080(02)00043-6`.

[164] Fleur Zeldenrust, Wytse J. Wadman, and Bernhard Englitz. "Neural Coding With Bursts—Current State and Future Perspectives". In: *Frontiers in Computational Neuroscience* 12 (July 2018). ISSN: 1662-5188. DOI: `10.3389/fncom.2018.00048`.

[165] Pawel Kudela, Piotr J. Franaszczuk, and Gregory K. Bergey. "Changing excitation and inhibition in simulated neural networks: effects on induced bursting behavior". In: *Biological Cybernetics* 88.4 (Apr. 2003), pp. 276–285. ISSN: 1432-0770. DOI: `10.1007/s00422-002-0381-7`.

[166] Fleur Zeldenrust and Wytse J. Wadman. "Modulation of spike and burst rate in a minimal neuronal circuit with feed-forward inhibition". In: *Neural Networks* 40 (Apr. 2013), pp. 1–17. ISSN: 0893-6080. DOI: `10.1016/j.neunet.2012.12.008`.

[167] György Buzsáki, Costas A. Anastassiou, and Christof Koch. "The origin of extracellular fields and currents — EEG, ECoG, LFP and spikes". In: *Nature reviews. Neuroscience* 13.6 (May 2012), pp. 407–420. ISSN: 1471-003X. DOI: `10.1038/nrn3241`.

[168] Rosalyn J. Moran et al. "A neural mass model of spectral responses in electrophysiology". In: *NeuroImage* 37.3 (Sept. 2007), pp. 706–720. ISSN: 1053-8119. DOI: `10.1016/j.neuroimage.2007.05.032`.

[169] Rosalyn J. Moran et al. "Bayesian estimation of synaptic physiology from the spectral responses of neural masses". In: *NeuroImage* 42.1 (Aug. 2008), pp. 272–284. ISSN: 1053-8119. DOI: `10.1016/j.neuroimage.2008.01.025`.

[170] Peng Wang and Thomas R. Knösche. "A Realistic Neural Mass Model of the Cortex with Laminar-Specific Connections and Synaptic Plasticity – Evaluation with Auditory Habituation". In: *PLOS ONE* 8.10 (Oct. 2013), e77876. DOI: `10.1371/journal.pone.0077876`.

[171] Henry Markram, Yun Wang, and Misha Tsodyks. "Differential signaling via the same axon of neocortical pyramidal neurons". In: *Proceedings of the National Academy of Sciences* 95.9 (Apr. 1998), pp. 5323–5328. ISSN: 0027-8424, 1091-6490. DOI: `10.1073/pnas.95.9.5323`.

[172] Gilad Silberberg, Caizhi Wu, and Henry Markram. "Synaptic dynamics control the timing of neuronal excitation in the activated neocortical microcircuit". In: *The Journal of Physiology* 556.1 (2004), pp. 19–27. ISSN: 1469-7793. DOI: `https://doi.org/10.1113/jphysiol.2004.060962`.

[173] Joshua C. Brumberg and Boris S. Gutkin. "Cortical pyramidal cells as non-linear oscillators: Experiment and spike-generation theory". In: *Brain Research* 1171 (Sept. 2007), pp. 122–137. ISSN: 0006-8993. DOI: `10.1016/j.brainres.2007.07.028`.

[174] Alex M. Thomson and Jim Deuchars. "Temporal and spatial properties of local circuits in neocortex". In: *Trends in Neurosciences* 17.3 (Jan. 1994), pp. 119–126. ISSN: 0166-2236. DOI: `10.1016/0166-2236(94)90121-X`.

[175] Juan A. Varela et al. "A Quantitative Description of Short-Term Plasticity at Excitatory Synapses in Layer 2/3 of Rat Primary Visual Cortex". In: *Journal of Neuroscience* 17.20 (Oct. 1997). ISSN: 0270-6474, 1529-2401. DOI: `10.1523/JNEUROSCI.17-20-07926.1997`.

[176] Chris M. Hempel et al. "Multiple Forms of Short-Term Plasticity at Excitatory Synapses in Rat Medial Prefrontal Cortex". In: *Journal of Neurophysiology* 83.5 (May 2000), pp. 3031–3041. ISSN: 0022-3077. DOI: `10.1152/jn.2000.83.5.3031`.

[177] Alex D. Reyes. "Synaptic short-term plasticity in auditory cortical circuits". In: *Hearing Research*. Synaptic Plasticity 279.1 (Sept. 2011), pp. 60–66. ISSN: 0378-5955. DOI: `10.1016/j.heares.2011.04.017`.

[178] Anna Levina, J. Michael Herrmann, and Theo Geisel. "Dynamical synapses causing self-organized criticality in neural networks". In: *Nature Physics* 3.12 (Dec. 2007), pp. 857–860. ISSN: 1745-2481. DOI: `10.1038/nphys758`.

[179] Richard Gast et al. "On the role of arkypallidal and prototypical neurons for phase transitions in the external pallidum". In: *Journal of Neuroscience* (June 2021). ISSN: 0270-6474, 1529-2401. DOI: `10.1523/JNEUROSCI.0094-21.2021`.

[180] Garrett E. Alexander and Michael D. Crutcher. "Functional architecture of basal ganglia circuits: neural substrates of parallel processing." In: *Trends in neurosciences* 13.7 (July 1990), pp. 266–271. ISSN: 0166-2236.

[181] J. Paul Bolam et al. "Synaptic organisation of the basal ganglia". In: *Journal of Anatomy* 196.4 (2000), pp. 527–542. ISSN: 0002-9106.

[182] Ned Jenkinson, Andrea A. Kühn, and Peter Brown. "Gamma oscillations in the human basal ganglia". In: *Experimental Neurology*. Special Issue: Neuronal oscillations in movement disorders 245 (July 2013), pp. 72–76. ISSN: 0014-4886. DOI: `10.1016/j.expneurol.2012.07.005`.

[183] Roxanne Lofredi et al. "Pallidal beta bursts in Parkinson's disease and dystonia". In: *Movement Disorders* 34.3 (2019), pp. 420–424. ISSN: 1531-8257. DOI: `10.1002/mds.27524`.

[184] Henning Schroll and Fred H. Hamker. "Basal Ganglia dysfunctions in movement disorders: What can be learned from computational simulations". In: *Movement Disorders* 31.11 (Nov. 2016), pp. 1591–1601. ISSN: 1531-8257. DOI: `10.1002/mds.26719`. URL: `http://dx.doi.org/10.1002/mds.26719`.

[185] Jonathan E Rubin. "Computational models of basal ganglia dysfunction: the dynamics is in the details". In: *Current Opinion in Neurobiology*. Computational Neuroscience 46 (Oct. 2017), pp. 127–135. ISSN: 0959-4388. DOI: `10.1016/j.conb.2017.08.011`.

[186] Azzedine Abdi et al. "Prototypic and arkypallidal neurons in the dopamine-intact external globus pallidus". In: *Journal of Neuroscience* 35.17 (Apr. 2015), pp. 6667–6688. ISSN: 0270-6474, 1529-2401. DOI: `10.1523/JNEUROSCI.4662-14.2015`.

[187] Vivian M. Hernández et al. "Parvalbumin+ neurons and Npas1+ neurons are distinct neuron classes in the mouse external globus pallidus". In: *Journal of Neuroscience* 35.34 (Aug. 2015), pp. 11830–11847. ISSN: 0270-6474, 1529-2401. DOI: `10.1523/JNEUROSCI.4672-14.2015`. (Visited on 02/13/2020).

[188] Paul D. Dodson et al. "Distinct Developmental Origins Manifest in the Specialized Encoding of Movement by Adult Neurons of the External Globus Pallidus". In: *Neuron* 86.2 (Apr. 2015), pp. 501–513. ISSN: 0896-6273. DOI: `10.1016/j.neuron.2015.03.007`.

[189] David Terman et al. "Activity Patterns in a Model for the Subthalamopallidal Network of the Basal Ganglia". In: *The Journal of Neuroscience* 22.7 (Apr. 2002), p. 2963.

[190] Sacha J. van Albada et al. "Mean-field modeling of the basal ganglia-thalamocortical system. II: Dynamics of parkinsonian oscillations". In: *Journal of Theoretical Biology* 257.4 (Apr. 2009), pp. 664–688. ISSN: 0022-5193. DOI: `10.1016/j.jtbi.2008.12.013`.

[191] Alejo J. Nevado Holgado, John R. Terry, and Rafal Bogacz. "Conditions for the Generation of Beta Oscillations in the Subthalamic Nucleus–Globus Pallidus Network". In: *The Journal of Neuroscience* 30.37 (Sept. 2010), p. 12340. DOI: `10.1523/JNEUROSCI.0817-10.2010`.

[192] Rosalyn J. Moran et al. "Alterations in Brain Connectivity Underlying Beta Oscillations in Parkinsonism". In: *PLOS Computational Biology* 7.8 (Aug. 2011), e1002124. ISSN: 1553-7358. DOI: `https://doi.org/10.1371/journal.pcbi.1002124`.

[193] Alison J. Cooper and Ian M. Stanford. "Electrophysiological and morphological characteristics of three subtypes of rat globus pallidus neurone in vitro". In: *The Journal of Physiology* 527.2 (2000), pp. 291–304. ISSN: 1469-7793. DOI: `10.1111/j.1469-7793.2000.t01-1-00291.x`.

[194] Nicolas Mallet et al. "Dichotomous organization of the external globus pallidus". In: *Neuron* 74.6 (June 2012), pp. 1075–1086. ISSN: 0896-6273. DOI: `10.1016/j.neuron.2012.04.027`.

[195] Fumino Fujiyama et al. "A single-neuron tracing study of arkypallidal and prototypic neurons in healthy rats". In: *Brain Structure and Function* 221.9 (Dec. 2016), pp. 4733–4740. ISSN: 1863-2661. DOI: `10.1007/s00429-015-1152-2`.

[196] Maya Ketzef and Gilad Silberberg. "Differential synaptic input to external globus pallidus neuronal subpopulations in vivo". In: *Neuron* doi (Nov. 2020), 10.1016/j.neuron.2020.11.006. ISSN: 0896-6273. DOI: `10.1016/j.neuron.2020.11.006`.

[197] Arin Pamukcu et al. "Parvalbumin+ and Npas1+ Pallidal Neurons Have Distinct Circuit Topology and Function". In: *Journal of Neuroscience* 40.41 (Oct. 2020), pp. 7855–7876. ISSN: 0270-6474, 1529-2401. DOI: `10.1523/JNEUROSCI.0361-20.2020`.

[198] Matthew Henry Higgs et al. "Periodic unitary synaptic currents in the mouse globus pallidus during spontaneous firing in slices". In: *Journal of Neurophysiology* (Mar. 2021). ISSN: 0022-3077. DOI: `10.1152/jn.00071.2021`.

[199] Cristina Miguelez et al. “Altered pallido-pallidal synaptic transmission leads to aberrant firing of globus pallidus neurons in a rat model of Parkinson’s disease”. In: *The Journal of Physiology* 590.22 (2012), pp. 5861–5875. ISSN: 1469-7793. DOI: `10.1113/jphysiol.2012.241331`.

[200] Hitoshi Kita. “Globus pallidus external segment”. In: *Gaba and the Basal Ganglia* 160 (Jan. 2007), pp. 111–133. ISSN: 0079-6123. DOI: `10.1016/S0079-6123(06)60007-1`.

[201] Mahlon R. DeLong. “Activity of pallidal neurons during movement.” In: *Journal of Neurophysiology* 34.3 (May 1971), pp. 414–427. ISSN: 0022-3077. DOI: `10.1152/jn.1971.34.3.414`.

[202] Dieter Jaeger and Hitoshi Kita. “Functional connectivity and integrative properties of globus pallidus neurons”. In: *Neuroscience*. Function and Dysfunction of the Basal Ganglia 198 (Dec. 2011), pp. 44–53. ISSN: 0306-4522. DOI: `10.1016/j.neuroscience.2011.07.050`.

[203] Asier Aristieta et al. “A Disynaptic Circuit in the Globus Pallidus Controls Locomotion Inhibition”. In: *Current Biology* 31.4 (Feb. 2021), 707–721.e7. ISSN: 0960-9822. DOI: `10.1016/j.cub.2020.11.019`.

[204] Boris S. Gutkin, G. Bard Ermentrout, and Alex D. Reyes. “Phase-response curves give the responses of neurons to transient inputs”. In: *Journal of Neurophysiology* 94.2 (Aug. 2005), pp. 1623–1635. ISSN: 0022-3077. DOI: `10.1152/jn.00359.2004`.

[205] Nathan W. Schultheiss, Jeremy R. Edgerton, and Dieter Jaeger. “Phase response curve analysis of a full morphological globus pallidus neuron model reveals distinct perisomatic and dendritic modes of synaptic integration”. In: *Journal of Neuroscience* 30.7 (Feb. 2010), pp. 2767–2782. ISSN: 0270-6474, 1529-2401. DOI: `10.1523/JNEUROSCI.3959-09.2010`.

[206] Tomohiro Fujita, Tomoki Fukai, and Katsunori Kitano. “Influences of membrane properties on phase response curve and synchronization stability in a model globus pallidus neuron”. In: *Journal of Computational Neuroscience* 32.3 (June 2012), pp. 539–553. ISSN: 1573-6873. DOI: `10.1007/s10827-011-0368-2`. (Visited on 02/12/2020).

[207] Grégory Dumont and Boris Gutkin. “Macroscopic phase resetting-curves determine oscillatory coherence and signal transfer in inter-coupled neural circuits”. In: *PLOS Computational Biology* 15.5 (Sept. 2019), e1007019. ISSN: 1553-7358. DOI: `10.1371/journal.pcbi.1007019`.

[208] Cengiz Günay, Jeremy R. Edgerton, and Dieter Jaeger. “Channel density distributions explain spiking variability in the globus pallidus: A combined physiology and computer simulation database approach”. In: *Journal of Neuroscience* 28.30 (July 2008), pp. 7476–7491. ISSN: 0270-6474, 1529-2401. DOI: `10.1523/JNEUROSCI.4198-07.2008`.

[209] Karina P. Abrahao et al. “Ethanol-Sensitive Pacemaker Neurons in the Mouse External Globus Pallidus”. In: *Neuropsychopharmacology* 42.5 (Apr. 2017), pp. 1070–1081. ISSN: 1740-634X. DOI: `10.1038/npp.2016.251`.

[210] Helmut Schmidt and Thomas R. Knösche. “Action potential propagation and synchronisation in myelinated axons”. In: *PLoS Computational Biology* 15.10 (Oct. 2019), e1007004. ISSN: 1553-734X. DOI: `10.1371/journal.pcbi.1007004`.

[211] Hal Smith. “Distributed delay equations and the linear chain trick”. In: *An Introduction to Delay Differential Equations with Applications to the Life Sciences*. Texts in Applied Mathematics. New York, NY: Springer, 2011, pp. 119–130. ISBN: 978-1-4419-7646-8. DOI: `10.1007/978-1-4419-7646-8_7`.

[212] Kaoru Fujimura. “Centre manifold reduction and the Stuart-Landau equation for fluid motions”. In: *Proceedings of the Royal Society of London. Series A: Mathematical, Physical and Engineering Sciences* 453.1956 (Jan. 1997), pp. 181–203. DOI: `10.1098/rspa.1997.0011`.

[213] Dieter Jaeger, Sid Gilman, and J. Wayne Aldridge. “Neuronal activity in the striatum and pallidum of primates related to the execution of externally cued reaching movements”. In: *Brain Research* 694.1 (Oct. 1995), pp. 111–127. ISSN: 0006-8993. DOI: `10.1016/0006-8993(95)00780-T`.

[214] Marcel A. J. Lourens et al. “Exploiting pallidal plasticity for stimulation in Parkinson’s disease”. In: *Journal of Neural Engineering* 12.2 (Feb. 2015), p. 026005. ISSN: 1741-2552. DOI: `10.1088/1741-2560/12/2/026005`.

[215] Robert E. Sims et al. “Functional characterization of GABAergic pallidopallidal and striatopallidal synapses in the rat globus pallidus in vitro”. In: *European Journal of Neuroscience* 28.12 (2008), pp. 2401–2408. ISSN: 1460-9568. DOI: `10.1111/j.1460-9568.2008.06546.x`.

[216] Adriano B. L. Tort et al. “Measuring phase-amplitude coupling between neuronal oscillations of different frequencies”. In: *Journal of Neurophysiology* 104.2 (May 2010), pp. 1195–1210. ISSN: 0022-3077. DOI: `10.1152/jn.00106.2010`.

[217] Atsushi Nambu and Rodolfo R. Llinas. “Electrophysiology of globus pallidus neurons in vitro”. In: *Journal of Neurophysiology* 72.3 (Sept. 1994), pp. 1127–1139. ISSN: 0022-3077. DOI: `10.1152/jn.1994.72.3.1127`.

[218] Jon López-Azcárate et al. “Coupling between beta and high-frequency activity in the human subthalamic nucleus may be a pathophysiological mechanism in Parkinson’s disease”. In: *The Journal of Neuroscience* 30.19 (May 2010), p. 6667. DOI: `10.1523/JNEUROSCI.5459-09.2010`.

[219] Mariano Andrés Belluscio et al. “Oscillations in the basal ganglia in Parkinson’s disease: Role of the striatum”. In: *Basal Ganglia*. New views on entrainment, oscillations, bursting and perineuronal nets in basal ganglia function and dysfunction 3.4 (Apr. 2014), pp. 203–212. ISSN: 2210-5336. DOI: `10.1016/j.baga.2013.11.003`.

[220] Stefano Luccioli, David Angulo-Garcia, and Alessandro Torcini. “Neural activity of heterogeneous inhibitory spiking networks with delay”. In: *Physical Review E* 99.5 (May 2019), p. 052412. DOI: `10.1103/PhysRevE.99.052412`.

[221] Andrea Ceni et al. “Cross frequency coupling in next generation inhibitory neural mass models”. In: *Chaos: An Interdisciplinary Journal of Nonlinear Science* 30.5 (May 2020), p. 053121. ISSN: 1054-1500. DOI: `10.1063/1.5125216`.

[222] Andreas Horn et al. “Connectivity Predicts deep brain stimulation outcome in Parkinson disease”. In: *Annals of Neurology* 82.1 (2017), pp. 67–78. ISSN: 1531-8249. DOI: `10.1002/ana.24974`.

[223] Benoit Duchet et al. “Phase-dependence of response curves to deep brain stimulation and their relationship: from essential tremor patient data to a Wilson–Cowan model”. In: *Journal of Mathematical Neuroscience* 10 (Mar. 2020). ISSN: 2190-8567. DOI: `10.1186/s13408-020-00081-0`.

[224] Zixiao Yin et al. “Local field potentials in Parkinson’s disease: A frequency-based review”. In: *Neurobiology of Disease* 155 (July 2021), p. 105372. ISSN: 0969-9961. DOI: `10.1016/j.nbd.2021.105372`.

[225] Alejo J. Nevado-Holgado et al. “Effective connectivity of the subthalamic nucleus–globus pallidus network during Parkinsonian oscillations”. In: *The Journal of Physiology* (Nov. 2014), pp. 1429–1455. ISSN: 0022-3751. DOI: `10.1113/jphysiol.2013.259721@10.1002/(ISSN)1469-7793(CAT)VirtualIssues(VI)SfN2014`.

[226] Paula Sanz-Leon et al. “Mathematical framework for large-scale brain network modeling in The Virtual Brain”. In: *NeuroImage* 111 (May 2015), pp. 385–430. ISSN: 10538119. DOI: `10.1016/j.neuroimage.2015.01.002`.

[227] Karl J. Friston, Lee M. Harrison, and Will Penny. “Dynamic causal modelling”. In: *NeuroImage* 19.4 (Aug. 2003), pp. 1273–1302. ISSN: 1053-8119. DOI: `10.1016/S1053-8119(03)00202-7`.

[228] Trevor Bekolay et al. “Nengo: a Python tool for building large-scale functional brain models”. In: *Frontiers in Neuroinformatics* 7 (2014). ISSN: 1662-5196. DOI: `10.3389/fninf.2013.00048`.

[229] Marc-Oliver Gewaltig and Markus Diesmann. “NEST (NEural Simulation Tool)”. In: *Scholarpedia* 2.4 (Apr. 2007), p. 1430. ISSN: 1941-6016. DOI: `10.4249/scholarpedia.1430`.

[230] Julien Vitay, Helge Uelo Dinkelbach, and Fred H. Hamker. “ANNarchy: a code generation approach to neural simulations on parallel hardware”. In: *Frontiers in Neuroinformatics* 9 (2015). ISSN: 1662-5196. DOI: `10.3389/fninf.2015.00019`.

[231] Dan F. M. Goodman and Romain Brette. “The Brian simulator”. In: *Frontiers in Neuroscience* 3 (2009). ISSN: 1662-453X. DOI: `10.3389/neuro.01.026.2009`.

[232] Michael L. Hines and Nicholas T. Carnevale. “The NEURON Simulation Environment”. In: *Neural Computation* 9.6 (Aug. 1997), pp. 1179–1209. ISSN: 0899-7667. DOI: `10.1162/neco.1997.9.6.1179`.

[233] Sylvain Baillet, John C. Mosher, and Richard M. Leahy. “Electromagnetic brain mapping”. In: *IEEE Signal Processing Magazine* 18.6 (Nov. 2001), pp. 14–30. ISSN: 1558-0792. DOI: `10.1109/79.962275`.

[234] Nikos K. Logothetis and Brian A. Wandell. “Interpreting the BOLD Signal”. In: *Annual Review of Physiology* 66.1 (Feb. 11, 2004), pp. 735–769. ISSN: 0066-4278. DOI: `10.1146/annurev.physiol.66.082602.092845`.

[235] Ole Jensen et al. “On the human sensorimotor-cortex beta rhythm: Sources and modeling”. In: *NeuroImage* 26.2 (June 2005), pp. 347–355. ISSN: 1053-8119. DOI: `10.1016/j.neuroimage.2005.02.008`.

[236] Maxwell A. Sherman et al. “Neural mechanisms of transient neocortical beta rhythms: Converging evidence from humans, computational modeling, monkeys, and mice”. In: *Proceedings of the National Academy of Sciences* 113.33 (Aug. 2016), E4885–E4894. ISSN: 0027-8424, 1091-6490. DOI: `10.1073/pnas.1604135113`.

[237] Samuel A. Neymotin et al. *Human Neocortical Neurosolver*. 2018. DOI: `10.5281/zenodo.1446517`.

[238] Espen Hagen et al. “Multimodal Modeling of Neural Network Activity: Computing LFP, ECoG, EEG, and MEG Signals With LFPy 2.0”. In: *Frontiers in Neuroinformatics* 12 (2018). ISSN: 1662-5196. DOI: `10.3389/fninf.2018.00092`.

[239] Stephen Coombes. “Large-scale neural dynamics: simple and complex.” In: *NeuroImage* 52.3 (Sept. 2010), pp. 731–739. ISSN: 1095-9572 1053-8119. DOI: `10.1016/j.neuroimage.2010.01.045`.

[240] Olivier David and Karl J. Friston. “A neural mass model for MEG/EEG:: coupling and neuronal dynamics”. In: *NeuroImage* 20.3 (2003), pp. 1743–1755.

[241] Filippo Cona et al. “A neural mass model of interconnected regions simulates rhythm propagation observed via TMS-EEG”. In: *NeuroImage* 57.3 (Aug. 1, 2011), pp. 1045–1058. ISSN: 1053-8119. DOI: `10.1016/j.neuroimage.2011.05.007`.

[242] Michael Breakspear. “Dynamic models of large-scale brain activity”. In: *Nat Neurosci* 20.3 (Mar. 2017), pp. 340–352. ISSN: 1097-6256.

[243] Olivier David et al. “Dynamic causal modeling of evoked responses in EEG and MEG”. In: *NeuroImage* 30.4 (May 1, 2006), pp. 1255–1272. ISSN: 1053-8119. DOI: `10.1016/j.neuroimage.2005.10.045`.

[244] Abbas Babajani and Hamid Soltanian-Zadeh. “Integrated MEG/EEG and fMRI model based on neural masses”. In: *IEEE Transactions on Biomedical Engineering* 53.9 (Sept. 2006), pp. 1794–1801. ISSN: 0018-9294. DOI: `10.1109/TBME.2006.873748`.

[245] Roberto C. Sotero et al. “Realistically Coupled Neural Mass Models Can Generate EEG Rhythms”. In: *Neural Computation* 19.2 (Jan. 5, 2007), pp. 478–512. ISSN: 0899-7667. DOI: `10.1162/neco.2007.19.2.478`.

[246] Ingo Bojak et al. “Connecting Mean Field Models of Neural Activity to EEG and fMRI Data”. In: *Brain Topography* 23.2 (June 1, 2010), pp. 139–149. ISSN: 1573-6792. DOI: `10.1007/s10548-010-0140-3`.

[247] Angela C. E. Onslow, Matthew W. Jones, and Rafal Bogacz. “A Canonical Circuit for Generating Phase-Amplitude Coupling”. In: *PLOS ONE* 9.8 (Aug. 19, 2014), e102591. DOI: `10.1371/journal.pone.0102591`.

[248] Tim Kunze et al. "Transcranial direct current stimulation changes resting state functional connectivity: A large-scale brain network modeling study". In: *NeuroImage* 140 (Supplement C Oct. 15, 2016), pp. 174–187. ISSN: 1053-8119. DOI: `10.1016/j.neuroimage.2016.02.015`.

[249] Ben H. Jansen, George Zouridakis, and Michael E. Brandt. "A neurophysiologically-based mathematical model of flash visual evoked potentials". In: *Biological Cybernetics* 68.3 (Jan. 1, 1993), pp. 275–283. ISSN: 1432-0770. DOI: `10.1007/BF00224863`.

[250] Andreas Spiegler et al. "Bifurcation analysis of neural mass models: Impact of extrinsic inputs and dendritic time constants". In: *NeuroImage* 52.3 (Sept. 1, 2010), pp. 1041–1058. ISSN: 1053-8119. DOI: `10.1016/j.neuroimage.2009.12.081`.

[251] Travis E. Oliphant. *A guide to NumPy*. USA: Trelgol Publishing, 2006.

[252] Oren Ben-Kiki, Clark Evans, and Ingy döt Net. *YAML Ain't Markup Language (YAML^{TM}) Version 1.2*. 2009. URL: `https://yaml.org/spec/1.2/spec.html`.

[253] Aric A. Hagberg, Daniel A. Schult, and Pieter J. Swart. "Exploring Network Structure, Dynamics, and Function using NetworkX". In: *Proceedings of the 7th Python in Science Conference*. Ed. by G. Varoquaux, T. Vaught, and J. Millman. Pasadena, CA USA, 2008, pp. 11–15.

[254] Martin Abadi et al. *TensorFlow: Large-Scale Machine Learning on Heterogeneous Systems*. 2015. URL: `http://tensorflow.org/`.

[255] Wes McKinney. "Data Structures for Statistical Computing in Python". In: *Proceedings of the 9th Python in Science Conference*. Ed. by Stéfan van der Walt and Jarrod Millman. 2010, pp. 51–56.

[256] Hugh R. Wilson and Jack D. Cowan. "A mathematical theory of the functional dynamics of cortical and thalamic nervous tissue". In: *Kybernetik* 13.2 (Sept. 1973), pp. 55–80. ISSN: 1432-0770. DOI: `10.1007/BF00288786`.

[257] Yoshiki Kuramoto. "Collective synchronization of pulse-coupled oscillators and excitable units". In: *Physica D: Nonlinear Phenomena* 50.1 (May 1991), pp. 15–30. ISSN: 0167-2789. DOI: `10.1016/0167-2789(91)90075-K`.

[258] Emden R. Gansner and Stephen C. North. "An open graph visualization system and its applications to software engineering". In: *Software - Practice and Experience* 30.11 (2000), pp. 1203–1233.

[259] Alexandre Gramfort et al. "MEG and EEG data analysis with MNE-Python". In: *Front. Neurosci.* 7 (2013). ISSN: 1662-453X. DOI: `10.3389/fnins.2013.00267`.

[260] Alexandre Gramfort et al. "MNE software for processing MEG and EEG data". In: *NeuroImage* 86 (Feb. 2014), pp. 446–460. ISSN: 1053-8119. DOI: `10.1016/j.neuroimage.2013.10.027`.

[261] Sergey L. Gratiy et al. "BioNet: A Python interface to NEURON for modeling large-scale networks". In: *PLOS ONE* 13.8 (Feb. 2018), e0201630. ISSN: 1932-6203. DOI: `10.1371/journal.pone.0201630`.

[262] Salvador Dura-Bernal et al. “NetPyNE, a tool for data-driven multiscale modeling of brain circuits”. In: *eLife* 8 (Apr. 2019), e44494. ISSN: 2050-084X. DOI: `10.7554/eLife.44494`.

[263] Petra Ritter et al. “The Virtual Brain Integrates Computational Modeling and Multimodal Neuroimaging”. In: *Brain Connectivity* 3.2 (Apr. 2013), pp. 121–145. ISSN: 2158-0014. DOI: `10.1089/brain.2012.0120`.

[264] *DiPDE Simulator [Internet].* 2015. URL: `https://github.com/AllenInstitute/dipde`.

[265] Marc de Kamps and Volker Baier. “Multiple Interacting Instantiations of Neuronal Dynamics (MIIND): a Library for Rapid Prototyping of Models in Cognitive Neuroscience”. In: *2007 International Joint Conference on Neural Networks.* Aug. 2007, pp. 2829–2834. DOI: `10.1109/IJCNN.2007.4371408`.

[266] Thomas Bäck and Hans-Paul Schwefel. “An Overview of Evolutionary Algorithms for Parameter Optimization”. In: *Evolutionary Computation* 1.1 (Mar. 1993), pp. 1–23. ISSN: 1063-6560. DOI: `10.1162/evco.1993.1.1.1`.

[267] Paul Shannon et al. “Cytoscape: a software environment for integrated models of biomolecular interaction networks”. In: *Genome Res.* 13.11 (Nov. 2003), pp. 2498–2504. ISSN: 1088-9051. DOI: `10.1101/gr.1239303`.

[268] Michael Waskom. *Seaborn: statistical data visualization.* 2012. URL: `https://seaborn.pydata.org/` (visited on 01/23/2019).

[269] Konstantin Weise et al. “Pygpc: A sensitivity and uncertainty analysis toolbox for Python”. In: *SoftwareX* 11 (Jan. 2020), p. 100450. ISSN: 2352-7110. DOI: `10.1016/j.softx.2020.100450`.

[270] Robert J. Sternberg, Karin Sternberg, and Jeff Mio. *Cognitive psychology.* Cengage Learning Press, 2012.

[271] Ezia Guatteo, Maria Letizia Cucchiaroni, and Nicola B. Mercuri. “Substantia Nigra Control of Basal Ganglia Nuclei”. In: *Birth, Life and Death of Dopaminergic Neurons in the Substantia Nigra.* Ed. by Giuseppe Giovanni, Vincenzo Di Matteo, and Ennio Esposito. Vienna: Springer Vienna, 2009, pp. 91–101. ISBN: 978-3-211-92660-4. DOI: `10.1007/978-3-211-92660-4_7`.

[272] Erik Ziegler et al. “Mapping track density changes in nigrostriatal and extranigral pathways in Parkinson’s disease”. In: *NeuroImage* 99.Supplement C (Oct. 2014), pp. 498–508. ISSN: 1053-8119. DOI: `10.1016/j.neuroimage.2014.06.033`.

[273] Roxanne Lofredi et al. “Beta bursts during continuous movements accompany the velocity decrement in Parkinson’s disease patients”. In: *Neurobiology of Disease* 127 (July 2019), pp. 462–471. ISSN: 0969-9961. DOI: `10.1016/j.nbd.2019.03.013`.

[274] Jovana J. Belić, Arvind Kumar, and Jeanette Hellgren Kotaleski. “Interplay between periodic stimulation and GABAergic inhibition in striatal network oscillations”. In: *PLOS ONE* 12.4 (Apr. 2017), e0175135. DOI: `10.1371/journal.pone.0175135`.

[275] Karthik Kumaravelu, David T. Brocker, and Warren M. Grill. “A biophysical model of the cortex-basal ganglia-thalamus network in the 6-OHDA lesioned rat model of Parkinson’s disease”. In: *Journal of Computational Neuroscience* 40.2 (Apr. 2016), pp. 207–229. ISSN: 1573-6873. DOI: `10.1007/s10827-016-0593-9`.

[276] Mark D. Humphries, Ric Wood, and Kevin Gurney. “Dopamine-modulated dynamic cell assemblies generated by the GABAergic striatal microcircuit”. In: *Neural Networks*. Cortical Microcircuits 22.8 (Oct. 2009), pp. 1174–1188. ISSN: 0893-6080. DOI: `10.1016/j.neunet.2009.07.018`.

[277] Joshua D. Berke. “Functional Properties of Striatal Fast-Spiking Interneurons”. In: *Frontiers in Systems Neuroscience* 5 (2011). ISSN: 1662-5137. DOI: `10.3389/fnsys.2011.00045`.

[278] Laurent Venance and Jacques Glowinski. “Heterogeneity of spike frequency adaptation among medium spiny neurones from the rat striatum”. In: *Neuroscience* 122.1 (Nov. 2003), pp. 77–92. ISSN: 0306-4522. DOI: `10.1016/S0306-4522(03)00553-0`.

[279] Charles J. Wilson et al. “A Model of Reverse Spike Frequency Adaptation and Repetitive Firing of Subthalamic Nucleus Neurons”. In: *Journal of Neurophysiology* 91.5 (May 2004), pp. 1963–1980. ISSN: 0022-3077. DOI: `10.1152/jn.00924.2003`.

[280] Nicolas Maurice et al. “Striatal Cholinergic Interneurons Control Motor Behavior and Basal Ganglia Function in Experimental Parkinsonism”. In: *Cell Reports* 13.4 (Oct. 2015), pp. 657–666. ISSN: 2211-1247. DOI: `10.1016/j.celrep.2015.09.034`. (Visited on 08/15/2018).